

Design and Fabrication of Micromachined Silicon Suspensions

Sunil Kumar

B.Tech.(H), Indian Institute of Technology, Kharagpur 1999

M.S., University of California, Irvine 2000

A dissertation submitted in fulfilment of the requirements for the degree of

Doctor of Philosophy of the University of London

Diploma of Imperial College London

Optical and Semiconductor Device Group

Department of Electrical and Electronic Engineering

Imperial College, London

May 2007

Abstract

This thesis presents the design and fabrication of a low noise lateral silicon suspension for seismic sensing. Optimizing for the sensor size, and performance, a lateral suspension is fabricated with a fundamental resonant frequency of 10 Hz, a quality factor of up to 40000, and Brownian noise equivalent acceleration (NEA) of 0.2 ng/ $\sqrt{\text{Hz}}$.

Low-noise, low-frequency (ω) and high-sensitivity inertial sensors are used to measure the displacement of the Earth's crust. Typical high performance seismometers are few kilograms in weight with NEA in the sub-nano-g range. The large size and high cost of current-state of the art seismometers however presents a barrier to its widespread use. The ability of seismometer to resolve vibrations is set by the self-noise of the system so to detect low level vibrations the self-noise of the sensor should be lower than the vibration being measured. The product of mass, period and quality factor is inversely proportional to the self-noise power spectrum of the sensor. Even though there are miniaturized vibration sensors like micromachined accelerometers, they have large self-noise due to the small mass and short period of the sensor.

To realize a micro seismometer with NEA near the low noise seismicity model, a single-axis silicon suspension was designed to be fabricated using through-wafer etching. Frames were placed between sets of springs to increase cross-axis spurious mode rejection. Analytical and numerical models are developed to simulate the suspension dynamics.

Fabricating high-aspect-ratio structures by through-wafer etching is made possible by the use of deep reactive ion etching (DRIE). The springs have an overall vertical profile with some bowing at mid-depth which is accounted for in the dynamical design. Etch parameters have been optimized to improve sidewall smoothness, resulting in higher fracture strength and Q . Deleterious artifacts of DRIE plasma processing are analyzed and reduced or eliminated by process engineering.

A first prototype single-axis micro seismometer was demonstrated by assembling the electromechanical components. The microseismometer has a Q of 252 leading to an NEA of $0.4 \text{ ng}/\sqrt{\text{Hz}}$ at a resonant frequency of 12.65 Hz. Electronic readout of resonant frequencies shows a frequency difference of 100 Hz between the fundamental and next mode.

The suspension developed here can be utilized for other sensing applications. Through-wafer DRIE has been shown to be a reliable process for creating very high- Q , low-frequency suspensions with excellent cross-axis separation.

Table of contents

List of Figures	vi
List of Tables	xiv
Acknowledgements	xv
1 Introduction	1
1.1 Background	2
1.2 Earth Noise	8
1.3 Instrument Noise	10
1.4 Micromachined Accelerometers	14
1.5 Silicon Suspension	17
1.6 Summary	21
1.7 Research Contributions and Scope	23
1.8 Organisation of this Dissertation	25
1.9 Bibliography	27
2 Suspension Design and Feasibility Study	30
2.1 Suspension Noise	31
2.2 Key Parameters affecting Self-noise	31
2.2.1 Resonant frequency	32
2.2.2 Quality factor	34
2.2.3 Proof-mass	37
2.2.4 Cross-axis sensitivity	37
2.3 Suspension: Generic Design Principle	38
2.3.1 Homogenous triaxial configuration	41
2.4 Design Inputs	43
2.5 Micromachining Process Design Limitations	50
2.6 Feasibility Study	52
2.7 Summary	53
2.8 Conclusion	54
2.9 Bibliography	56
3 Suspension Dynamics	58
3.1 Introduction	59
3.2 Lateral Suspension	60
3.2.1 On-axis compliance	63
3.2.2 Cross-axis translational compliance	65
3.2.3 Rotational compliance	67
3.2.4 Rejection ratios of spurious modes	70
3.3 Multiple Spring Suspension	72
3.3.1 Effect of spring mass	77
3.3.2 Rejection ratios of spurious modes	80
3.3.3 Vertical deflection under gravity	82
3.4 Intermediate Frames for Multiple Spring Suspension	84
3.4.1 Rejection ratio of spurious modes	87
3.4.2 Comparison of modes for frameless and with-frame suspension	92
3.4.3 Vertical sag under gravity	93
3.5 Effect of Linkage Geometry	95
3.6 Effect of End Connector (Elbow) Stiffness	97
3.7 Optimum Design Parameters	102
3.8 Summary	104

3.9	Conclusion	106
3.10	Bibliography.....	108
4	Suspension: Fabrication	110
4.1	Introduction.....	111
4.2	Deep Reactive Ion Etching (DRIE).....	112
4.2.1	Applications of DRIE.....	115
4.3	Fabrication Process Flow	116
4.3.1	System description	117
4.3.2	Mask preparation.....	119
4.3.3	Pattern transfer	122
4.3.4	Through-wafer etch.....	124
4.3.5	Wafer mounting techniques	126
4.4	DRIE Process Parameters	129
4.5	DRIE Induced Artefacts.....	132
4.5.1	Grassing	132
4.5.2	Etch lag	134
4.5.3	Loading effect	136
4.5.4	Top edge cavitations	137
4.5.5	Etch masking.....	138
4.5.6	Scalloping.....	138
4.5.7	Sidewall roughness.....	139
4.5.8	Etch profile evolution.....	149
4.5.9	Notching.....	154
4.6	Process Engineering.....	168
4.6.1	Process description.....	171
4.6.2	Fabricated devices.....	172
4.7	Summary	178
4.8	Conclusion	179
4.9	Bibliography.....	181
5	Suspension: Characterization	187
5.1	Measurement Techniques	188
5.1.1	Resonant frequencies	188
5.1.2	Quality factor	192
5.2	Experimental Work	193
5.2.1	Resonant frequencies	194
5.2.2	Quality factor at varying pressure.....	197
5.3	Effect of Etch Profile Shape on Suspension Dynamics	200
5.3.1	DRIE etch profile.....	201
5.3.2	Spring profile characterization.....	202
5.3.3	Analytical model.....	204
5.3.4	Compensation for a non-ideal etch profile.....	208
5.4	Summary	213
5.5	Conclusion	214
5.6	Bibliography.....	216
6	Microseismometer: Prototype	217
6.1	Seismometer.....	218
6.2	Lateral Differential Capacitive Array Transducer	220
6.3	Feedback Controller.....	222
6.4	Electromagnetic Actuator	223
6.5	Components of Microseismometer	225

6.5.1	Proof-mass wafer	225
6.5.2	Capping wafer	234
6.5.3	Magnetic unit	238
6.6	Device Assembly	241
6.6.1	Solder reflow	241
6.6.2	Glass frit bonding	244
6.6.3	Vacuum encapsulation	244
6.7	Microseismometer Damping	245
6.8	Experimental Result	247
6.8.1	Experimental measurement setup	248
6.8.2	Microseismometer dynamics measurements	249
6.8.3	Vibration and shock test	251
6.9	Other Issues	258
6.10	Summary	258
6.11	Conclusion	260
6.12	Bibliography	261
7	Conclusions and Future Work	262
7.1	Microseismometer Characterization	264
7.1.1	Alternate designs	264
7.1.2	Fully electrostatic geophone	264
7.2	Modelling Extension	265
7.2.1	Application to other inertial sensors	266
7.2.2	Application to other devices	267
7.3	Applications of Through-Wafer DRIE	267
7.3.1	Other through-wafer devices	267
7.3.2	Silicon molding	268
7.3.3	Single mask through-wafer devices	272
7.3.4	SOI replacement through-wafer devices	273
7.4	Bibliography	275
Appendix A:	Analytical model	276
A1.	Translational Modes	276
A1.1	On-axis compliant stiffness (k_x):	276
A1.2	Cross-axis spring constant along Y-axis (k_y):	277
A1.3	Cross-axis spring constant along Z-axis (k_z):	278
A2.	Rotational Modes	280
A2.1	On-axis rotational mode (k_α):	280
A2.2	Cross-axis rotational mode about Y-axis (k_β):	282
A2.3	Cross-axis rotational mode about Z-axis (k_γ):	284
A3.	Bibliography	285
Appendix B:	Numerical model	286
B1.	Finite Element Analysis (FEA)	286
B2.	Isotropic vs. Anisotropic model	287
B3.	Modal analysis using ANSYS	287
B4.	Input files for FEA using ANSYS	288
B5.	Bibliography	307
Appendix C:	Fabrication process flow	308
C1.	Process Flow for Microseismometer Sensor Unit	308
C2.	DRIE Processing of Lateral Suspensions	309

List of Figures

Figure 1.1 Wang Chen-To's visualization of Chang Teng's 132 A.D. design of a seismoscope. Image taken from [1.5].	3
Figure 1.2 Principle of seismometer: the mass is almost stationary due to inertia while the frame moves with the ground [1.1].	5
Figure 1.3 State-of-the-art commercial seismometers, (a) Streckheisen STS-2, (b) Guralp CMG-40T, (c) Guralp CMG-3T without outer housing, (d) Sercel L-4, (e) Geotech KS-2000 borehole seismometer, and (f) Nanometrics Trillium 120P. These are all big, heavy and expensive.	6
Figure 1.4 The USGS New Low Noise Model [1.17], here expressed as Noise Estimated Acceleration in $m/s^2/\sqrt{Hz}$ of ground motion relative to frequency. Mechanical noise levels are plotted for the proposed microseismometer.	9
Figure 1.5 Comparison of noise and resonant frequency of seismometers and a variety of commercial and research accelerometers (datasheet, [1.14, 19, 20]).	12
Figure 1.6 Comparison of noise and volume for traditional seismometer and MEMS accelerometers (datasheet, [1.14, 19, 20]).	13
Figure 1.7 Commercial MEMS accelerometers with sub μg noise levels, (a) Honeywell Q-flex QA3000 with an exploded view of the sensor and its suspension, and (b) Sercel/Tronics GPU3 with SEM of the suspension.	14
Figure 1.8 MEMS accelerometers developed by research groups, (a,b) A $1.0 \mu g/\sqrt{Hz}$ self-noise accelerometer developed by Bernsetin et al. [1.22] at Charles Stark Draper Laboratory, (c,d) Parylene based low-noise accelerometer developed by Suzuki and Tai [1.23] at University of Tokyo, and (e,f) one of the very first miniaturized accelerometer developed at Stanford university by Roylance and Angell [1.26].	16
Figure 1.9 (a) Lateral suspension used in Analog Devices ADXL series accelerometers fabricated by LPCVD deposition of polysilicon and then RIE etch [1.35], (b) Vertical suspension created by anisotropically etching silicon by KOH (Potassium hydroxide) [1.21], and (c) Leaf spring part of a lateral suspension fabricated by DRIE of silicon bonded to an underlying silicon substrate [1.36].	19
Figure 1.10 DRIE devices (a) Endevco accelerometer [1.41], (b) Extended travel range microactuator [1.42].	20
Figure 2.1 Schematic of a mass-spring-damper system.	32
Figure 2.2 Response vs. frequency for a resonating system showing the bandwidth of the systems defined as the frequency width at $1/2$ total energy of the signal.	35
Figure 2.3 An oscillating system with exponential decay of amplitude in time. Decay time constant, τ is the time it takes for the amplitude to decay to $1/e$ times its initial value.	36
Figure 2.4 A simple suspension with folded cantilever beams as spring on either side of a proof-mass attached to a fixed external frame. The pair of springs on either side of the suspension only allows dual planes of mirror symmetry about xy and xz planes as shown by the arrow in the middle of the proof-mass.	39
Figure 2.5 A center-of-gravity suspension design with symmetry along all the three axes. The joint folded cantilever pairs on either side of the proof-mass provide symmetry about xy , yz and xz planes. Symmetry in the lateral plane is shown by the arrows in the middle of the proof-mass. The cantilever pairs are linked at the center to increase the stiffness compared to an unconnected pair.	40
Figure 2.6 Homogenous triaxial configuration also called Galperin configuration (Source: [2.15]). u , v , w are the responses of the sensor along the Galperin axes UVW .	41
Figure 2.7 (a) A typical single spring suspension with preformed springs, (b) showing the off-centred proof-mass in horizontal position and (c) Centring of the proof-mass under gravity in Galperin orientation.	43
Figure 2.8 Schematic of the suspension showing the proof-mass and spring dimensions.	44
Figure 2.9 Variation of natural frequency with die size. Doubling the die length and width (quadrupling the area) decreases the resonant frequency by $4\sqrt{2}$.	45

Figure 2.10 Variation of mechanical noise with resonant frequency for varying Q	46
Figure 2.11 Schematic of the suspension design with one spring and mass which is assumed to be 50% of the die area for initial estimates.....	47
Figure 2.12 Variation of resonant mode with spring thickness for a 20mm×20mm die size and 10mm×16mm proof-mass.....	49
Figure 2.13 Metal traces running on the springs connecting the electromagnetic feedback coil and electrostatic capacitive feedback electrodes.....	50
Figure 2.14 Quality factor (due to squeeze film damping), Q_{squeeze} variation for multiple spring suspension (N).....	53

Figure 3.1 Schematic of a lateral suspension illustrating the model geometry and the critical dimensions.....	60
Figure 3.2 Schematic of a single spring set for the lateral suspension showing the geometry and critical dimensions.....	63
Figure 3.3 Fundamental mode shape of a single spring set lateral suspension. The proof-mass is resonating along the X-axis.....	64
Figure 3.4 ω_y , Mode shape of a single spring set suspension resonating along Y-axis.....	65
Figure 3.5 ω_z , Mode shape of a single spring set suspension resonating along Z-axis.....	66
Figure 3.6 ω_w , Mode shape of a single spring set suspension resonating about X-axis.....	68
Figure 3.7 ω_β , Mode shape of a single spring set suspension resonating about Y-axis.....	69
Figure 3.8 ω_γ , Mode shape of a single spring set suspension resonating about the Z-axis.....	70
Figure 3.9 Schematic of a lateral suspension with multiple springs, (a) a lateral suspension with n set of spring, and (b) a specific lateral suspension with two ($n=2$) spring sets.....	72
Figure 3.10 FEA (Finite Element Analysis) model of a lateral suspension with two set of springs solved using Ansys. The inset shows the arrangement of the nodes and elements in the model.....	74
Figure 3.11 The transition elements are designed such that the nodes at the common boundary are coincident and there is no extreme size change across structures.....	75
Figure 3.12 Fundamental resonant frequency for lateral suspension with varying number of spring sets. The values are calculated using the analytical expression from equation 3.20 and compared against FEA derived values. The deviation of the analytical model from the FEA model can be attributed to the mass of the suspension and the effect of end-connector geometry.....	76
Figure 3.13 To model the first on-axis harmonic ω_{x1} , the spring units of the lateral suspension can be considered as discrete masses separated by massless springs. M is the mass of the proof-mass, the spring are considered as discrete masses m with massless springs of stiffness k connecting them.....	78
Figure 3.14 Plot of the first spurious mode along X-axis (ω_{x1}) with increasing number of spring sets (n). With larger number of spring sets the analytical model approaches the FEA model.....	80
Figure 3.15 Rejection ratio of spurious modes calculated using FEA model for lateral suspension with 1, 2, 3, 4, 5 and 6 sets of springs. The rejection ratio drops significantly for multiple springs except for the rotational mode about X-axis.....	81
Figure 3.16 Logarithmic plot of vertical sag of a lateral suspension in horizontal and Galperin configuration. The sag due to gravity increases with higher number of springs.....	83
Figure 3.17 Schematic of a lateral suspension with a single intermediate frame between two set of springs. The intermediate frame decouples the additional spring sets.....	85
Figure 3.18 Plot of ω_{x1}/ω_x for lateral suspension with n (one to six) spring sets and ($n-1$) intermediate frames. The FEA model used to calculate the rejection ratio is based on the model parameters of Table 3.2 with a frame thickness (f) of 60 μm	87
Figure 3.19 Plot of rejection ratio for lateral suspension with multiple springs calculated using analytical expressions from Table 3.3.....	88
Figure 3.20 Plot of rejection ratio for lateral suspension with multiple springs calculated using a FEA model.....	89
Figure 3.21 Error between the FEA model and analytical expressions for the rejection ratios.....	90

Figure 3.22 Plot of rejection ratio for lateral suspension with three spring sets and two intermediate frames of varying thickness. Most of the rejection ratio except ω_{x1}/ω_x improves with thicker frames though the gain is marginal beyond a certain thickness.	91
Figure 3.23 (a) Reinforced intermediate frames to reduce the weight of the frame while maintain higher rigidity of a thicker frame, as compared to (b) Solid intermediate frame which reduces the on-axis rejection ratio due to the higher weight of the spring-frame unit.	91
Figure 3.24 Comparison of the rejection ratio for a model lateral suspension with multiple springs without frames and with frames. (a) Log-log variation as calculated by FEA of the rejection ratio for the spurious modes as the number of suspension units is increased from 1 to 6. Three fits for the rejection ratio are shown: for x_1 , $1/\sqrt{n}$; for α , independent of n ; for z , $1/n$, and (b) Log-log variation as calculated by FEA of the rejection ratio for the spurious modes of a suspension incorporating intermediate frames as the number of suspension units is increased from 1 to 6. Fits for the rejection ratio are shown: for x_1 , $1/\sqrt{n}$; for α , independent of n	92
Figure 3.25 Effect of intermediate frames on the vertical sag of proof mass under gravity, (a) multiple spring set suspension under gravity with equal deflection of all spring beams as shown in the cross-section view, as compared to (b) multiple spring set suspension with intermediate frame showing a reduction in vertical sag under gravity due to the intermediate frame.	93
Figure 3.26 Reduction ratio for vertical sag under gravity for multiple spring suspension with intermediate frames as compared to frameless suspensions.	94
Figure 3.27 Effect of link width on rejection ratio of the suspension.	95
Figure 3.28 Maximum stress at the sharp corner of the linkage shown by the red pointer in the globe.	96
Figure 3.29 (a) Link design with sharp corners, (b) Link design with corner filleting.	96
Figure 3.30 Schematic of spring element showing the end connector.	97
Figure 3.31 Distortion of the spring beam under an out-of-plane force. The forces acting at the opposite ends of the elbow causes a torque which leads to an angular rotation of θ	98
Figure 3.32 Deflection of the spring beams depending on elbow rigidity, (a) completely rigid elbow with $c = 1$ where the bending is that for a fixed-free cantilever and (b) completely flexible elbow with $c = 4$ where the bending is representative of a fixed-guided cantilever.	99
Figure 3.33 Plot of ω_z and $z_{sag,g}$ from expression in Table 3.5.	101
Figure 4.1 Passivation and etch cycle in a typical DRIE step. (a) Isotropic etch of silicon in exposed regions on the wafer, (b) Deposition of polymer CFn on all surfaces, (c) Preferential etching of polymer from the bottom of the trench by vertically directed positive ions, and (d) Isotropic etching of the trench bottom by fluorine radicals.	113
Figure 4.2 Model for inductively coupled plasma etch showing the positive and negative species in the plasma, their energy angular distribution function (ADF) and the potential drop across the sheath which accelerates the positive ions.	114
Figure 4.3 DRIE devices (a) Actuator-mirror structure fabricated on SOI (Prof. de Rooji, IMT), (b) MicroSEM deflector structure (Prof. de Rooji, IMT), (c) A MEMS gyroscope fabricated on SOI (silicon-on-insulator), and (d) Micro-machined intracellular needle [4.15], pillar etched using DRIE and then post processed to achieve the sharp tip.	116
Figure 4.4 (a) STS DRIE Kit [4.18], (b) STS ICP Multiplex process chamber Schematic (Source: [4.19]).	118
Figure 4.5 A halo mask and its various components for a 2D mask designed on a mask plate for transferring the pattern onto photoresist.	120
Figure 4.6 Sidewall quality for varying channel/trench width, (a) 40 μ m gap, (b) 60 μ m gap showing a widening of the gap towards the bottom of the trench as the profile diverges away from vertical, (c) 80 μ m gap shows the increase in profile shape divergence from vertical with bigger gap, (d) beams with gap varying from 40-400 μ m show the increased breakdown of the sidewall with larger gap.	121
Figure 4.7 SEM image of 9 μ m thick AZ9260 photoresist.	122
Figure 4.8 (a) SEM of 5 μ m thick oxide etched using CHF ₃ , (b) SEM of damaged photoresist (AZ9260, 7 μ m thick) after oxide etch.	123
Figure 4.9 Process flow schematic for through-wafer silicon etching using DRIE.	125

Figure 4.10 Grass formation during silicon etch.....	133
Figure 4.11 Reduced grass formation under increasing platen power, (a) 12W: trench is completely covered with grass, (b) 14W: the centre of the trench bottom is clear but grass is still forming along the sidewall, (c) 16W: clear trench bottom but the sidewalls have grass curtains, (d) 20W: the trench bottom and the sidewall is etched cleanly without any grass formation.	134
Figure 4.12 (a) SEM of etch cross section showing etch lag between small and large trench, (b) Etch depth vs. channel width (all dimensions in μm).	135
Figure 4.13 Process parameters optimized to reduce etch lag lead to grass formation in larger width trench while smaller trenches etch cleanly.	136
Figure 4.14 SEM of top edge damage.	137
Figure 4.15 Micromasking in etch channel resulting in oxford spires.....	138
Figure 4.16 Scalloping (a) Scalloping on a sidewall, (b) AFM scan of top edge of sidewall shows scallops (courtesy: Sanjay Vijendran), (c) SEM of large scalloping on trench sidewall suggesting high etch rate.	139
Figure 4.17 SEM image of sidewall quality of 500 μm high sidewall. a,b,c show tapping mode AFM scan of the top (a), middle (b) and bottom (c) of the trench sidewall. The roughness of the sidewall increases from peak-to-peak 0.4 μm at the top of the trench sidewall to 0.7 μm at the middle of the sidewall and 1.4 μm at the bottom of the sidewall.....	140
Figure 4.18 Schematic of test structure showing region of interest (ROI). A tapered trench was selected to examine sidewall surface quality with varying channel width. The individual structures (beams) can be separated for ease of measurement (courtesy: Werner Karl).	141
Figure 4.19 Sidewall SEM of through-wafer deep reactive-ion etched beam. Zones of varying sidewall morphology are labelled as: A. Overetched, B. Ion damaged, C. Overpassivated, and D. Striations.	142
Figure 4.20 Interferometric measurement of sidewall topography near narrow trench end. The ion bombardment causes holes in the sidewall near the trench bottom where the re-entrant surface emerges above the top edge.....	143
Figure 4.21 SEM picture showing the damage observed at narrow etch-gaps towards the trench bottom caused by ion bombardment (Inset: zoomed, rotated view at a tilt angle of 85°) (courtesy: Werner Karl).	144
Figure 4.22 Passivation build-up observed at wide etch-gaps leading to striations and therefore to rough sidewalls.....	145
Figure 4.23 EDX analysis of the beam shows fluorine presence in the darker areas which were charging up in the SEM, proving the hypothesis of CF ₂ deposition. (a) SEM image of the beam section analysed for Fluorine content showing a higher concentration of carbon and fluorine at the top darker region of SEM image than at the lighter part towards the bottom of the sidewall, (b) Elemental map of the sidewall highlighting (red) the carbon and fluorine dominated regions, and (c) Linescan from the top edge of the beam to the bottom edge showing the concentration of fluorine, carbon and silicon along the etch direction.	146
Figure 4.24 Profile shape of etched trench for various processing conditions in DRIE. (a) Negative profile, (b) Positive profile, (c) Bowed profile.	149
Figure 4.25 Surface potential build-up due to flux imbalance of isotropic electrons and anisotropic ions leading to lateral etching of the trench sidewalls.	152
Figure 4.26 Notching damage at the bottom of a through-wafer etched feature. The wafer was bonded to a handle wafer using photoresist.	155
Figure 4.27 Charge distribution in deep trench and positive charge accumulation at Silicon-insulator interface resulting in lateral undercutting at the trench foot (notching).....	156
Figure 4.28 Process flow schematic for through-wafer etching using a metal backside coating to eliminate notching.....	159
Figure 4.29 Schematic of etch setup with metal coating directly on the wafer backside and then bonded to a handle wafer.....	159
Figure 4.30 (a) Notching damage observed at the foot of a through-wafer etched structure; the wafer was bonded to a handle wafer using thin photoresist. (b) The same structure on a wafer with a thin metal coating on the backside; no damage at the foot of the sidewall is visible.	160
Figure 4.31 Backside of an etched wafer. (a) Etched trenches with no backside metal coating, showing extensive notching. (b) Etched trenches with backside metal coating, showing no visible notching.	161

Figure 4.32 Charge dissipation at metal surface in a silicon trench with a metal coating on the wafer backside.....	161
Figure 4.33 (a) Schematic of test setup with metal coated handle wafer glued to the device wafer at the outside edges, (b) Schematic of the test setup with silicon handle wafer bonded to the device wafer at the outside edge using photoresist.....	162
Figure 4.34 Schematic of experimental setup, (a) metal layer connected to the plasma at edges, (b) metal layer completely isolated.....	162
Figure 4.35 (a) Damage due to partially floating metal layer, (b) Notching damage due to completely floating metal layer.....	163
Figure 4.36 Schematic of test setup with electroplated metal on device wafer backside.....	164
Figure 4.37 Optical image of dry release process by peeling the metal layer from the wafer backside..	164
Figure 4.38 SEM image of trench profile etched for 30 minutes using (a) LF plasma mode showing thinning down of the structures towards the bottom as compared to, (b) HF plasma mode which maintains profile anisotropy better and (c) scallop size for LF mode is 260nm × 818 nm compared to, (d) HF mode scalloping which is 217nm × 770nm.....	165
Figure 4.39 Schematic of experimental setup to investigate effect of good thermal contact between the device and handle wafer, (a) Wafer bonded on the periphery such that when the structures are etched through-wafer, the structures are thermally isolated from the handle wafer, and (b) the device wafer is completely bonded to the handle wafer allowing the isolated structures thermal connectivity to the handle wafer.....	166
Figure 4.40 (a) Optical image of burnt photoresist due to thermal sinking problem – the reflective surface shows normal photoresist, (b) photoresist is burnt in this case on the proof-mass which has bad thermal connectivity through the long springs – the grey non-refelctive surface is burnt resist.....	167
Figure 4.41 Full wafer mask design included 20×20 mm dies as well as 10×10 mm and 5×5 mm dies with lateral suspensions.....	172
Figure 4.42 Mask layout of the horizontal lateral suspension, the inset shows the spring connector and the linkages with the filleting along with the packing pieces.....	173
Figure 4.43 Mask layout of the Galperin configuration lateral suspension, the insets show the spring and linkage along with the packing pieces.....	173
Figure 4.44 Silicon lateral suspension with six sets of springs and three intermediate frames fabricated by DRIE.....	175
Figure 4.45 Close-up of silicon lateral suspension with reduced mass frame and spring with cross-bar.....	175
Figure 4.46 Close-up of spring sidewall.....	176
Figure 4.47 Etch profile shape, (a) spring beam cross-section showing an etch profile which is slightly bowed towards the center, and (b) the profile shape of a cross-section of an intermediate frame showing a similar bow like the spring beam.....	177
Figure 4.48 SEM of a silicon lateral suspension within a 5mm×5mm die.....	177
Figure 5.1 Slow-scan image of suspension under excitation, the edges of the spring and proof mass appear as a sinusoid due to the rastering of the electron beam orthogonal to the direction of motion of the proof mass. The sinusoidal edges show the fundamental mode of the suspension.....	189
Figure 5.2 Overlap of the first spurious mode along the x-axis (ω_{x1}) on top of the normal x-axis mode (ω_x). The $x1$ mode is visible as the higher frequency mode on the springs. The x mode is visible as the low-frequency sinusoid of the proof mass and the springs.....	190
Figure 5.3 SEM of the suspension with the electron beam scanning along the Y-axis of the suspension, the insets show the ω_z and ω_β modes. Inset 1 shows the see-saw motion of the proof mass due to the rotational mode (ω_β) about Y-axis of the suspension. The out-of-plane mode (ω_z) is clearly visible at the center of the proof mass in inset 2 as a constant amplitude oscillation.....	191
Figure 5.4 Ringdown of suspension in SEM slow-scan. Measuring the time taken for the amplitude of oscillations to drop to 1/e of its initial value gives the decay time constant (τ) of the system.....	192
Figure 5.5 Plot of measured quality factor as a function of pressure for 10 Hz silicon suspension.....	197

Figure 5.6 SEM image of beam cross-section. The mask design was for a spring width of 24 μm which is reduced to 22 μm at top edge of the spring during the etch and the middle section of the beam is thinner than the top and bottom.....	202
Figure 5.7 Undercut measurement using Zygo white light interferometer of spring cross-section.	203
Figure 5.8 Measured lateral undercut for 24 μm and 31 μm wide beam.	203
Figure 5.9 Beam cross section of an anisotropically etched beam, (a) rectangular cross-section, (b) bowed cross-section.	204
Figure 5.10 Discretization of the spring cross-section into trapezoidal elements to calculate the bending and torsional constants.	205
Figure 5.11 Etch profile of the spring - total spring thickness vs. etch depth.....	207
Figure 5.12 Compensation for spring etch profile. (a) Ideal, (b) Actual after fabrication, and (c) Compensated beam cross-section showing the addition of a rectangular area of width Δw to increase the second moment of area I_x for the fabricated spring beam to specification.....	209
Figure 5.13 Spring profile for 30 μm wide beam, (a) total spring thickness vs. etch depth, (b) SEM of the beam cross-section.	211
Figure 6.1 Two implementation of capacitive sensing, (a) distance (gap) changing: the distance between the plates is varied and (b) overlap area changing: the overlap area between the plates is varied with position.....	218
Figure 6.2 Block diagram of the microseismometer. The four major functional units are the mechanical suspension, capacitive transducer which converts the mechanical motion of the proof mass to electrical signal, feedback controller which drives the electro-magnetic actuator to keep the proof-mass at equilibrium.	219
Figure 6.3 Cross-sectional view of the microseismometer showing the Capacitive array transducer with the drive electrodes on the proof-mass and a set of overlapping output electrodes on the top capping die.	221
Figure 6.4 (a) Configuration of the drive and output electrodes, and (b) alternate drive electrodes are driven out-of-phase by a +DRIVE and -DRIVE square-wave pulse train. The output electrodes provide a differential output signal.	222
Figure 6.5 Perspective view of the magnetic circuit. The planar coil on the proof mass is enclosed by magnetic field from the pair of magnets on either arm of the coil. The feedback force is generated by running a current through the coil.	224
Figure 6.6 Proof-mass die showing the mechanical suspension with the circuit fabricated on top of the suspension to control and measure the displacement of the proof-mass.....	225
Figure 6.7 Process schematic for the complete suspension fabrication with metal and insulator layers.....	227
Figure 6.8 (a) Contact resistance of pads prior to anneal, and (b) Post-anneal I-V curve for contact pads showing a contact resistance of 200 ohms.	228
Figure 6.9 Contact pad post-anneal showing a rough surface, the brighter islands is the Au layer which dissolves in the underlying NiCr layer.	228
Figure 6.10 Mask layout of the metal-1 layer showing the ground-plane, interconnects for the coil and traces. Metal 1 is 30nm Cr and 200nm Au and is patterned by wet chemical etching.....	229
Figure 6.11 Metal-1 interconnect underneath the insulator layer for making the connection between two segments of metal-2 across the edge seal layer.....	230
Figure 6.12 Photoneece, a photo-definable positive polyimide is spin coated on the wafer and lithographically patterned. The developed and cured photoneece layer has sloping sidewalls suitable for running thin metal traces across the edge of the insulator pads (courtesy: Werner Karl).	231
Figure 6.13 Metal-2 mask layout showing the coil, traces, edge seal layer, pickup electrodes and the interconnect pads for connectivity between the proof-mass die and capping die.	232
Figure 6.14 (a) Electroplated Cu in the photoresist mold, and (b) Electroplated Cu/Au after removal of the photoresist mold and etching of the initial Cr/Cu seed layer.	232
Figure 6.15 Optical micrograph of the circuit on top of the proof-mass die prior to DRIE.	233
Figure 6.16 (a) A complete proof-mass die, and (b) Closeup of the metal traces on a spring (courtesy: Werner Karl).	234

<i>Figure 6.17 Exploded view of the capping and proof mass dies. The DT (Differential transducer) die contains the drive LCAT electrodes. The cavity die is underneath the suspension die and is required for vacuum encapsulating the suspension.</i>	235
<i>Figure 6.18 Schematic steps for metallization of the glass wafer and the subsequent sand powder blasting to etch the cavities.</i>	236
<i>Figure 6.19 (a) Mask layout for the top capping wafer metal layer, and (b) Top capping die with the metal layer.</i>	237
<i>Figure 6.20 On the top capping wafer, the side containing the circuit is powder sand blasted first to etch the cavities, then the wafer is turned over and with a different decal dicing lines are etched through the glass wafer. This allows for easy release of the dies (courtesy: Trevor Semple).</i>	238
<i>Figure 6.21 Magnetic circuit for the microseismometer comprising of magnets, yoke and coil. The yoke closes the circuit between the set of magnets on either side of the die sandwich. The yoke under the magnet smoothes the magnetic flux lines and creates a larger linear region for the coil to move within.</i>	239
<i>Figure 6.22 Location of the coil within the magnetic field. For maximum deflection force the coil should be in the linear region of the magnetic field.</i>	239
<i>Figure 6.23 Magnetic flux density at the coil for varying level of bevelling on the yoke. As expected a sharper bevelling leads to a higher magnetic flux density but the linear range is reduced.</i>	240
<i>Figure 6.24 Cross-sectional view of the microseismometer assembly showing the yoke, magnets, top and bottom capping dies, proof mass die and electrode pads for signal readout and feedback.</i>	241
<i>Figure 6.25 Schematic of the contact and seal between the top capping die and the proof mass die.</i>	242
<i>Figure 6.26 (a) Solder electroplating, (b) Solder jetting, and (c) Solder ball placement (courtesy: Trevor Semple).</i>	242
<i>Figure 6.27 Mechanism of solder ball transfer using grooves on wafers, the grooves are etched using DRIE. The solder balls are transferred to the top capping die. The top capping and proof-mass dies are then aligned and bonded.</i>	243
<i>Figure 6.28 Glass frit bonding to form seal between the bottom capping die and the proof mass die.</i>	244
<i>Figure 6.29 Schematic of the hermetically sealed cavity enclosing the mechanical resonator.</i>	245
<i>Figure 6.30 A fully assembled microseismometer, for size reference a British penny is placed next to it.</i>	248
<i>Figure 6.31 Experimental measurement setup for measuring the resonant frequency and Q-factor of the prototype microseismometer.</i>	249
<i>Figure 6.32 Close-up of the electronic conditioning unit containing the microseismometer.</i>	249
<i>Figure 6.33 Response plot for the suspension. The coil generates a current when driven under the external magnetic field. The peak in the response curve corresponds to the normal resonant modes. The first peak is at a frequency of 12.35 Hz.</i>	250
<i>Figure 6.34 Ringdown test of the suspension. The current generated in the coil reduces as the vibration decays.</i>	251
<i>Figure 6.35 Minimum intensity exposure for transportation of packaged die using a combination of truck, rail and air transport.</i>	253
<i>Figure 6.36 Ling Dynamic Shaker at AOPP, University of Oxford used for doing shock and vibration analysis of packaged suspension.</i>	254
<i>Figure 6.37 Fracture of the spring at the linkage.</i>	254
<i>Figure 6.38 Frame and proof-mass damage due to collision at the corners.</i>	255
<i>Figure 6.39 Redesigned linkages to reduce the stress concentration.</i>	255
<i>Figure 6.40 Damper designs to avoid frames and proof-mass collision, (a) Cavity damper, (b) Comb finger dampers, (c) Spring constraining tabs, and (d) Frame spring damper.</i>	256
<i>Figure 6.41 Damage to the frames and proof-mass at Ariane super vibration levels for packaged suspension.</i>	257
<i>Figure 6.42 Friction damage on proof-mass due to cavity die support fingers.</i>	257
<i>Figure 7.1 (a) 2D model of a fully electrostatic inertial sensor, (b) a fabricated geophone.</i>	265

<i>Figure 7.2 Damping structures to increase damping when the suspension is at its maximum deflection.</i>	266
<i>Figure 7.3 Some prototype devices fabricated using the MIMD (Metal-Insulator-Metal-DRIE) process, (a) geophone sensor, 5mm × 5mm, (b) μSEM components, (c) a tuning-fork gyroscope, (e) comb drive based suspension.</i>	268
<i>Figure 7.4 Fabrication sequence for the silicon mold, substrate preparation, electroplating, and release.</i>	269
<i>Figure 7.5 SEM image of a silicon mold after DRIE (inset shows the mold with a 10 μm thick PMMA release layer).</i>	271
<i>Figure 7.6 SEM image of a molded metal test structure electroplated to 236 μm height. The sidewall is vertical except where the structure is anchored to the substrate. Reflow of the release layer forms a hump at the mold-substrate interface leading to profile variation.</i>	271
<i>Figure 7.7 Suspended metal structures molded using the fabrication steps depicted earlier. The plated structure is 50 μm high and is suspended 14 μm over the base plate.</i>	272
<i>Figure 7.8 Process schematic for single-mask DRIE device fabrication.</i>	273
<i>Figure 7.9 Process schematic of a SOI replacement through-wafer process.</i>	274

List of Tables

<i>Table 1.1 Comparison of conventional seismometers (Datasheets, [1.14]).</i>	7
<i>Table 1.2 Miniaturized seismometers.</i>	8
<i>Table 1.3 Specification of MEMS accelerometers.</i>	15
<i>Table 1.4 Comparison of silicon's mechanical properties with other materials.</i>	18
<i>Table 2.1 Dimensional parameters for suspension design.</i>	48
<i>Table 3.1 Rejection ratios of spurious modes for a lateral suspension.</i>	71
<i>Table 3.2 Dimensional parameters for suspension design with multiple set of springs.</i>	75
<i>Table 3.3 Resonant frequencies for lateral suspension with n spring sets and (n-1) intermediate frames.</i>	86
<i>Table 3.4 Effect of varying amount of filleting of link-spring corner on stress.</i>	97
<i>Table 3.5 Resonant frequencies for lateral suspension with n spring sets and (n-1) intermediate frames incorporating the effect of end connector (elbow) geometry.</i>	100
<i>Table 3.6 Value of c (elbow compliance) for various elbow topography.</i>	101
<i>Table 3.7 Dimensional parameters for selected designs.</i>	103
<i>Table 4.1 Comparison of oxide and photoresist as a masking layer for DRIE.</i>	124
<i>Table 4.2 Comparison chart for various wafer bonding techniques.</i>	128
<i>Table 4.3 Effect of process parameters on the etch characteristics.</i>	169
<i>Table 4.4 Etch Parameters for through-wafer etching.</i>	171
<i>Table 5.1 Vibration modes of silicon suspension with 24 μm wide springs. The suspension has two set of springs with one intermediate frame.</i>	194
<i>Table 5.2 Resonant modes for a 24 μm wide spring suspension. Comparison between analytical, numerical and experimental data incorporating beam profile shape.</i>	208
<i>Table 5.3 Modal frequency for suspension with 24 μm spring which is increased to 30 μm to compensate for the reduction in resonant frequency due to etch profile shape.</i>	212
<i>Table 5.4 Resonant modes for 1 spring set suspension with 24 μm wide spring.</i>	212
<i>Table 6.1 Suspension dimensional parameters for damping calculation for microseismometer.</i>	246

Acknowledgements

Even though this thesis bears my name it would not have been possible without the support, inspiration and enthusiasm of many people. My journey in Microsystems started with a course taught by Prof. Andrei Shkel at University of California, Irvine. If it were not for those glossy posters exhorting the exciting field of micro sensors and actuators I would perhaps still be an Aerospace engineer. The real introduction to the world of MEMS was while working with Dr. Saroj Sahu, Dr. Chris Kenney and Dr. Jim Aroyan at Jasmine Networks and later at MuSquared, Inc. Their support, patience and friendship have been the most crucial in not only expanding my knowledge of Microsystems but also in my personal growth.

It was perfect timing for me to hop over the pond to London when Dr. Tom Pike offered me a position on his microseismometer project. I knew I would have an interesting time at Imperial College after seeing his performance in the comedy play on my first day. I am extremely grateful for his guidance and support throughout the research. I am also grateful to Kinometrics, Inc for sponsoring this research and to Ian Standley for the electronics circuit design and test setup.

The Optical and Semiconductor Devices group is an extremely dynamic group full of talented people. In particular I would like to thank Dr. Munir Ahmed, who with his encyclopaedic knowledge of chemicals always had useful suggestions to help me out of the processing nightmares. Dr. Tom Tate for keeping the cleanroom running and Dr. John Stagg for his help with processing. I thank Prof. Richard Syms for his tireless effort at consistently expanding and improving the fabrication facility.

The effort involved in research was made all the more enjoyable by the excellent company provided by the many friends in the group. London would be very complicated but for the navigational skills of Werner who always knew the best pub whatever be the area. I am extremely thankful for his help and guidance throughout the research. The many evenings I have spent in the company of Ariel and Werner not just discussing work but pondering over the philosophy of it all has kept me sane. Ariel with his ability to invent, cook, paint, and still managing to be a doting dad is an inspiration. The enjoyable dinners at Trevor's place were always great while getting to see (not play) the fantastic guitars he makes. Hanna's parties were always great to test one's drinking abilities and her tennis returns can floor the best. Sanjay is always a lesson in planning. Lunch would not be the same without Robert (and his theories on cave people), Kai (and his projects) and the discussions which always lead to the two great topics. It has only gotten better with Michail (and his myths), Rob, Wen, Anshu, Anisha and Vinita. Economic discussions would not have been same without Anke and her scepticism of my "economist" data. Michael who was always ready to help and advise be it research or business. Migel, Nick, Youngki and Lek – members of the lab who now live in various parts of world and with whom I had some great time and memories. Yun, Li, and Justin for the fantastic badminton games, and all the other wonderful members of the lab. It certainly would have taken longer to complete this research if it were not for the cheerful support of Caroline.

Outside of the group, I am deeply thankful to my friends here in London and elsewhere with whom I have enjoyed so much. Srini, who accompanied me on many trips and never lost his cool even when I got him stuck in the middle of two glaciers and three

lakes in Iceland, and who so patiently explains the real economic world. Prabhala for his constant motivation, and insights. Mr. Alun Parry for his 2 a.m. coffees and endless discussions. Arnab, Ashish, and Paretha for their company and many others whose friendship I deeply cherish.

Finally and most importantly I would like to thank my parents who have influenced me throughout my life and my brothers Onkar, Anil, and Ravi who have always been there for me and encouraged me all the way. It would not be possible for me to have come this far but for their faith in me.

This thesis is dedicated to

papa, mummi

who raised me with so much love

and to

bhaiya, ravi and anil

for their unwavering encouragements

and to

bhabhi, aashna, anish

who have added even more fun to our lives

One

1 Introduction

In this chapter we present the motivation for designing and fabricating a single crystal silicon lateral suspension. The suspension forms part of an under development microseismometer. The microseismometer is a miniaturised seismometer with the ability to detect extremely low-level vibrations. The microseismometer will fill the gap between the huge conventional seismometers and the low-resolution micromachined accelerometers and enable widespread usage in structure health monitoring, remote arrays of seismometers, undersea vibration monitoring for tsunami early warning systems, oil and gas exploration and space seismology.

1.1 Background

Mankind has always been interested in understanding all aspects of the Earth and over the centuries we have expanded our knowledge of the land masses, water bodies and atmosphere by direct observation and interaction with them. The internal structure however has always been a mystery which started unravelling only after the advent of seismology which is the study of propagation of seismic waves through the surface and interior of the Earth.

The beginnings of seismology were rooted in humanity's interests and bewilderment at earthquakes. The oldest instrument probably designed to detect earthquakes is credited to Chinese scientist and philosopher Chang Heng who inventing a seismoscope in 132 A.D. (Figure 1.1)[1.1, 2]. This was a primitive but ingenious device which registered the arrival and direction of the earthquake. The device consisted of a pot with a pendulous arrangement within and on the outer surface had eight dragons with spheres in their mouth and eight toads under them. Depending on the direction of the seismic tremor the appropriate ball would fall in the toad's mouth allowing observer to infer the direction of the tremor. The design influenced mercury and other liquid based seismoscopes in Europe in the eighteenth century and the first seismograph which could continuously record earthquakes was developed by Cecchi in Italy at the end of nineteenth century [1.2-4].

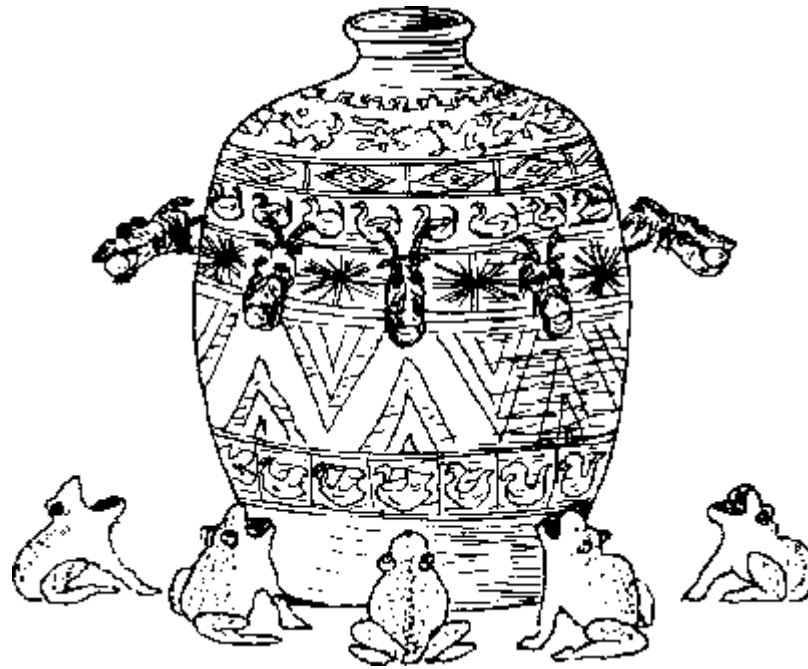


Figure 1.1 Wang Chen-To's visualization of Chang Teng's 132 A.D. design of a seismoscope. Image taken from [1.5].

The beginnings of modern seismic instrumentation is ascribed to John Milne who developed a horizontal pendulum based seismoscope in 1895 in Japan which had extremely low natural frequency allowing unprecedented resolution in measuring seismic vibrations [1.1, 2].

Seismology until the nineteenth century was mostly devoted to the study of earthquakes which ultimately led to the first systematic study of the Earth's seismicity. With the advancement in understanding of elastic wave propagation through various media, analysis of the seismic wave propagation led to the first understanding of the internal structure of the Earth. Analysis of the travel time of teleseismic (long distance) body waves through the Earth enabled R. D. Oldham (Assam, India 1897) [1.2] to propose a model of the Earth with a liquid core whose outer boundary was calculated by Beno Gutenberg in 1913 [1.4]. Andrija Mohorovičić postulated crust-mantle boundary theory

Introduction

in 1909 [1.1] and Inge Lehmann deduced the existence of a solid inner core in 1936 [1.4]. A whole new understanding of the Earth's internal structure was being made possible by the developments in seismological instrumentations.

In the 1920s and 1930s exploration to find oil and gas reserves beginning in Texas and Mexico led to significant improvements in the understanding of the reflection and refraction of teleseismic waves through the terrestrial surface allowing prospectors to find and map underground reservoirs [1.6]. This was also the first significant commercial application of seismology and led to significant improvement in commercial seismic instrumentations.

Seismology received a significant boost in 1950s and 1960s as a means to detect nuclear explosions [1.1, 7]. This allowed the world powers to keep an eye on their adversaries by detecting their nuclear tests. The necessity to discriminate a nuclear explosion from earthquakes and to ascertain the location and strength of the explosion resulted in the establishment of new world wide network of seismic stations like the WWSSN (World wide standardized seismograph network, established 1962) [1.3]. These developments in turn provided an important impetus for major improvements in seismological instrumentations.

Seismometers are (usually) based on the principle of inertia. A heavy mass is loosely coupled to the ground, for example by suspending from a thin wire (Figure 1.2). The motion of the Earth is only partly transferred to the mass. The relative displacement between the mass and ground is recorded as a seismogram.

Introduction

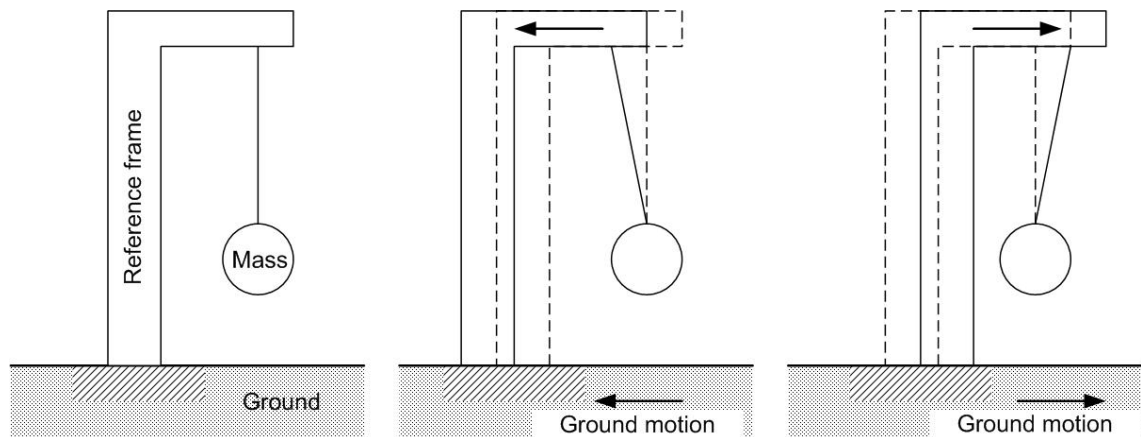


Figure 1.2 Principle of seismometer: the mass is almost stationary due to inertia while the frame moves with the ground [1.1].

Early seismoscopes were based on undamped oscillation and so provided an accurate estimate of ground motion only at the start of the shaking. Emil Wiechert introduced the viscously damped seismometer in 1898 [1.4, 8] which could record ground motion continuously over an extended period, thus recording not only the major earthquakes but also the after-shakes. Significant progress was made at the beginning of the twentieth century by the development of the first electromagnetic seismometers by Prince Boris Galitzin in 1906 in Russia [1.2]. The electromagnetic seismometer has a coil attached to the mass of the pendulum that moves in a magnetic field created by magnets attached to the reference frame. Upon ground motion, the reference frame moves, which creates a varying magnetic field causing a current to flow through the coil. The electric current generated in the coil is passed to a galvanometer whose deflection is recorded by a light beam reflected off a mirror on photographic paper wrapped around a rotating drum. The electromagnetic seismometer enabled higher magnification of the ground motion compared to the previous seismometers. The new age in seismic instrumentation was heralded by the development of the broadband seismometer by Wielandt and Streckeisen in 1983 [1.2]. The broadband seismometer

can record ground motion over a large range of periods made possible by a feed-back circuit that extends the response to very long periods. Some of the commercial seismometers are shown in Figure 1.3.

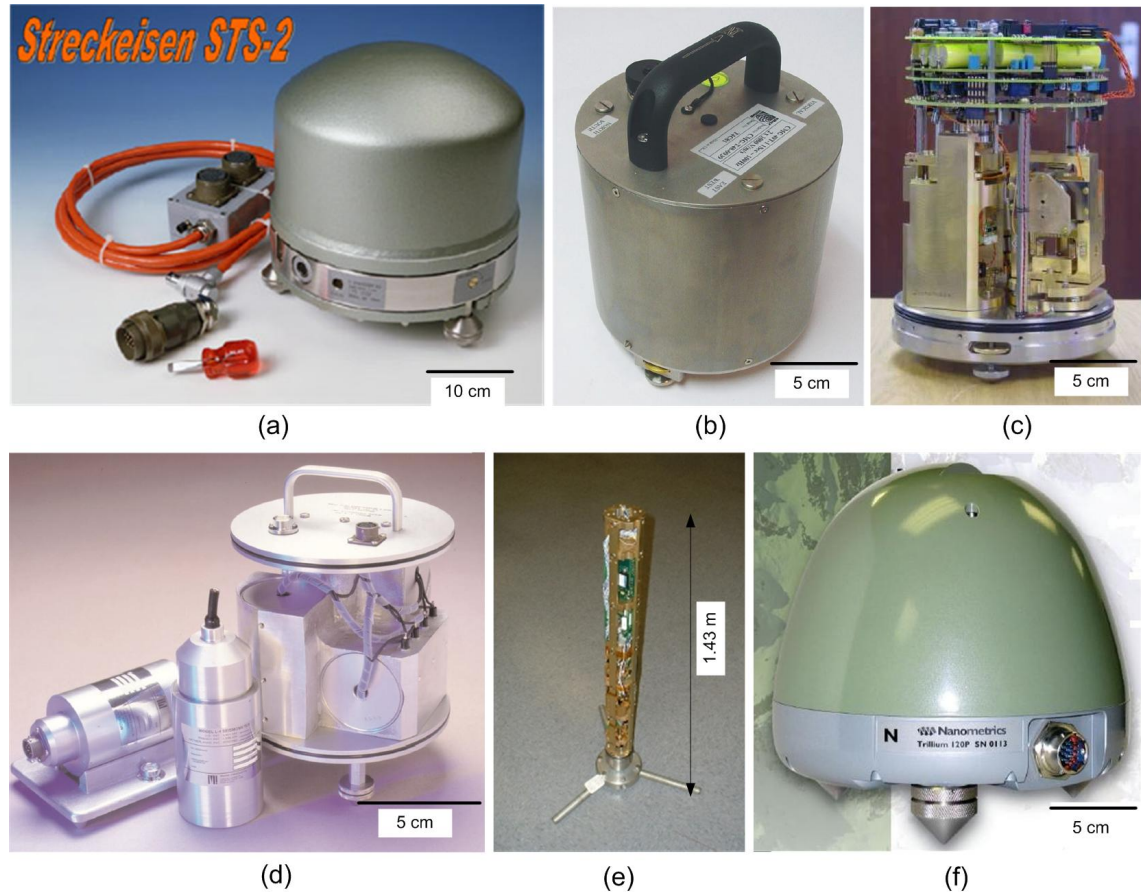


Figure 1.3 State-of-the-art commercial seismometers, (a) Streckeisen STS-2, (b) Guralp CMG-40T, (c) Guralp CMG-3T without outer housing, (d) Sercel L-4, (e) Geotech KS-2000 borehole seismometer, and (f) Nanometrics Trillium 120P. These are all big, heavy and expensive.

Streckeisen [1.9] manufactures some of the most sensitive seismometers, their STS-1 and STS-2 designs were some of the first widely available broadband seismometers. STS-1, now out of production was a single axis seismometer (can measure vibration only along one axis) with a mechanical period of 360 seconds. STS-2 (Figure 1.3a) is a three component seismometer which can record vibrations along all three axes; it has a mechanical time period of 120 second. CMG-40T (Figure 1.3b) and CMG-3T (Figure

1.3c) are Gralp's [1.10] three component seismometers. CMG-3T competes in the same market as STS-2 and has comparable specifications. Sercel [1.11], Geotech [1.12] and Nanometrics [1.13] (Figure 1.3d-f) are some of the other key players in the seismometer market and have a wide range of offerings. Table 1.1 compares a range of seismometers from various vendors. As we can see from Table 1.1 and Figure 1.3 conventional state-of-the-art seismometers are large (~125,000 cubic cm), heavy (~10 kilograms), and expensive (~\$50k-\$100k). They are also power hungry (few watts), tricky to install and expensive to maintain. This presents a major obstacle to their widespread use in seismic monitoring of common structures like buildings, bridges (cost consideration), building remote large field networks for earthquake monitoring or oil prospecting (cost and power consideration) and space seismology (size, power and weight consideration).

Table 1.1 Comparison of conventional seismometers (Datasheets, [1.14]).

Vendor/Model	Size (cm)	Weight (kg)	Self Noise (m/s ² /√Hz)	Natural Frequency	Proof-mass (kg)
Streckheisen STS-1	12×17×18	4	3.16×10 ⁻¹¹	360 sec	0.5
	φ20×16	5.5 kg			
Streckheisen STS-2	φ23×26	13	3.16×10 ⁻¹¹	120 sec	0.3
Guralp CMG-3T	φ17×38	14	1.78×10 ⁻¹⁰	120 sec	
Guralp CMG-40T	φ15.4×20.7	2.49	1.78×10 ⁻⁹	30 sec	
Lennartz Le3D/5s	φ19.5×16.5	6.5	4.98×10 ⁻⁹	5 sec	
Nanometrics Trillium 120P	φ22×18	11	5.62×10 ⁻¹⁰		
Geotech S-13	φ16.8×38.1	10.4	4.47×10 ⁻¹⁰	1 Hz	5
Geotech GS-13	φ16.8×38.1	10.4	2.66×10 ⁻¹⁰	1 Hz	5
Geotech KS-2000	φ8.9×143	19	7.08×10 ⁻⁸		7.7
Kinometrics SS-1 [1.15]	φ14×30.5	5	4.98×10 ⁻¹⁰	1 Hz	1.45

φ is used to denote the diameter of the sensor.

The size and weight restrictions of conventional seismometers limit their usability in many areas, which has led, in recent times to the development of miniaturized seismometers. Table 1.2 presents the specifications of a few miniaturized seismometers from Sercel and Oyo-Geospace [1.16]. The key concern while miniaturizing seismometers is the sensor's ability to resolve vibrations from the ambient noise. The noise can have two origins: noise generated in the instrument and the "real" seismic noise of the Earth vibrations. Conventional seismometers like STS-1, STS-2 and CMG-3T have instrument noise well below the seismic noise but for miniaturized seismometers it is important to design the instrument to keep the instrument noise below the Earth noise in its range of operation. As we see in Table 1.2 the self-noise of the seismometers are increasing with decreasing size. Self-noise of the instrument gives a measure of the smallest signal that the sensor is able to distinguish from background noise.

Table 1.2 Miniaturized seismometers. ϕ is used to denote the diameter of the sensor.

Vendor/Model	Size (cm)	Weight (kg)	Self-Noise ($\text{m/s}^2/\sqrt{\text{Hz}}$)	Natural Frequency	Proof-mass (kg)
Sercel L-4A/C	$\phi 7.6 \times 13$	2.15-1.7	4.98×10^{-10}	1-2 Hz	0.5 - 1
Sercel L-22	$\phi 6.03 \times 5.08$	0.425	4.48×10^{-9}	2 Hz	72.8 gram
Oyo-Geospace HS-1	$\phi 4.2 \times 4.7$	0.24	1.07×10^{-8}	4.5 Hz	22.7 gram

1.2 Earth Noise

Many factors contribute to the Earth noise, including human activity, wind, ocean, temperature fluctuations, solar and lunar interactions. Man made noise is generally from traffic and machinery and is high-frequency (2-4 Hz). Wind sways structures causing high-frequency noise though sometimes with very large structures it generates low-

frequency vibrations. Oceans are the source of most widespread seismic noise seen globally; it is significantly higher in coastal areas than inland. The waves and tides cause shorter period vibrations in the 0.1-0.2 Hz range. These factors are constantly at work making the crust vibrate continuously.

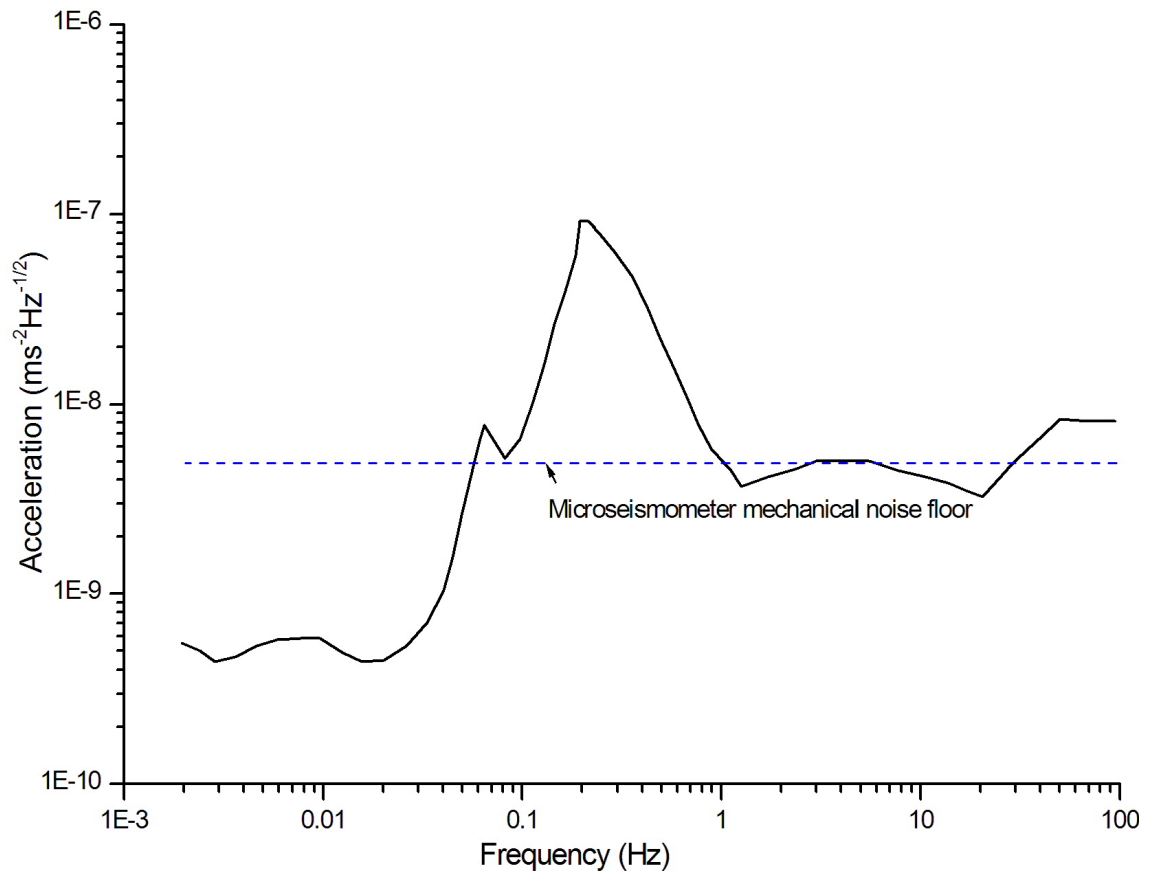


Figure 1.4 The USGS New Low Noise Model [1.17], here expressed as Noise Estimated Acceleration in $m/s^2/\sqrt{Hz}$ of ground motion relative to frequency. Mechanical noise levels are plotted for the proposed microseismometer.

The lowest noise levels on the Earth are represented by a USGS (United States Geographical Society) New Low Noise Model (NLNM) [1.17] (Figure 1.4). The curves (also known as Peterson-curves) represent lower bounds of cumulative compilation of representative ground acceleration amplitude spectral density at 75 seismic stations

worldwide. These Peterson-curves are a useful reference for predicting the noise levels of a seismic station and to quantify the usability of a seismometer to resolve the smallest seismic motion. The figure shows the target microseismometer mechanical noise floor on the plot which will be discussed in the chapter 2.

1.3 Instrument Noise

An important consideration while designing seismometers is the Earth noise. The key requirement is creating sensors sensitive enough to detect the smallest seismic signals, given that noise sets a limit to the level of detection. The instrument noise is due to both the electronic noise and the mechanical noise of the suspension. The electronic noise is generally well quantified for the amplifiers and the feedback circuit and can be designed to be below the NLNM in the range of operation required.

Mechanical self-noise of the suspension is dependant on the damping of the resonating structure which is due to viscous damping from surrounding air molecules. By vacuum encapsulating the resonating structure the viscous damping from air can be reduced.

At the lower end, the fundamental limit to the self-noise or noise floor is set by the Brownian motion of gas molecules hitting the proof mass. Usher [1.18] shows the noise-equivalent acceleration (NEA) for a unit bandwidth at any frequency is given by

$$NEA^2 = 4k_b T \frac{\omega_0}{mQ} \tag{1.1}$$

where k_b is the Boltzmann constant, T is the temperature in Kelvin. NEA is expressed in units of $m/s^2/\sqrt{Hz}$ and also in terms of gravity as g/\sqrt{Hz} where the relation is $1 g/\sqrt{Hz} = 9.81 m/s^2/\sqrt{Hz}$.

From equation 1.1 we can see that the three critical parameters for a low-noise sensor are large mass (m), long period ($1/\omega_0$) and high quality factor (Q). Quality factor (Q) is the measure of the energy loss in the suspension and the higher the Q , the better is the ability of the suspension to minimize energy loss. Conventional seismometers have a very large mass and an extremely long period which reduces the mechanical noise of the suspension. With miniaturization, the weight of the suspension decreases and it also becomes harder to fabricate low resonant frequency suspensions. Figure 1.5 compares the NEA and natural frequency of the suspension for a variety of vibration sensors from conventional high-performance seismometers to miniaturized seismometers and micromachined accelerometers. The self-noise of conventional seismometers scale approximately in proportion to the mass of their respective suspensions. STS-1 has a 4 kg mass on leaf springs which gives it a time period of 360 seconds and is installed in vacuum to give it one of the smallest noise floor. STS-2 and CMG-3T have a 13 kg and 14 kg proof-mass respectively and a time period of 120 seconds allowing them to reach less than 10^{-10} m/s²/√Hz NEA. Sercel L-4 and Oyo-Geospace HS-1 with their much smaller mass of 0.5 kg and 22.7 g and resonant frequency of 1 Hz and 4.5 Hz have significantly higher self-noise.

In addition to the seismometers, Figure 1.5 includes accelerometers both commercially available and from research. Accelerometers are typically high-g vibration measuring sensors and have significantly higher resonant frequency. The accelerometers shown in Figure 1.5 are fabricated using semiconductor processing techniques and have extremely low mass. This leads to extremely high mechanical noise rendering these accelerometers unusable for detecting small seismic signals. To improve the resolution

of high-g accelerometers a new generation of accelerometers called navigational/inertial grade accelerometers are being manufactured commercially and have been the subject of intensive research over the past few years. These accelerometers offer significantly lower noise floor, some of them finding applications in seismic sensing (ex. Sercel DSU3, Honeywell QA-3000).

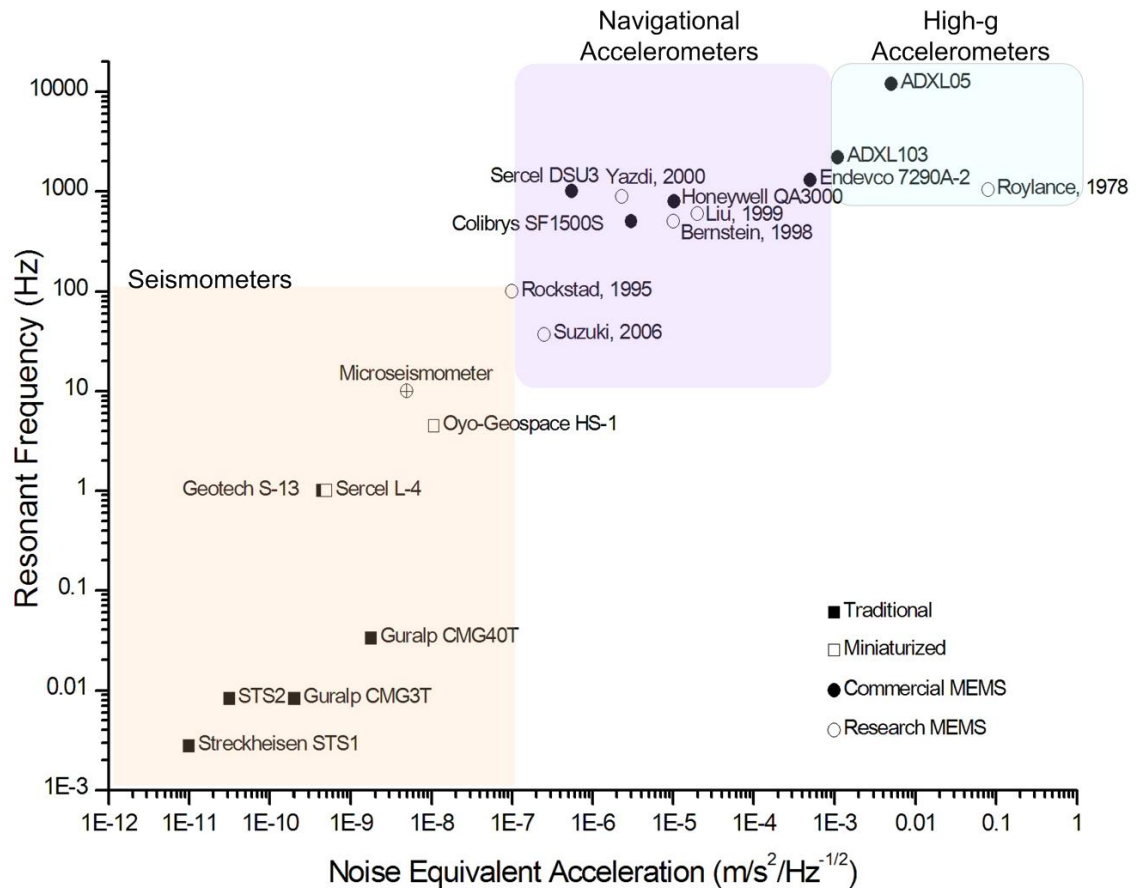


Figure 1.5 Comparison of noise and resonant frequency of seismometers and a variety of commercial and research accelerometers (datasheet, [1.14, 19, 20]).

Figure 1.6 compares the self-noise of seismometers and accelerometers with respect to their volume. We can see the strong correlation between the size (related to the mass) of the sensor and its noise floor as predicted from equation 1.1. Different groups of sensors are highlighted as falling under various classifications. Seismometers as we have discussed upto now are typically low-noise low-frequency and high-mass sensors.

Accelerometers are subdivided in two categories: high-g accelerometers and navigation/inertial grade accelerometers. Navigation grade accelerometers have much lower self-noise than high-g accelerometers and have generally higher volume and hence mass. Some navigational grade accelerometers like ones developed by Yazdi et al. [1.21], Bernstein et al. [1.22] and Suzuki et al. [1.23] have similar or lower volume than high-g accelerometers – this is due to the high quality factor of the material used to make the suspension or the extremely low resonant frequency of the suspension as with Suzuki’s parylene based accelerometer.

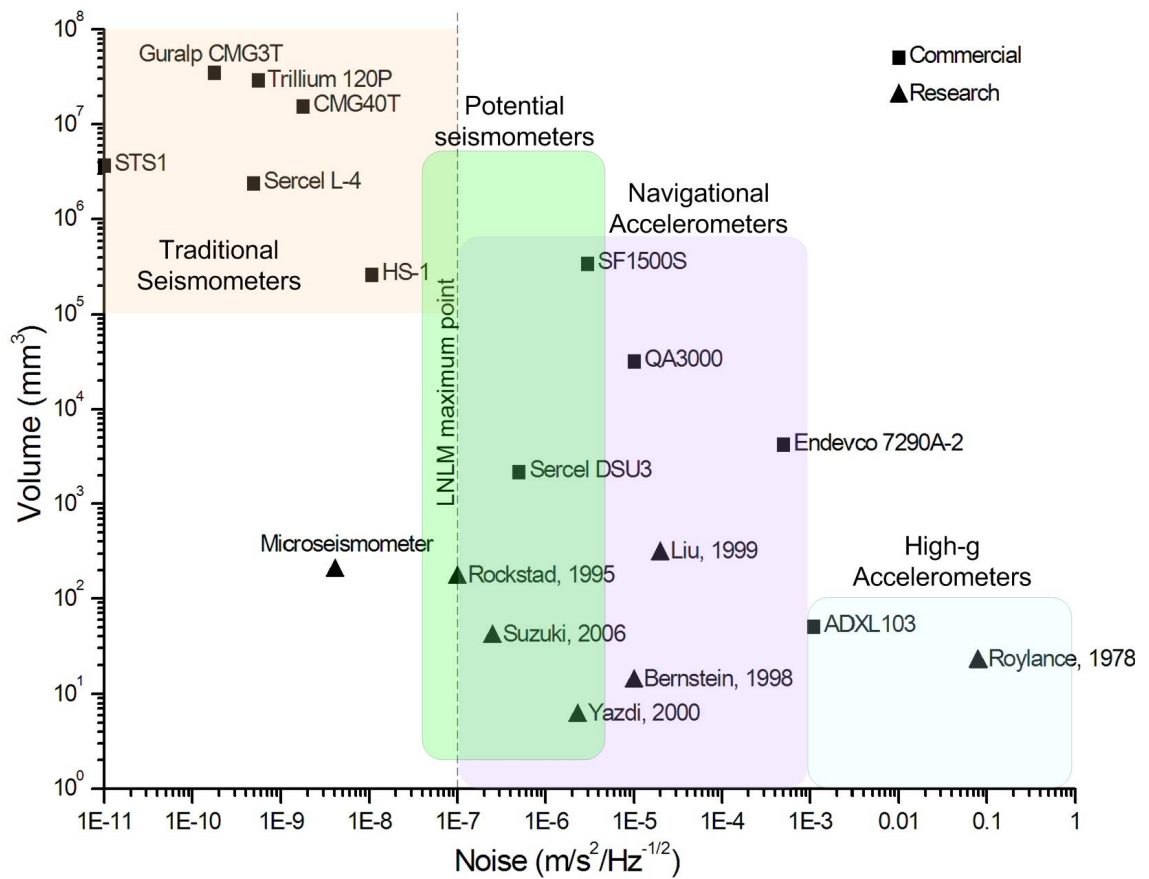


Figure 1.6 Comparison of noise and volume for traditional seismometer and MEMS accelerometers (datasheet, [1.14, 19, 20]).

1.4 Micromachined Accelerometers

Considering the improvement in the noise floor of navigational grade accelerometers it could be possible to implement improvements to existing designs or materials, which can reduce the self-noise even further. Most of the current crop of accelerometers are batch fabricated using semiconductor processing techniques and are collectively known as MEMS (Micro-Electro-Mechanical System) accelerometers. The specifications of some of the industry standard ones are presented in Table 1.3. Honeywell QA-3000 (Figure 1.7a) uses a suspension made of quartz which is a very high- Q material. The low mass of the suspension and the high-frequency of the suspension are compensated significantly by the high- Q of the suspension to yield a $0.1 \mu\text{g}$ self-noise sensor. The Sercel DSU3 has a lateral suspension made of polysilicon yielding an extremely low mass of the suspension and a high resonant frequency but the high- Q of the vacuum packaged device reduces the self-noise floor to 10 ng level. The SEM of the suspension for the Sercel DSU3 is shown in Figure 1.7b. It bears noting that one of the major advantages of small form factor accelerometers is the ability to package them in a vacuum environment reducing the noise-floor to the Brownian noise of the suspension.

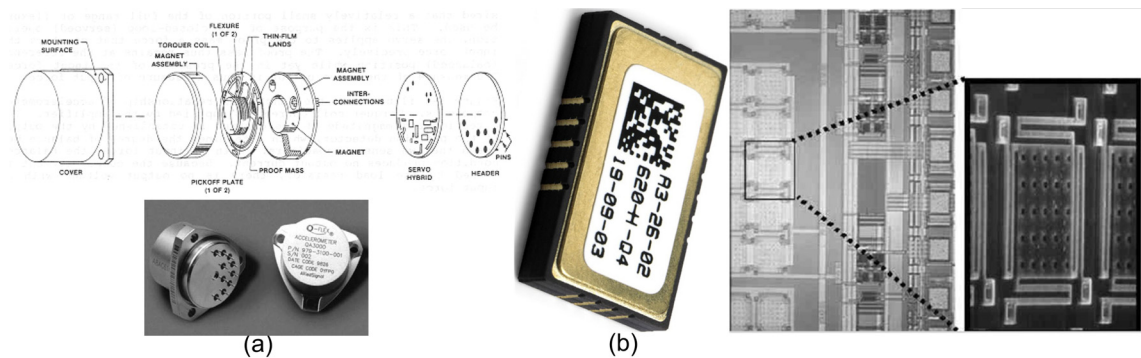


Figure 1.7 Commercial MEMS accelerometers with sub μg noise levels, (a) Honeywell Q-flex QA3000 with an exploded view of the sensor and its suspension, and (b) Sercel/Tronics GPU3 with SEM of the suspension.

Table 1.3 Specification of MEMS accelerometers. ϕ represents diameter of the sensor body.

Vendor/Model	Size (cm)	Weight (kg)	Self Noise (m/s ² /√Hz)	Natural Frequency	Proof- mass (kg)
Honeywell QA-3000	$\phi 2.6 \times 1.5$	0.071	1.04×10^{-6}	800 Hz	
Colibrys SF1500S [1.24]	$8 \times 7.5 \times 5.7$	0.45	3.00×10^{-6}		
Sercel DSU3	$1.6 \times 0.7 \times 1.9$	0.43	5.00×10^{-7}	1 kHz	
Analog Devices ADXL103 [1.25]	$5 \times 5 \times 2$ mm	<1 gram	1.10×10^{-3}	2.2 kHz	~few μ g
Analog Devices ADXL05	$5 \times 5 \times 2$ mm	<1 gram	5.00×10^{-3}	1.2 kHz	1.86 μ g
Proposed Device (expected)	$2 \times 2 \times 0.5$ mm	<1 gram	4.25×10^{-9}	10 Hz	26.6 mg

Various research groups have also designed low-noise suspensions for use as an accelerometer. Figure 1.5 and Figure 1.6 show the noise level, natural frequency and size of some of the notable accelerometers from various research groups. Roylance and Angell [1.26] developed one of the first silicon micromachined accelerometers in 1978 at Stanford with a 0.02 mg mass suspended from a silicon cantilever (Figure 1.8e,f) to give an out-of-plane resonant frequency of 1040 Hz and a noise floor of 8 mg/√Hz. Bernstein et al [1.22] demonstrated an out-of-plane accelerometer with 0.1 μ g/√Hz noise floor made out of silicon, this was similar to the Roylance suspension in terms of having a large proof-mass over thin flexures (Figure 1.8a,b). Rockstad et al [1.27] developed an out-of-plane tunnelling accelerometer which had a noise floor of 0.1 μ g/√Hz and 0.01 μ g/√Hz near the resonant frequency of the suspension. Silicon has been a very popular material of late due to the availability of standard equipments to machine it easily and also has excellent material properties, though recently a low-noise lateral suspension (Figure 1.8c,d) based on Parylene (a polymer) was demonstrated by Suzuki et al [1.23] which showcases the advantage of using polymer to build very low resonant frequency suspensions.

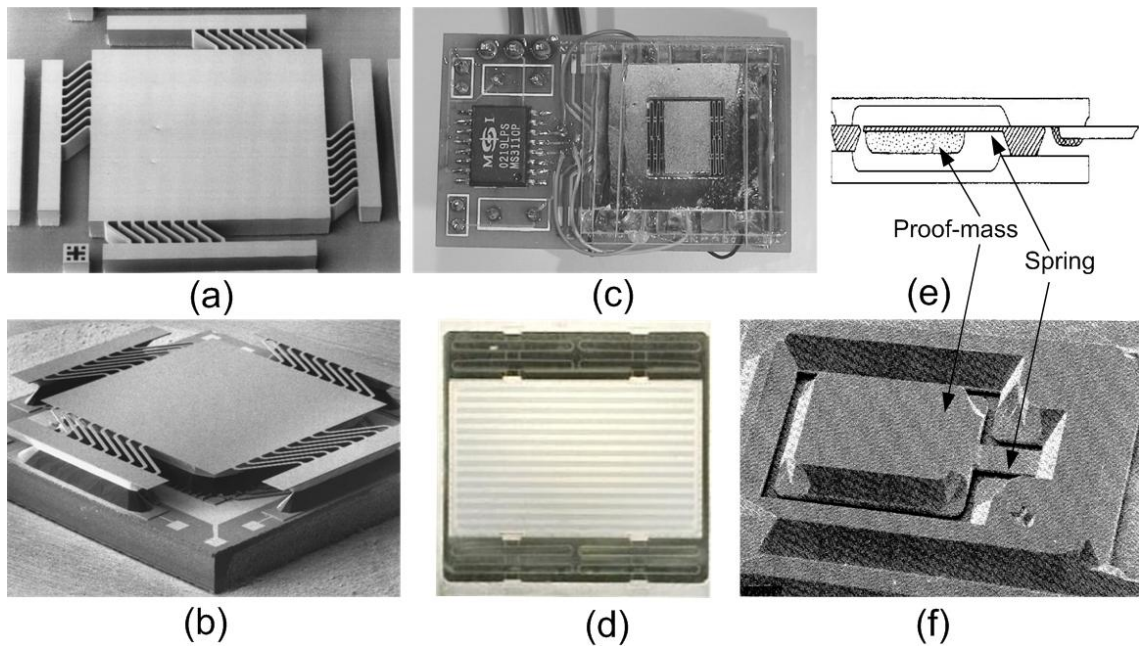


Figure 1.8 MEMS accelerometers developed by research groups, (a,b) A $1.0 \mu\text{g}/\sqrt{\text{Hz}}$ self-noise accelerometer developed by Bernsetin et al. [1.22] at Charles Stark Draper Laboratory, (c,d) Parylene based low-noise accelerometer developed by Suzuki and Tai [1.23] at University of Tokyo, and (e,f) one of the very first miniaturized accelerometer developed at Stanford university by Roylance and Angell [1.26].

From the review of low-noise accelerometer, it seems reasonable to expect that it is possible to develop sensors with nano-g or even sub nano-g self-noise by choosing a suitable design and material for the mechanical suspension.

A wide variety of materials from silicon to quartz to polymer have been used to fabricate accelerometers some of which have sub- μg noise. The choice of material is dictated more from the availability of tools to pattern the material and by the suitability of the material to create a low-loss suspension. Even though the mass of a MEMS accelerometer is substantially lower than the conventional seismometers, it is still imperative to maximize the mass to the extent possible. This requires a fabrication technique which can create thick structures but that can lead to thick flexures increasing

the resonant frequency of the suspension. High aspect ratio structures can solve the problem of both a large mass and slender flexures for low resonant frequency. Recent improvements in high aspect ratio micromachining of silicon due to the availability of Deep Reactive Ion Etching based on the Bosch [1.28] process allows the flexibility to create high-mass low-frequency suspensions.

1.5 Silicon Suspension

Silicon has excellent mechanical properties [1.29] and a wide variety of standard fabrication processes which are exploited to make micromechanical devices. Table 1.4 compares the mechanical characteristics of silicon with various other materials.

Stainless steel is a popular material used for manufacturing some of the conventional seismometers, as we can see from the table it has similar modulus of rigidity as silicon but has three times the density which could be useful for making a high-mass suspension. The disadvantage of metals is their polycrystalline grain boundary which increases material damping as energy is lost due to grain boundary slips, dislocations, interface slips etc. resulting in low quality factor (Q) of the suspensions made from them. Single crystal silicon is a crystalline material with silicon atoms in very stable energy levels eliminating losses through grain boundary slips etc. The loss mechanisms in silicon are through thermoelastic dissipation, phonon-phonon interactions and internal friction (dependent on defects in crystal lattice) which are much lower compared to losses through grain boundary slips thus enabling extremely high Q resonators, at times as high as 600,000 [1.30]. Silicon also has a much higher yield strength compared to most metals and polymers. Quartz has significantly higher yield strength and is also a very low-loss material but is harder to pattern due to lack of standard industry tools compared to silicon.

The high Young's modulus and large yield strength are extremely attractive for mechanical systems. In addition, low crystal defect allows fabrication of high- Q and high-reliability devices. Silicon also has a high melting point (1683 °C), is radiation safe, non-magnetic and impervious to many chemicals. Single crystal silicon is a moderately anisotropic material [1.34] and is available in various crystal plane configurations giving device designers flexibility in orienting structures along suitable crystal planes. Silicon is a brittle material so failure in silicon devices is generally due to brittle fracture along $\langle 111 \rangle$ plane.

Table 1.4 Comparison of silicon's mechanical properties with other materials.

Material	Silicon ^[1.31] <111>	Nickel [1.32]	Stainless Steel ^[1.33]	Aluminium [1.31]	Quartz [1.31]	Parylene [1.23]
Young's modulus (GPa)	190	207	200	70	380	2-4
Yield strength (MPa)	6.9×10^3	360	2.1×10^3	50	14×10^3	27-70
Density (kg/m ³)	2300	8908	7900	2699	1544	1100-1400

Utilizing semiconductor processing methods the devices can be batch fabricated out of silicon. Traditional semiconductor tools like LPCVD (Low-Pressure Chemical Vapour Deposition) deposition of polysilicon, RIE (Reactive Ion Etching), wet isotropic and anisotropic wet etching is supplanted by specialized MEMS tools like DRIE (Deep Reactive Ion Etching) allowing increased freedom to the suspension designer. Figure 1.9 shows suspensions fabricated from polysilicon and single crystal silicon by various fabrication methods.

Introduction

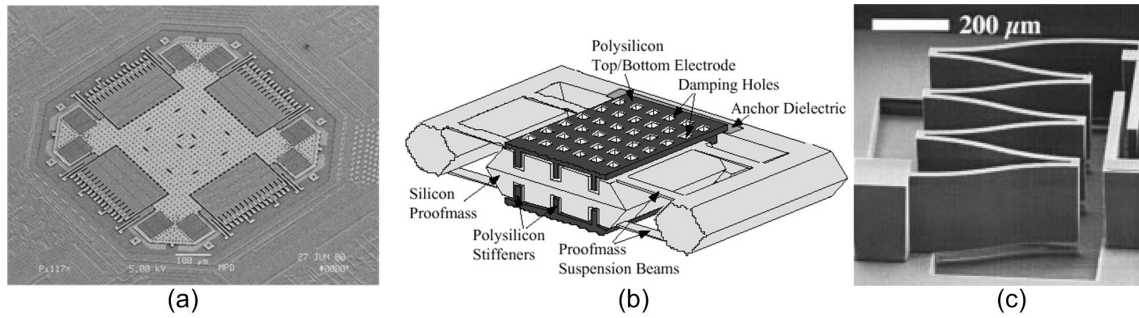


Figure 1.9 (a) Lateral suspension used in Analog Devices ADXL series accelerometers fabricated by LPCVD deposition of polysilicon and then RIE etch [1.35], (b) Vertical suspension created by anisotropically etching silicon by KOH (Potassium hydroxide) [1.21], and (c) Leaf spring part of a lateral suspension fabricated by DRIE of silicon bonded to an underlying silicon substrate [1.36].

Polysilicon suspensions are fabricated by surface micromachining where thin layers are deposited by LPCVD and subsequently either reactive ion etched or chemically etched to fabricate the suspension. These suspensions have extremely low mass due to thin layers and generally have high resonant frequency, a typical example is the Analog devices ADXL50 accelerometer which uses a polysilicon lateral suspension (Figure 1.9a) with a resonant frequency of 2.5 kHz and a $\text{mg}/\sqrt{\text{Hz}}$ noise level.

Anisotropic wet etching using KOH (Potassium hydroxide) or TMAH (Tetra-methyl ammonium hydroxide) is used to create single crystal silicon structure with (111) or (110) limiting plane. This particular fabrication technique imposes severe limits on the device geometry. It is mostly suitable for fabricating out-of-plane suspension with large proof-mass like the accelerometer developed by Yazdi et al. [1.37](Figure 1.9b) which has 885 Hz suspension with 2.1 mg mass and $0.2 \mu\text{g}/\sqrt{\text{Hz}}$ noise floor.

LIGA (Lithographie Galvanoformung Abformung) [1.38] uses X-ray lithography to create high-aspect ratio resist molds for electroplating. The metal structures thus created

can be used for injection molding plastic components. It is a suitable technique for creating high-aspect ratio structures in metals (like Nickel) and plastics but the need for X-ray source makes it an expensive technique with limited availability.

RIE (Reactive Ion Etching) has allowed new freedom in suspension fabrication by allowing vertical etched structures in silicon. Lately, the requirements for structuring of silicon as a mechanical structure is moving towards high aspect ratio structures, from 10's of micrometers deep etch for SOI (silicon-on-insulator) wafers to through-wafer etching ($\sim 500 \mu\text{m} - 1\text{mm}$). An advanced plasma etching method for structuring of silicon is the Bosch time multiplexed etching technique [1.28] also known as Deep Reactive Ion Etching (DRIE), where etching and passivating cycles are alternated during the process. The method has been used to fabricate high-aspect ratio devices like accelerometers, gyroscope, micro-SEM, actuators, micro-mirror arrays [1.39] and through-wafer interconnect [1.40]. Figure 1.10 shows some devices fabricated using DRIE of silicon.

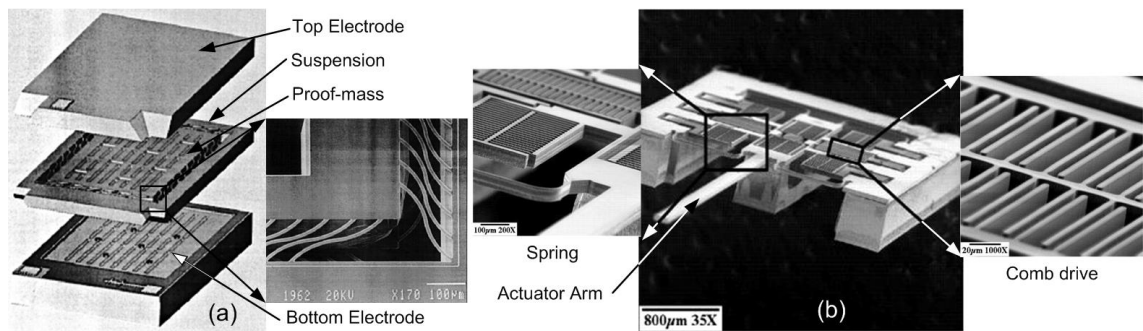


Figure 1.10 DRIE devices (a) Endeveco accelerometer [1.41], (b) Extended travel range microactuator [1.42].

In this thesis we use DRIE for fabricating the lateral silicon suspension which forms the backbone of the microseismometer. Silicon lateral suspensions have been used in many

applications like clockwork springs for storing energy, accelerometer, gyroscopes, shear stress sensors, and actuators.

1.6 Summary

A brief history of seismology and seismic instrumentation was presented and the development of seismometers from the early undamped pendulum to the state-of-the-art broadband electromagnetic seismometer was followed. Conventional seismometers such as Streckheisen's STS-1, STS-2, Guralp CMG-3T were discussed and their key specifications were compared to miniaturized seismometers and accelerometers such as Analog Devices ADXL05, Honeywell QA-3000 and Sercel DSU3. The ability of the conventional seismometers to resolve the smallest seismic signals was attributed to low mechanical suspension noise (self-noise). The suspension self-noise was shown to be dependent on the mass, quality factor and time period of the suspension. Maximizing these three factors leads to a low noise floor for the suspension. With miniaturized sensors particularly with MEMS accelerometers, the suspension self-noise is found to be very high due to the low-mass and high frequency of the suspension. To overcome the reduction in mass due to miniaturization, it is proposed to compensate using very high quality factor material like silicon to fabricate the suspension. The availability of anisotropic fabrication tools like DRIE was shown to make it possible to fabricate suspensions with high aspect ratio leading to long period, large mass and high- Q thus reducing the self-noise of the suspension.

The batch fabrication of the mechanical suspension with integrated electronics to measure and control the resonator will enable substantial reduction in size, weight, cost, power consumption and possibly improve performance characteristics while making it

repeatable across devices. These attributes will lead to a bigger envelope of usage of seismometry in areas that are currently outside its purview due to prohibitive cost, size or weight restrictions of their macroscale counterparts. Even though the performance of these MEMS devices will be lower than the macroscale versions from Streckheisen, and Guralp, they can still be many orders of magnitude better than comparable miniaturized seismometers or inertial navigation grade accelerometers.

Some of the potential applications of microseismometers are:

1. Seismic monitoring (terrestrial): Distributed earthquake monitoring stations, Tsunami alert networks.
2. Structure health monitoring: Bridge, Building, Flyover, and Stadium
3. Oil and gas: Sensor networks for reservoir mapping, Borehole status monitoring, Oil prospecting.
4. Space seismology: Observation of seismic waves on celestial bodies to understand the internal structure. Seismometer payloads have been sent on missions to Mars (Voyager) and are planned for future missions to Mars and Moon by ESA and NASA.
5. Explosion detection for anti-terrorist operation and enforcing NPT (Nuclear non Proliferation Treaty).

Many of these applications are currently either not undertaken or use low-resolution devices such as accelerometers or geophones thus compromising the data quality. It is therefore expected that a MEMS seismometer will open a spectrum of applications for system designers requiring seismic sensing for their applications of interest.

1.7 Research Contributions and Scope

Major Contributions:

1. Generic analytical and parametric numerical model for a lateral suspension with multiple springs and frames. The model incorporates the effects of fabrication process on structure geometry and is applied to the silicon suspension presented in this thesis, predicting the modes of the fabricated suspension to within 5% accuracy. The model can be modified for other suspension designs with folded cantilever flexures.
2. Through-wafer etching of silicon wafers using DRIE – There has been a significant amount of research and development of devices using DRIE, but through etching of 525 μm to 1 mm thick wafers is uncommon. This work covers all aspects of deep silicon etching. Wafer thick suspensions with thin flexures have been successfully fabricated to achieve one of the lowest resonant frequency (10 Hz) single crystal silicon suspensions.
3. Development of a state-of-the-art, low-noise lateral silicon suspension. The lateral silicon suspension developed in this thesis has sub-nano-g/ $\sqrt{\text{Hz}}$ self-noise and a low resonant frequency (10 Hz). The suspension self-noise and volume are two to three orders of magnitude better than the best inertial-grade accelerometers commercially available and reach the self-noise levels of some of the best conventional seismometers while still having a volume three to four orders of magnitude lower. The microseismometer based on this lateral suspension is in discussion for a mission to Mars led by ESA (European Space Agency).

Introduction

To achieve a prototype microseismometer needs other components like sensing and actuation modules besides the mechanical resonator. It is not within the scope of this thesis to cover sensing and actuation though a brief summary is provided to present a complete picture. The microseismometer project is a collaboration of various people and organisations and therefore the thesis also contains work which was carried in a team effort with major contributions from the author. Wherever this has happened it has been pointed out in the text. In general, the author's major field of work has been the numerical analysis and fabrication of silicon suspensions.

The work carried out in this thesis has been published in various international conferences and journals. The list in chronological order is:

S. Kumar, W. J. Karl, S. Vijendran, W. T. Pike, and T. Semple, "Analysis of sidewall quality in through-wafer deep reactive-ion etching," presented at International conference on Micro- and Nano-Engineering, Cambridge, UK, 2003.

W. T. Pike, W. J. Karl, S. Kumar, S. Vijendran, and T. Semple, "Analysis of sidewall quality in through-wafer deep reactive-ion etching," *Microelectronic Engineering*, vol. 73-74, pp. 340-345, 2004.

W. T. Pike, I. M. Standley, S. Kumar, W. Karl, T. Semple, and S. Vijendran, "Determination of the dynamics of micromachined lateral suspensions in the scanning electron microscope," presented at 15th European Micromechanics Workshop, MME '04, Leuven, Belgium, 2004.

S. Kumar and W. T. Pike, "Technique for eliminating notching in through-wafer etching," presented at 16th MME Micromechanics Europe Workshop, Gothenburg, Sweden, 2005.

W. T. Pike and S. Kumar, "Effect of profile shape on mechanical performance of silicon lateral suspension," presented at 16th MME Micromechanics Europe Workshop, Gothenburg, Sweden, 2005.

W. T. Pike and S. Kumar, "Improved Design of Micromachined Lateral Suspensions using Intermediate Frames," (accepted) *Journal of Micromechanics and Microengineering*, 2007.

1.8 Organisation of this Dissertation

This thesis describes the design and fabrication of a low resonant frequency low-noise silicon lateral suspension. The design and analysis cycle to hit performance benchmark for a lateral suspension is explained. Experimental results are presented to demonstrate the design methodology. The fabrication of through-wafer silicon suspension is analysed and issues related to processing are examined.

The design and feasibility study of a lateral suspension for seismic sensing is presented in Chapter 2. Chapter 3 describes the analytical and numerical modelling of the suspension and presents a design flow to satisfy the performance criteria. Chapter 4 deals with the fabrication of silicon suspensions. Issues with DRIE and through-wafer etching are discussed and a fully functional silicon lateral suspension is fabricated. Chapter 5 analyses the fabricated suspension and compares the experimental results

with the analytical and numerical models of Chapter 2. Variation in suspension behaviour from the model is examined, explained, and the model refined to accommodate fabrication deviations from the ideal geometry. Chapter 6 looks at the microseismometer built around the silicon lateral suspension. The processing steps required to build sensing and actuation components are discussed, and packaging considerations are presented. Chapter 7 explores the potential use of the demonstrated silicon lateral suspension, and extends the modelling and fabrication methods described in the thesis to the manufacturing of other devices. The appendices contain the derivation of the analytical expressions to calculate the resonant modes of lateral suspensions, input files for finite element analysis, and the fabrication process description.

The content of the thesis has been divided into separate chapters on design, analysis and fabrication even though in reality they feed into each other and a fully functional device is the outcome of multiple iterations between the design and fabrication cycles. We start with a model for the lateral suspension and optimize its design based on the desired specifications. The design is then fabricated by following a set of process parameters based on some initial presumption; the process is then modified to achieve the etching characteristics required to achieve the final geometry. The fabricated suspension is then tested and any discrepancy in results is attributed to either design or fabrication steps. The models for the design and fabrication are then updated to achieve the final device. This involved multiple iteration between design and fabrication cycles.

1.9 Bibliography

- [1.1] W. Lowrie, *Fundamentals of Geophysics*, Cambridge University Press, 1997.
- [1.2] A. U. Vallina, *Principles of Seismology*, Cambridge University Press, 1999.
- [1.3] S. Stein and M. Wysession, *Introduction to Seismology, Earthquakes, and Earth Structure*, Blackwell Publishing, 2002.
- [1.4] P. M. Shearer, *Introduction to Seismology*, Cambridge University Press, 1999.
- [1.5] J. Dewey and P. Byerly, "The early history of seismometry (to 1900)," *Bulletin of the Seismological Society of America*, vol. 59, pp. 183-227, 1969.
- [1.6] W. M. Telford, R. E. Sheriff, and L. P. Geldart, *Applied Geophysics*, 2 ed: Cambridge University Press, 2003.
- [1.7] K.-H. Barth, "The Politics of Seismology: Nuclear Testing, Arms Control, and the Transformation of a Discipline," *Social Studies of Science*, vol. 33, pp. 743-781, 2003.
- [1.8] E. Wiechert, http://www.geo.physik.uni-goettingen.de/~eifel/Seismo_HTML/seismograph_pic.htm.
- [1.9] G. Streckeisen AG, Dattlikonerstrasse 5, CH-8422 Pfungen, Switzerland.
- [1.10] Guralp Systems Limited, 3 Midas House, Reading RG7 8EA, UK
<http://www.guralp.net>.
- [1.11] Sercel, 16 rue de Bel Air, 44474 Cedex, France <http://www.sercel.com>.
- [1.12] Geotech Instruments LLC, 10755 Sanden Drive, Dallas, Texas 75238, USA
<http://www.geoinstr.com>.
- [1.13] Nanometrics inc, 250 Herzberg Road, Kanata, Ontario K2K 2A1, Canada
<http://www.nanometrics.ca>.
- [1.14] P. W. Rodgers, "Self-noise spectra for 34 common electromagnetic seismometer/preamplifier pairs," *Bulletin of the seismological society of america*, vol. 84, pp. 222-228, 1994.
- [1.15] Kinometrics inc, 222 Vista Avenue, Pasadena, CA 91107, USA
<http://www.kinometrics.com>.
- [1.16] Oyo Geospace Corporation, 7007 Pinemont Drive, Houston, Texas 77040, USA
<http://www.oyogeospace.com>.
- [1.17] J. Peterson, "Observations and modelling of background seismic noise," U. S. Geological Survey, Albuquerque, New Mexico 1993.

- [1.18] M. J. Usher, "Developments in seismometry," *Journal of Physics E: Scientific Instruments*, pp. 501-507, 1973.
- [1.19] C.-H. Liu and T. W. Kenny, "A high-precision, wide-bandwidth micromachined tunneling accelerometer," *Journal of Microelectromechanical Systems*, vol. 10, pp. 425-433, 2001.
- [1.20] W.-T. Park, R. N. Candler, V. Ayanoor-Vitikkate, M. Lutz, A. Partridge, G. Yama, and T. W. Kenny, "Fully encapsulated sub-millimeter accelerometers," presented at 18th IEEE International Conference on Micro Electro Mechanical Systems, 2005.
- [1.21] N. Yazdi, F. Ayazi, and K. Najafi, "Micromachined inertial sensors," *Proceedings of the IEEE*, vol. 86, pp. 1640-1659, 1998.
- [1.22] J. Bernstein, R. Miller, W. Kelley, and P. Ward, "Low-noise MEMS vibration sensor for geophysical applications," *Journal of Microelectromechanical Systems*, vol. 8, pp. 433-438, 1999.
- [1.23] Y. Suzuki and Y.-C. Tai, "Micromachined high-aspect-ratio parylene beam and its application to low-frequency seismometer," presented at The 16th IEEE International Conference on Micro Electro Mechanical Systems, Kyoto, Japan, 2003.
- [1.24] Colibrys Ltd, Maladière 83, CH-2007 Neuchâtel, Switzerland
<http://www.colibrys.com>.
- [1.25] Analog Devices Inc, 20 Cotton Road, Nashua NH 03063, USA
<http://www.analog.com>.
- [1.26] L. M. Roylance and J. B. Angell, "A batch-fabricated silicon accelerometer," *IEEE Transactions on Electron Devices*, vol. 26, pp. 1911-1917, 1979.
- [1.27] H. K. Rockstad, J. K. Reynolds, T. K. Tang, T. W. Kenny, W. J. Kaiser, and T. B. Gabrielson, "A Miniature, High-sensitivity, Electron Tunneling Accelerometer," presented at The 8th International Conference on Solid-State Sensors and Actuators and Eurosensors IX, 1995.
- [1.28] A. Schilp and F. Laermer, Method of anisotropically etching silicon, US Patent 5501893: Robert Bosch GmbH, March 26, 1996
- [1.29] K. E. Petersen, "Silicon as a Mechanical Material," *Proceedings of the IEEE*, vol. 70, pp. 420-457, 1982.

- [1.30] R. A. Buser and N. F. De Rooij, "Very high Q-factor resonators in monocrystalline silicon," *Sensors and Actuators A: Physical*, vol. 21, pp. 323-327, 1990.
- [1.31] J. W. Gardner, *Microsensors: principles and applications*, John Wiley & Sons, 1999.
- [1.32] K. J. Hemker and H. Last, "Microsample tensile testing of LIGA nickel for MEMS applications," *Materials Science and Engineering A*, vol. 319-321, pp. 882-886, 2001.
- [1.33] G. T. A. Kovacs, *Micromachined transducers sourcebook*, McGraw-Hill, 1998.
- [1.34] W. A. Brantley, "Calculated elastic constants for stress problems associated with semiconductor devices," *Journal of Applied Physics*, vol. 44, pp. 534-535, 1973.
- [1.35] ADXL50, "Analog devices ADXL50," <http://www.analog.com>.
- [1.36] G. T. A. Kovacs, N. I. Maluf, and K. E. Petersen, "Bulk micromachining of silicon," *Proceedings of the IEEE*, vol. 86, pp. 1536-1551, 1998.
- [1.37] N. Yazdi and K. Najafi, "An all-silicon single-wafer micro-g accelerometer with a combined surface and bulk micromachining process," *Journal of Microelectromechanical Systems*, vol. 9, pp. 544-550, 2000.
- [1.38] W. Bacher, W. Menz, and J. Mohr, "The LIGA technique and its potential for microsystems-a survey," *IEEE Transactions on Industrial Electronics*, vol. 42, pp. 431-441, 1995.
- [1.39] P.-A. Clerc, L. Dellmann, F. Gretillat, M.-A. Gretillat, P.-F. Indermuhle, S. Jeanneret, P. Luginbuhl, C. Marxer, T. L. Pfeffer, G.-A. Racine, S. Roth, U. Stauffer, C. Stebler, P. Thiebaud, and N. F. d. Rooij, "Advanced deep reactive ion etching: a versatile tool for microelectromechanical systems," *Journal of Micromechanics and Microengineering*, vol. 8, pp. 272-278, 1998.
- [1.40] S. J. Ok, C. Kim, and D. F. Baldwin, "High density, high aspect ratio through-wafer electrical interconnect vias for MEMS packaging," *IEEE Transactions on Advanced Packaging*, vol. 26, pp. 302-309, 2003.
- [1.41] R. D. Sill, "A 70g full scale accelerometer designed to survive 100,000g overrange," *Endevco Technical Paper TP300*.
- [1.42] Y. Sun, D. Piyabongkarn, A. Sezen, B. J. Nelson, and R. Rajamani, "A high-aspect-ratio two-axis electrostatic microactuator with extended travel range," *Sensors and Actuators A: Physical*, vol. 102, pp. 49-60, 2002.



2 Suspension Design and Feasibility Study

In this chapter we set the noise floor of the suspension. The parameters affecting the self-noise of the suspension are then analysed. We then develop a generic lateral suspension in section 2.3 and explore the design space in section 2.4. The fabrication constraints are presented in section 2.5. The ability of the lateral suspension designed to attain the self-noise specified is analysed in section 2.6.

2.1 Suspension Noise

Design of the micromechanical suspension for seismic sensing requires us to set a target noise level for the mechanical suspension. The target noise level for the device should be below the lowest signal that is to be measured using the device. The overall noise (NEA_{device}) of the system is comprised of the mechanical ($NEA_{mechanical}$) and electronic noise ($NEA_{electronic}$) of the system as given by

$$NEA_{device}^2 = NEA_{mechanical}^2 + NEA_{electronic}^2 \quad (2.1)$$

Generally the optimal design for lowest noise occurs when the electronic and mechanical noise are similar [2.1]. The target total noise for the microseismometer (NEA_{device}) is set to $0.5 \text{ ng}/\sqrt{\text{Hz}}$ ($4.9 \times 10^{-9} \text{ ms}^{-2}/\sqrt{\text{Hz}}$) for the seismometer giving a mechanical noise $NEA_{mechanical}$ of $0.35 \text{ ng}/\sqrt{\text{Hz}}$ ($3.43 \times 10^{-9} \text{ ms}^{-2}/\sqrt{\text{Hz}}$). This allows the microseismometer to operate below NLNM in the frequency range between $0.05 - 1 \text{ Hz}$ as shown on Figure 1.4. As we discussed in section 1.4 the NEA of the seismometer is ultimately limited by the Brownian motion of the suspension given by [2.2],

$$NEA_{mechanical}^2 = 4k_b T \frac{\omega_0}{mQ} \quad (2.2)$$

From equation 2.2 it is clear that low resonant frequency, high quality factor and a large mass are prerequisite for low-noise mechanical suspension. In the next section we will discuss these parameters in detail.

2.2 Key Parameters affecting Self-noise

The important figures of merit for a lateral suspension to be used for seismic sensing are the resonant frequency, quality factor, and cross-axis sensitivity (the separation of fundamental and spurious modes). These are a partial set of parameters pertinent to a suspension design for vibration sensing, a full set of all the relevant parameters for

vibration sensors can be found in IEEE standard 528-2001 for inertial sensor technology.

2.2.1 Resonant frequency

Resonant frequency is the property of a system where the system retains input energy with minimum loss. By driving the devices at their resonant frequency the effect of small forces is enhanced along with the device signal-to-noise ratio (SNR) [2.3].

In mechanical systems, operating them at resonant frequency ultimately leads to large amplitude vibration even from low-power driving. It is also desirable at times to reduce the fundamental frequency of a lateral suspension as far as possible. For instance, below the fundamental frequency, the displacement of the proof mass due to an applied acceleration is inversely proportional to the square of the fundamental frequency, and so to maximize the sensitivity, if used in an accelerometer, the fundamental frequency of the lateral suspension should be as low as possible.

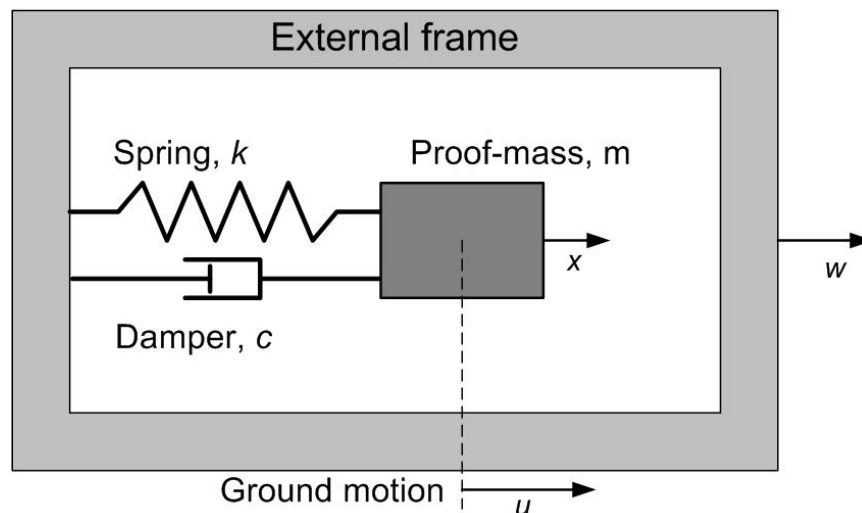


Figure 2.1 Schematic of a mass-spring-damper system.

For a mass-spring-damper system (Figure 2.1), the resonant frequency is given by

$$\omega_0 = \sqrt{\frac{k}{m}} \quad (2.3)$$

where k is the effective spring stiffness and m is the effective mass of the resonating system.

x = relative motion of proof-mass

w = motion of external frame

u = absolute motion of the suspension

The equation of motion for the suspension is given by

$$k(u - w) + s(\dot{u} - \dot{w}) = -m\ddot{u} \quad (2.4)$$

$$x = u - w$$

$$kx + s\dot{x} + m\ddot{x} = -m\ddot{w} \quad (2.5)$$

$$w = w_0 e^{j\omega t}$$

$$x = x_0 e^{j\omega t} e^{j\phi}$$

where ω and ϕ are the frequency and phase.

$$\dot{x} = j\omega x \text{ and } \ddot{x} = -\omega^2 x \quad (2.6)$$

Substituting equation 2.6 in equation 2.5,

$$(k + j\omega s - \omega^2 m)x = m\omega^2 w \quad (2.7)$$

The response is given by

$$\frac{x_0}{w_0} = \frac{|x|}{|w|} = \left| \frac{m\omega^2}{k + j\omega s - \omega^2 m} \right| = \frac{\omega^2}{\left[\left(\frac{k}{m} - \omega^2 \right) + (\omega s)^2 \right]^{1/2}} \quad (2.8)$$

For $\omega \ll \omega_0$,

$$\frac{x_0}{w_0} \cong \frac{\omega^2}{\omega_0^2} \quad (2.9)$$

For a suspension with low ω_0 the response will be large for measurements below the resonant frequency.

In a mechanical resonator, the system operates by interconversion of energy between kinetic and potential forms. Potential energy is stored in compressed springs and when the spring releases, the mass attached to the spring absorbs this energy resulting in motion. Each cycle of energy transfer is subjected to loss in some form of energy dissipation in the damper. At resonant frequency this transfer between kinetic and potential form proceeds with minimum loss, resulting in an enhanced signal-to-noise ratio.

The response of the seismometer is restricted below the first resonant frequency of the suspension though it is possible to design equalization circuits which can extend the velocity amplitude response below the natural frequency [2.4]. Designing a low frequency suspension thus helps avoid such circuits or increases the effectiveness of the circuit to improve the response to lower frequencies of vibration.

2.2.2 Quality factor

The quality factor (Q) is a measure of the rate at which a vibrating system dissipates energy and is defined as the ratio of the energy stored per cycle to the energy dissipated per radian.

For a vibrating mass-spring-damper system with high- Q , the system responds strongly to frequencies close to the natural frequency.

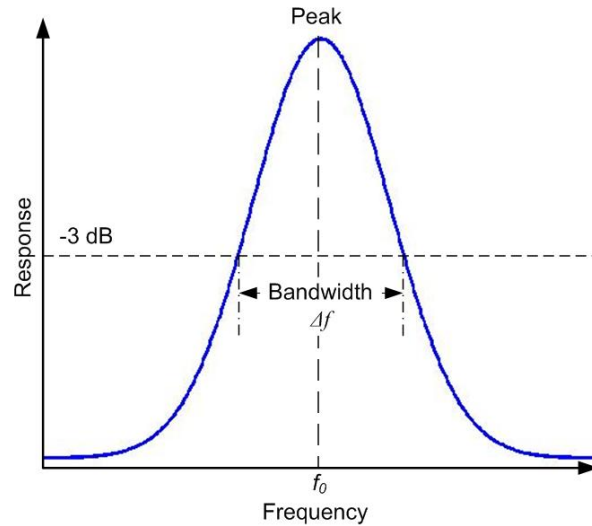


Figure 2.2 Response vs. frequency for a resonating system showing the bandwidth of the systems defined as the frequency width at $\frac{1}{2}$ total energy of the signal.

Mathematically, Q can be calculated in several ways. When a system is driven the relationship to the width of resonance is given by

$$Q = \frac{f_0}{\Delta f} \quad (2.10)$$

where f_0 is the resonant frequency and Δf is the bandwidth, which is defined as the width in frequency when the energy falls to half its peak value (shown in Figure 2.2).

For oscillations with exponential decay in time (Figure 2.3), Q is given by

$$Q = \frac{\omega_0 \tau}{2} \quad (2.11)$$

where $\omega_0 = 2\pi f_0$ and τ is decay time and is defined as the time it takes for the amplitude of oscillation to decay to $1/e$ (~37%) of its initial value.

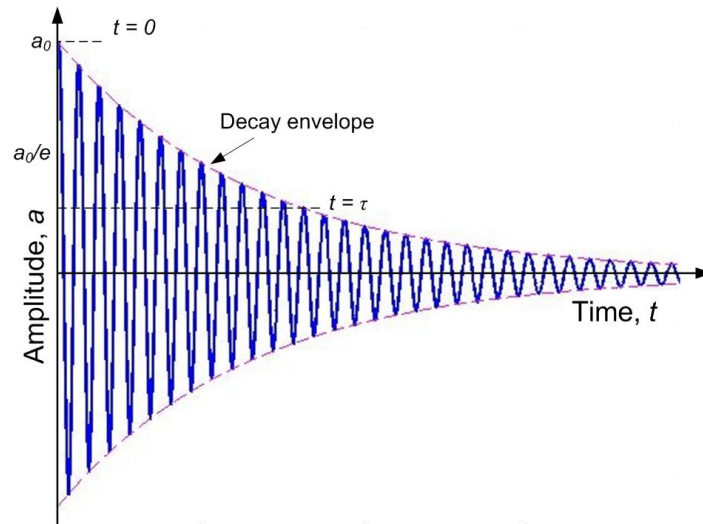


Figure 2.3 An oscillating system with exponential decay of amplitude in time. Decay time constant, τ is the time it takes for the amplitude to decay to $1/e$ times its initial value.

Factors that affect Q for silicon suspensions are:

- surface layers (oxide, metal and polymer layers)
- material impurity and defects (using single crystal silicon reduces material defects)
- temperature
- enclosure pressure (evacuating the enclosure reduces air damping)
- anchor loss
- interfering modes (mode decoupling to reject unwanted signals)

The advantage of using single crystal silicon for fabricating low-noise suspensions is the high- Q attainable in the material. Single crystal silicon has been used to fabricate mechanical resonators with Q 's as high as 600,000 [2.5, 6].

2.2.3 Proof-mass

The NEA of the suspension is inversely proportional to the mass of the seismic weight (proof-mass). We saw in Figure 1.6, the self-noise of larger seismometers is substantially lower than the miniaturized versions due to the advantage of a large mass used in conventional seismometers. With miniaturization the proof-mass is typically small which adversely affects the self-noise so in designing the suspension we will attempt to maximize the proof-mass to the extent possible.

When choosing a fabrication technique for making the suspension it is important to select one which can create thicker structures. Typical semiconductor processes are geared towards thin film technology (100's of nm to 1-5 μm) which leads to extremely low mass of the suspensions. Recent availability of high aspect ratio micromachining tools based on reactive ion etching makes it possible to fabricate suspensions 500 μm to 1 mm thick.

2.2.4 Cross-axis sensitivity

Even though cross-axis sensitivity does not directly affect NEA, we will see in section 3.3.2 that this can restrict our ability to design very low resonant frequency suspension as the rejection ratios for the spurious modes drops with reducing resonant frequency, thus reducing the bandwidth of the suspension. The proof mass should move only along one direction to minimize erroneous readings from displacements in other directions. This is achieved by increasing the spring compliance along the direction of motion, which is also necessary for achieving low-resonant frequency, while increasing stiffness to translations along the other two axes and rigidity to rotation about all axes. The

suspension needs to be designed to have symmetry along the orthogonal axes to the compliant axes to avoid cross-coupling between the axes.

The sensitivity to measure vibrations along any axis is inversely proportional to the square of the resonant frequency (equation 2.9), so a low resonant mode along the compliant axis (X -axis) leads to high sensitivity to motion along that axis. Pushing the other modes (spurious modes) higher reduces the sensitivity of the suspension to measuring vibration along any other axes.

The bandwidth of an accelerometer is the range of frequencies over which it is operational. For an open-loop accelerometer the resonant frequency of the suspension sets the higher limit for the bandwidth. With the use of a feedback circuit, the bandwidth of the system is pushed up and is dependent on the gain of the feedback circuit, which is the reason we have not considered bandwidth as one of the key parameters here. In the presence of a feedback circuit, the first spurious mode defines the bandwidth of the system, as the sensor response will not be linear when the frequencies of vibration to be detected are near the spurious mode. This means one needs to design a suspension with spurious resonant frequencies much higher than the fundamental frequency to increase the bandwidth of the suspension. Chapter 3 will look in detail at design features which are used to increase the cross-axis decoupling of modes.

2.3 Suspension: Generic Design Principle

Lateral suspensions have been utilized in MEMS to produce resonant structures like comb drive resonators, inertial sensors like accelerometers and gyroscopes and for

lateral translational stages used in optical devices. In all these devices performance will be enhanced by maximizing the separation of the fundamental and other spurious modes thus increasing the usable bandwidth of the suspension. As we discussed in section 2.2.3 the ideal suspension would be solely compliant along the direction of motion (X -axis) of the proof-mass with maximum stiffness in all other axes. In its simplest form the suspension will consist of two springs either side of a proof-mass connected to an external fixed frame.

A 6DOF (Degree of Freedom) system will have six simultaneous equations for the general case but it becomes separable in their coordinates if there are three planes of symmetry to the suspension [2.7]. Such a suspension has no coupling between motion in each coordinates. We will see in section 3.2 how this decoupling greatly simplifies the analysis by removing off-diagonal terms from the equation of motion matrices for the 6DOF system. Hence, to decouple the motion along the various axes we consider center-of-gravity systems, so called as symmetry implies that the elastic forces of the suspension are directed through the center of the suspended mass.

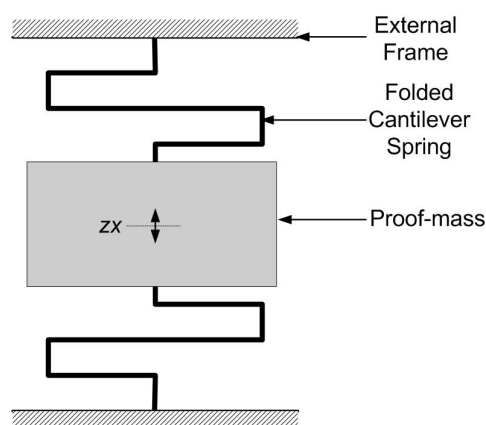


Figure 2.4 A simple suspension with folded cantilever beams as spring on either side of a proof-mass attached to a fixed external frame. The pair of springs on either side of the suspension only allows dual planes of mirror symmetry about xy and xz planes as shown by the arrow in the middle of the proof-mass.

Folded cantilever beams have been a frequent design choice to best accommodate these constraints in lateral suspensions [2.8-12]. A simple suspension can be designed with a series of folded cantilevers on either side of the proof-mass (Figure 2.4) which softens the suspension as well as improves the linearity as the deflection of each cantilever is a lower multiple of the beam thickness.

However, a simple series of folded cantilevers lacks symmetry in the plane perpendicular to the compliant direction and to avoid the dynamic and analytical problems of cross-coupling between the axes mentioned earlier, the unit of suspension is taken as a mirror pair of folded cantilevers [2.13, 14], which reintroduces the plane of symmetry to the resulting center-of-gravity system. The folded cantilever pairs are linked at their central attachment points as shown in Figure 2.5. This results in an increased stiffness of the suspension to motion along the Z-axis. This is due to the additional constraint of no relative motion in the x-direction for the pair at the linkage.

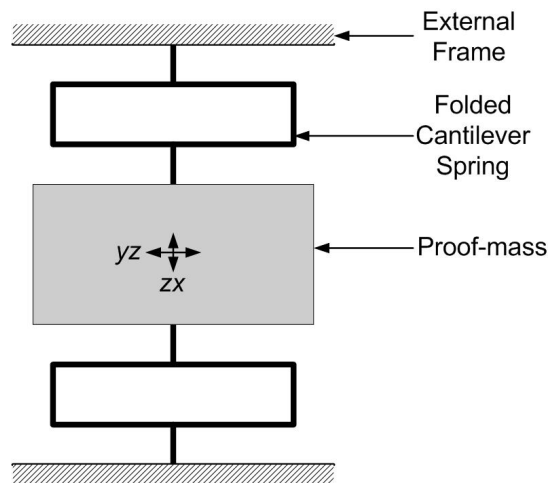


Figure 2.5 A center-of-gravity suspension design with symmetry along all the three axes. The joint folded cantilever pairs on either side of the proof-mass provide symmetry about xy , yz and zx planes. Symmetry in the lateral plane is shown by the arrows in the middle of the proof-mass. The cantilever pairs are linked at the center to increase the stiffness compared to an unconnected pair.

The suspension design shown in Figure 2.5 is the basis of the all the lateral suspension designed and fabricated in this thesis. Various configurations using multiple joint-cantilever pairs as springs are considered along with more advanced designs incorporating intermediate frames as will be discussed in chapter 3.

In addition to symmetry, there are further constraints on the design of the suspension. It should be possible to fabricate the suspension using MEMS processing techniques which sets restrictions on minimum feature size and gap. A minimal area should be required for fabrication to reduce cost. The proof-mass should have sufficient throw in the compliant direction to cover required motion. Damping should be considered for the suspension and complete assembly. These issues are considered in later chapters on analysis, fabrication and assembly of the suspension.

2.3.1 Homogenous triaxial configuration

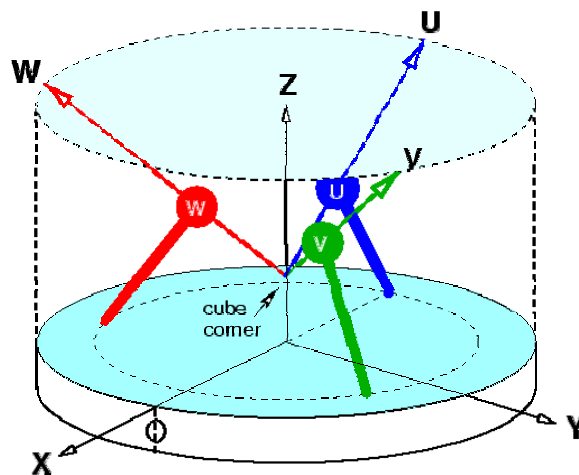


Figure 2.6 Homogenous triaxial configuration also called Galperin configuration (Source: [2.15]). u , v , w are the responses of the sensor along the Galperin axes UVW.

To observe the vibration in all directions, a triple set of sensors are oriented along the three axes X , Y and Z . For seismic sensing, the standard way is to place a seismometer

for detecting ground motion along East, North and Upwards (Z) [2.15]. The designs for horizontal and vertical vibration sensors are different, and to integrate them into a single response is non-trivial. An alternative design for a three-component system is to use three identical horizontal sensors whose sensitive axis is inclined against the vertical at same angle ($\theta_{galperin} = 54.74^\circ$) like the edges of a cube standing on its corner [2.16],[2.17] as shown in Figure 2.6.

The response along the three axes can be calculated from the response along the sensitive axis of each of the sensor by using the transformation matrix given by

$$\begin{pmatrix} x \\ y \\ z \end{pmatrix} = \frac{1}{\sqrt{6}} \begin{pmatrix} -2 & 1 & 1 \\ 0 & \sqrt{3} & -\sqrt{3} \\ \sqrt{2} & \sqrt{2} & \sqrt{2} \end{pmatrix} \begin{pmatrix} u \\ v \\ w \end{pmatrix} \quad (2.12)$$

For a seismometer the X axis is normally oriented towards East, and the Y axis points North. Presently there are two commercial seismometers with homogenous triaxial configuration, Streckheisen STS-2 and Nanometrics Trillian 120P.

The microseismometer under development is intended for tri-axial measurement using the homogenous triaxial configuration. The fabricated suspensions will deform under gravity when placed in the Galperin configuration. To avoid having to compensate for lateral deflection the springs are preformed such that under gravity the proof mass is centred (Figure 2.7).

The lateral deflection of the proof mass under gravity which is compensated by preformed springs imposes a design constraint on the natural frequency of the suspension when the die size is fixed.

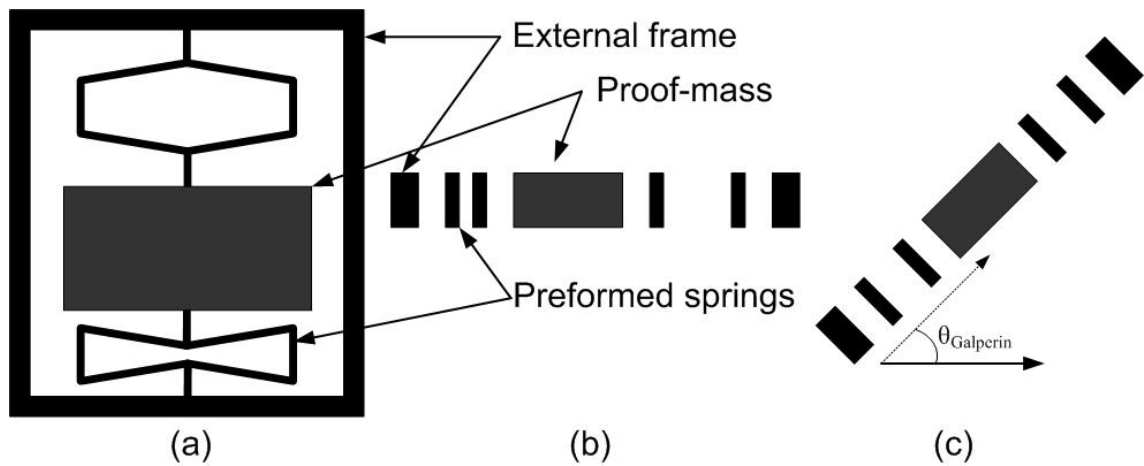


Figure 2.7 (a) A typical single spring suspension with preformed springs, (b) showing the off-centred proof-mass in horizontal position and (c) Centring of the proof-mass under gravity in Galperin orientation.

2.4 Design Inputs

One of the key goals of MEMS device fabrication is to batch fabricate multiple devices on the same wafer. For our design we have considered a widely available 100 mm diameter silicon wafer of 525 μm nominal thickness.

The device die size sets the natural frequency of the suspension. The larger the device die, the lower will be the natural frequency of the suspension assuming we use the same fraction of the die as proof mass and the springs are the same thickness and equal in number. From mass and natural frequency considerations, fabricating a single suspension out of the whole wafer will give us the best performance but the cost will be high and a single defect can reduce the yield to zero. Taking production and cost issues into consideration, a reasonable device size might be one which can lead to an acceptable natural frequency and yield multiple devices in a single run.

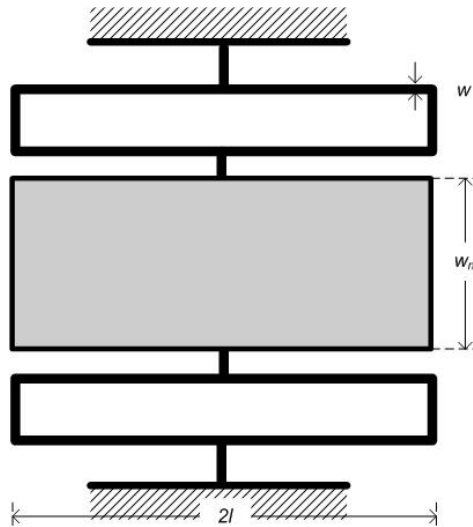


Figure 2.8 Schematic of the suspension showing the proof-mass and spring dimensions.

Assuming suspension geometry similar to Figure 2.5 we can look at the relation between die size (the overall size of the substrate containing a single suspension) and the resonant frequency of the largest single spring pair suspension which can be fabricated within that die. The suspension is assumed to have a uniform thickness of t , considering the spring pair in Figure 2.8 supporting the proof-mass (dimension $l \times w_m$) is made of 8 cantilevers of length l , and width w , the spring stiffness for the suspension is given by

$$k = 8 \times \frac{3EI}{l^3} \quad (2.13)$$

$$I = \frac{1}{12} w^3 t \quad (2.14)$$

The resonant frequency ω is given by

$$\omega = \sqrt{\frac{k}{m}} \quad (2.15)$$

Assuming the proof-mass is always the same fraction of the overall die size and the spring and proof-mass length are the maximum length possible in the die (approximated

to the length of the die) and the spring width and thickness are the same across the die sizes. Doubling the width of the die doubles the width of the proof mass as well. The resonant frequency ω is then proportional to the die dimensions as

$$\omega^2 = \frac{24EI}{ml^3} = \frac{24Ew^3t}{12\rho l^4 w_m t} = \frac{2Ew^3t}{\rho l^4 w_m t} \propto \frac{1}{l^4 w_m} \quad (2.16)$$

From equation 2.16 doubling the die length and width (quadrupling the area of the die) decreases the resonant frequency by a factor of $4\sqrt{2}$. Figure 2.9 shows the variation of natural frequency with die size. This implies that if we are able to design a 20 mm \times 20 mm die with 10 Hz resonant frequency, a similar design with same spring thickness and proof-mass:die ratio will lead to 56.57 Hz for 10 mm \times 10 mm die and 314.75 Hz for a 5 mm \times 5 mm die.

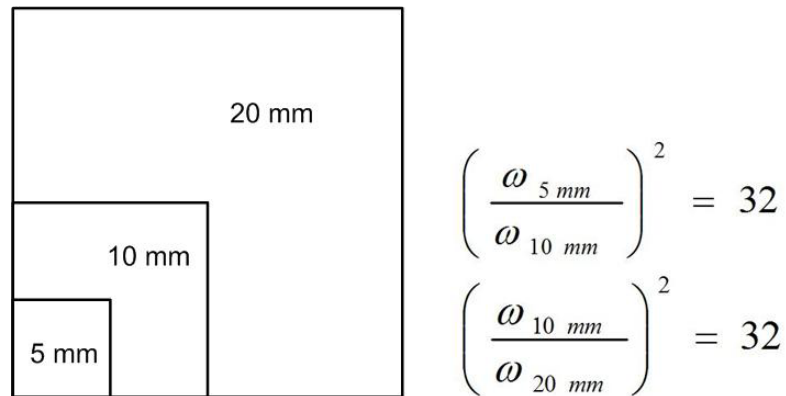


Figure 2.9 Variation of natural frequency with die size. Doubling the die length and width (quadrupling the area) decreases the resonant frequency by $4\sqrt{2}$.

As we discussed in section 1.3, suspension self-noise is a critical parameter, NEA is dependent on the resonant frequency and Q of the suspension and generally a suspension with low resonant frequency and high- Q will have a low NEA as seen from Figure 2.10. The mass of the suspension is taken as 0.26 grams and the temperature is 300 K for the Q measure.

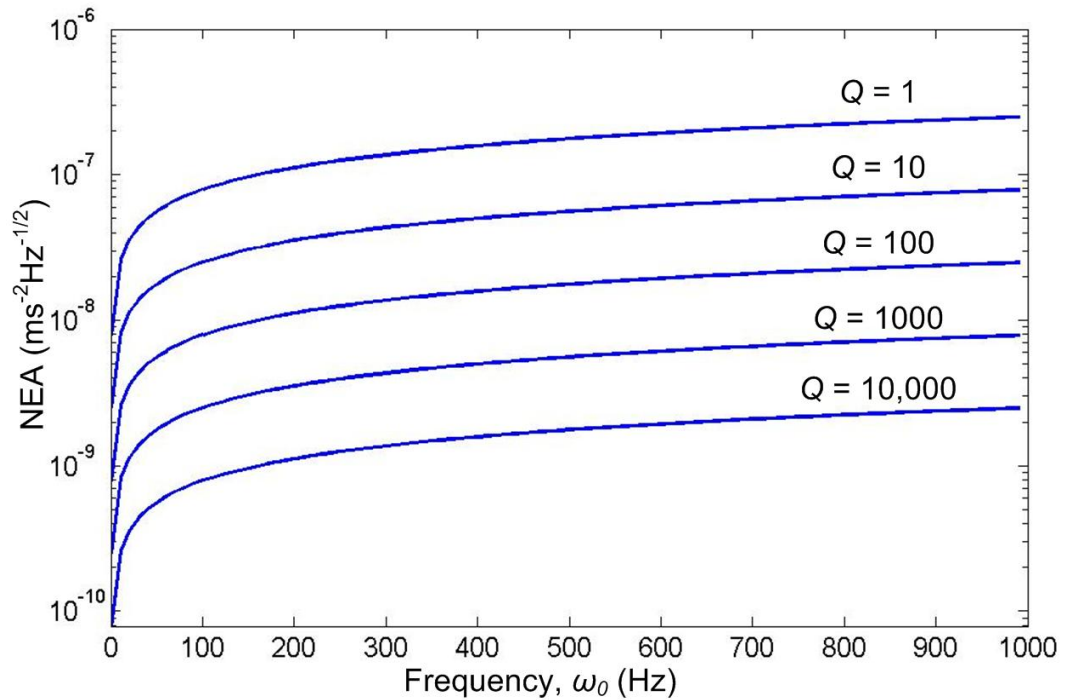


Figure 2.10 Variation of mechanical noise with resonant frequency for varying Q. The mass of the suspension is 0.26 grams and temperature is 300K.

We have fixed the die size at $20 \text{ mm} \times 20 \text{ mm}$ as this allows for the fabrication of 12 dies on a single 100 mm wafer which means a yield of even 8% will lead to a single functioning suspension, as we will see later for fabricating a suspension the die yield is close to 100% after sufficient process development.

Commercial long period seismometers have a time period of 1 to 10 seconds or higher. It is possible to fabricate a suspension with a natural frequency of 1 Hz, but when the suspension is tilted to the Galperin angle the lateral deflection of the proof mass brings the springs in contact with each other making the suspension useless for measuring the movement of the proof mass. In these cases the suspension with preformed springs can not be fabricated as the preforming will not be sufficient to counter-balance the force under gravity acting on the proof-mass.

For initial suspension dimension calculations we will consider a design geometry shown in Figure 2.11 which is similar to the design in Figure 2.5 and in addition includes space for an electrical connector pad and an external frame which supports the suspension within.

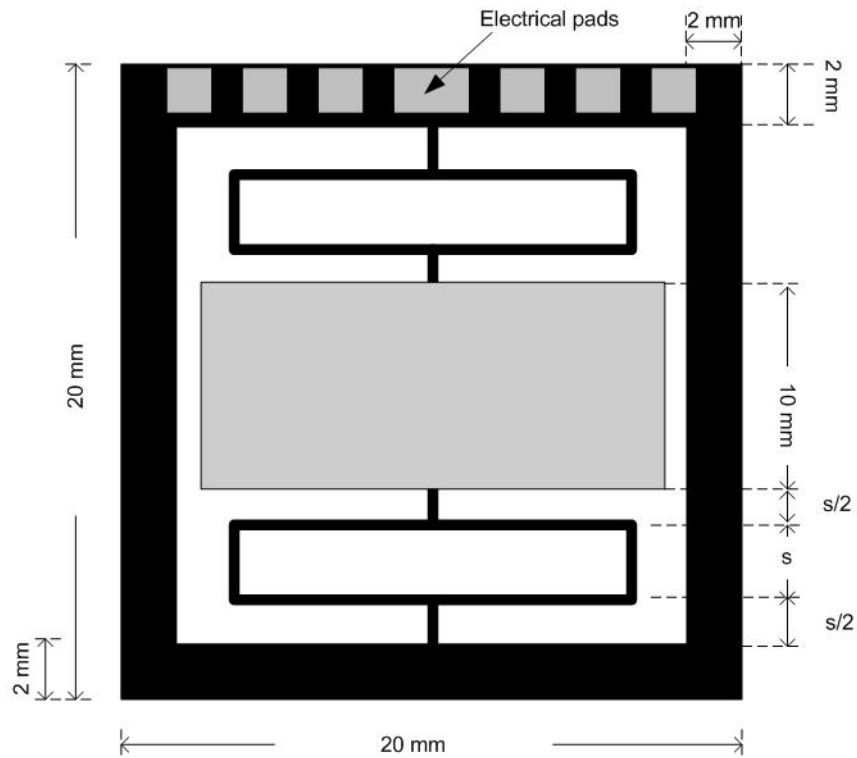


Figure 2.11 Schematic of the suspension design with one spring and mass which is assumed to be 50% of the die area for initial estimates.

As we discussed in section 2.3.1 the intent of the current design is to preform the springs so that when the suspension is oriented along the Galperin axis the proof mass is centred (Figure 2.7c). The lateral suspension sag in Galperin configuration is given by

$$\Delta x_{galperin} = \frac{g_{galperin}}{\omega_0^2} \quad (2.17)$$

$$g_{galperin} = g \cos(\theta_{galperin}), \theta_{galperin} = 54.74^\circ \quad (2.18)$$

The dimensional limits on the mass and springs are set by considering some standard dimensions for frames, connector pads, and proof mass. We will initially assume that 50% of the area is proof mass, in addition the external frame is assumed to be 2 mm thick with 2 mm connector on one side (Figure 2.11). This allows 16 mm as the spring-mass length.

Table 2.1 Dimensional parameters for suspension design.

Parameter	Value
Die length, L_{die}	20 mm
Die width, W_{die}	20 mm
Frame thickness, w_{frame}	2 mm
Connector area width, w_{conn}	2 mm
Proof mass length, l_{mass}	10 mm
Proof mass width, w_{mass}	$W_{die} - 2*w_{frame} = 16$ mm
Spring length, l_{spring}	l_{mass}

From Figure 2.7a we can see that for a preformed spring we have 4 mm on each side of the proof mass. The spring element can be seen as composed of a link, two spring beams and another link. The gap between the spring beams is s and the link width is $s/2$. For preforming we can assume the proof mass sag to be 4 mm (neglecting spring thickness for initial estimate). Using equations 2.17 and 2.18 we calculate the minimum resonant frequency for a one-spring suspension.

$$\omega_0^2 = \frac{g_{galperin}}{\Delta x_{galperin}} = \frac{5.662}{4 \times 10^{-3}} s^{-2} \Rightarrow \omega_0 = 37.62 s^{-1} \Rightarrow f_0 = 6 Hz \quad (2.19)$$

So we can ideally design a suspension with 6 Hz resonant frequency with the dimensions given above, now we need to calculate the spring width which will be needed for achieving 6 Hz suspension. We will use equations 2.16 for calculating the width of the spring for the specified spring geometry.

$$\omega_0 = \frac{24EI_{x,spring}}{m_{mass}l_{spring}^3} = \frac{2Ew_{spring}^3t_{spring}}{m_{mass}l_{spring}^3} \quad (2.20)$$

$$m_{mass} = l_{mass} \times w_{mass} \times t_{mass} \times \rho = 2.19 \times 10^{-4} \text{ kg} \quad (2.21)$$

Using equation 2.20 and dimensional parameters from Table 2.1 we calculate the resonant frequency for various spring thicknesses as shown in Figure 2.12.

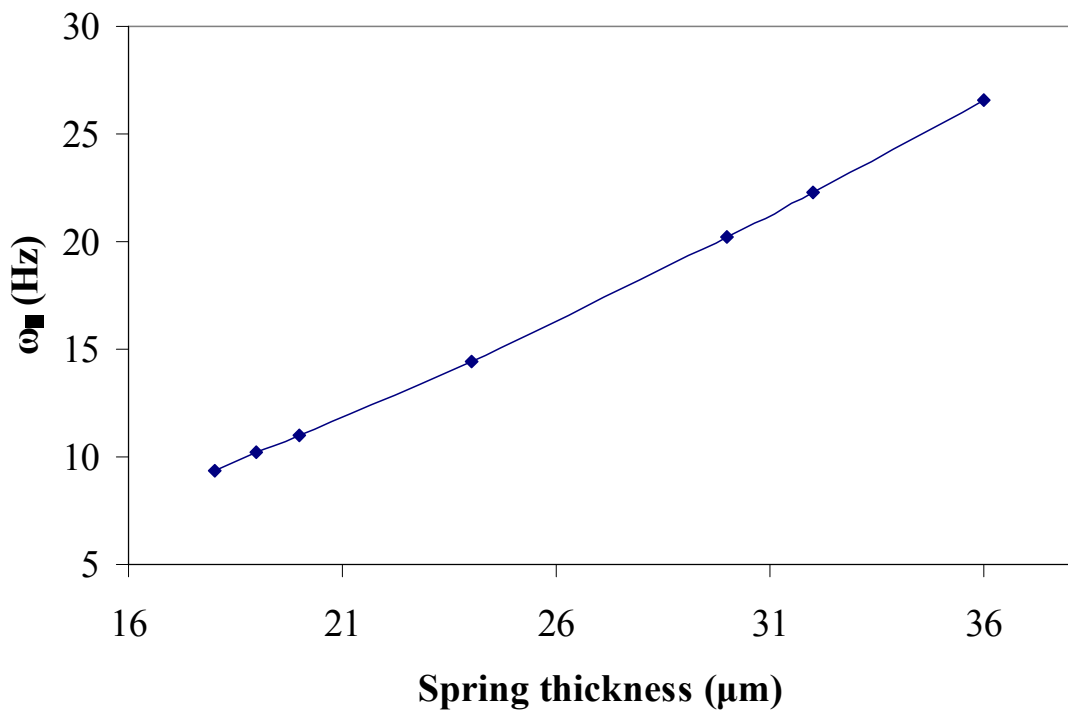


Figure 2.12 Variation of resonant mode with spring thickness for a 20mm×20mm die size and 10mm×16mm proof-mass.

From Figure 2.12 it is evident that for a 6 Hz suspension the ideal thickness determined theoretically is $18.2 \mu\text{m}$. As we will see in section 2.5 this may need to be modified to satisfy other design and process constraints.

2.5 Micromachining Process Design Limitations

The design limitations discussed here are analyzed in detail in chapter 4 on fabrication but it becomes imperative to handle these parameters here to set the ground work for the next chapter on analytical and numerical modelling.

To maximize the proof mass weight, the suspension is fabricated by through-wafer etching of a $525 \mu\text{m}$ thick silicon wafer. This imposes a constraint on the minimum feature size which can be etched through the thickness of the wafer.

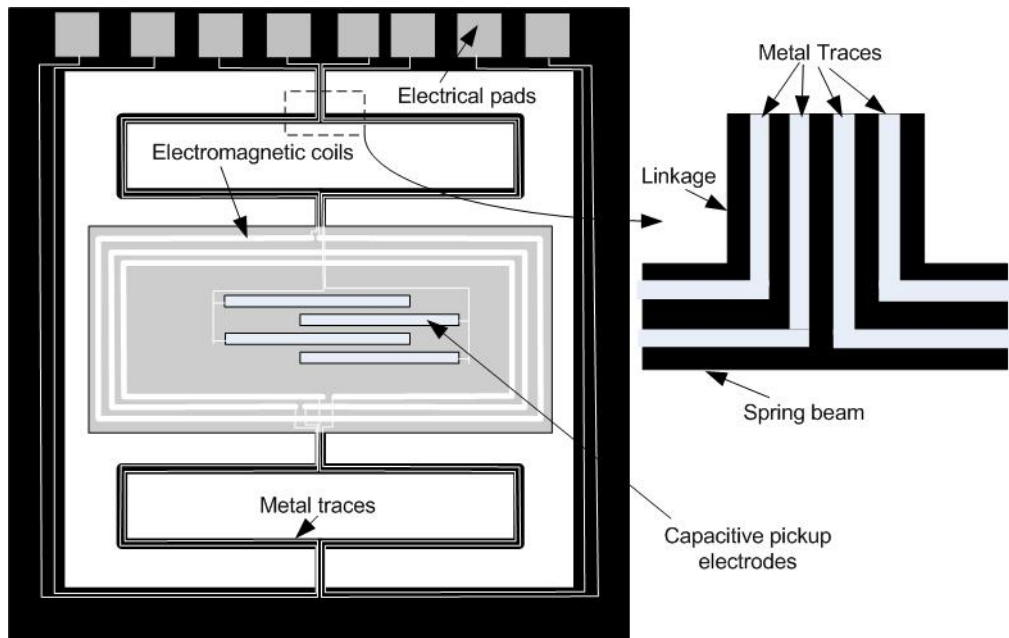


Figure 2.13 Metal traces running on the springs connecting the electromagnetic feedback coil and electrostatic capacitive feedback electrodes.

The first constraint is on the width of a gap that can be etched through the thickness of the wafer; this gap is about 40 μm for best etching characteristics with our silicon thickness.

The second constraint is on the minimum width of a spring which will be able to support the metal traces running on the top. Eight traces are required to connect the three set of coils and a pair of pickup electrodes on the proof-mass resulting in two trace per spring beam. The minimum width of metal trace is 6 μm with a gap of 4 μm between the traces to satisfy local fabrication facility processing limitations. This leads to a minimum spring thickness of 24 μm for two traces running on the springs as shown in Figure 2.13. The two traces on each spring is needed for the differential capacitive pickup circuit and electromagnetic feedback coil, both these components are discussed in chapter 6.

$$w_{gap,min} = 40\mu m \quad (2.22)$$

$$w_{spring,min} = 24\mu m \quad (2.23)$$

We can see that the spring thickness we calculated in section 2.4 of 18.2 μm is below the minimum spring thickness allowed by the fabrication process. So we can either increase the number of springs so the thickness is higher for the spring beams or increase the resonant frequency of the suspension by using a thicker spring. Using equation 2.9 for spring width of 24 μm the resonant frequency is calculated to be 9.08 Hz. Giving leeways for design dimensions and processing constraints, we set a target resonant frequency of 10 Hz for the lateral suspensions. We will analyze the suspension dimensions further in chapter 3 with a set of optimum designs whose fabrication is covered in chapter 4.

2.6 Feasibility Study

High performance macroscale seismometers have noise floor of 10^{-10} m/s²/√Hz. Given our aim to fabricate a sub-nano-g suspension, our target noise floor is 0.35 ng/√Hz.

From the die size, target suspension noise and initial design value for the suspension resonant frequency we can assess the feasibility of the design in regards to the required Q and the amount of the die area required for “sag” of the device under Galperin tilt.

$$NEA_{target} = 0.35ng / \sqrt{Hz} = 3.43 \times 10^{-9} m / s^2 / \sqrt{Hz} \quad (2.24)$$

$$\omega_0 \approx 10Hz \quad (2.25)$$

Using equation 2.2 for calculating the NEA of suspension, we can calculate the required Q for the target NEA at a nominal operating temperature of 20°C.

$$Q_{target} = \frac{4k_b T \omega_0}{NEA_{target}^2 \cdot m_{mass}} \approx 330 \quad (2.26)$$

So if the fabricated device has a resonant frequency of 10 Hz and Q of above 330, the device will be able to achieve the mechanical self-noise target.

We have to check that the suspension damping will be low enough to allow a Q of above 330. For the suspension without any encapsulation squeeze film damping will be most dominant, the expressions for squeeze film damping for two surfaces with overlap l , spacing between the surfaces h and depth t is given by [2.18]

$$Q_{squeeze} = \frac{m \omega_0}{\alpha_{squeeze}}, \alpha_{squeeze} = \frac{14\eta l t^3}{N h^3} \quad (2.27)$$

For $l = l_{spring}$, $t = t_{spring}$, and $h = \text{spacing between the spring beam} = 2 \text{ mm}$, we can use equation 2.27 to calculate the $Q_{squeeze}$ for the suspension with $N = 1$ springs to be ~ 7400 which is significantly higher than the required Q_{target} . Figure 2.14 shows $Q_{squeeze}$ vs. number of springs, N . The Q -factor due to squeeze damping reduces with smaller spring gap for multiple sets of springs as the damping is higher. For $N < 4$, $Q_{squeeze}$ is above Q_{target} .

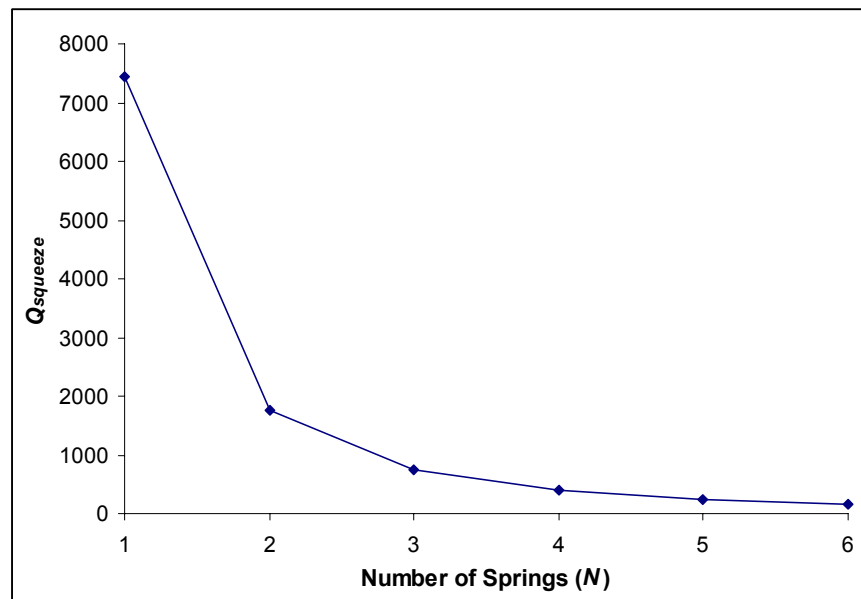


Figure 2.14 Quality factor (due to squeeze film damping), $Q_{squeeze}$ variation for multiple spring suspension (N).

2.7 Summary

The targeted noise floor for the suspension was set to $0.35 \text{ ng}/\sqrt{\text{Hz}}$. To attain such low self-noise the suspension should have large mass, low resonant frequency and high quality factor.

The lateral suspension is covered in US patent 6776042 (Pike et al.). The author's role in the design process is to help model various suspensions to set the dimensional parameters to attain the target characteristics.

The lateral suspension design is based on folded cantilever beams which are commonly used in designing suspensions for MEMS accelerometers. The lack of symmetry perpendicular to the motion of the suspension leads us to develop a suspension with a mirror pair of folded cantilever springs joined at the center.

To measure vibration along all three axes and avoid different designs for vertical and horizontal suspensions, we decided to use a Galperin configuration. The suspension springs are preformed so that under gravity at Galperin tilt, the proof-mass is centred. This puts constraint on the resonant frequency of the suspension for a specific die size due to the lateral deflection of the proof-mass under gravity at Galperin tilt.

The lowest resonant frequency suspension possible in a 20 mm × 20 mm die with 50% proof-mass area was 6 Hz. With folded cantilever springs, this leads to a spring thickness of 18.2 μm which is below the 24 μm minimum feature size constraint of the fabrication process. A 24 μm spring thickness results in a 9.08 Hz suspension.

Assuming a 10 Hz resonant frequency and a mass of 0.26 grams (50% of the die area) we can attain the NEA of 0.35 ng/√Hz (3.43×10^{-9} m/s²/√Hz) if the suspension has a Q higher than about 330. The squeeze flow damping of a suspension with less than four sets of springs was shown to satisfy the Q requirement.

2.8 Conclusion

We have demonstrated the feasibility of a lateral suspension which can attain the target self-noise by designing a mirrored folded cantilever suspension. Availability of

fabrication tools like DRIE allows us to design suspensions which are hundreds of microns thick thus increasing the seismic mass.

The key parameters for the silicon lateral suspension set from device design and fabrication constraints are:

$$NEA_{target} = 0.35ng / \sqrt{Hz} = 3.43 \times 10^{-9} m / s^2 / \sqrt{Hz}$$

$$\omega_0 \approx 10Hz$$

$$Q_{target} \geq 330$$

$N \leq 3$, for suspension within 20 mm \times 20 mm die size and 50% proof-mass area

Devices made of single crystal silicon have been reported in literature to attain Q 's as high as 100,000 [2.19] and 600,000 [2.5] which increases our confidence that the suspension design can achieve the self-noise target. We can design suspensions with up to three sets of springs while still staying within the target Q levels in normal atmosphere. Vacuum packaging the device will remove all consideration for squeeze film damping and remove any restriction imposed on putting the springs close together.

In the next chapter we analyze the suspension analytically and numerically considering an ideal processing environment where the design is transferred into silicon rectilinearly to what is many times referred as a 2.5D structure – A 2D design extruded vertically in the third dimension.

2.9 Bibliography

- [2.1] J. M. Tsai and G. K. Fedder, "Mechanical noise-limited CMOS-MEMS accelerometers," presented at 18th IEEE International Conference on Micro Electro Mechanical Systems, Miami Beach, FL, USA, 2005.
- [2.2] M. J. Usher, "Developments in seismometry," *Journal of Physics E: Scientific Instruments*, pp. 501-507, 1973.
- [2.3] A. A. Seshia, *Integrated Micromechanical Resonant Sensors for Inertial Measurement Systems*, Ph.D. Thesis, Electrical Engineering and Computer Science, University of California, Berkeley, 2002
- [2.4] P. M. Roberts, "A versatile equalization circuit for increasing seismometer velocity response below the natural frequency," *Bulletin of the Seismological Society of America*, vol. 79, pp. 1607-1617, 1989.
- [2.5] R. A. Buser and N. F. De Rooij, "Very high Q-factor resonators in monocrystalline silicon," *Sensors and Actuators A: Physical*, vol. 21, pp. 323-327, 1990.
- [2.6] J. L. Yang, M. Despont, U. Drechsler, B. W. Hoogenboom, P. L. T. M. Frederix, S. Martin, A. Engel, P. Vettiger, and H. J. Hug, "Miniaturized single-crystal silicon cantilevers for scanning force microscopy," *Applied Physics Letters*, vol. 86, pp. 134101, 2005.
- [2.7] H. J. Himmelbau and S. Rubin, *Vibration of a resiliently supported rigid body*, in *Shock and Vibration Handbook*, C. M. Harris, Ed., 4th ed. New York: McGraw-Hill, 1996, pp. 3.1-3.57.
- [2.8] H. Seidel and L. Csepregi, "Design optimization for cantilever-type accelerometers," *Sensors and Actuators*, vol. 6, pp. 81, 1984.
- [2.9] J. D. Grade, K. Y. Yasumura, and H. Jerman, "A drive comb-drive actuator with large, stable deflection range for use as an optical shutter," presented at 12th International Conference on Solid-State Sensors, Actuators and Microsystems, Boston, USA, 2003.
- [2.10] Y. Suzuki and Y.-C. Tai, "Micromachined high-aspect-ratio parylene beam and its application to low-frequency seismometer," presented at The 16th IEEE International Conference on Micro Electro Mechanical Systems, Kyoto, Japan, 2003.

- [2.11] J. A. Yeh, C.-N. Chen, and Y.-S. Lui, "Large rotation actuated by in-plane rotary comb-drives with serpentine spring suspension," *Journal of Micromechanics and Microengineering*, vol. 15, pp. 201-206, 2005.
- [2.12] G. Zhou, "Tilted folded-beam suspension for extending the stable travel range of comb-drive actuators," *Journal of Micromechanics and Microengineering*, vol. 13, pp. 178, 2003.
- [2.13] H. Seidel, H. Riedel, R. Kolbeck, G. Mueck, and W. Kupke, "Capacitive silicon accelerometer with highly symmetrical design.," *Sensors and Actuators B: Chemical*, vol. 21, pp. 312, 1990.
- [2.14] E. Peeters, S. Vergote, B. Puers, and W. Sansen, "A highly symmetrical capacitive micro-accelerometer with single degree-of-freedom response," presented at International Conference on Solid-State Sensors and Actuators, San Francisco, CA, USA, 1991.
- [2.15] E. Wielandt, *Seismometry*, in *International Handbook of Earthquake and Engineering Seismology, Part A*, W. H. K. Lee, H. Kanamori, P. Jennings, and C. Kisslinger, Eds.: Academic Press, 2000, pp. 283.
- [2.16] E. I. Gal'perin, "Azimutal'nij metod sejsmicekich nabludenij," *Gostoptechizdat* 1955.
- [2.17] B. S. Melton and B. M. Kirkpatrick, "The symmetric triaxial seismometer - its design for application in long-period seismometry," *Bulletin of the Seismological Society of America*, vol. 60, pp. 717-739, 1970.
- [2.18] W. A. Clark, *Micromachined Vibratory Rate Gyroscope*, Ph.D. Thesis, Electrical Engineering and Computer Science, University of California, Berkeley, 1997
- [2.19] S. Pourkamali, A. Hashimura, R. Abdolvand, G. K. Ho, A. Erbil, and F. Ayazi, "High-Q single crystal silicon HARPSS capacitive beam resonators with self-aligned sub-100-nm transduction gaps," *Journal of Microelectromechanical Systems*, vol. 12, pp. 487-496, 2003.

three

3 Suspension Dynamics

In this chapter we analyze the suspension design developed in chapter 2. We use an analytical model to explore the design space and verify the results using finite element analysis. To design low resonant frequency suspensions we consider multiple spring sets and look at the pros and cons of the design. Intermediate frames are shown as a way to decouple the effect of multiple spring sets on spurious modes. Various other design modifications like reduced mass frames, spring end connector compliance and linkage geometries are analyzed. Finally, a set of suspension designs fulfilling the specifications on NEA and resonant frequency are proposed.

3.1 Introduction

The behaviour of the fundamental mode of lateral suspensions can be analysed in terms of a one-degree-of-freedom (1DOF) system [3.1, 2] but this neglects all potential spurious modes. Finite element analysis (FEA), which is able to extract any number of spurious modes, has been applied to the uniaxial suspension of the Analog Devices accelerometer [3.3]. Analytic approaches and FEA have been used to optimize the design of a dual-axis suspension [3.4]. In this chapter we apply analytical and numerical models to optimize the design of lateral suspensions with folded-cantilever flexures.

As described in chapter 2 we consider a canonical folded-cantilever lateral suspension of the simplest symmetric design. A complete set of analytical expressions (derived in Appendix A) is considered in conjunction with a finite element model for the six degrees of freedom (6 DOF) system. Further modes due to the finite mass of the suspension are then included. We also analyze dependence of the spurious-mode rejection ratios on simple multiples of the aspect ratios of the suspensions giving straight forward heuristic design for suspension optimization. Next, suspensions with multiple spring sets are studied to lower the fundamental frequency. Finally, intermediate frames coupling portions of the suspension are explored as a novel approach for enhancing the performance [3.5]. A full set of analytical equations and numerical analysis is applied to the off-axis modes of a suspension incorporating such frames.

The analysis is focused on developing a model for the suspension to predict its dynamical characteristics prior to fabrication. It also offers a test bed to investigate the design space and improve the cross-axis rejection ratio of spurious modes.

3.2 Lateral Suspension

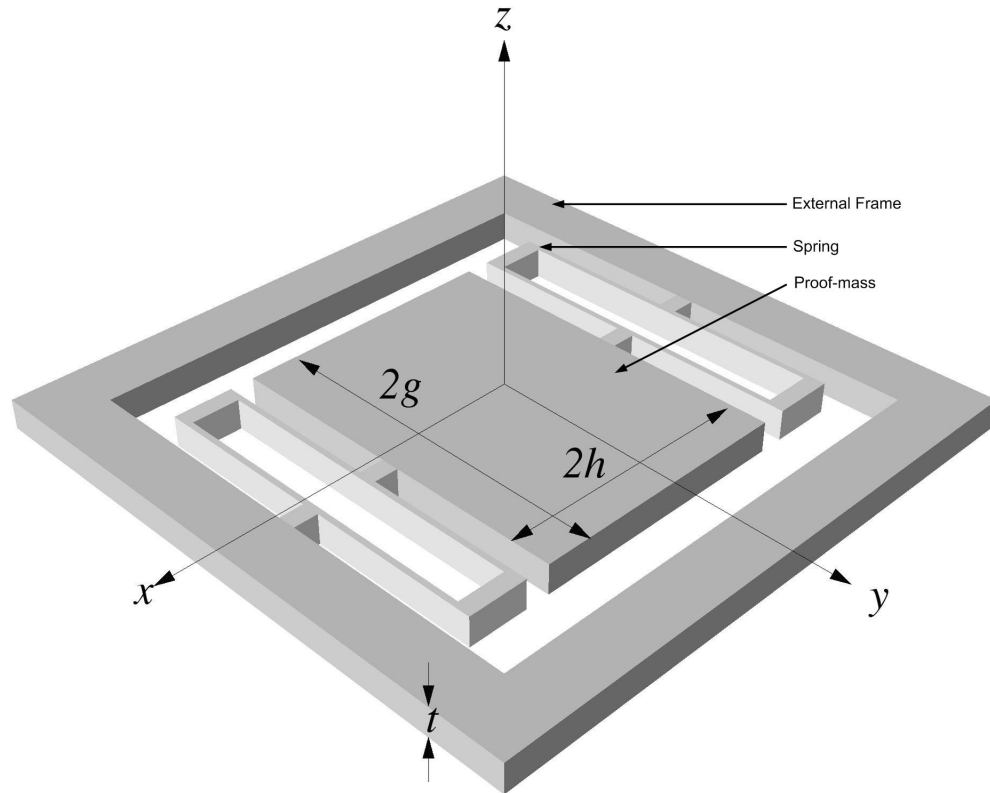


Figure 3.1 Schematic of a lateral suspension illustrating the model geometry and the critical dimensions.

The lateral suspension is shown schematically in Figure 3.1. Geometrically, the suspension is an extrusion of a two-dimensional pattern. Physically, the depth of the extrusion is given by the thickness of the etched layer, which is the full wafer thickness (t). The suspension consists of two springs either side of a proof mass connected to an external fixed frame. The ideal suspension would be solely compliant along the X -axis with maximum stiffness to translations along the other two axes and rigidity to rotation about all axes. It is assumed that the suspended mass is perfectly rigid. It is further assumed, at least initially, that the suspension is massless, which is reasonable when considering cross-axis dynamics. A massive suspension is later treated as a perturbation

on the massless solution. Under these assumptions the analysis of such a suspension involves the solution of the equations of motion for a 6DOF system [3.6]:

$$[\mathbf{M}]\ddot{\mathbf{u}} + [\mathbf{C}]\dot{\mathbf{u}} + [\mathbf{K}]\mathbf{u} = \mathbf{0} \quad (3.1)$$

where \mathbf{u} is the coordinate vector,

$$\mathbf{u} = [x, y, z, \alpha, \beta, \gamma]^T \quad (3.2)$$

x, y, z are displacement along the three axes, α, β, γ are the rotational components about the axes X, Y, Z respectively.

$[\mathbf{M}]$ is the inertial matrix, which has the diagonal components $(m, m, m, I_{xx}, I_{yy}, I_{zz})$ and symmetric off-diagonal terms dependent on the shape of the suspended mass, $[\mathbf{C}]$ is a symmetric matrix of the damping terms and $[\mathbf{K}]$ is a symmetric stiffness matrix. The six simultaneous equations for the general case become separable in their coordinates if there are three planes of symmetry to the suspension [3.7]. Such a suspension has no coupling between motion in each coordinate implying that all the off-diagonal terms in \mathbf{M} and \mathbf{C} are zero. This decoupling not only greatly simplifies analysis but is necessary if the suspension is used for transduction. Here we consider only such center-of-gravity systems, so-called as symmetry implies that the elastic forces of the suspension are directed through the centre of the suspended mass. In addition, the system is further simplified by neglecting damping as the aim of the analysis is to optimize the design in terms of compliance. The resulting six separable equations are:

$$\begin{bmatrix} m & m & m & I_{xx} & I_{yy} & I_{zz} \end{bmatrix}
 \begin{bmatrix} \ddot{x} \\ \ddot{y} \\ \ddot{z} \\ \ddot{\alpha} \\ \ddot{\beta} \\ \ddot{\gamma} \end{bmatrix}
 - \begin{bmatrix} k_x & k_y & k_z & k_\alpha & k_\beta & k_\gamma \end{bmatrix}
 \begin{bmatrix} x \\ y \\ z \\ \alpha \\ \beta \\ \gamma \end{bmatrix} = 0 \quad (3.3)$$

which has the customary normal-mode solution, $u_i = a_i \sin(\omega_i t + \phi)$ where normal mode frequencies are

$$\omega_i = \sqrt{K_{ii}/M_{ii}} \quad (3.4)$$

with a_i and ϕ set by the initial conditions. The spring constants, and hence the frequencies of the normal modes, determine the performance of the suspension. To optimize, the frequency ratio of the cross-axis modes to the on-axis mode, $\omega_{i \neq x}/\omega_x$ should all be as high as possible. As there could often be opposing effects on the various rejection ratios $\omega_{i \neq x}/\omega_x$ for a particular design parameter, a near optimum suspension design will in general have its two lowest cross-axis-mode frequencies approximately equal.

The canonical status of this suspension is evident in its application in a number of designs, e.g. [3.8-12]. A detailed analysis of this suspension is therefore justified in order to set a rational design methodology. One obvious approach, optimization through FEA, has already been applied to this suspension design in order to optimize harmonic modes for a differential capacitive accelerometer [3.3] but FEA does not produce general design rules. The analytical formulas developed in Pike et al [3.5] (derivation presented in Appendix A) and used here should provide a more heuristic approach to lateral suspension design. In deriving these analytical formulas, FEA (ANSYS, Inc., Canonsburg PA), was applied to elements of the suspension to ensure that all the important modes of deflections were included, and also to crosscheck numerically the analytical expressions. In order to produce reasonable FEA simulation run times and node numbers, the suspension was taken as a simple extrusion. In the first instance, a

minimal suspension consisting of a single spring unit either side of the proof-mass is considered. Complete derivation for the various modes is presented in Appendix A.

3.2.1 On-axis compliance

The planar geometry (Figure 3.2) of each spring unit can be characterized by the values of the beam length l , beam width w , beam spacing (from beam axis to beam axis) s , linkage length width w_s , and linkage length, taken here to be $(s-w)/2$ to give a unit dimension in the compliant direction of $2s$. The detailed elbow geometry is left undefined. There are two important geometric ratios defining the suspension; the beam cross-sectional aspect ratio, w/t ; the suspension ratio of the beam spacing to the beam length, s/l . The simplest suspension consists of one unit on each side of the proof mass (Figure 3.1). Such a suspension satisfies the required symmetry conditions and the six spring constants can be solved separately for motion along and about each axis.

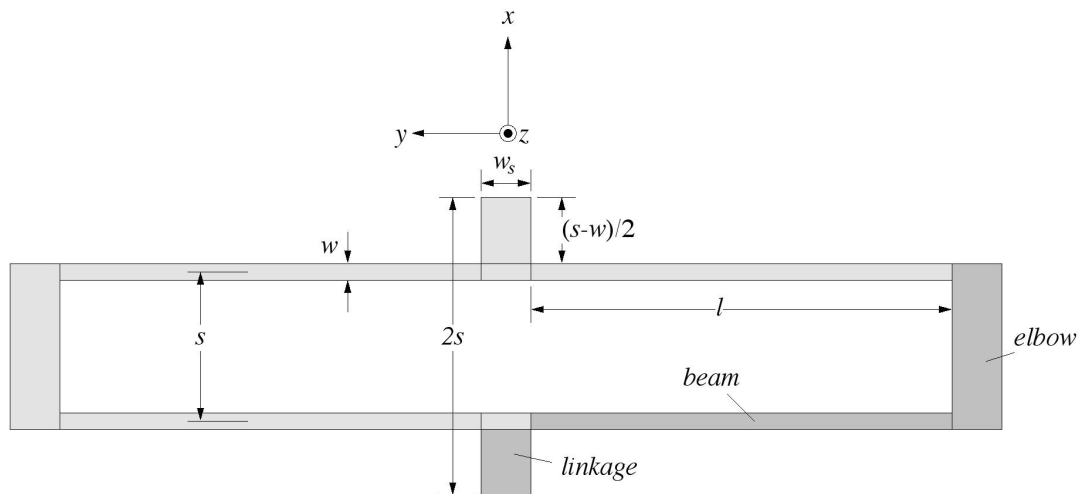


Figure 3.2 Schematic of a single spring set for the lateral suspension showing the geometry and critical dimensions.

The compliant direction for the lateral suspension is taken along X -axis while Z -axis is the out-of-plane direction. Using cantilever bending formula from Roark[3.13], the spring stiffness constant for the suspension along the compliant direction is given by

$$k_x = \frac{24EI_x}{l^3} \quad (3.5)$$

where E is the Young's modulus of silicon, I_x is the area moment of inertia given by

$\frac{1}{12} w^3 t$ and l is the length of the spring as shown in Figure 3.2. The fundamental mode

along the X -axis is given by

$$\omega_x = \sqrt{\frac{k_x}{m}} \quad (3.6)$$

where m is the mass of the proof-mass. The mode shape is shown in Figure 3.3.

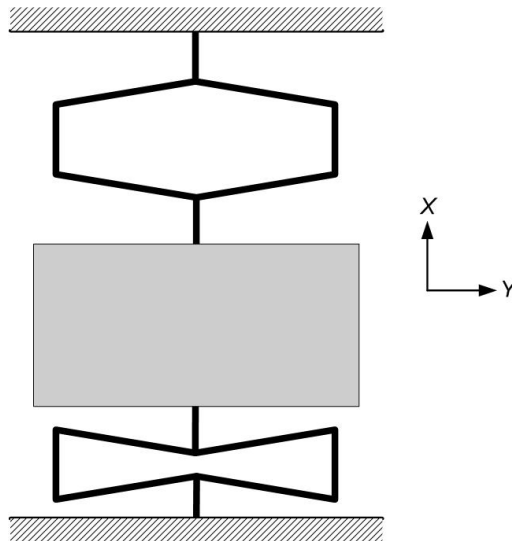


Figure 3.3 Fundamental mode shape of a single spring set lateral suspension. The proof-mass is resonating along the X -axis.

To maximize the compliance along this direction for a suspension fabricated in an anisotropic crystal such as silicon, the beams should be orientated to minimize E . For silicon this corresponds to the $\langle 100 \rangle$ directions [3.14].

3.2.2 Cross-axis translational compliance

Cross-axis translational compliance of the complete suspension is determined by the spring constants in the y and z direction which are derived by considering the deflections of the suspended mass due to a test force applied at the centroid of the mass in the required direction.

The spring stiffness constant in the y direction for the lateral suspension with a single set of springs is given by

$$k_y = \frac{8EI_x}{lS^2} \quad (3.7)$$

The rejection of the y mode can then be calculated as

$$\frac{\omega_y}{\omega_x} = \frac{l}{\sqrt{3}S} \quad (3.8)$$

The mode shape is shown in Figure 3.4.

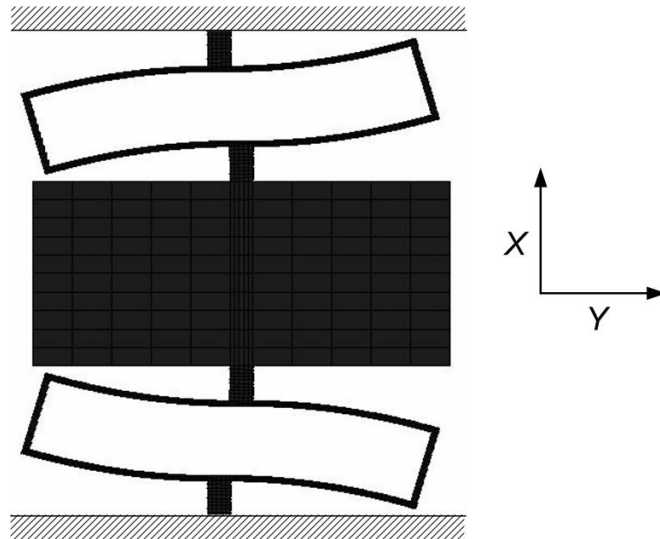


Figure 3.4 ω_y , Mode shape of a single spring set suspension resonating along Y -axis.

Next, the deflection in the out-of-plane z direction, often the most important deflection to minimize, is considered. The linkages are considered perfectly rigid. To calculate the

spring stiffness along the Z-axis, an axial force impressed in the z direction at the centroid of the proof mass is assumed.

The spring compliance for deflections in the z direction is given by

$$\frac{1}{k_z} = \frac{l^3}{24EI_z} + \frac{ls^2}{8GJ} \quad (3.9)$$

The two terms in the expression for out-of-plane spring stiffness are due to deflection of the beam (first term) under an out-of-plane force and twisting of the elbow (second term) due to the torque generated from opposing forces at the end of the beams. I_z is the area moment of inertia about Z-axis and is given by $\frac{1}{12} wt^3$. G is the modulus of rigidity and J is the torsional constant for the spring beam about Z-axis given by $\frac{1}{3} w^3 t$.

The rejection ratio for the z mode is given by

$$\frac{\omega_z}{\omega_x} = \left(3 \frac{EI_x s^2}{GJl^2} + \frac{I_x}{I_z} \right)^{-1/2} \quad (3.10)$$

The mode shape is as shown in Figure 3.5.

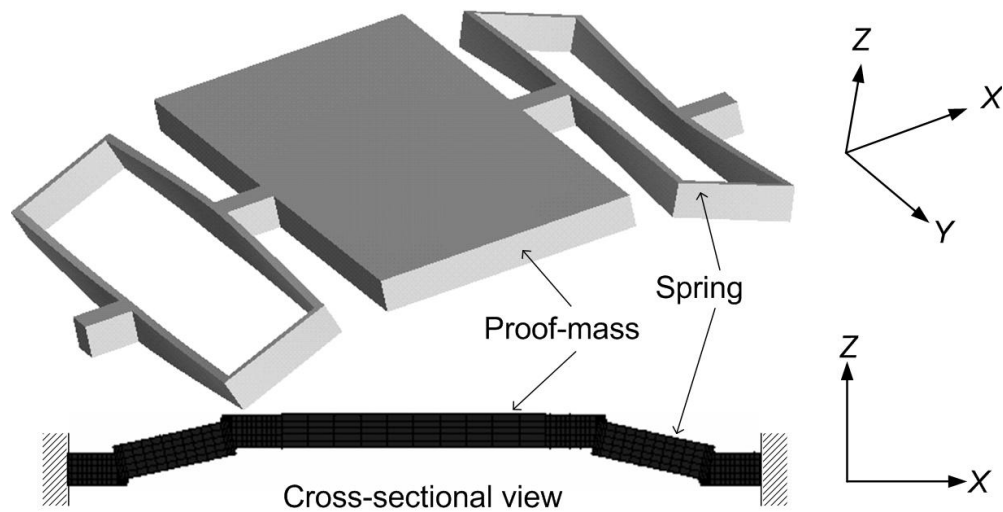


Figure 3.5 ω_z , Mode shape of a single spring set suspension resonating along Z-axis.

3.2.3 Rotational compliance

The rotational mode about the X -axis, ω_α is the angular deflection of the proof-mass about X -axis. The angular deflection consists of contribution from twisting occurring about X -axis of the linkages and the combination of twisting and bending of the spring beams. The compliance about the X -axis, $1/k_\alpha$ is thus a sum of the compliance due to torsion of linkages ($1/k_{\alpha,link}$) and the compliance contribution of the beams ($1/k_{\alpha,beam}$).

$$\frac{1}{k_\alpha} = \frac{1}{k_{\alpha,link}} + \frac{1}{k_{\alpha,beam}} \quad (3.11)$$

The spring stiffness about X -axis due to torsion of the linkages is given by

$$k_{\alpha,link} = \frac{2GJ_s}{s-w} \quad (3.12)$$

where J_s is the torsion constant of the linkage given by $\frac{1}{3} w_s^3 t$. The linkage torsional stiffness can be made very high by increasing the width (w_s) of linkage. In that case, the torsional stiffness of the beam will be dominant in determining the resonant mode about the X -axis. The compliance due to the bending and twisting of the beam is given by

$$\frac{1}{k_{\alpha,beam}} = \frac{l}{4EI_z} \left(1 - \frac{3}{4 + 3 \frac{EI_z s^2}{GJ^2}} \right) \quad (3.13)$$

The linkage width should therefore be chosen to restrict the contribution of the torsion of the linkage to the total compliance. The condition $k_{\alpha,link} \gg \max(k_{\alpha,beam})$ for a comparatively stiff linkage corresponds, for $s \gg w$, to

$$w_s \gg \left[2 \frac{E}{G} \left(\frac{t}{w} \right)^2 \frac{s}{l} \right]^{1/3} w \quad (3.14)$$

As the beam aspect ratio and suspension aspect ratio will often be comparable, and certainly no more than fifty each, condition 3.14 will be met for a linkage of width, w_s , greater than about ten times the beam width, w .

The rejection ratio for the resonant mode about the X -axis is given by

$$\frac{\omega_\alpha}{\omega_x} = \left\{ \frac{4EI_x(s-w)g^2}{GJ_s l^3} + \frac{4I_x g^2}{I_z l^2} \left[1 - \frac{3}{4 + \frac{3s^2 EI_z}{l^2 GJ}} \right] \right\}^{-1/2} \quad (3.15)$$

The mode shape is as shown in Figure 3.6.

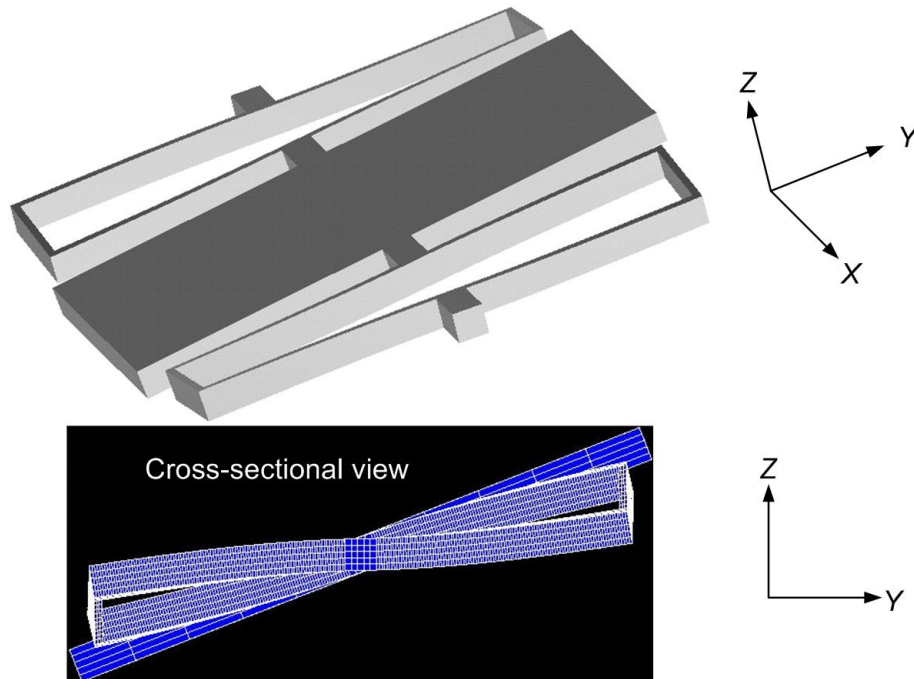


Figure 3.6 ω_α , Mode shape of a single spring set suspension resonating about X -axis.

The rotational spring constants about the y and z axis, k_β and k_γ , is composed of contributions from the effective translational springs and additional angular deflection from the torques arising out of effective torsional springs.

The rotational stiffness about Y -axis is given by

$$k_{\beta} = k_z h^2 \quad (3.16)$$

The rejection ratio of the frequency of the rotational mode about the Y -axis to the translational mode about Z -axis is given by

$$\frac{\omega_{\beta}}{\omega_z} = \sqrt{3} \quad (3.17)$$

The mode shape is shown in Figure 3.7.

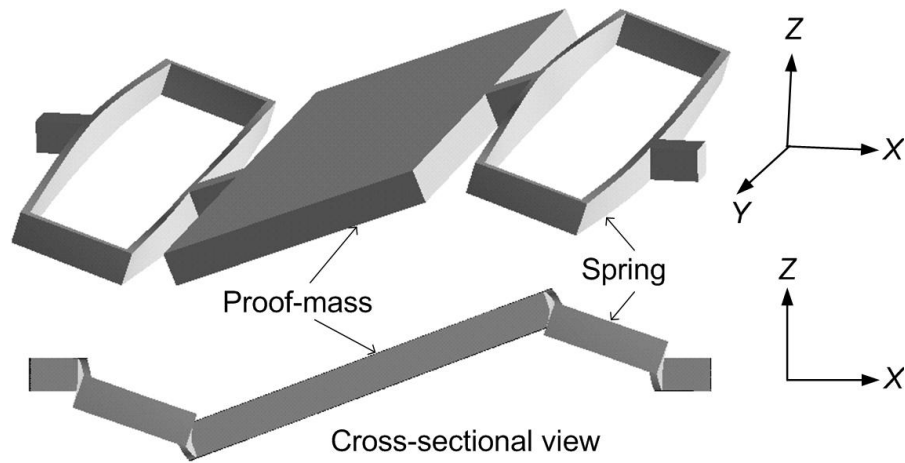


Figure 3.7 ω_{β} , Mode shape of a single spring set suspension resonating about Y -axis.

Similarly for rotation about the Z -axis, again neglecting torsional effects, the rejection ratio of the frequency of rotational mode about Z -axis to the translational mode along Y -axis is given by

$$\frac{\omega_{\gamma}}{\omega_y} = \frac{\sqrt{3}}{\sqrt{1 + g^2/h^2}} \quad (3.18)$$

where g , h are the half width and half length of the proof-mass respectively. Therefore maximizing the off-axis translational-mode frequencies will automatically maximize the off-axis rotational-mode frequencies, simplifying the design approach. The mode shape for ω_{γ} is shown in Figure 3.8.

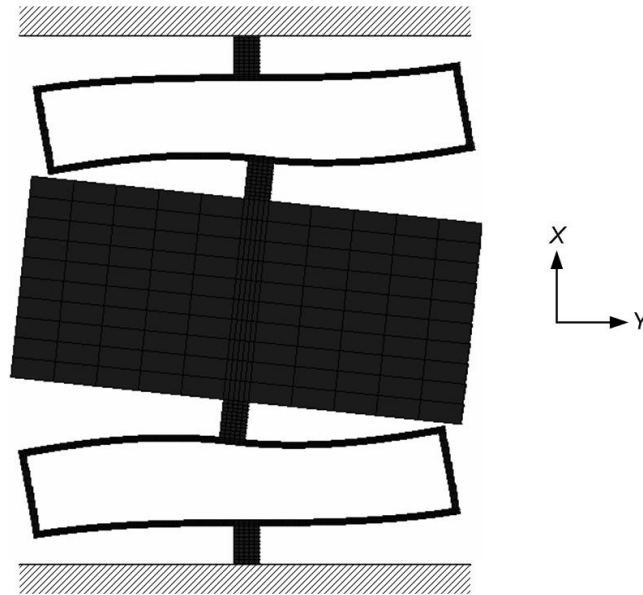


Figure 3.8 ω_7 , Mode shape of a single spring set suspension resonating about the Z-axis.

The additional torsional contribution will cause the rotational-mode frequencies to be higher, which means the expressions given by 3.17 and 3.18 underestimate the rejection ratio and so the design rules developed based on these expressions satisfy the key criteria of increasing the rejection ratio.

3.2.4 Rejection ratios of spurious modes

By making some reasonable approximations, it is possible to achieve some very simple expressions for the rejection ratios of all the spurious modes. First, the beam cross sections are assumed to be rectangular. Second, the ratio of Young's modulus to the shear modulus, E/G is assumed to be 3, which corresponds to an incompressible solid (for silicon $\{100\}$ E/G is 2.56 [3.15]). Third, it is assumed that the linkages and elbows are completely rigid ($1/k_{\alpha, link} = 0$) and of zero width. In this case the spring mass will be $8\rho ltw$. Fifth, the suspension is assumed to extend the width of the proof mass so that $2l = g$. Last, the proof mass is assumed to be square. Under these conditions, the rejection ratios are shown in final column of Table 3.1. Further, if it is assumed that the

suspension and beam aspect ratios are equal, $s/l = w/t = R$, the simple multiples shown in the final column are obtained.

Table 3.1 Rejection ratios of spurious modes for a lateral suspension.

Mode, ω_i^2	$\frac{\omega_x^2}{\omega_i^2}$ for rectangular beam cross sections, $E/G = 3$, and rigid, zero width links and elbows, and square proof mass	$\frac{\omega_x^2}{\omega_i^2}$, with $s/l = w/t = R$	
x	$\frac{24EI_x}{ml^3}$	1	1
x_l	$\pi^2 \frac{m}{m_s} \omega_x^2$	$\frac{2}{\pi^2} \frac{w}{h}$	$\frac{2}{\pi^2} \frac{t}{h} R$
y	$\frac{8EI_x}{m_s l^3} = \frac{l^2}{3s^2} \omega_x^2$	$3 \frac{s^2}{l^2}$	$3R^2$
z	$\frac{1}{\frac{m_s l^3}{8GJ} + \frac{ml^3}{24EI_z}} = \frac{\omega_x^2}{\frac{3EI_x s^2}{GJl^2} + \frac{I_x}{I_z}}$	$\frac{s^2}{l^2} + \frac{w^2}{t^2}$	$2R^2$
α	$\left\{ \frac{4EI_x(s-w)g^2}{GJ_s l^3} + \frac{4I_x g^2}{I_z l^2} \left[1 - \frac{3}{4 + \frac{3s^2 EI_z}{l^2 GJ}} \right] \right\}^{-1} \omega_x^2$	$4 \frac{w^2}{t^2} \left(1 - \frac{3}{4 + \frac{1}{4} \frac{s^2}{l^2} \frac{t^2}{w^2}} \right)$	$\sim R^2$
β	$3\omega_z^2$	$\frac{1}{3} \left(\frac{s^2}{l^2} + \frac{w^2}{t^2} \right)$	$\frac{2}{3} R^2$
γ	$\frac{3}{1 + g^2/h^2} \omega_y^2$	$2 \frac{s^2}{l^2}$	$2R^2$

Table 3.1 presents the expressions for calculating the modes of a single spring set suspension. The rejection ratios are shown to be proportional to the R a parameter dependent on the suspension and beam aspect ratios. In the simplified case, most modes are linearly dependent on the fundamental. The first on-axis spurious mode ω_{x_l} as a square root multiple of R .

3.3 Multiple Spring Suspension

As we discussed in chapter 2, it is often desirable to reduce the fundamental frequency of a lateral suspension as far as possible to maximize the sensitivity in certain applications like an accelerometer for low frequency vibration sensing. For a given device area this can be achieved by either reducing the width of the beams or adding additional suspension units on either side of the proof mass. There is a limit to how thin the beams can be fabricated due to inherent process limitations and so the addition of suspension units may be required.

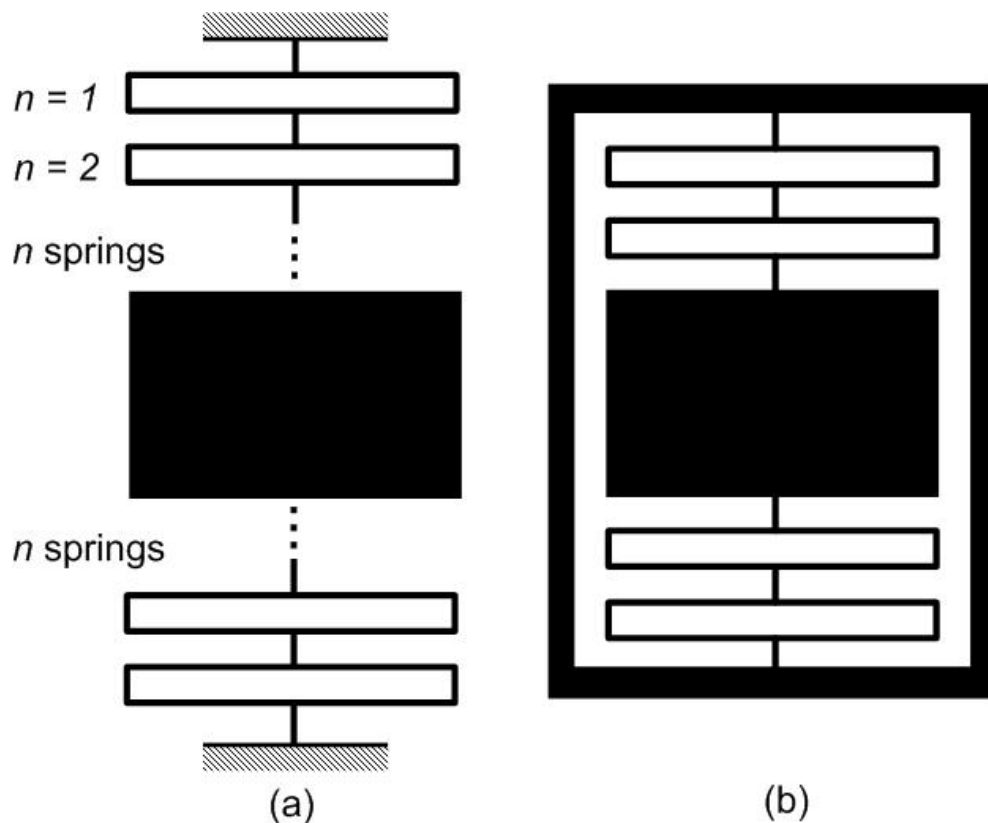


Figure 3.9 Schematic of a lateral suspension with multiple springs, (a) a lateral suspension with n set of spring, and (b) a specific lateral suspension with two ($n=2$) spring sets.

A series of n folded cantilevers each of spring constant k will have a summed spring constant of k/n . As well as softening the suspension, the use of multiple units improves the linearity as the deflection of each cantilever is a lower multiple of the beam

thickness. For a suspension with n pair of springs as shown in Figure 3.9, the spring constant along x axis is given by

$$k_x = \frac{24EI_x}{nl^3} \quad (3.19)$$

The frequency for the fundamental mode for a suspension with n spring sets is given by

$$\omega_x = \sqrt{\frac{k_x}{nm}} = \sqrt{\frac{24EI_x}{nml^3}} \quad (3.20)$$

For a set of parameters given in Table 3.2 for lateral suspension and applying equation 3.20 we calculate the resonant frequencies for suspensions with 1 to 6 spring sets. A FE (Finite Element) model using Ansys (Figure 3.10) is used to verify the analytical expressions.

The numerical simulation was performed using commercially available FE simulation program ANSYS [3.16]. A parametric FE model was developed using the input file capability of ANSYS for a generic spring-mass lateral suspension. This allowed a single model file to be modified parametrically to set the number of spring sets, spring and proof-mass dimensions. The suspension was initially designed as a 2-D model and meshed with quadrilateral PLANE42 elements. The 2-D model was then extruded vertically 525 μm to form a volume with SOLID45 elements with three degrees of freedom at each of the eight nodes. The model contains large volumes like the proof-mass and high aspect ratio structures such as spring beams. Automated meshing of the complete structure uses irregular shaped tetrahedral elements causing multiple problems:

1. Large number of elements require larger memory and is slower to compute, additionally the version of ANSYS used has maximum element limit,
2. Automated meshing of the structure leads to very high aspect ratio elements with narrow widths in the spring beams. At the linkages there is extreme size transition from the larger elements in proof-mass to the smaller elements in spring beams. This leads to large simulation errors.

To avoid problems associated with irregular tetrahedral elements, the 2-D model was initially map meshed with PLANE42 elements with lower density of elements filling the proof-mass (Figure 3.10) and larger density of elements in spring beams with low aspect ratio elements at the transition boundary. The extruded 3-D model then contains brick elements as shown in Figure 3.11.

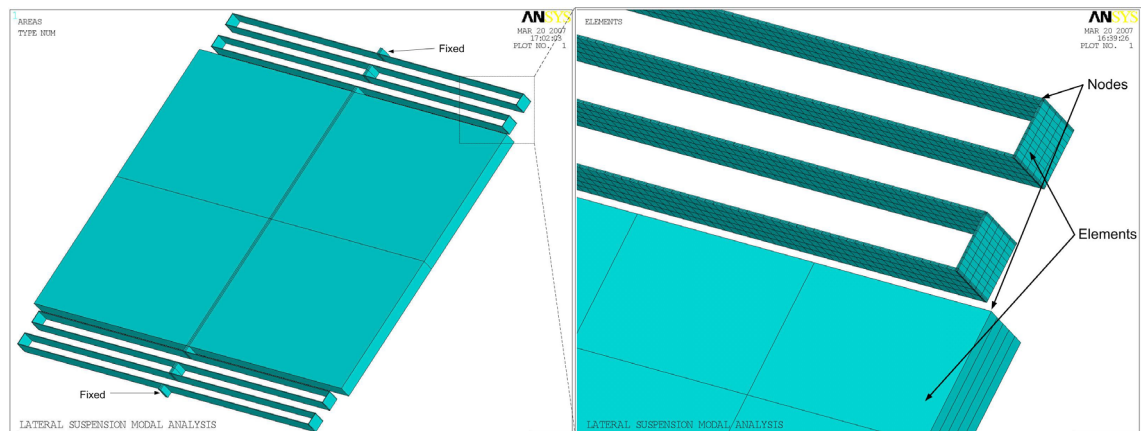


Figure 3.10 FEA (Finite Element Analysis) model of a lateral suspension with two set of springs solved using Ansys. The inset shows the arrangement of the nodes and elements in the model.

The mode shape and frequencies are calculated using Block Lanczos method. FE simulation allows inclusion of effects of a number of factors that are neglected in the simplified analytical model like mass of the spring, and anisotropic property of single crystal silicon. The input files for the ANSYS simulation are presented in Appendix B.

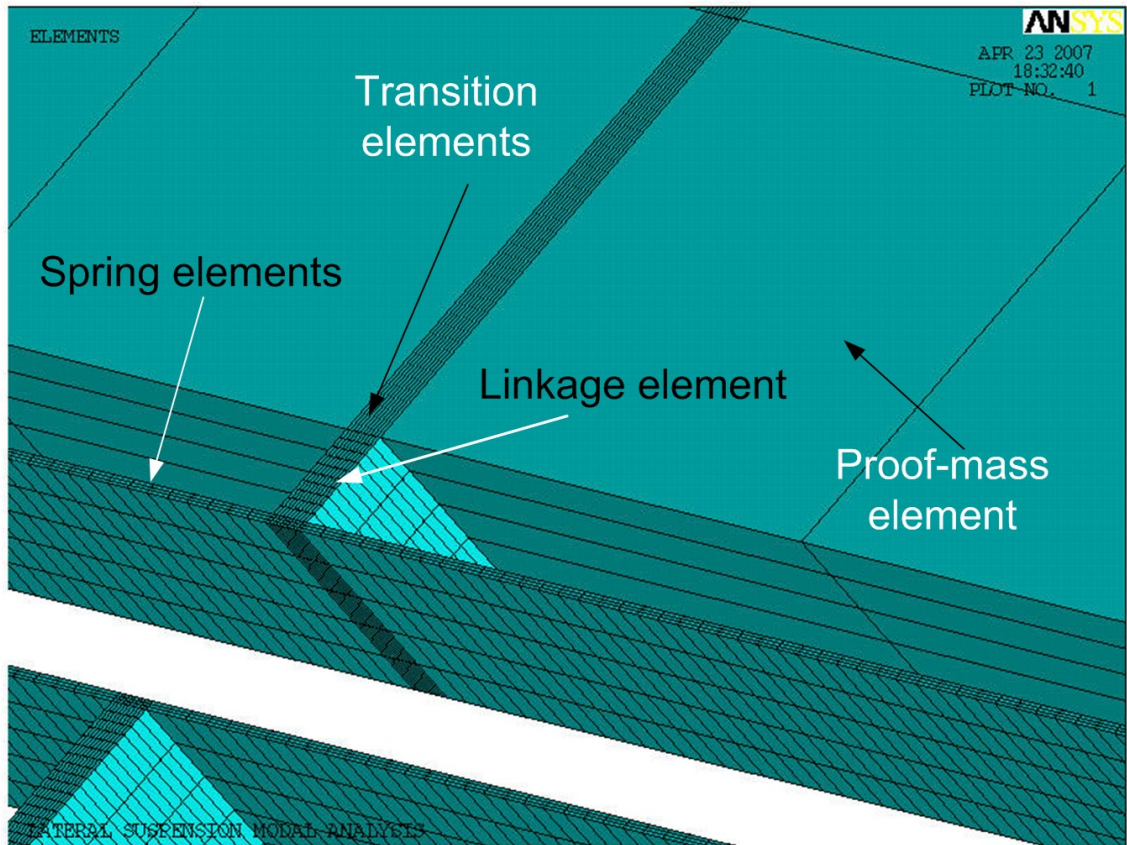


Figure 3.11 The transition elements are designed such that the nodes at the common boundary are coincident and there is no extreme size change across structures.

Table 3.2 Dimensional parameters for suspension design with multiple set of springs.

Parameter	Value
Young's modulus, E (GPa)	129
Silicon density, ρ (kg/m^3)	2330
Wafer thickness, t (μm)	528
Proof mass length, $2g$ (mm)	17.92
Proof mass width, $2h$ (mm)	12.06
Spring length, l (μm)	8320

Figure 3.12 shows the fundamental mode calculated using the analytical expressions along with the FEA calculated values. The FEA model estimates for the resonant modes are lower than analytically calculated values as the FEA considers the effect of the spring mass which reduces the fundamental mode slightly. The FEA model also considers the effect of the end connectors (elbow) of the spring which is neglected for calculating the fundamental mode in the analytical model.

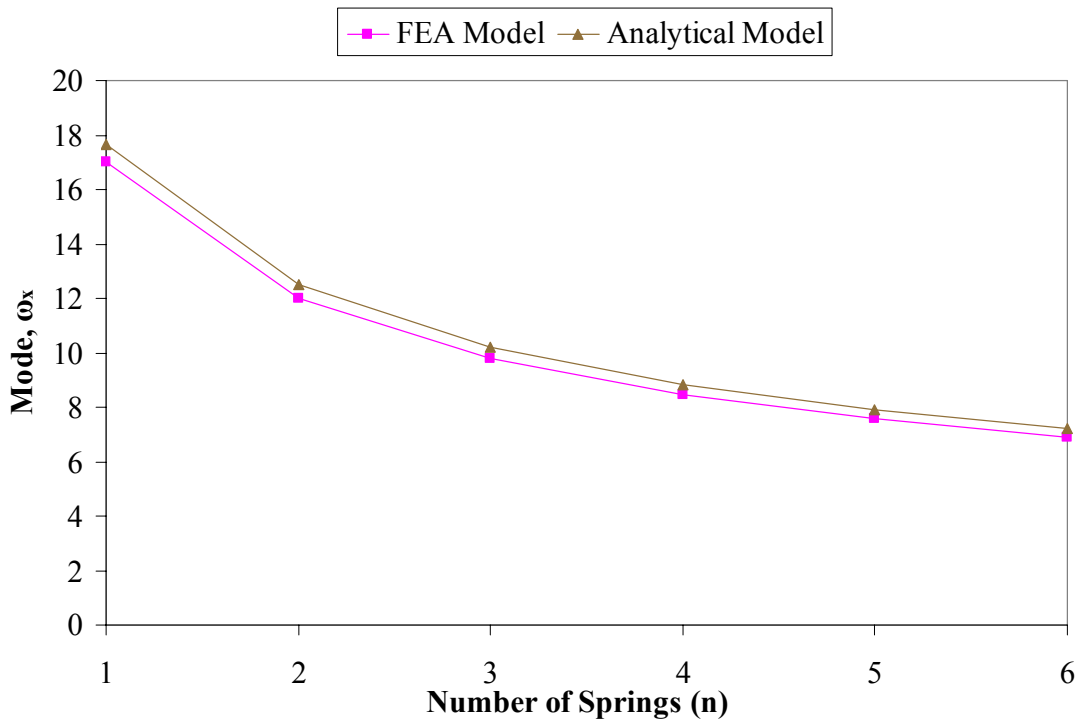


Figure 3.12 Fundamental resonant frequency for lateral suspension with varying number of spring sets. The values are calculated using the analytical expression from equation 3.20 and compared against FEA derived values. The deviation of the analytical model from the FEA model can be attributed to the mass of the suspension and the effect of end-connector geometry.

The discrepancy between the analytical and FEA model is under 5% and can be reduced within 1-2% if the springs are considered massless and the end connectors are made rigid.

3.3.1 Effect of spring mass

Up to this point the springs have been considered massless. The mass of the spring beams will both reduce the frequency of the fundamental mode and produce additional modes in all degrees of freedom. The frequency will be reduced according to Rayleigh's method [3.17] to calculate the effective mass of the spring, leading to an updated fundamental mode given by

$$\omega_x^* = \sqrt{\frac{k_x}{m + \frac{33}{140}m_s}} \quad (3.21)$$

where m_s is the total mass of the suspension. For most suspension designs, $m \gg m_s$, and the mass-loading effect is very small. Corresponding reductions will be seen for the other modes. If the suspension mass is comparable to the suspended mass, m in equation 3.20 should be replaced by $m + \frac{33}{140}m_s$. For a suspension with a single set of springs, incorporating the mass of the spring causes a deviation in the fundamental frequency, ω_x of 0.5%.

The most important additional modes are in the x direction, as they will be excited by the same signals as the fundamental. In general, an analytical solution is not obtainable. One can split the suspension into a series of discrete masses separated by massless springs. To determine the normal modes we have to solve the homogeneous linear equations of the appropriate Lagrangian:

$$|\mathbf{B} - \omega^2 \mathbf{A}| = 0 \quad (3.22)$$

where \mathbf{B} is the potential energy matrix and \mathbf{A} is the kinetic energy matrix [3.18]. Figure 3.13 show a suspension model where the spring beams are considered as discrete

masses connected with massless springs of stiffness k . The point masses (m) are an approximation to the distributed masses of the spring sets of the actual suspension.

For the suspension the matrices are symmetric:

$$A = \frac{1}{2} \begin{pmatrix} m & 0 & 0 & 0 & 0 & 0 & 0 \\ 0 & m & 0 & 0 & 0 & 0 & 0 \\ 0 & 0 & m & 0 & 0 & 0 & 0 \\ 0 & 0 & 0 & M & 0 & 0 & 0 \\ 0 & 0 & 0 & 0 & m & 0 & 0 \\ 0 & 0 & 0 & 0 & 0 & m & 0 \\ 0 & 0 & 0 & 0 & 0 & 0 & m \end{pmatrix}, B = \frac{k}{2} \begin{pmatrix} 2 & -1 & 0 & 0 & 0 & 0 & 0 \\ -1 & 2 & -1 & 0 & 0 & 0 & 0 \\ 0 & -1 & 2 & -1 & 0 & 0 & 0 \\ 0 & 0 & -1 & 2 & -1 & 0 & 0 \\ 0 & 0 & 0 & -1 & 2 & -1 & 0 \\ 0 & 0 & 0 & 0 & -1 & 2 & -1 \\ 0 & 0 & 0 & 0 & 0 & -1 & 2 \end{pmatrix} \quad (3.23)$$

and we solve the equation 3.22 to determine the eigenvalues. Using *Mathematica* (version 4, Wolfram Inc.) to solve this equation we obtain, as $m/M \rightarrow 0$,

$$\omega_i^2 = \left\{ \frac{k}{2M}, \left(2 - \sqrt{2}\right) \frac{k}{m}, \left(2 - \sqrt{2}\right) \frac{k}{m}, \frac{2k}{m}, \frac{2k}{m}, \left(2 + \sqrt{2}\right) \frac{k}{m}, \left(2 + \sqrt{2}\right) \frac{k}{m} \right\} \quad (3.24)$$

implying

$$\frac{\omega_1}{\omega_0} = \sqrt{\left(4 - 2\sqrt{2}\right) \frac{M}{m}} \approx \sqrt{\frac{M}{m}} \quad (3.25)$$

where ω_1 is the first on-axis harmonic ω_{x1} and ω_0 is the fundamental mode ω_x .

Unless the number of elements is low, this analysis gives little physical insight.

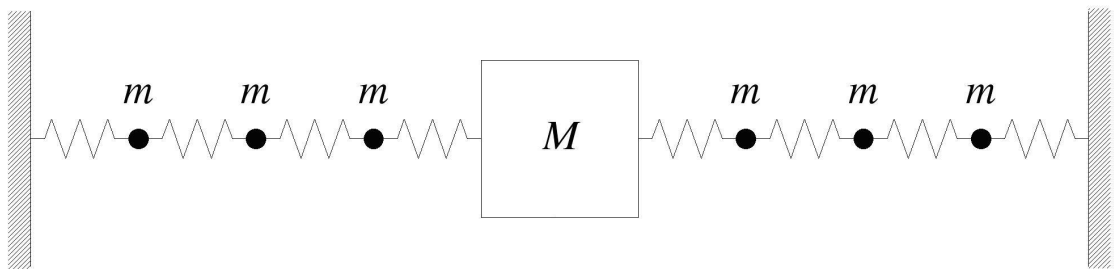


Figure 3.13 To model the first on-axis harmonic ω_{x1} , the spring units of the lateral suspension can be considered as discrete masses separated by massless springs. M is the mass of the proof-mass, the spring are considered as discrete masses m with massless springs of stiffness k connecting them.

Alternatively the suspension can be considered as having both a continuously distributed mass and spring constant. This approach leads to simpler results, more amenable to design optimization. Treating the spring as a uniformly distributed mass is self-consistent if the resulting modes have periodicities which are much greater than the periodicities in the distribution of the mass of the spring along the compliant direction. For the suspension geometry under consideration this implies that the mode periods should be much greater than s , the spring spacing.

Consideration of the mass of the suspension introduces additional on-axis modes with the displacement in the x direction of the suspensions on either side either symmetric or antisymmetric about the suspended mass [3.19]. The symmetric mode has a node at the suspended mass and is therefore relatively benign to the overall dynamic performance. However, the antisymmetric mode drives an oscillation of the suspended mass, the amplitude of which is proportional to m_s/m . The derivation for the on-axis symmetric and anti-symmetric modes are covered in Pike et al. [3.19]. The rejection ratio of the frequencies of the first harmonic ω_{x1} to the fundamental is

$$\frac{\omega_{x1}}{\omega_x} \approx \pi \sqrt{\frac{m}{m_s}} \tag{3.26}$$

Figure 3.14 shows the drop in rejection ratio for the first spurious mode along X -axis (ω_{x1}) with increasing number of spring sets (n). The analytical model gets better at predicting the mode with increasing number of spring sets, approaching the numerically calculated values. The improvement is due to the basic assumption of a continuously distributed mass to model the springs and with higher number of spring sets the assumption is strengthened.

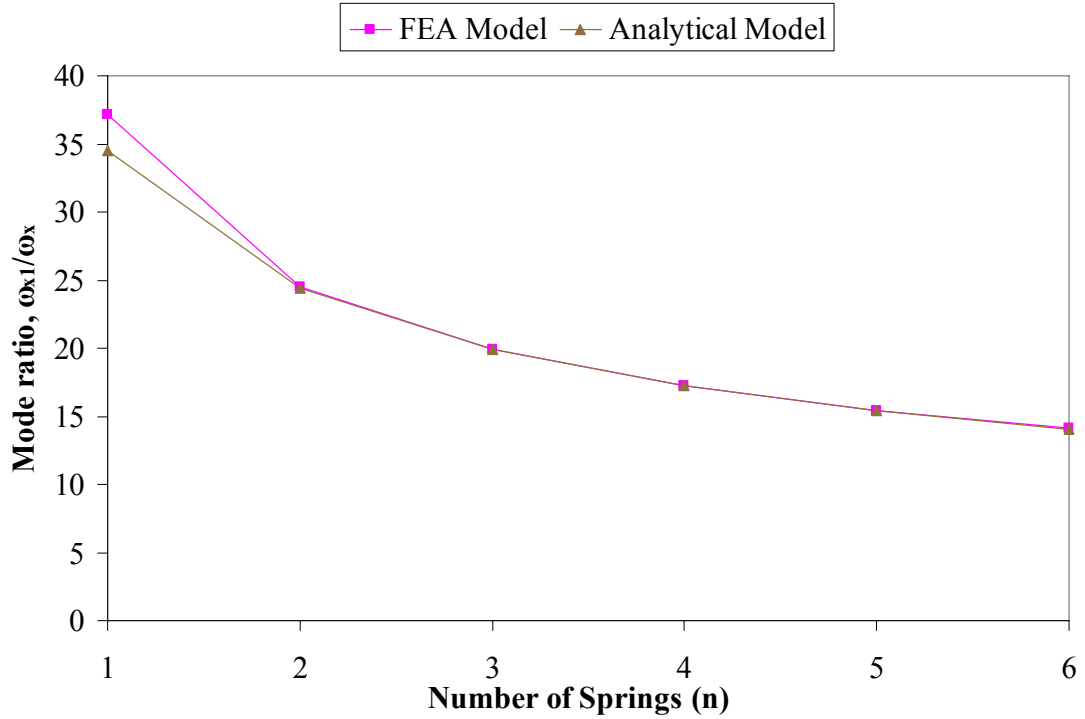


Figure 3.14 Plot of the first spurious mode along X -axis (ω_{x1}) with increasing number of spring sets (n). With larger number of spring sets the analytical model approaches the FEA model.

The lowest-frequency antisymmetric mode is of particular concern as motion of the suspended mass will occur. Both the amplitude and frequency of this mode depend on the ratio m/m_s , linearly and to the square root respectively, and hence it is important to minimize the mass of the springs as far as possible.

3.3.2 Rejection ratios of spurious modes

Figure 3.15 shows the rejection ratios calculated from FEA models for lateral suspensions with multiple spring sets. The ordering of the rejection ratios for one suspension unit agrees well with the rules of thumb established in the last column of Table 3.1. As the number of units increase, the FEA rejection ratio drops as approximately $1/n$ for y , z , and β ; as $1/n^{0.6}$ for γ ; as $1/\sqrt[3]{n}$ for x_I ; and is independent of n for α .

The reduction in the rejection ratios of the y , z , and β modes can be explained by considering that the translational compliance of an elastic member increases with the cube of the length of the member, so that while from equation 3.20 the fundamental frequency drops inversely as the square root of n , the cross-axis frequencies fall as $1/n^{3/2}$ and so the rejection ratio will scale as $1/n$. The γ mode depends more on the twisting compliance of a member, which increases with the square of the length, and hence the rejection ratio might be expected to be inversely proportional to the square root of n , reasonably close to the $1/n^{0.6}$ behaviour seen. For the x_1 mode, the mass of the suspension is proportional to n , and so the rejection from equation 3.22 will fall as the inverse square root. Like the fundamental, the α mode frequency is inversely proportional to n and so there is no change in the rejection ratio with additional suspension units.

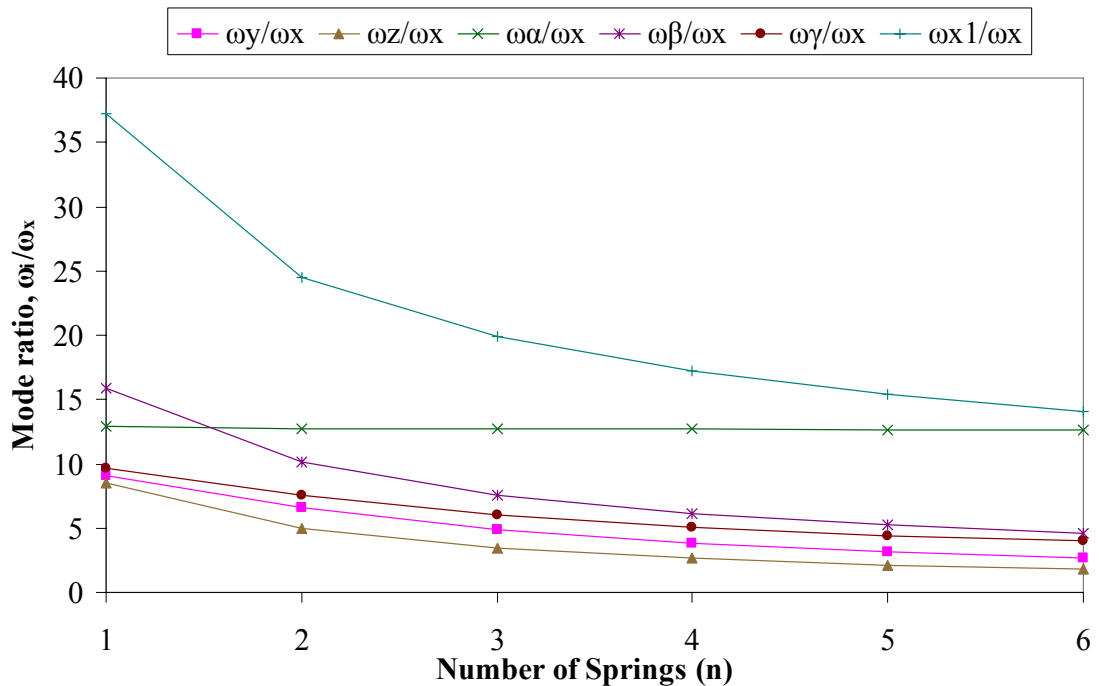


Figure 3.15 Rejection ratio of spurious modes calculated using FEA model for lateral suspension with 1, 2, 3, 4, 5 and 6 sets of springs. The rejection ratio drops significantly for multiple springs except for the rotational mode about X-axis.

Even though multiple spring suspensions achieve lower fundamental modes (Figure 3.12), the dramatic drop in rejection ratio is of serious concern and will affect the sensitivity of a suspension based on multiple spring design. As we will see in the next section there is a significant vertical deflection of the proof-mass when using multiple springs. In section 3.4 we will introduce intermediate frames to stabilize the rejection ratio.

3.3.3 Vertical deflection under gravity

For a horizontal lateral suspension, the vertical deflection (sag) of the proof mass under gravity is given by

$$z_{sag} = \frac{mg^*}{k_z} = \frac{g^*}{\omega_z^2} \quad (3.27)$$

where mg^* is the weight of proof mass, g^* is the acceleration due to gravity and k_z is the spring constant along Z -axis.

For a Galperin configuration (section 2.3.1), the vertical and lateral component of g^* causes the proof mass to deflect both in-plane as well as out-of-plane and is given by

$$z_{sag,in-plane} = \frac{mg^* \cos(\theta_{galperin})}{k_x} = \frac{g^* \cos(\theta_{galperin})}{\omega_x^2} \quad (3.28)$$

$$z_{sag,out-of-plane} = \frac{mg^* \sin(\theta_{galperin})}{k_z} = \frac{g^* \sin(\theta_{galperin})}{\omega_z^2} \quad (3.29)$$

We use equations 3.27-29 to calculate the vertical sag for lateral suspensions with multiple springs using parameters from Table 3.2.

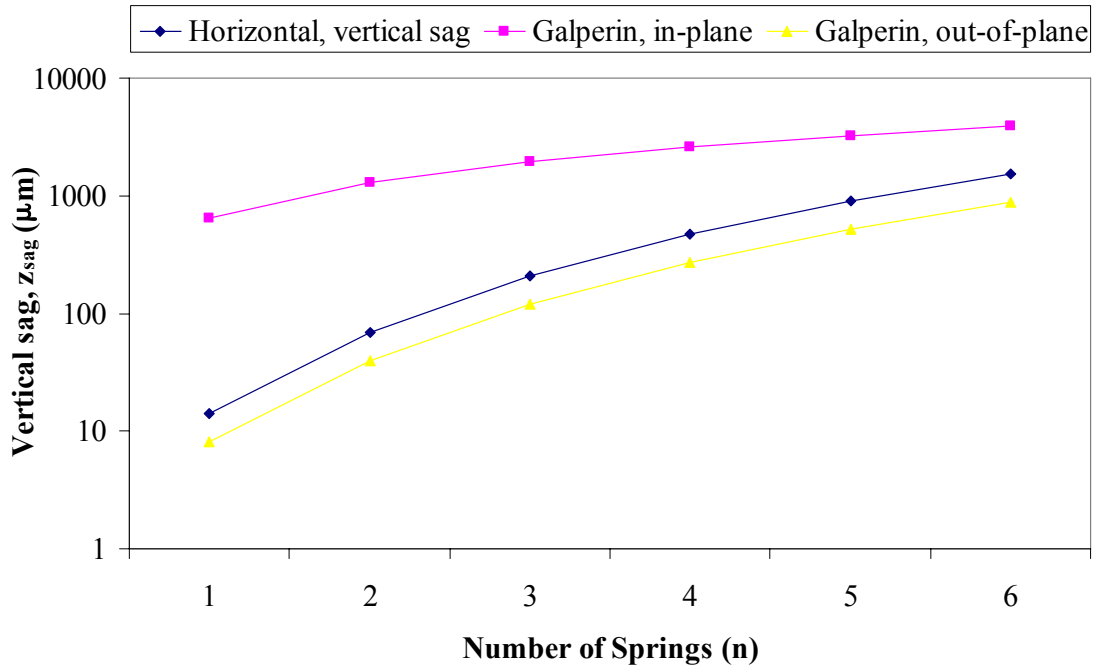


Figure 3.16 Logarithmic plot of vertical sag of a lateral suspension in horizontal and Galperin configuration. The sag due to gravity increases with higher number of springs.

As is evident from Figure 3.16 suspensions with higher spring sets have larger deflection under gravity. For the horizontal configuration of lateral suspension the springs are not preformed and the deflection due to gravity of the proof-mass increases linearly with the number of spring, n . For the Galperin configuration, the spring is preformed to compensate for the in-plane deflection of the proof-mass such that when the lateral suspension is placed in the Galperin configuration the proof-mass is centred. The vertical deflection of the proof-mass under gravity is slightly better than in the horizontal configuration but will need to be reduced within reasonable limits to allow workable capacitive pickup between the proof-mass die and the capping die.

The vertical sag under gravity can be reduced by introducing frames between sets of springs, a discussion of which follows in the next section.

3.4 Intermediate Frames for Multiple Spring

Suspension

As we discussed in section 3.3 there is a considerable price to be paid for reducing the fundamental frequency by increasing the number of spring sets – the rejection ratio drops precipitously for most of the off-axis modes and the vertical deflection is significant.

In order to overcome this considerable shortcoming (drop in the rejection ratios), it is necessary to decouple the additional spring sets, so the off-axis compliances add linearly rather than scale as the cube or square of the units added. Intermediate frames [3.20] can be introduced into the suspension to increase the cross-axis rigidity. Figure 3.17 shows a schematic of a suspension with a single intermediate frame. These frames are symmetric about the suspended mass and couple together the two sets of springs on either side of the proof mass. As they join parts of the suspension which move synchronously in the fundamental mode, they have very little effect on the fundamental frequency. However, by imposing additional boundary conditions on the cross-axis modes the frames can greatly increase the frequencies of these modes. The effect of the frames is first analysed assuming they are massless and perfectly rigid.

Pike et al [3.5] presents a detailed analysis of the advantages of using an intermediate frame for lateral suspension. By using intermediate frames, the suspension is stiffened in the z direction with a linear dependence on number of intermediate frames (n). Since the fundamental mode is also linearly dependent on n , the rejection ratio for out-of-plane mode ω_z is unaffected by the introduction of additional spring units. The beneficial effect on the Y -axis rejection ratio is identical.

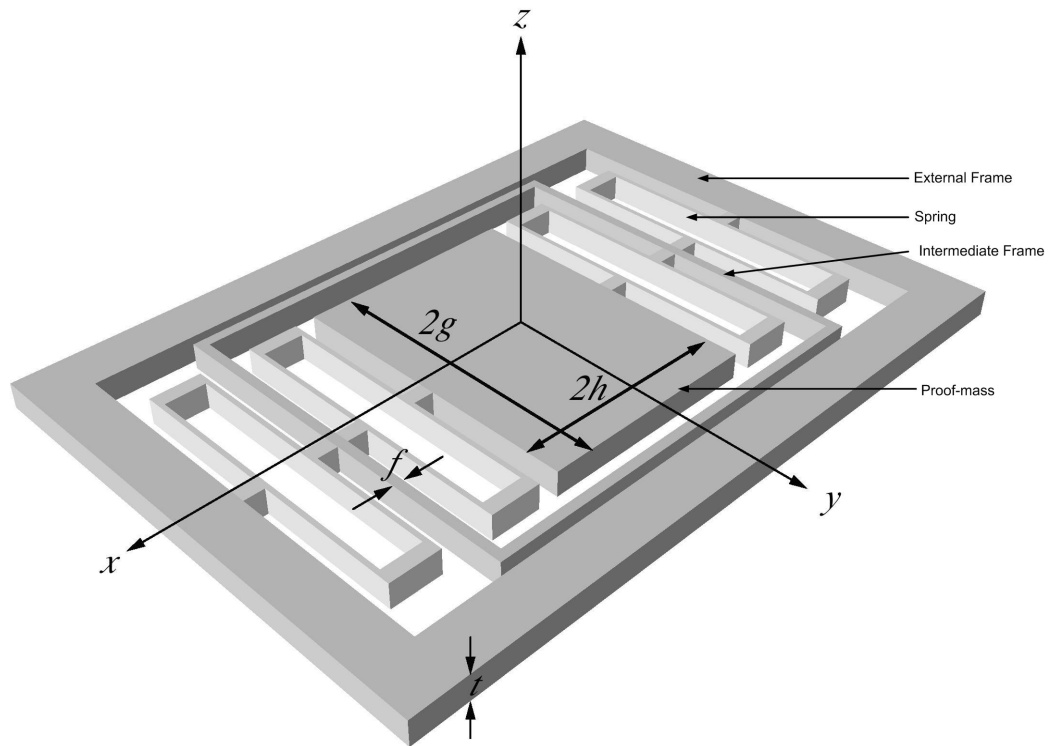


Figure 3.17 Schematic of a lateral suspension with a single intermediate frame between two set of springs. The intermediate frame decouples the additional spring sets.

The cross-dependence of the rotational rigidities to the translational rigidities produces a corresponding increase in rotational rigidity with the introduction of frames for rotations about the Y and Z axes. For rotation about the Y and Z axes, there is further stiffening as the elastic forces are applied further away from the rotation axis as the number of suspension units increases. This leads to a better rejection ratio for β mode as n increases. There is similar stiffening about the Z -axis due to the increased moment arm for in-plane rotations as spring units are added improving rejection ratio for γ mode.

The frames have no effect on rotation about the X -axis as they introduce no additional constraints for this motion. The analytical expressions for all the modes for n spring sets and $(n-1)$ frames are given in Table 3.3.

Table 3.3 Resonant frequencies for lateral suspension with n spring sets and $(n-1)$ intermediate frames.

Mode, i	ω_i^2
x	$\frac{24EI_x}{mnl^3}$
y	$\frac{8EI_x}{mnl^2} = \frac{l^2}{3s^2} \omega_x^2$
z	$\frac{1/n}{\frac{m l s^2}{8GJ} + \frac{m l^3}{12EI_z}} = \frac{\omega_x^2}{\frac{3EI_x s^2}{GJ l^2} + \frac{2I_x}{I_z}}$
α	$\left\{ \frac{4EI_x(s-w)g^2}{GJ_s l^3} + \frac{4I_x g^2}{I_z l^2} \left[1 - \frac{3}{4 + \frac{3s^2 EI_z}{l^2 GJ}} \right] \right\}^{-1} \omega_x^2$
β	$3 \left[1 + (n-1) \frac{(s+f/2)}{h} \right] \omega_x^2$
γ	$\frac{3 \left[1 + (n-1) \frac{(s+f/2)}{h} \right]}{1 + g^2/h^2} \omega_y^2$
x_1	$3 \frac{m + nm_{\text{spring}}}{m + n(m_{\text{spring}} + m_{\text{frame}})} \omega_x^2$

The frames will have a detrimental effect on harmonics along the X -axis due to the increased mass of the suspension. The first harmonic will have a frequency of

$$\frac{\omega_{x1}}{\omega_x} = \pi \sqrt{\frac{m}{m_s + m_f}} \quad (3.30)$$

for a total frame mass of m_f . Therefore the frames should be made as light as possible while maintaining sufficient rigidity. Figure 3.18 shows the drop in rejection ratio for on-axis spurious mode ω_{x1}/ω_x for suspension with intermediate frames as compared to the suspensions without intermediate frames.

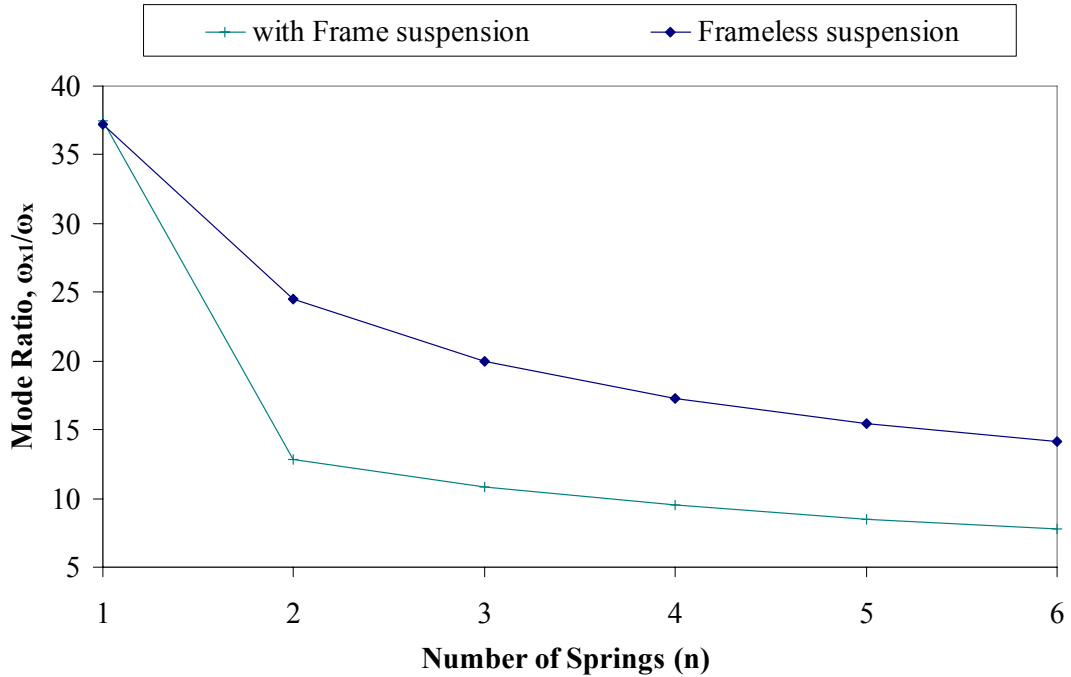


Figure 3.18 Plot of ω_{x1}/ω_x for lateral suspension with n (one to six) spring sets and $(n-1)$ intermediate frames. The FEA model used to calculate the rejection ratio is based on the model parameters of Table 3.2 with a frame thickness (f) of 60 μm .

3.4.1 Rejection ratio of spurious modes

The rejection ratio for lateral suspensions with multiple spring sets (with dimensions similar to the model used in section 3.3.2) but with intermediate frames in shown in Figure 3.19. By including intermediate frames into the design, all modes except for x_1 maintain or, in the case of β or γ , improve their rejection ratio as additional suspension units are added, in agreement with the analytical formulas of Table 3.3.

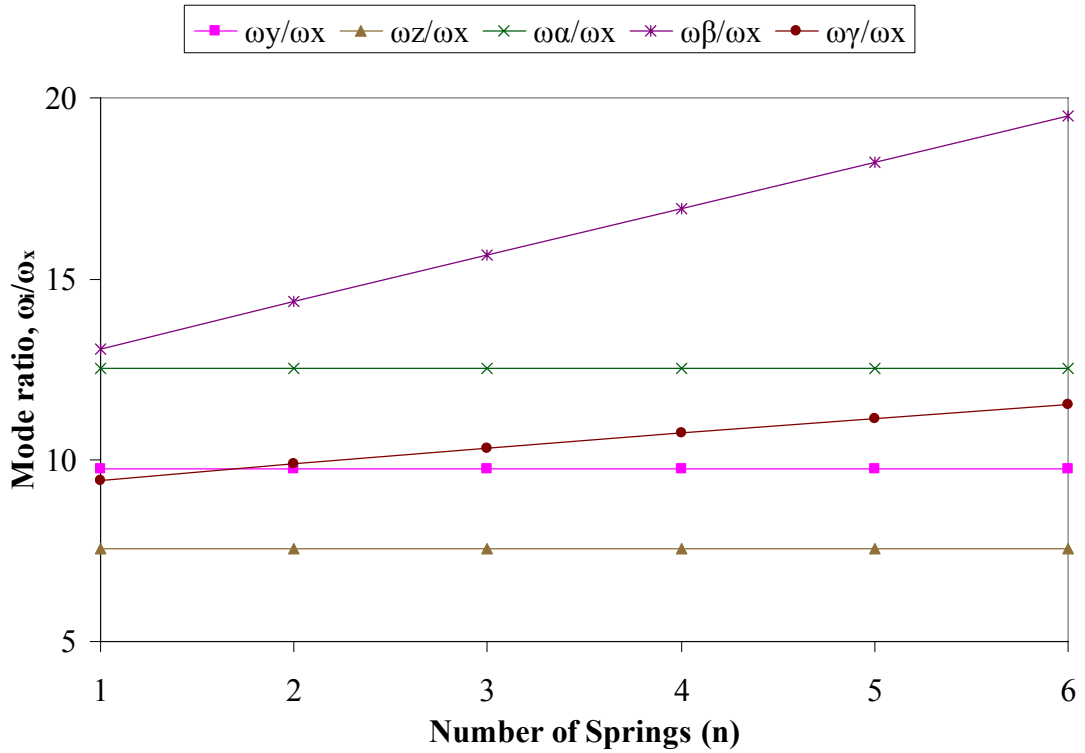


Figure 3.19 Plot of rejection ratio for lateral suspension with multiple springs calculated using analytical expressions from Table 3.3.

FEA model based on the same parameters as in Table 3.2 is solved using Ansys to verify the analytical calculations. Figure 3.20 shows similar trend as the analytically calculated values (Figure 3.19) with improvement in the mode rejection ratio for β and γ modes and smaller improvement in y and z modes.

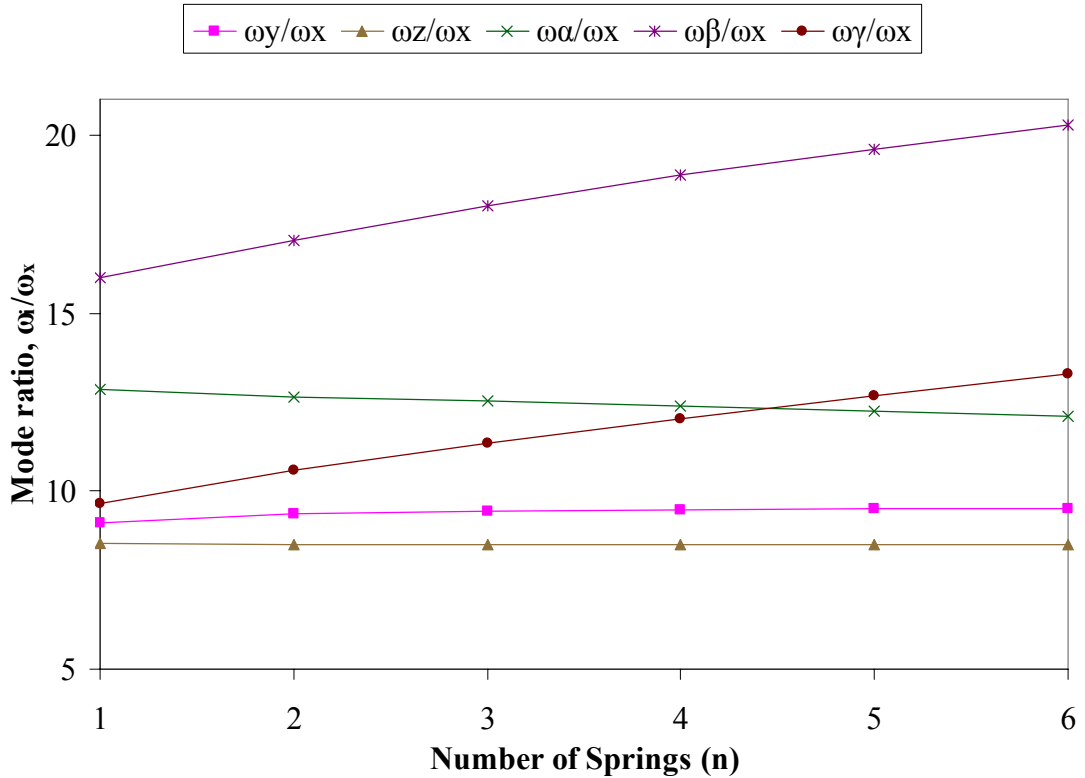


Figure 3.20 Plot of rejection ratio for lateral suspension with multiple springs calculated using a FEA model.

The relative error of the analytical model as compared to the FEA model is shown in Figure 3.21. The error in calculating the mode rejection ratio for most of the modes are within 10% except for β mode where the error, though high initially, reduces significantly with higher number of frames. The error in calculating γ mode seems to be increasing but plateaus at around 15%. Even though the analytical model for calculating β and γ modes are significantly in error with the FEA model, the analytical model still predicts most of the other modes with significant accuracy and accurately estimates the first few spurious modes. Additionally since the analytical model underestimates the out-of-plane rejection ratio (ω_z/ω_x) which is the first spurious mode for the suspension, any design developed using this model will satisfy the criteria to increase the rejection ratio.

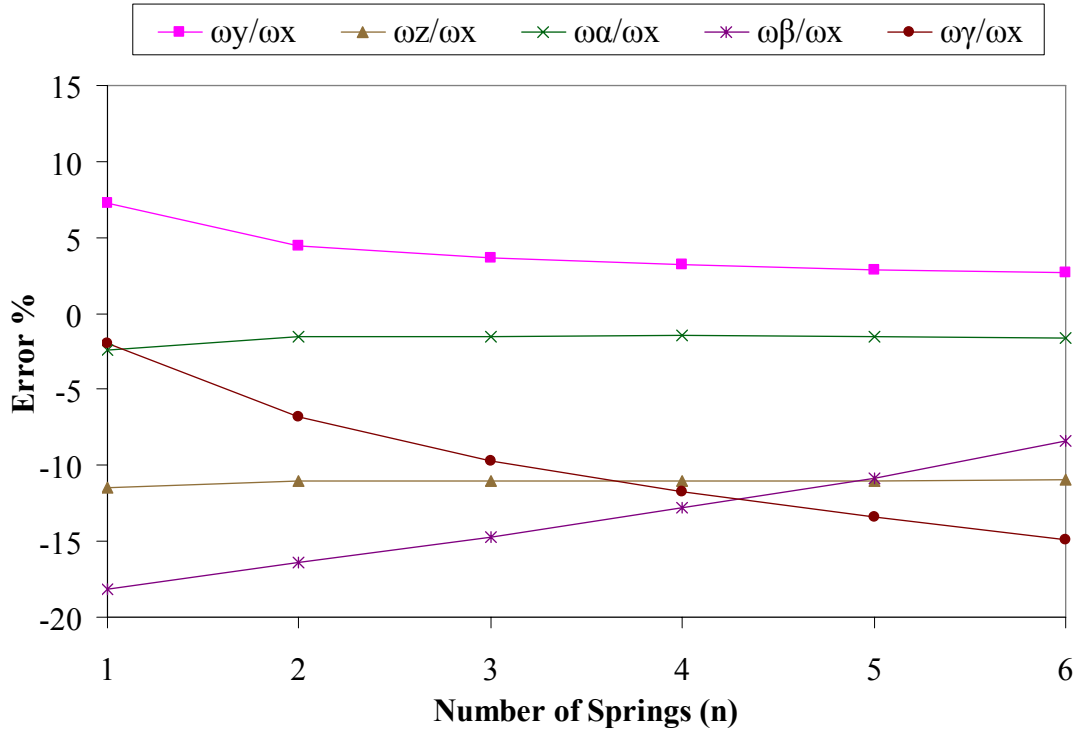


Figure 3.21 Error between the FEA model and analytical expressions for the rejection ratios.

In Figure 3.18 we discussed how the rejection ratio for the first on-axis spurious mode gets worse due to the weight of the intermediate frame, but increased rigidity provided by the frame could be useful in pushing up the rejection ratio for other modes. Figure 3.22 shows the rejection ratio (normalized against a suspension design with 3 spring set and 2 20 μm thick intermediate frames) for suspensions with multiple spring sets and intermediate frames. Except for the first on-axis spurious mode (ω_{x1}), the rejection ratio for most other modes are significantly increased by increasing the thickness and hence the rigidity of the intermediate frames.

To reduce the weight of the intermediate frame and increase the rigidity, it is possible to design intermediate frames with slots in them as shown in Figure 3.23. Even though mechanically it is stronger to design them like a truss structure as used in bridges,

fabrication constraints due to minimum etch feature size of 40 μm leaves little room to have a cross-bar geometry, instead holes are etched in a solid frame.

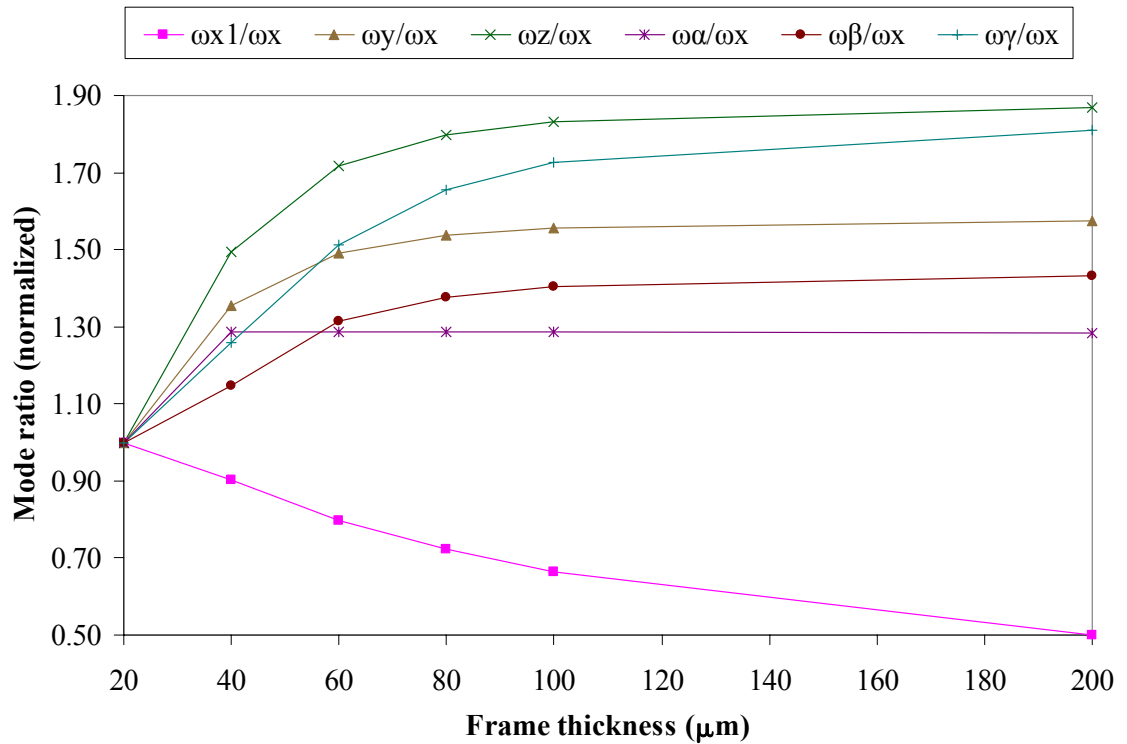


Figure 3.22 Plot of rejection ratio for lateral suspension with three spring sets and two intermediate frames of varying thickness. Most of the rejection ratio except ω_{x1}/ω_x improves with thicker frames though the gain is marginal beyond a certain thickness.

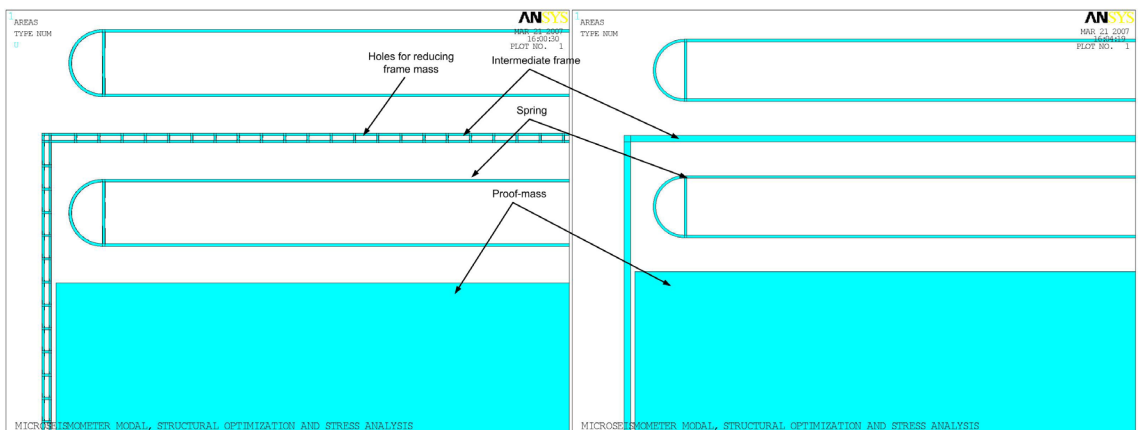


Figure 3.23 (a) Reinforced intermediate frames to reduce the weight of the frame while maintain higher rigidity of a thicker frame, as compared to (b) Solid intermediate frame which reduces the on-axis rejection ratio due to the higher weight of the spring-frame unit.

3.4.2 Comparison of modes for frameless and with-frame suspension

Figure 3.24 compares the rejection ratio calculated using FEA for multiple spring suspension with and without intermediate frames. As we can see in Figure 3.24a the rejection ratio for all modes drop precipitously with increasing number of spring units whereas the same suspension with intermediate frames between each spring unit leads to an improvement in the rejection ratio for all modes (Figure 3.24b) except the first on-axis harmonic, ω_{x1} .

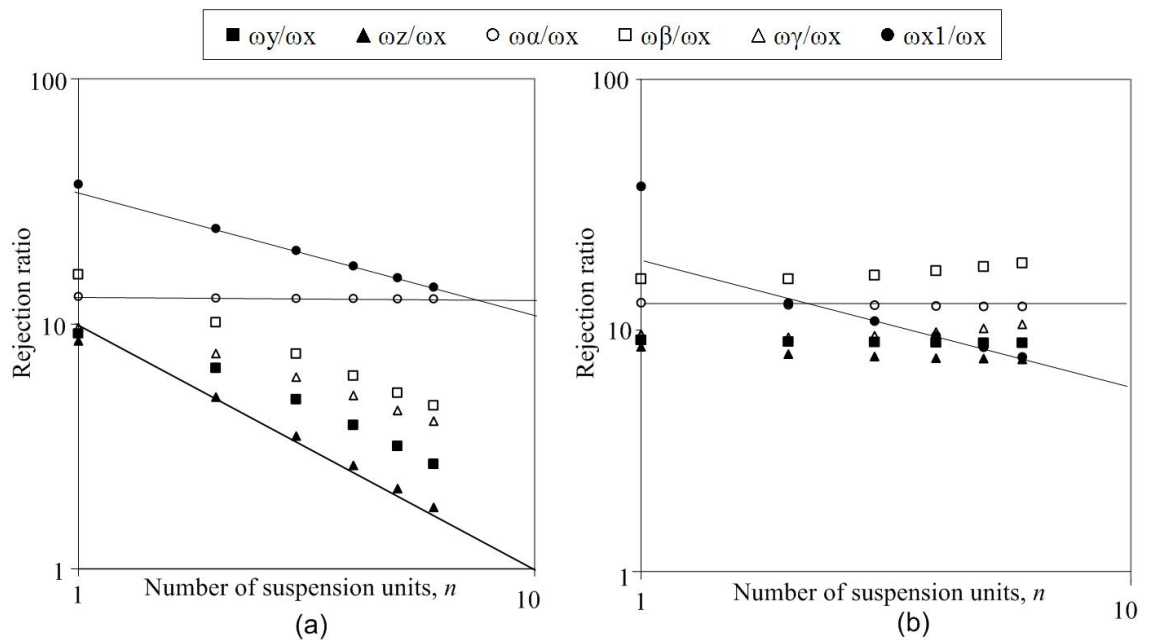


Figure 3.24 Comparison of the rejection ratio for a model lateral suspension with multiple springs without frames and with frames. (a) Log-log variation as calculated by FEA of the rejection ratio for the spurious modes as the number of suspension units is increased from 1 to 6. Three fits for the rejection ratio are shown: for x_1 , $1/\sqrt{n}$; for α , independent of n ; for z , $1/n$, and (b) Log-log variation as calculated by FEA of the rejection ratio for the spurious modes of a suspension incorporating intermediate frames as the number of suspension units is increased from 1 to 6. Fits for the rejection ratio are shown: for x_1 , $1/\sqrt{n}$; for α , independent of n .

The trend line showing the slope of the rejection ratio for the multiple spring suspensions agree with the analytical model. For frameless suspensions the rejection ratio varies between $1/n$ and $1/\sqrt{n}$ whereas for the suspension with intermediate frames the rejection ratios are almost flat or improve slightly and $x1$ mode has a slope of $1/\sqrt{n}$. α mode in both cases stay constant as shown by the flat line in the plots.

3.4.3 Vertical sag under gravity

As we discussed earlier, intermediate frames are used between sets of springs to increase out-of-plane stiffness. The frames have the effect of changing the boundary condition at the linkage of springs as shown in Figure 3.25.

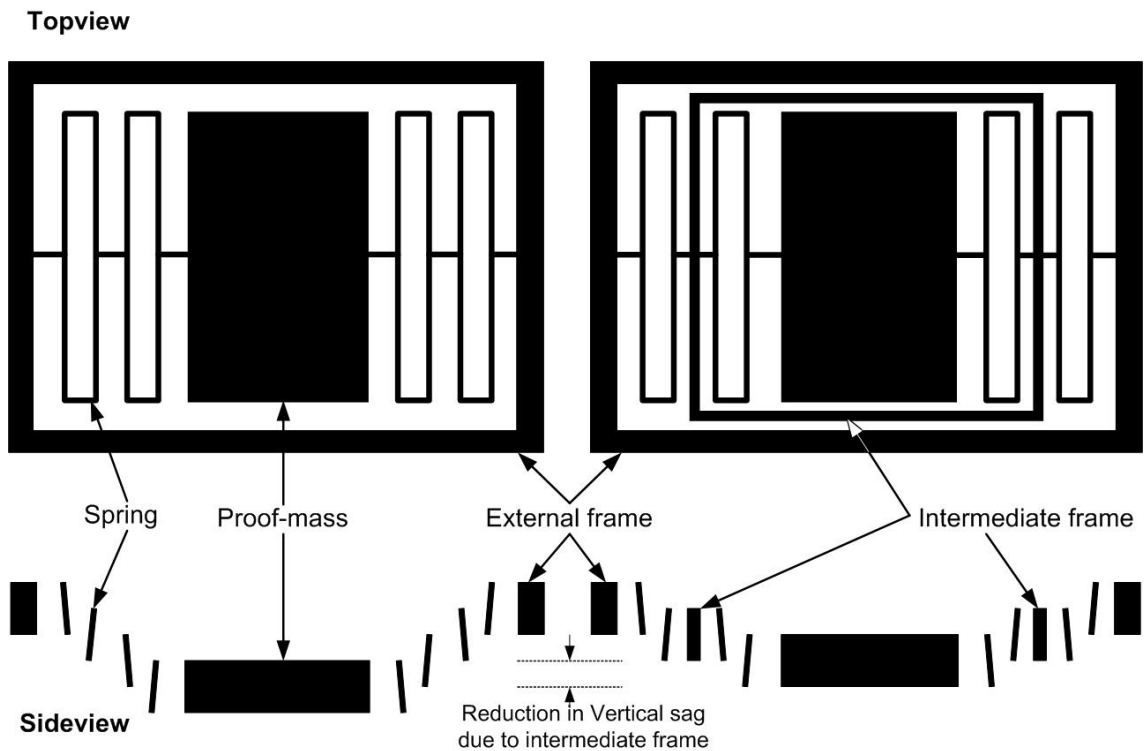


Figure 3.25 Effect of intermediate frames on the vertical sag of proof mass under gravity, (a) multiple spring set suspension under gravity with equal deflection of all spring beams as shown in the cross-section view, as compared to (b) multiple spring set suspension with intermediate frame showing a reduction in vertical sag under gravity due to the intermediate frame.

The frames increase the torsional stiffness of the suspension along the Z-axis. The ratio is given by [3.5]

$$\frac{k_{z,frame}}{k_{z,frameless}} = \frac{3}{4n^2 - 1} \tag{3.31}$$

$k_{z,frames}$ is the torsional stiffness with $n - 1$ frames and $k_{z,frameless}$ is torsional stiffness for a frameless suspension with n spring sets.

The vertical sag (z_{sag}) under gravity is inversely proportional to the out-of-plane stiffness, k_z . Figure 3.26 shows the reduction in vertical sag with increasing number of spring units when intermediate frames are used compared to the frameless case. As we can see from the curve the reduction in vertical sag is significant particularly with higher number of springs: for six sets of springs the vertical sag with intermediate frames is almost forty five times less than frameless suspension.

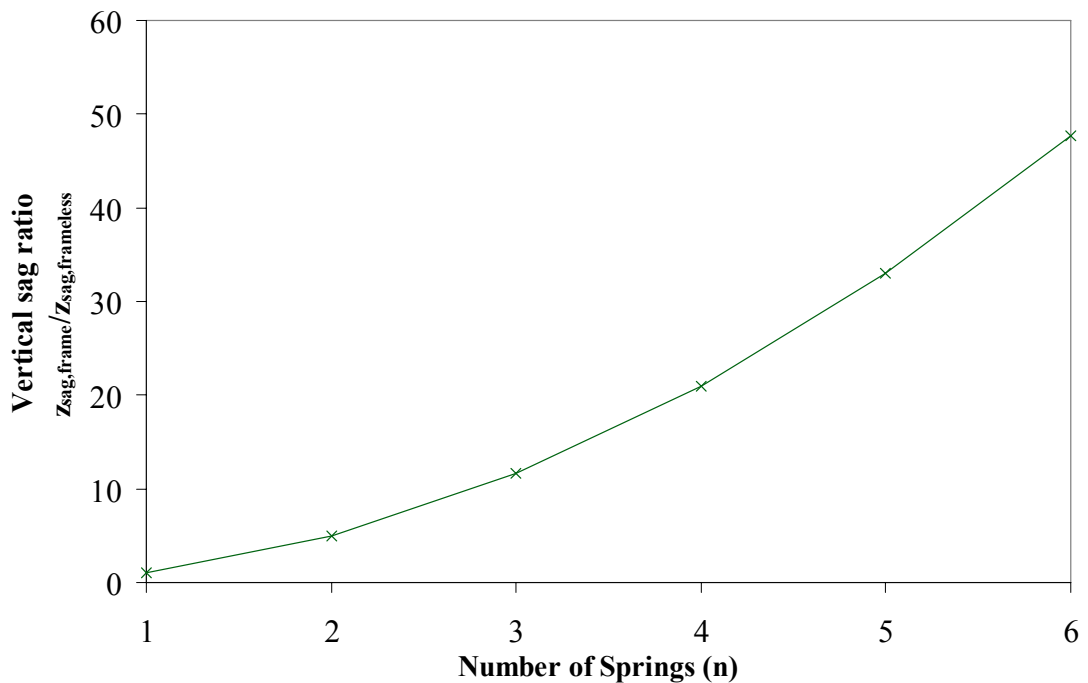


Figure 3.26 Reduction ratio for vertical sag under gravity for multiple spring suspension with intermediate frames as compared to frameless suspensions.

3.5 Effect of Linkage Geometry

The linkage affects the twisting about X -axis. A rigid link is therefore important to increase the rejection ratio of the mode about X -axis.

Various link thicknesses are investigated and its effects are quantified on α and $x1$ mode as shown in Figure 3.27.

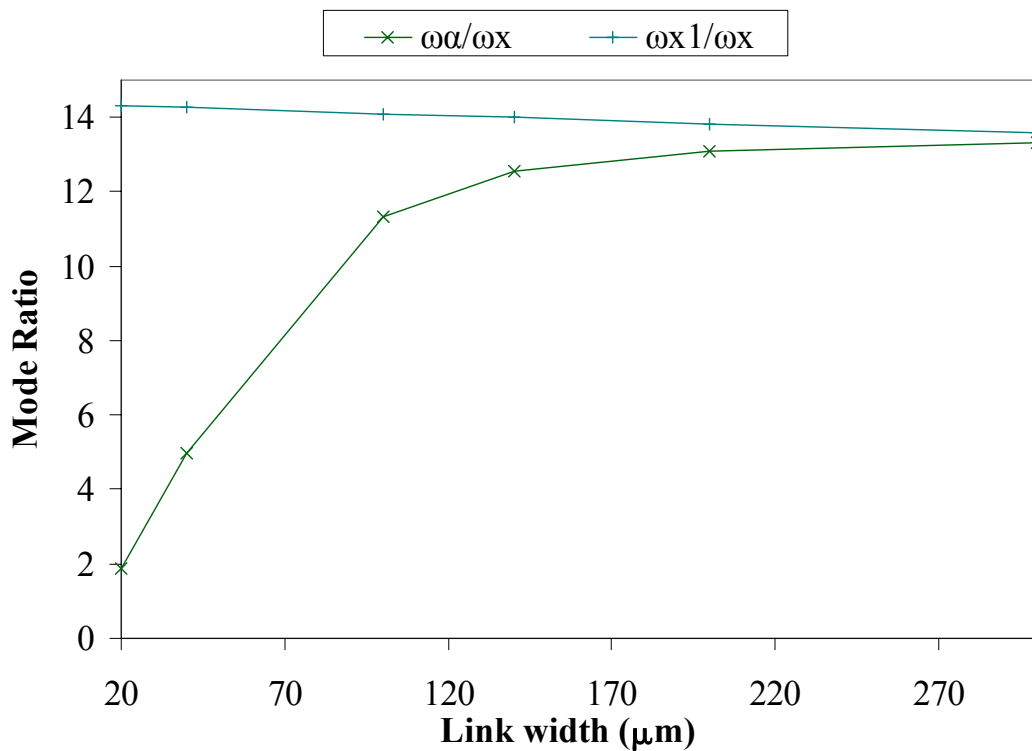


Figure 3.27 Effect of link width on rejection ratio of the suspension.

With increasing linkage width, ω_{x1}/ω_x decreases slightly due to increased mass of the linkage but the effect is small enough to not merit a design modification. Rejection ratio of the rotational mode about the X -axis (ω_{α}) improves significantly with increasing linkage width as the rigidity of the linkage reduces the compliance to torsion. After a certain linkage width the gain in α rejection ratio does not improve any further as the compliance contribution of the spring beams dominates.

Steady state numerical simulation of the suspension shows maximum stress concentration at the linkages with sharp corner. The linkage is filleted to reduce the stress concentration at the corners (Figure 3.29) for similar applied force. Various designs were investigated with the aim to reduce the stress concentration. Stress concentrators are potential regions where fracture happens and shock test of structures (chapter 6) have shown that most of the suspensions fail near the linkage.

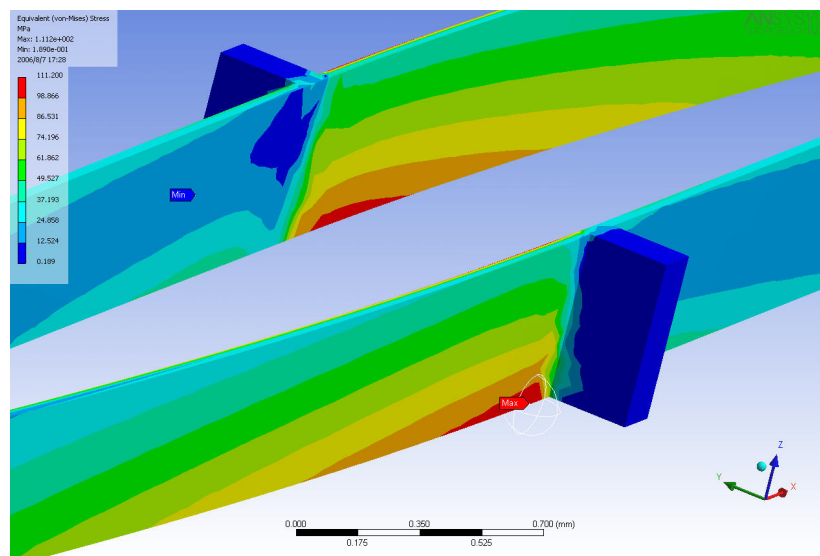


Figure 3.28 Maximum stress at the sharp corner of the linkage shown by the red pointer in the globe.

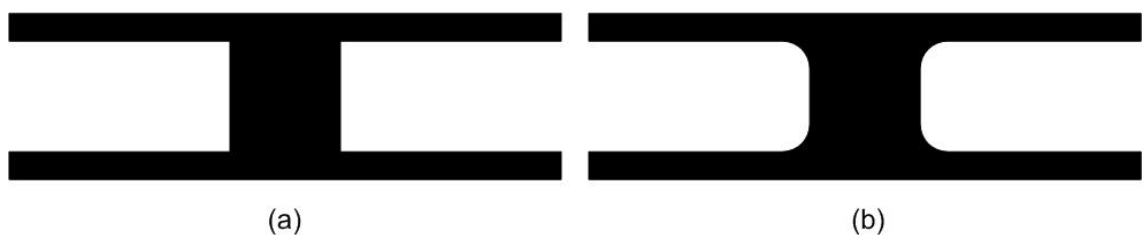
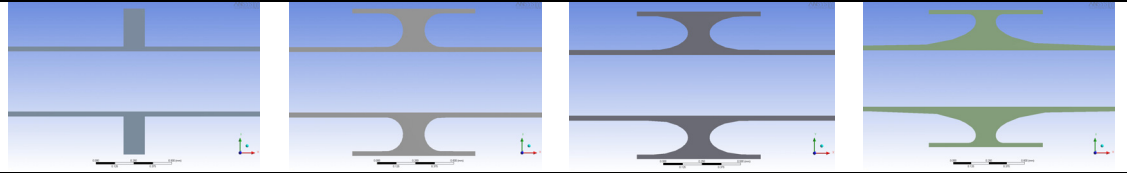


Figure 3.29 (a) Link design with sharp corners, (b) Link design with corner filleting.

Numerical simulation using Ansys was carried out to investigate the effect of filleting and the results are presented in Table 3.4.

Since filleting the link increases the effective thickness of the spring, there is an increase in ω_x which can be compensated for by increasing the spring beam length. The stress at the linkage is reduced with larger filleting at the corners as seen by the trend in Table 3.4. The Von Mises stress is calculated by applying a fixed displacement of 332 μm along X-axis, and 15 μm along Z-axis to simulate maximum deflection of the spring linkage.

Table 3.4 Effect of varying amount of filleting of link-spring corner on stress.

Link design			
			
Radius of curvature			
Sharp corner	Circular 110 μm	Elliptical 230 μm , 110 μm	Elliptical 500 μm , 170 μm
Von Mises Stress (MPa)			
117.4	113.2	105.6	102.1

3.6 Effect of End Connector (Elbow) Stiffness

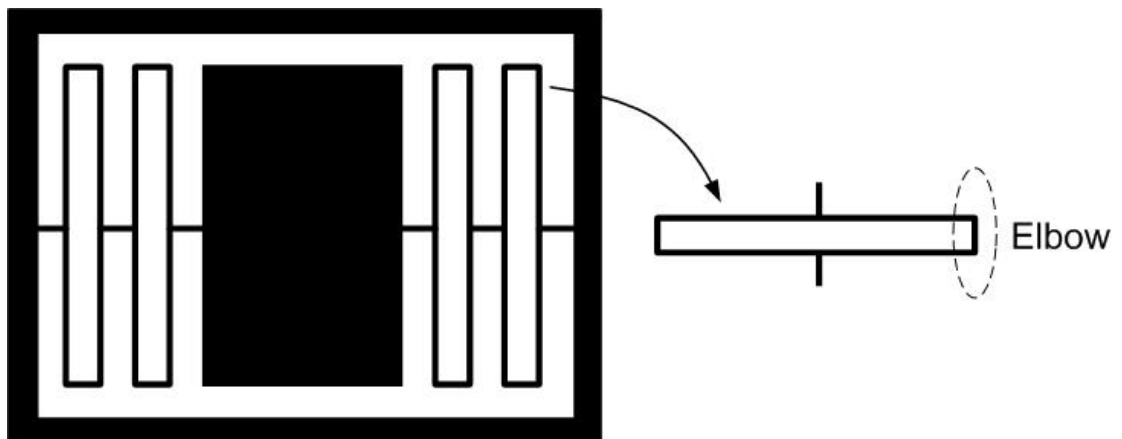


Figure 3.30 Schematic of spring element showing the end connector.

The analytical expressions in Table 3.1 and Table 3.3 are derived assuming rigid spring end connectors (Figure 3.30). However, the rigidity of the end connector (elbow) plays a crucial role in determining the out-of-plane compliance.

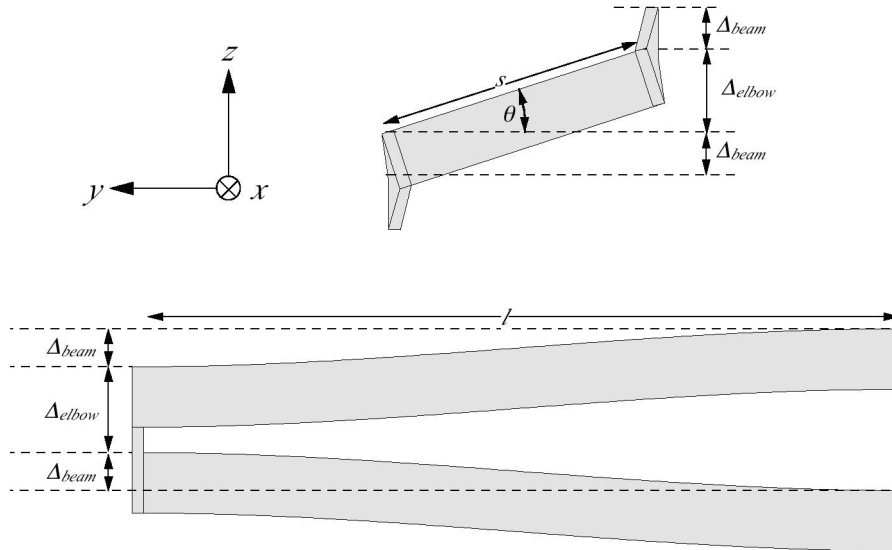


Figure 3.31 Distortion of the spring beam under an out-of-plane force. The forces acting at the opposite ends of the elbow causes a torque which leads to an angular rotation of θ .

The total deflection in the z direction is the sum of the deflection at the elbow, Δ_{elbow} , as a result of the twisting of the beams from the torque generated from the opposing forces acting at the beam ends and the two cantilever deflections, Δ_{beam} of the beams as a result of the impressed out-of-plane force and the resulting torques as shown in Figure 3.31.

This torque will produce a constant twist along each beam [3.13], and produce a resulting deflection at the elbows given by

$$\Delta_{elbow} = \frac{F_z l s^2}{8GJ} \quad (3.32)$$

for small loads where G is the relevant shear modulus for the beam direction, and J is the torsion constant which depends only on the cross-sectional dimensions of the beam,

F_z is the out-of-plane force acting on each beam, l is the length of the beam and s is the spacing between the two beams of a spring unit.

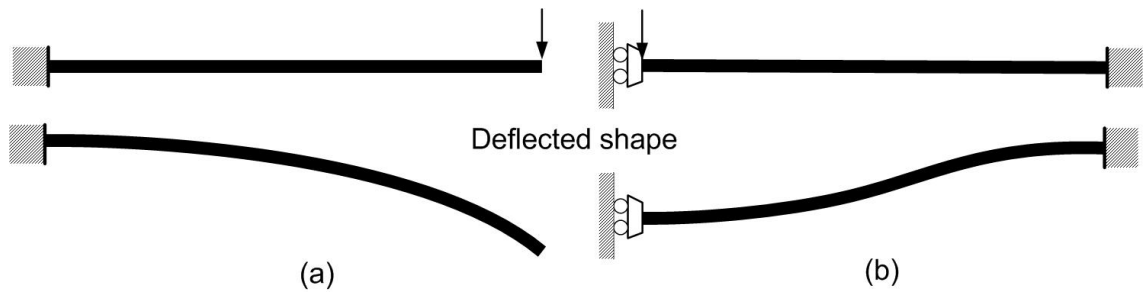


Figure 3.32 Deflection of the spring beams depending on elbow rigidity, (a) completely rigid elbow with $c = 1$ where the bending is that for a fixed-free cantilever and (b) completely flexible elbow with $c = 4$ where the bending is representative of a fixed-guided cantilever.

The beam deflection will be given by $F_z l^3 / (48EI_z)$ where the elbow is considered as completely rigid as shown in Figure 3.32a. The rigidity of the elbow about this axis is much more difficult to maintain compared to the rigidity about the z axis for deflections in the compliant x direction. If the elbow has no rigidity, each beam acts as a single cantilever with a maximum angle of deflection at the elbow (Figure 3.32b) and the beam deflection is $F_z l^3 / (12EI_z)$. Hence an elbow-compliance factor, c , which depends on the rigidity of the elbow and varies between a value of 1 and 4, is introduced into the analysis:

$$\Delta_{beam} = \frac{cFl^3}{48EI_z} \quad (3.33)$$

This leads to a modified compliance about Z -axis dependent on c and given by

$$\frac{1}{k_z} = \frac{cl^3}{24EI_z} + \frac{ls^2}{8GJ} \quad (3.34)$$

Table 3.6 presents this compliance factor for some representative geometries as determined by finite element analysis. Where present, the elbow cross bar is half the

beam spacing s from the end on the elbow. It is evident that to minimize the Z -axis deflection some webbing of the elbow is required. Table 3.5 incorporates the elbow compliance factor (c) into the analytical expressions for normal modes of the suspension.







Table 3.5 Resonant frequencies for lateral suspension with n spring sets and $(n-1)$ intermediate frames incorporating the effect of end connector (elbow) geometry.

Mode, i	ω_i^2
x	$\frac{24EI_x}{mnl^3}$
y	$\frac{8EI_x}{mnl s^2} = \frac{l^2}{3s^2} \omega_x^2$
z	$\frac{1/n}{\frac{mls^2}{8GJ} + \frac{cml^3}{12EI_z}} = \frac{\omega_x^2}{\frac{3EI_x s^2}{GJl^2} + \frac{cI_x}{I_z}}$
α	$\left\{ \frac{4EI_x(s-w)g^2}{GJ_s l^3} + \frac{4I_x g^2}{I_z l^2} \left[1 - \frac{3}{4 + \frac{3s^2 EI_z}{l^2 GJ}} \right] \right\}^{-1} \omega_x^2$
β	$3 \left[1 + (n-1) \frac{(s+f/2)}{h} \right] \omega_x^2$
γ	$\frac{3 \left[1 + (n-1) \frac{(s+f/2)}{h} \right]}{1 + g^2/h^2} \omega_y^2$
x_1	$3 \frac{m + nm_{\text{spring}}}{m + n(m_{\text{spring}} + m_{\text{frame}})} \omega_x^2$

Numerically we have investigated various end connector topography to understand its effect on the modes. It is evident from Figure 3.33 that rejection ratio for out-of-plane

mode ω_z improves with increasing elbow stiffness, at elbow stiffness of $c = 1.0$ (completely rigid) the rejection ratio is 25% better than at $c = 4$ (completely flexible). Increasing the stiffness of the spring end connector also reduces the vertical sag under gravity of the proof mass with 20% improvement from $c = 4$ to $c = 1$. There will be a slight drop in rejection ratio for the on-axis spurious mode ω_{xI} due to the increased mass of the spring.

Table 3.6 Value of c (elbow compliance) for various elbow topography.

End connector geometry (Aspect ratio ~20)						
Design	(a)	(b)	(c)	(d)	(e)	(f)
Compliance, c	1.05	1.07	1.48	1.20	2.68	2.70

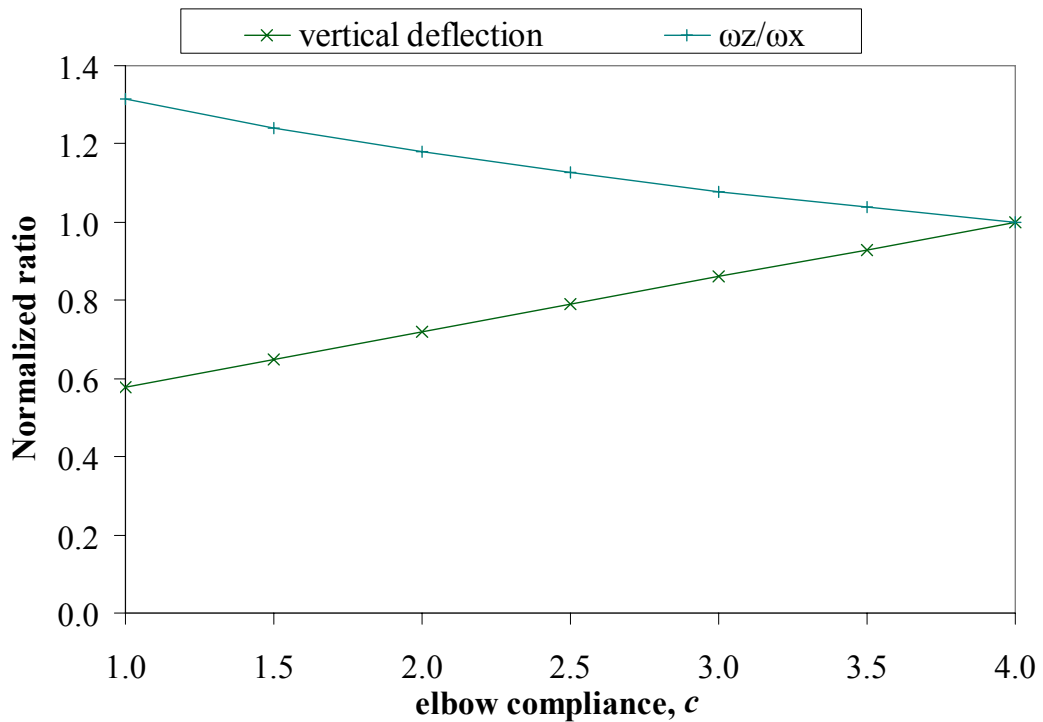


Figure 3.33 Plot of ω_z and $z_{sag,g}$ from expression in Table 3.5.

The outcome of the investigation of various designs is to select a design which increases rejection ratio for the spurious modes. Semicircular elbow geometry (design (d) in Table 3.6) with cross bar, unfilled, represents a reasonable compromise between good stiffness and low suspension mass.

3.7 Optimum Design Parameters

By analysing the various designs we have selected three potential configurations which seem to satisfy the criteria for a 10 Hz suspension and at least 10 times separation between the fundamental and first on-axis spurious mode while trying to maximize the other rejection ratios as well.

Table 3.7 gives the dimensional parameters and expected normal modes for those designs. Variance from these characteristics are expected for the final device as the fabrication methods described in chapter 4 will not yield an ideal geometry, this is discussed in chapter 5 and the models modified to accommodate process induced variations.

The lowest spurious mode rejection ratio for one spring set suspension is better than the two and three spring set suspensions but the superior rejection ratio comes as a result of the higher fundamental mode of the one spring set suspension. For the three spring set suspension the first on-axis spurious mode is ten times the fundamental satisfying the design criteria of a 10 Hz suspension with a rejection ration to on-axis spurious mode of at least 10.

Table 3.7 Dimensional parameters for selected designs.

	1-spring	2-spring 1-frame		3-spring 2-frame		
Material constants						
E , GPa	129 (for Si <100>)					
G , GPa	52.4 (for Si <100>)					
ν	0.23					
ρ , kg/m ³	2330					
Dimensional parameters						
t , μm	525					
w , μm	24	24		24		
l , mm	8.32	8.32		8.21		
$g \times h$, mm	8.96 \times 6.03		8.96 \times 6.03		8.96 \times 6.03	
w_s , mm	100	100		140		
c	1.20	1.20		1.20		
n	1	2		3		
Resonant frequencies						
	Calc.	FEA	Calc.	FEA	Calc.	FEA
ω_x	17.65	17.01	12.48	11.98	10.40	9.74
ω_{x1}/ω_x	24.41	37.43	13.99	12.82	10.78	10.87
ω_y/ω_x	9.76	9.10	9.76	8.98	9.63	8.92
ω_z/ω_x	9.13	8.53	9.13	7.98	9.07	7.80
ω_a/ω_x	12.54	12.85	12.54	12.64	12.32	12.55
ω_β/ω_x	15.82	15.99	17.19	16.01	18.42	16.55
ω_γ/ω_x	9.44	9.63	9.84	9.35	10.09	9.50

3.8 Summary

The author's key work covered in this chapter is the numerical modelling of the suspension dynamics and statics. The numerical models are also used to refine the analytical models (created by Tom Pike to estimate suspension dynamics) to incorporate important parameters while keeping them simple for heuristic examination of the design space. The concept of intermediate frame is covered in US Patent number 7036374 (Pike, Stanley, Syms). The dimensional characterization and modelling was performed by the author.

Analytical and numerical models were used to simulate the dynamics of the lateral suspensions. The analytical formulas have the advantage of allowing the immediate characterization of a suspension design and giving a heuristic approach to optimization. The numerical model incorporates effects of factors which are neglected in analytical model like silicon anisotropy and mass loading effect of the springs, additionally it allows visualization of the resonant modes.

The models were used to analyze multiple spring set suspensions which due to their larger number of springs allows for a lowering of the resonant frequency of the suspension. The disadvantage of the increasing number of spring sets was the dramatic drop in the rejection ratio for spurious modes.

The introduction of intermediate frames into lateral suspension is beneficial to cross-axis rejection in the out-of-plane direction. Intermediate frames also improved rejection

ratio for all other modes. The price to be paid for the introduction of the frames is in the lowering of the first on-axis spurious mode ($x1$) due to the increased mass loading. The mass loading is minimized by using a relieved structure for the intermediate frames, although at the expense of some loss in torsional strength. The extra cross-axis stiffness introduced by the intermediate frames outweighs the deterioration of the on-axis dynamics and frames are incorporated between each suspension unit. In addition to intermediate frames, webbing at the elbows of the suspensions greatly reduces the out-of-plane bending with little loss of compliance in the on-axis direction.

The analytical expressions of Table 3.3 and Table 3.5 are used to first determine the lowest-frequency spurious mode of a candidate design. Examination of the parameters then leads to possible variations on the geometry to push up the rejection ratio of this mode. In general, as the lowest-frequency spurious mode is thus pushed away from the fundamental, other spurious modes will be lowered in frequency. The widest separation between the fundamental and first spurious value occur as the two lowest spurious modes have the same frequency.

The three suspensions presented in Table 3.7 give an example of this approach for an increase in the number of frames. As the number of suspension sets increases from one, to two, to three, the lowest rejection ratio is raised compared to non-intermediate frame suspensions while the other spurious mode rejection ratios decrease. For three suspension sets several modes have a very similar rejection ratio, representing a near optimum design for clean bandwidth.

3.9 Conclusion

The agreement between analytical and FEA model provides confidence in formulas for the lateral suspension. Further calculations of model suspensions show excellent agreement of FEA and analytical results across a broad range of unfabricated geometries.

Intermediate frames were demonstrated to decouple the rejection ratio from number of spring sets for multiple spring set suspensions. They improved the rejection ratio for all modes except the first on-axis mode.

The models were used to determine the dimensional characteristics of a set of suspensions with varying number of spring sets and intermediate frames. The selected suspensions are near optimum solutions for attaining the requisite resonant frequency and cross-axis rejection as the mode rejection ratios plateau around 10 for a range of designs based on the same original configuration of mirrored joint folded cantilever spring suspensions with intermediate frames. The spring end connectors are designed with a cross-bar to improve the out-of-plane rigidity of the springs.

Particular design or performance constraints can be incorporated to preferentially reject a particular mode. An example may be if the out-of-plane z -axis deflection should be minimized to allow for minimum gaps between the suspension and any sandwiching structures. In this case maximizing the rejection of one specific mode may be preferable to overall maximization of the clean, spurious-mode-free, bandwidth above the fundamental.

The suspension designs presented in Table 3.7 are then prepared for fabrication, which is covered in the next chapter.

3.10 Bibliography

- [3.1] W. C. Tang, T.-C. H. Nguyen, and R. T. Howe, "Laterally driven polysilicon resonant microstructures," presented at IEEE international conference on Micro Electro Mechanical Systems and published in proceedings 'An Investigation of Micro Structures, Sensors, Actuators, Machines and Robots', 1989.
- [3.2] W. C. Tang, T. C. H. Nguyen, M. W. Judy, and R. T. Howe, "Electrostatic-Comb Drive of Lateral Polysilicon Resonators," *Sensors and Actuators A: Physical*, vol. 21, pp. 328-331, 1990.
- [3.3] A. S. Tamsir, F. Saharil, and B. Y. Majlis, "The optimization of mechanical harmonic modes of the 75 g balanced weight distribution capacitive accelerometer," presented at IEEE International Conference on Semiconductor Electronics, 2002.
- [3.4] T. Harness and R. R. A. Syms, "Characteristic modes of electrostatic comb-drive X-Y microactuators," *Journal of Micromechanics and Microengineering*, vol. 10, pp. 7-14, 2000.
- [3.5] W. T. Pike and S. Kumar, "Improved Design of Micromachined Lateral Suspensions using Intermediate Frames," (*accepted*) *Journal of Micromechanics and Microengineering*, 2007.
- [3.6] W. Weaver, S. P. Timoshenko, and D. H. Young, *Vibration problems in engineering*, 5 ed: John Wiley & Sons, 1990.
- [3.7] H. J. Himmelbau and S. Rubin, *Vibration of a resiliently supported rigid body*, in *Shock and Vibration Handbook*, C. M. Harris, Ed., 4th ed. New York: McGraw-Hill, 1996, pp. 3.1-3.57.
- [3.8] ADXL50, "Analog devices ADXL50," <http://www.analog.com>.
- [3.9] H. Luo, G. Zhang, L. R. Carley, and G. K. Fedder, "A post-CMOS micromachined lateral accelerometer," *Journal of Microelectromechanical Systems*, vol. 11, pp. 188-195, 2002.
- [3.10] Y. Suzuki and Y.-C. Tai, "Micromachined high-aspect-ratio parylene beam and its application to low-frequency seismometer," presented at The 16th IEEE International Conference on Micro Electro Mechanical Systems, Kyoto, Japan, 2003.

- [3.11] I. Y. Park, C. W. Lee, H. S. Jang, Y. S. Oh, and B. J. Ha, "Capacitive sensing type surface micromachined silicon accelerometer with a stiffness tuning capability," presented at The IEEE 11th Annual International Workshop on Micro Electro Mechanical Systems, Heidelberg, Germany, 1998.
- [3.12] G. Zhang, H. Xie, L. E. de Rosset, and G. K. Fedder, "A lateral capacitive CMOS accelerometer with structural curl compensation," presented at The 12th IEEE International Conference on Micro Electro Mechanical Systems, Orlando, FL, USA, 1999.
- [3.13] R. J. Roark, *Roark's formulas for stress and strain*, 6 ed: McGraw-Hill, 1989.
- [3.14] R. Liu, B. Paden, and K. Turner, "MEMS resonators that are robust to process-induced feature width variations," *Journal of Microelectromechanical Systems*, vol. 11, pp. 505-511, 2002.
- [3.15] A. Kelly and G. W. Groves, *Crystallography and Crystal Defects*, Harlow, UK Longman, 1970.
- [3.16] Ansys Multiphysics, Ansys inc., Southpointe, 275 Technology dirve, Canonsburg, PA 15317 USA <http://www.ansys.com>.
- [3.17] W. T. Thomson and M. D. Dahleh, *Theory of Vibration with Applications*, 5 ed: Prentice-Hall, Inc., 1998.
- [3.18] K. F. Riley, *Mathematical Methods for the Physical Sciences*, Cambridge University Press, 1974.
- [3.19] W. T. Pike and I. M. Standley, "Determination of the dynamics of micromachined lateral suspensions in the scanning electron microscope," *Journal of Micromechanics and Microengineering*, pp. S82-S88, 2005.
- [3.20] W. T. Pike, I. M. Standley, and R. R. A. Syms, Improved micro-machined suspension plate with integral proof mass for use in a seismometer or other device, US Patent US7036374: May 2, 2006

four

4 Suspension: Fabrication

This chapter covers the fabrication of the lateral silicon suspension. Processing of the silicon wafer using DRIE has been analyzed along with issues relating to high aspect ratio micromachining. Finally a set of processing parameters is developed to achieve the desired geometry of the lateral suspension in silicon.

4.1 Introduction

Subsequent to suspension design analysis using analytical and numerical methods, the suspension is fabricated by etching single crystal silicon wafers. The full thickness of the silicon wafer is used to maximize the inertial mass. To etch through the wafer and maintain a vertical profile, the etching has to be highly anisotropic. Common techniques for creating highly anisotropic structures from silicon are anisotropic wet etching utilizing silicon crystal planes, and fluorine based high-density low-pressure inductively-coupled plasma etching.

Anisotropic wet etching using KOH (potassium hydroxide) or TMAH (tetramethylammonium hydroxide) to create silicon structures with (111) limiting plane or (110) limiting plane is unsuitable for a geometry which has vertical spring elements with sidewalls along planes other than (111) and (110). Such etching is generally suitable for only rectangular geometry.

Plasma processing is the most widely used process in the microelectronics industry. It has become popular for fabricating high-aspect-ratio MEMS devices after the development of Deep Reactive Ion etching (DRIE) systems based on the Bosch process [4.1] which alternates between an etching and a passivation cycle to achieve an anisotropic etch.

The complete fabrication sequence is discussed in section 4.3 and 4.4. As with most processing methods DRIE has its own set of problems such as grassing, etch lag, sidewall roughness, etch profile, notching, etc., which we will discuss in section 4.5.

4.2 Deep Reactive Ion Etching (DRIE)

Plasma is a largely ionized gas, consisting of positive (ions) and negative (electrons, negatively charged ions) particles. It is electrically neutral due to the equal number of positive and negative charges. The plasma generates electrons, atomic and molecular ions, and atomic and molecular radicals. These plasma species undergo chemical, physical and chemo-physical reactions with atoms of silicon to form volatile reaction products. For directional etching the ions can be accelerated using an external electric field. The accelerated ions remove the target atoms by physical ion bombardment. The radicals are chemical species which generally cause chemical isotropic etching. Low pressure inductively-coupled plasma creates a high density of ions and has become the preferred source for high rate DRIE systems.

There are two main established technologies for deep anisotropic plasma etching of silicon: cryogenic [4.2] and Bosch [4.1] (also known as time-multiplexed or pulsed etching). In the cryogenic process the wafer is cooled down to below $-100\text{ }^{\circ}\text{C}$, which slows down spontaneous chemical etching by radicals that is isotropic in nature and only vertically accelerated ions drive the etching process. The need to cool down the chamber to cryogenic temperatures makes this process expensive and there is a lack of standard industry cryogenic etchers though some (ex. METlab system of Alcatel, and Plasmalab 100 system of Oxford Plasma Technology) companies are starting to commercialize this technique.

The Bosch process works by passivation of the sidewalls in between etching steps (see Figure 4.1). The process starts by first isotropically etching exposed substrate (Figure 4.1a). After a brief period (typically few seconds) the etching is stopped and a polymer

passivation layer is deposited (Figure 4.1b). The passivation layer protects the substrate from further chemical attack by the radicals in the plasma. The process then returns to the etching cycle where the vertically accelerated ions bombard the bottom of the previously etched trench removing the passivating layer (Figure 4.1c). The etch then proceed isotropically to extend the etched trench (Figure 4.1d). Etching therefore is preferentially in the vertical direction.

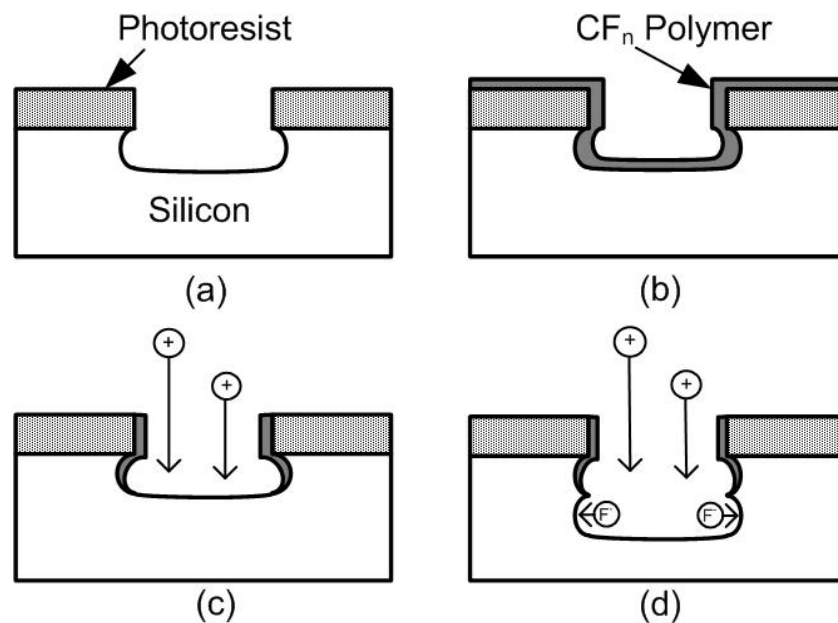
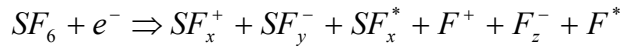


Figure 4.1 Passivation and etch cycle in a typical DRIE step. (a) Isotropic etch of silicon in exposed regions on the wafer, (b) Deposition of polymer CF_n on all surfaces, (c) Preferential etching of polymer from the bottom of the trench by vertically directed positive ions, and (d) Isotropic etching of the trench bottom by fluorine radicals.

Sulphur hexafluoride (SF_6) and octafluorocyclobutane (C_4F_8) are used for etching and passivation respectively. SF_6 plasma generates fluorine atoms, positive ions SF_x^+ (x varying from 0 to 5), positive fluorine ions F^+ , and negative ions SF_y^- (y varying from 4 to 6), F^- and F_2^- [4.3, 4]. Rauf et al. [4.5] reports that in inductively coupled SF_6 plasmas, the primary ions produced directly from SF_6 are SF_3^+ and SF_5^+ , however they

indicate SF_2^+ to be one of the important ions, where SF_2^+ is mainly produced due to ionization of the SF_2 radicals.



where $x = \{0, 1, 2, 3, 4, 5\}$, $y = \{4, 5, 6\}$, $z = \{1, 2\}$.

The chemical etching reactions are

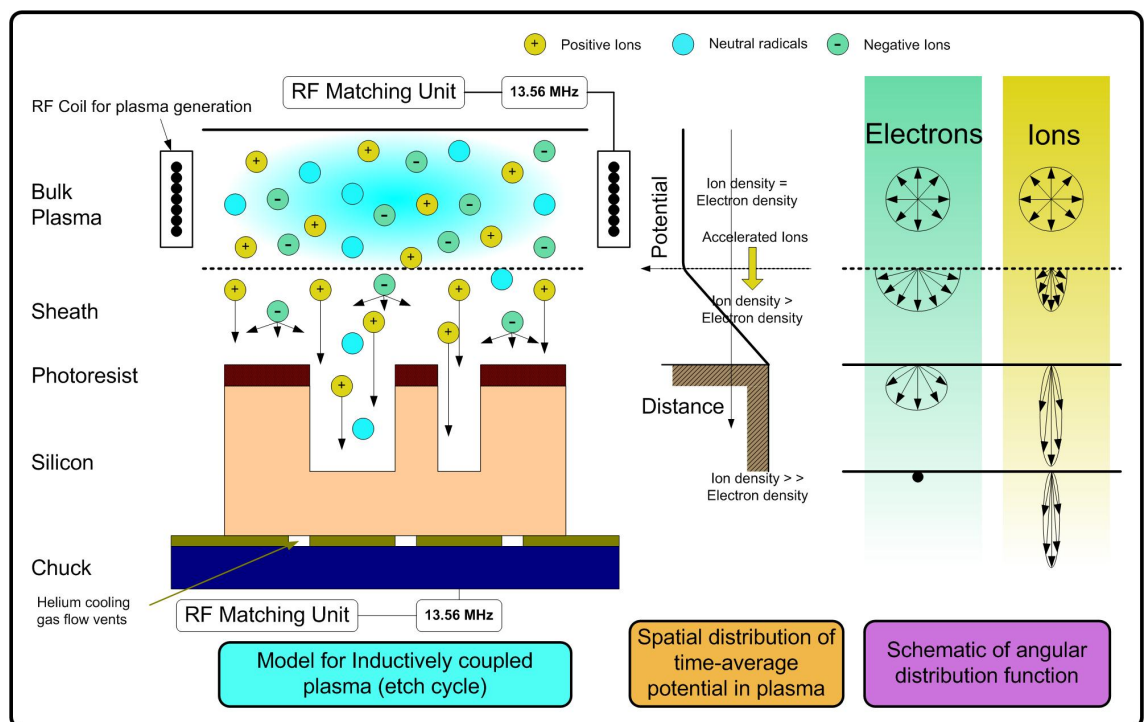
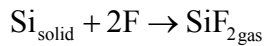
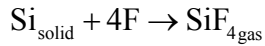


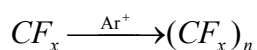
Figure 4.2 Model for inductively coupled plasma etch showing the positive and negative species in the plasma, their energy angular distribution function (ADF) and the potential drop across the sheath which accelerates the positive ions.

Figure 4.2 shows the model of the plasma etcher. The positive fluorine ions are accelerated across the plasma sheath and causes the ion bombardment induced etching. Neutral radicals cause chemical isotropic etching. Electrons and other negative ions seep across the sheath and are isotropic in nature so are confined to the top surface of

the substrate whereas positive ions due to their higher energy (higher velocity due to acceleration by sheath potential) are able to reach the trench bottom. The model shows how the electrons and ions have similar energy angular distribution function (ADF) inside the plasma. Due to the presence of a potential drop across the sheath the positive ions have a higher energy ADF at the substrate.

The etching comprises of physical and chemical etching. Physical etching or sputtering relies on energy and momentum transfer from an impinging particle by means of elastic/inelastic scattering [4.6]. Chemical etching takes place due to the disassociation of SF_x by ion bombardment into fluorine radicals which chemically react with silicon.

To achieve vertical sidewalls or anisotropic etching, during the passivation cycle the etched sidewall is covered with CF or CF_x ($x = 1..3$) monomer which is generated by plasma dissociation of C_nF_{2n+2} . The SF_x plasma species reacts with the CF_x plasma species deposited on the polymer, forming non-volatile reaction products which guard the sidewall from etching [4.7].



4.2.1 Applications of DRIE

DRIE has been used to make a variety of Microsystems devices [4.8], from inertial sensors such as accelerometers [4.9, 10], gyroscopes [4.11], to optical passive and active components like switches [4.12], tunable optical filters [4.13], energy conversion devices [4.14], biomedical devices like needles [4.15], magnetic resonance imaging Helmholtz coil [4.16], and for creating through-wafer interconnects [4.17] (Figure 4.3).

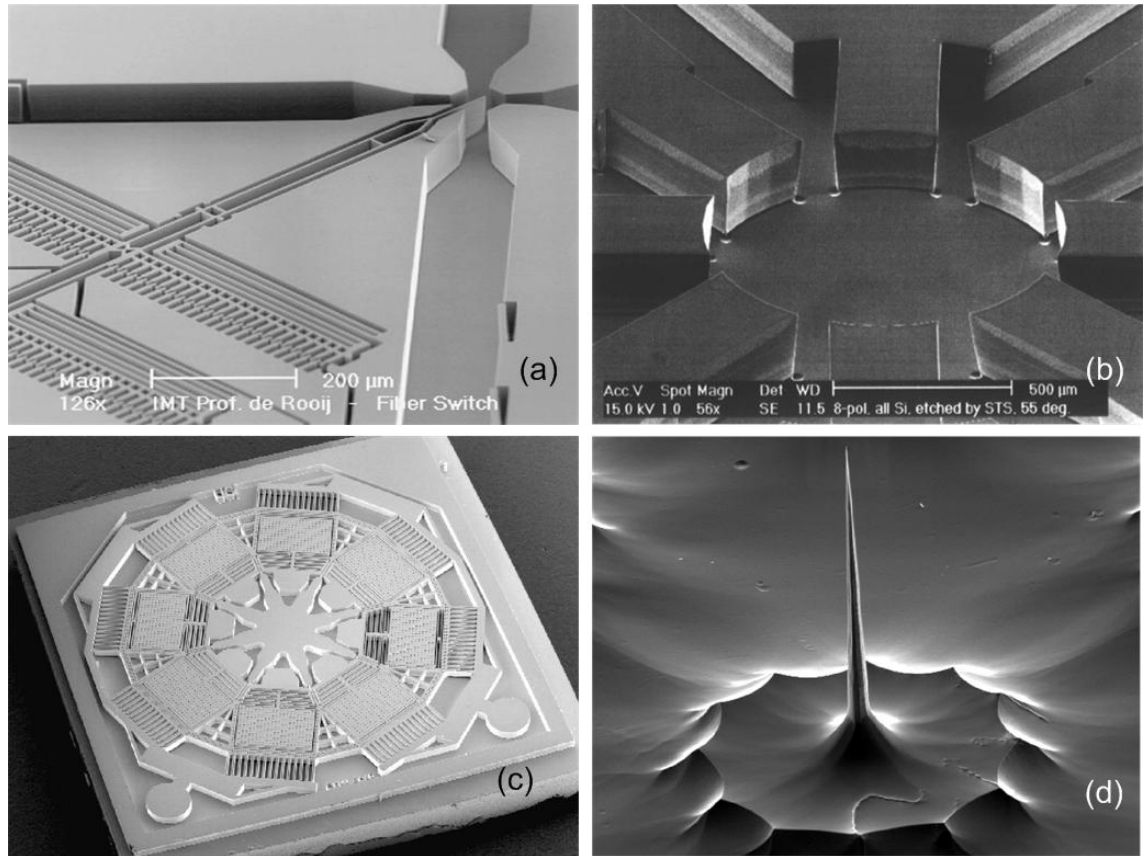


Figure 4.3 DRIE devices (a) Actuator-mirror structure fabricated on SOI (Prof. de Rooji, IMT), (b) MicroSEM deflector structure (Prof. de Rooji, IMT), (c) A MEMS gyroscope fabricated on SOI [4.11], and (d) Micro-machined intracellular needle [4.15], pillar etched using DRIE and then post processed to achieve the sharp tip.

There are multiple commercial DRIE systems on the market by STS (Surface Technology Systems), Alcatel, Oxford instruments, and Plasma-therm which are able to provide high-rate anisotropic etching of very high-aspect-ratio features. The availability of high-rate industrial systems is important for through-wafer etching 500 μm to 1 mm thick wafers.

4.3 Fabrication Process Flow

Through-wafer etching needs special considerations compared to conventional semiconductor etching where etched features are shallower and the silicon substrate's

bottom surface is not breached. In this section we will look at these special considerations for through-wafer DRIE.

The DRIE process is carried out in a computer-controlled system which is described in section 4.3.1. The process depends on many parameters like gas flow rates, cycle times, number of cycles or total process times, chamber pressure, chamber temperature, coil power used to generate plasma, platten power to apply a bias voltage to the ions, and the gases. In the systems used for fabricating this suspension, SF₆ is used for etching (though a small amount of Oxygen is added to remove any sticking residue in the chamber or in the residue extraction system) and C₄F₈ is used for passivating the surfaces undergoing etching.

4.3.1 System description

The suspensions are fabricated using a Surface Technology Systems multiplex ICP (Figure 4.4a). The etching chamber is maintained at a low pressure by a turbo pump. The system has two independent 13.56 MHz RF power sources. As shown in Figure 4.4b, the Coil RF Matching unit is driven by a 1000 W RF power supply. The coil is inductively coupled to the plasma to maintain a high-density plasma. A second 200 W RF power source drives a Plasma Matching unit which is used to vary the RF bias potential of the wafer with respect to the plasma.

The etching chamber has a single feed on top for the etching/passivating and auxiliary gases (SF₆, C₄F₈, O₂, and Ar). The etching chamber is connected to an automatic load lock which eliminates the need to open the chamber to load the wafer thus allowing the chamber to be maintained continuously at low vacuum. The wafer is loaded into a twin wafer capacity loading tray which automatically loads the wafer on the chuck in the

etching chamber. The chuck is an electrostatic “clicks” plate which uses a high potential (up to 1000V) across its coating of dielectric layer to grip the wafer. The chuck has 12 μm deep grooves on the top surface and a pressurized helium inlet. The wafer is kept at a constant temperature of 40°C by helium flowing on its backside during the processing. The chamber walls are kept at 60°C by water flowing on the outside of the chamber wall to avoid any residue depositing on the sidewalls of the chamber. The etch chamber is continuously pumped to remove all volatile etch by-products.

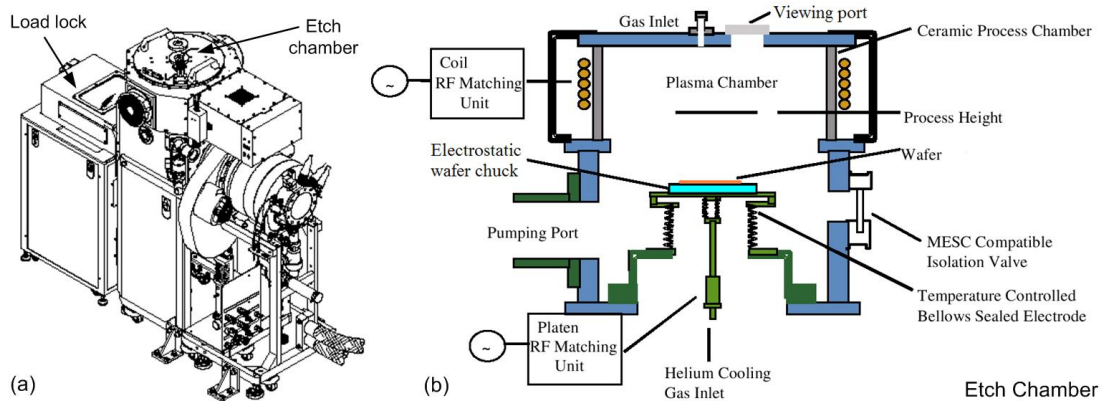


Figure 4.4 (a) STS DRIE Kit [4.18], (b) STS ICP Multiplex process chamber Schematic (Source: [4.19]).

The silicon etch rate, photoresist selectivity, profile shape of the etched trench, surface quality and etch rate uniformity is dependent on various parameters such as gas flow rates, platen and coil power, etch and passivate cycle times and chamber pressure. The operator can change the etching and passivation times by changing the etch/passivate time ratio while keeping the cycle time constant or by increasing the cycle time. The gas flow rate for SF_6 , O_2 , C_4F_8 and Ar can be modified and is usually represented in sccm (standard cubic centimeters per minute). The total etch time can be given and the software automatically calculates the number of cycles needed. The coil and platen power can be varied: coil power refers to RF power used for plasma generation, platen

power is the bias between the chamber walls and substrate holder to accelerate the ions vertically to achieve anisotropy. The chamber pressure is varied either by setting the pressure to a specific milli-torr value or by varying the valve angle, also called APC (automatic pressure control) angle in which case the pressure is measured by the flow rates of the various gases.

The basic requirement of successfully patterning the silicon wafer to desired geometry is to develop a process flow which transfers the pattern from mask to the silicon wafer. To etch areas of silicon selectively needs other areas on the wafer to be guarded against the etchants. This needs a suitable masking material which can withstand the etchants longer than the silicon to be etched. The etching process parameters are then tuned to achieve the desired etch. An iteration of this cycle is generally needed to achieve the desired result.

4.3.2 Mask preparation

To transfer the design pattern onto silicon, a mask is prepared which transfers the layout onto the masking layer (oxide, photoresist, nitride etc) so only areas which need etching are exposed to the plasma.

A key concern with plasma processes is the loading effect. In DRIE due to the dependence of etch rate on silicon exposure area, feature rich regions etch slower than feature scarce regions. This effect is generally known as microloading [4.20] and is due to the reactant depleted condition in areas with higher silicon exposure (a higher consumption of reactant species for etching silicon with constrained replenishing of fresh reactants).

Additionally smaller areas etch slower than larger areas which is commonly known as etch lag [4.21]. To avoid both microloading and etch lag we need to design the mask so that the silicon exposure is similar across the wafer and the etch channels are of similar dimensions.

To achieve uniform etching throughout the wafer, the features are etched using constant channel width on either side. This scheme is commonly referred to as halo mask [4.22]. An example is shown in Figure 4.5 which shows a spring and frame (dark grey) feature surrounded by constant width etch gap.

Regions which are not structural parts, but are present to minimize silicon exposure and give a constant channel width for all the etchings, are called “packing” pieces. After a through-wafer etch, the “packing” pieces which are not attached to any structure on the wafer fall-off during the release process.

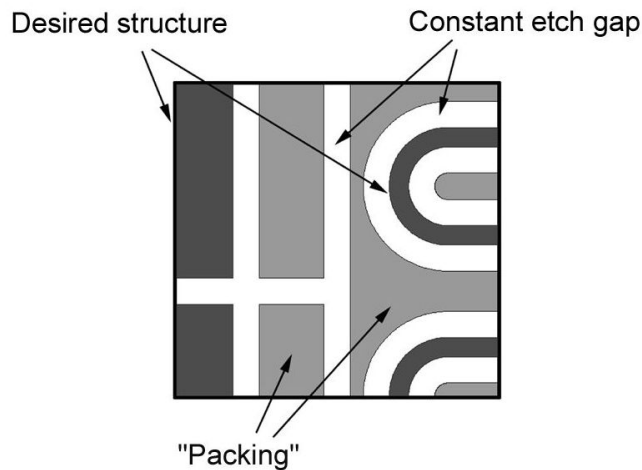


Figure 4.5 A halo mask and its various components for a 2D mask designed on a mask plate for transferring the pattern onto photoresist.

The etch channel width was set to 40 μm after doing test studies with varying etch gaps. With the same process parameters, gaps wider than 40 μm etch faster but results in poor

sidewall quality (see Figure 4.6). Smaller gaps take longer to etch through and for gaps smaller than $20\ \mu\text{m}$, the etchant flux density is extremely low at the foot of the etch trench resulting in etch cessation.

Another aim of the process engineering is to achieve a single “process parameter set” for the complete etch run instead of parameter ramping. Automatic process parameter ramping though a useful method available with DRIE system needs to be constantly modified with changing mask designs, resulting in a higher process development time. Figure 4.6d shows etched sidewalls for varying trench width. For trench width above $40\ \mu\text{m}$ we can see significant damage to the sidewall. Additionally Figure 4.6a-c show the profile shape becomes less vertical with higher gap width.

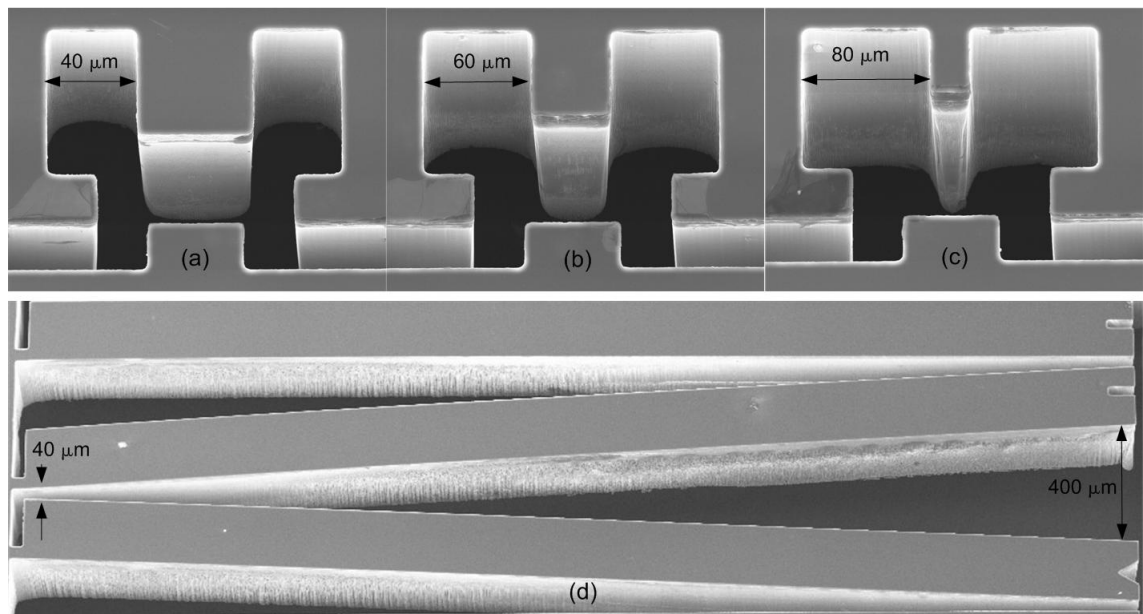


Figure 4.6 Sidewall quality for varying channel/trench width, (a) $40\ \mu\text{m}$ gap, (b) $60\ \mu\text{m}$ gap showing a widening of the gap towards the bottom of the trench as the profile diverges away from vertical, (c) $80\ \mu\text{m}$ gap shows the increase in profile shape divergence from vertical with bigger gap, (d) beams with gap varying from $40\text{-}400\ \mu\text{m}$ show the increased breakdown of the sidewall with larger gap.

4.3.3 Pattern transfer

Etching silicon needs a masking layer with higher resistance to plasma etching than silicon. Typical masking materials for DRIE are photoresist, nitride and oxide. The etch rate for the DRIE system is on the order of 1-2.5 $\mu\text{m}/\text{min}$, though it can be as high as 10-50 $\mu\text{m}/\text{min}$ for the latest high etch rate DRIE systems. At 2 $\mu\text{m}/\text{min}$ etch rate it takes 4 hours 20 minutes to etch a 525 μm thick wafer so we need a mask layer that can last such a long etch. Thick photoresist and oxide are therefore investigated as appropriate mask material for the etch.

AZ9260[4.23] is a high resolution thick resist distributed by Clariant with an aspect ratio of up to 6:1. It is easily spun to 4-12 μm thickness. A process was developed to spin 9 μm (Figure 4.7) and 14 μm thick AZ9260. The selectivity of the resist is 80:1 for the DRIE process parameters, so requires about 7 μm thick resist coating for etching a silicon wafer 525 μm thick.

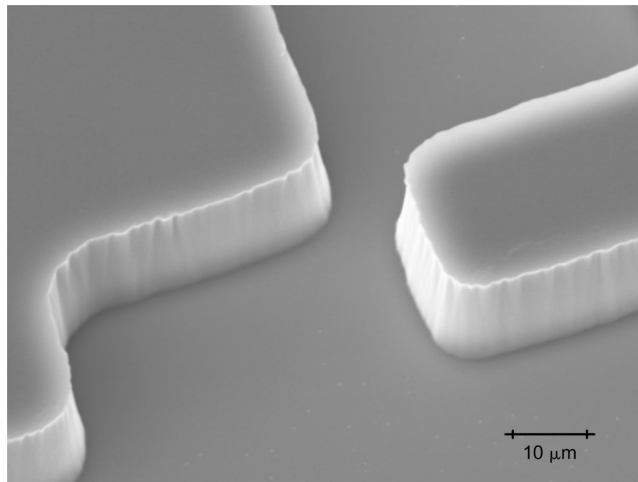


Figure 4.7 SEM image of 9 μm thick AZ9260 photoresist.

Thick oxide was also investigated as a mask material as oxide has a high selectivity to SF_6 plasma etch, typically 180-200:1 [4.24] requiring approximately a 3 μm thick oxide

layer for the etch. Silicon wafers with 3 μm thick oxide grown using wet oxidation process is procured. The oxide is then dry etched using CHF_3 plasma. The sidewall and pattern transfer to oxide is poor due to high-temperature damage to the photoresist used for oxide etching and the isotropic nature of the etch (Figure 4.8). Etching oxide using buffered HF (49%) gives poor results due to the isotropic nature of the etch leading to extremely high undercut.

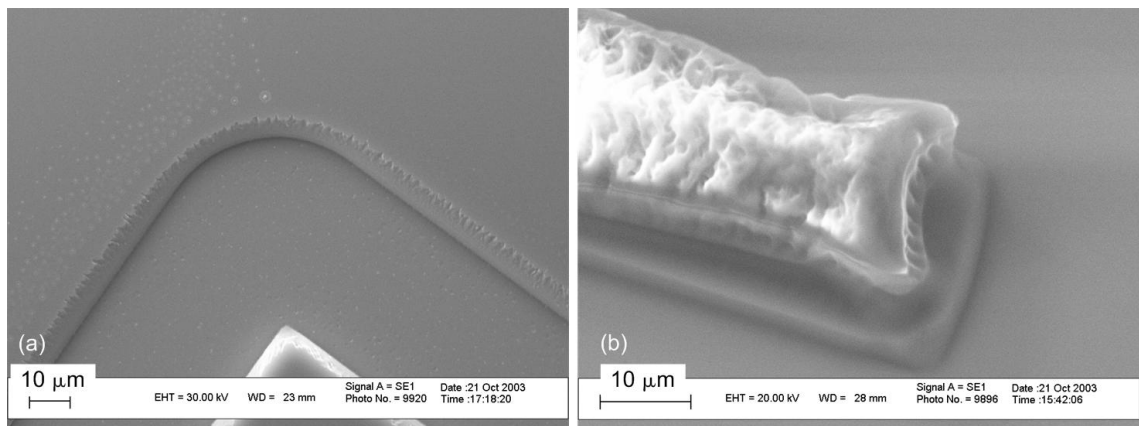


Figure 4.8 (a) SEM of 5 μm thick oxide etched using CHF_3 , (b) SEM of damaged photoresist (AZ9260, 7 μm thick) after oxide etch.

For through-wafer DRIE we decided to use photoresist as the masking layer, Table 4.1 presents the pros and cons of oxide and photoresist as a masking layer in DRIE. The photoresist layer needs to be thicker than oxide to withstand the etchants but in all other respect they are similar or better than oxide when used as a masking layer. Photoresists are organics and provide an additional supply of carbon during the etch thus helping the overall passivation.

Even though oxide is removed from consideration as a masking layer for silicon DRIE, a thin layer of oxide is grown that prevents photoresist mask erosion and acts as a insulation layer for any electrical circuit fabricated over the suspension. A process is

developed to grow 200 nm and 500 nm thermal oxide on silicon wafer and etch using CHF_3 .

Table 4.1 Comparison of oxide and photoresist as a masking layer for DRIE.

Characteristics	Oxide	Photoresist
Selectivity	180-200:1	80:1
Processing time	Long	Short
Processing cost	High	Very low
Compatibility with pre-existing layers	Need another layer to protect any features on pre-processed substrate	Fine
Pattern transfer from mask	Plasma etch or HF etch	Alkaline developer
Pattern transfer onto Silicon	Very good	Good

An oxide etch recipe is developed to avoid damaging the photoresist mask, which also works as mask for the silicon etch. The key reason for the damage to photoresist during oxide etching (Figure 4.8b) is the high temperature that the photoresist was exposed to during the etch. The temperature of the wafer exceeded 150°C in just 5 minutes of etch. To make sure the temperature of the wafer is not allowed to exceed 60°C the etch cycle is kept short, 1 minute long and the wafer is cooled for 2 minutes before resuming the etch. This time-multiplexing of etching and cooling cycles results in good etch profile of the oxide and avoids damaging the photoresist.

4.3.4 Through-wafer etch

Availability of high-rate DRIE systems which allows highly anisotropic silicon etching, makes wafer thick suspensions possible. The process needs to be tuned to perform wafer thick etching and precautions are taken to avoid etchant contact with the wafer

holder by using a handle wafer underneath the device wafer. The mask needs to be thick enough to sustain etchant bombardment for the total etch time. The etch area needs to be optimized (through mask design) to attain a maximum rate of etch to minimize etch cost as well as to minimize uniformity variations.

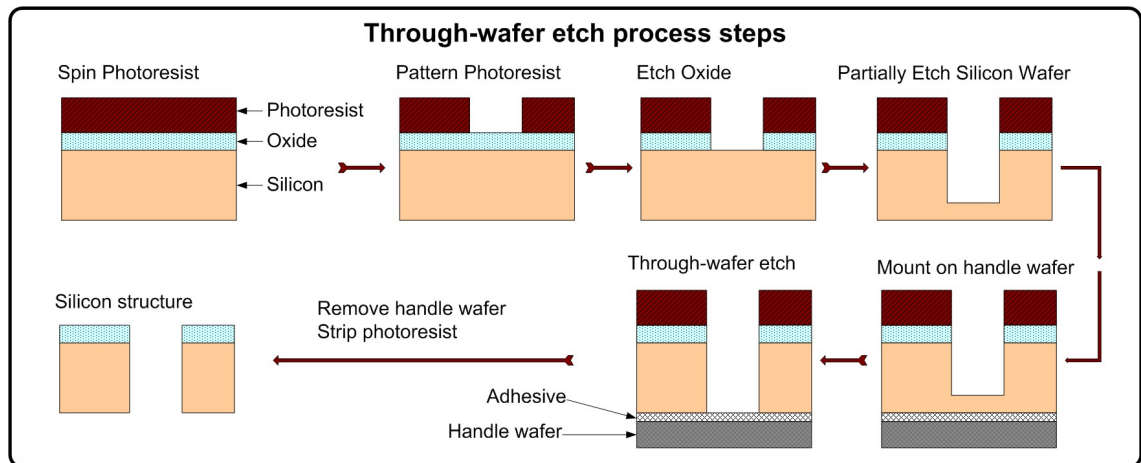


Figure 4.9 Process flow schematic for through-wafer silicon etching using DRIE.

Figure 4.9 shows typical steps in through-wafer etching a silicon wafer. A 200 nm SiO_2 layer is first grown on the silicon wafer and then covered with photoresist. The mask pattern is photolithographically transferred to the photoresist. The oxide is patterned using CHF_3 plasma, thereafter the wafer undergoes a partial DRIE short of the etch breaching the backside of the wafer. The wafer is then removed from the etcher and bonded to a handle wafer using a temporary adhesive. The etch is then resumed to completion. The wafer is thereafter released from the handle wafer and the photoresist is stripped yielding the final device. The need for a handle wafer and the subsequent release process are the additional steps involved over conventional DRIE. In the next section we discuss various ways of protecting the etcher substrate holder from plasma by using a handle wafer or protective layer.

4.3.5 Wafer mounting techniques

For through-wafer etching, it is mostly desirable and sometimes critical to have a protective surface on the other side of the wafer so that when the etch gets through the first wafer it is contained by the underlying surface. In DRIE we need a protective layer on the backside of the wafer which acts as an etch stop to avoid damaging the chuck (substrate holder in the etcher). The STS system flows helium on the backside of wafer to maintain a lower temperature so a mechanically strong and sealing layer is needed to stop the helium leaking into the plasma chamber. It is quite common to remove the handle wafer once the through-wafer etching is done, so a system of temporarily bonding wafers is an important consideration in through-wafer etching. We present various techniques for temporarily bonding wafers, which are mechanically robust and releasable. In DRIE the added concern of etch variation with temperature makes it critical to have a bonding method which does not affect the thermal sinking of the substrate with the chuck.

The protective surface is applied either at the start of the etch or after a significant portion of the etch has finished though always before the etch has breached the wafer backside. The surface is generally another silicon wafer bonded to the substrate wafer. It protects the chuck which is used to bias the substrate to vertically direct the ions in the plasma, and also to flow helium for maintaining the wafer at a low temperature. In the absence of a handle wafer the ions etch through the substrate wafer causing micro holes leading to helium leaks into the chamber and premature termination of the etch run (dependent on the Helium leak rate value set in the etching process parameter). Directly exposing the chuck to plasma ions reduces its life due to failure of the dielectric coating. The handle layer is also needed if there are loose structures on the wafer which will

come off when the wafer is etched through; this is always the case with halo geometries. Etched structures can also fall off when using the DRIE as a way to dice the wafer; though using tabs (die connecting structures) can avoid the dies from falling onto the chuck plate during removal. Etching small wafers or a piece of wafer also requires a handle wafer to form a leak-proof seal with the chuck.

The etch rate, sidewall surface smoothness, trench profile, and mask selectivity varies with temperature of the substrate wafer. It is normally seen that a higher temperature of the substrate wafer leads to a fast erosion of the mask layer so it becomes crucial to have a thermally conductive protective layer on the backside of the wafer which allows the Helium flow on the backside of wafer to keep the 'substrate-handle wafer' sandwich thermally stable. Another issue with through-wafer etching is notching (discussed in section 4.5.9) which happens at the silicon-insulator interface, which is a concern if the protective layer is electrically insulating leading to charging up of surfaces during etch. This can be avoided by having an electrically conducting layer on the wafer backside.

The handle wafer or the protective layer should be easy to release after etch is completed, so that the fragile devices can be handled without any mechanically or chemically aggressive release mechanism. To summarize, the ideal protective coating or handle wafer bonding mechanism, it should have the following characteristics –

- Mechanically strong, to sustain the helium pressure difference and hold the etched structures together.
- Flat to make a leak proof seal with the chuck
- Should not affect chamber composition (no out-gassing etc)
- Thermally conductive to keep the substrate at a stable temperature

- Electrically conducting to avoid notching (section 4.5.9)
- Easy to release without resorting to aggressive mechanical or chemical methods (chemically benign release process to prevent damaging other layers on the wafer)
- Process cleanliness

We investigated various ways of bonding a handle wafer to the substrate wafer using various adhesives as well as tested a metal protective layer. The pros and cons of each system are presented in Table 4.2.

Table 4.2 Comparison chart for various wafer bonding techniques.

Bonding method	Photoresist	Mounting	Cool-	Staystik	Metal
Characteristics	SPR 1813 [4.25]	wax	grease		(Protective Layer)
Mechanical	Strong	Strong	Strong	Strong	Medium
Flatness	Excellent	Good	Good	Good	Good
Outgas	None	None	None	None	None
Thermal Conductivity	Bad	Bad	Good	Fair	Excellent
Electrical Conductivity	Bad	Bad	Bad	Fair	Excellent
Release Process	Easy	Easy	Hard	Hard	Medium
Cleanliness	Good	Good	Bad	Fair	Excellent

It is evident from the comparison chart of wafer bonding technique that the best method for through-wafer etching is to use a metal layer which is mechanically strong thus removing the need for a separate handle wafer. The metal layer should be compatible with the overall process and suitable for electroplating to 10-20 μm thickness. Nickel plated to 5 μm thickness was found to be suitable for use as a protective layer. The disadvantage of metal on the wafer backside is the necessity for a chemical etch to

remove the metal layer to release the features. The next best method is to use a thin photoresist layer to bond the wafers. It is post-baked to improve adhesion and thermal conductivity and is easy to release.

For relatively shorter etch, where silicon is already etched through most of the wafer thickness, a handle wafer is attached using a thin layer of photoresist. Shipley SPR 1813 was spun on a single-side-polished wafer and then bonded to the device wafer. The photoresist bonded wafer stack was found to perform good thermal sinking for shorter etches on the order of 60-90 minutes.

4.4 DRIE Process Parameters

The effect of each of the processing parameters is covered in detail by Chen et al. [4.26-28]. The major parameters which can be varied during the etch are etch:passivate ratio, cycle (etch+passivate) time, coil power, platen power, chamber pressure or APC, gas flow rates, gas flow rate ratio ($\text{SF}_6 : \text{C}_4\text{F}_8$), and some minor ones like O_2 flow rate with SF_6 , and overlap of etching and passivation steps. All these parameters have an effect on the silicon etch rate, photoresist etch rate, sidewall quality, profile shape of the etch trench, and uniformity of etch across the wafer.

SF₆ and C₄F₈ flow rates: Increasing the flow of SF_6 increases the concentration of the etchants in the chamber leading to higher etch rate of silicon, as well as higher etch rate of photoresist decreasing selectivity. At low SF_6 flow rates the concentration of fluorine is limited and so the etch rate plateaus even if other parameters which increase ionization and dissociation of SF_6 are increased, the amount of SiF_4 that redeposits also increases [4.27]. Increasing the flow rate of C_4F_8 increases the passivation species CF_x

decreasing the silicon etch rate and increasing the selectivity of photoresist. The deposition of the Teflon like CF_x polymer on the sidewall is self-limiting [4.29, 30] but is dependent on the ion bombardment and with a higher ion density it can be significantly thicker. As we will see in section 4.5 depending on the relative concentration of the etchant and passivating species, the sidewall quality can vary from smooth to extremely rough, and trench profile shape can go from positive for a etchant rich environment to negative or reentrant for passivation rich environment. With increasing trench depth, the flow rate of SF_6 needs to be increased to counteract the reduction in etching rate.

Etch:Passivate ratio (EPR): Similar to the etching and passivating gas flow rates, a higher EPR will lead to higher etchant species density compared to passivation species. Generally for deep etches it is desirable to have a higher EPR as the etch depth increases as the density of ions reaching the trench bottom decreases with increasing trench depth.

Cycle time: The total time a single set of etch and passivate steps take is the cycle time. Increasing the cycle time for an etching dominant EPR leads to larger scalloping on the sidewalls as in each cycle the etchant radicals are active for longer leading to increased isotropic etching of the sidewall.

Coil power: The ionisation and dissociation of SF_6 and C_4F_8 is dependent on the coil power. Higher coil power leads to a higher density of the ions and radicals in the plasma. Depending on the EPR and gas flow rates, the concentration of the species which is dominant will be increased.

Platen (electrode) power: The platen bias is typically used to accelerate the ions only during the etching step so increasing the platen power increases the directionality of the ions allowing for a higher density of ions to reach the trench bottom increasing the silicon etch rate, and verticality of the trench. As the platen power has no effect on the radicals which are neutral species, the isotropic part of the etch remains unaffected but due to an increase in vertical etch rate the scallop size can be reduced by decreasing the density of the etchants without affecting the vertical silicon etch rate. Increasing the platen power increases the photoresist etch rate, reducing selectivity, as the photoresist is now exposed to higher energy ion bombardment.

APC: The silicon etch rate increases initially with increasing pressure as the fluorine density increases but then as the pressure is increased further it starts decreasing as the mean free path for the ions decrease with increasing pressure lowering the ion energy.

Etching and Passivation step overlap: The overlap of SF₆ extends the etching step and reduces the discontinuity in plasma potential while switching from etching to passivating plasma. This helps maintain a stable glow discharge which leads to improved uniformity. For electronic devices it is critical at times to have a stable plasma as a nonuniform plasma can induce current in the electronic circuit damaging it [4.27].

O₂ flow during etching: A small amount of Oxygen is added to SF₆ during the etching step, this increases both the silicon and photoresist etch rates. The selectivity is however unaffected as the etch rate increase is almost similar. Oxygen plasma also removes the passivating layer though its effect on reducing passivation film from the sidewalls is

limited due to a lower flux at the sidewall. Oxygen is also added in the system to reduce sulphur deposition on the chamber sidewall and residue in the extraction pipes.

DRIE is dependent on a large number of process parameters and has a wide process window allowing the process engineer a large amount of flexibility. The initial goal of any process engineering is generally to remove or reduce any deleterious effects of the processes, as we see in the next section DRIE has a number of problems which need to be addressed to enable the desired micromachining of silicon.

4.5 DRIE Induced Artefacts

Plasma induced damage are a common occurrence in any plasma processing. Some of these effects are inherent to plasma-surface interaction and can be reduced by changing processing parameters but cannot be completely eliminated while others can be completely eliminated. In DRIE, effects of plasma-surface interaction besides the desirable anisotropic etching are evident as deleterious artefacts which can compromise the performance of the fabricated structures. In section 4.5.1 to 4.5.6 we will look at some of the deleterious artefacts which can be easily removed or do not compromise the performance of the suspension. In section 4.5.7 we look at sidewall quality of through-wafer etching; smooth sidewalls are important to increase the fracture strength of the silicon springs as well as to reduce structural defects that can affect the quality factor. Section 4.5.8 concerns etch profile shapes and ways to control them. We examine a technique to eliminate notching in through-wafer etching in section 4.5.9.

4.5.1 Grassing

During etching, large open areas develop tall sharp silicon features due to incomplete removal [4.28], this is particularly common with increasing etch depth due to lack of

sufficient etchant species reaching the etch channel floor. Figure 4.10 shows grass formation in large open squares.

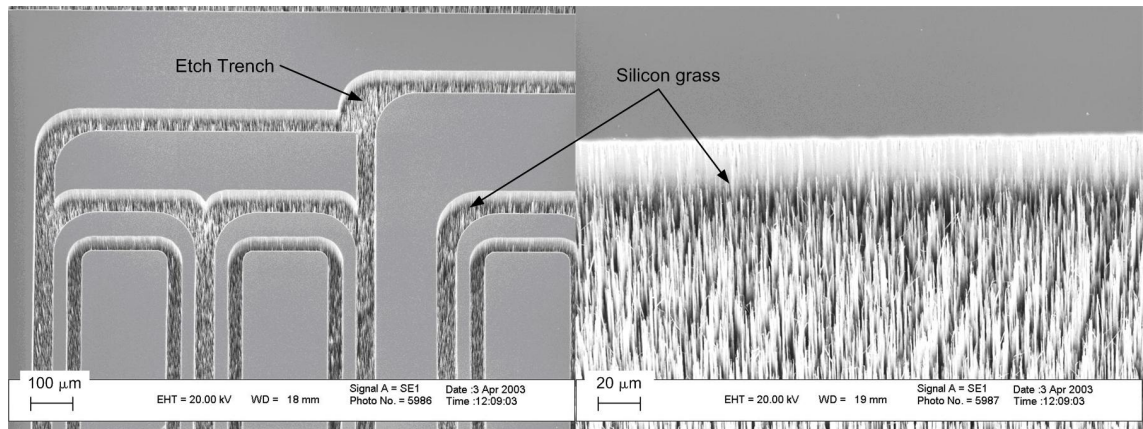


Figure 4.10 Grass formation during silicon etch.

Grass formation is generally lower in smaller areas and is reduced by decreasing the chamber pressure. Enclosing the etched area with packing pieces reduce the effective etch area thus increasing the etchant density leading to reduced grassing. Decreasing the APC angle or chamber pressure reduces grass formation. Increasing the platen power decreases grass build-up by increasing the directionality and energy of the ions. Figure 4.11 shows reduction in grass formation with increasing platen power while keeping all processing parameters constant. At 12W platen power the complete etch trench is covered with grass (Figure 4.11a), increasing the power to 14W removes the grass from the centre of the large trenches but still has grass near trench sidewalls. At 16W there is no grass in the trench but has a grass like curtain at the sidewall which is completely removed by increasing the platen power to 20W (Figure 4.11d).

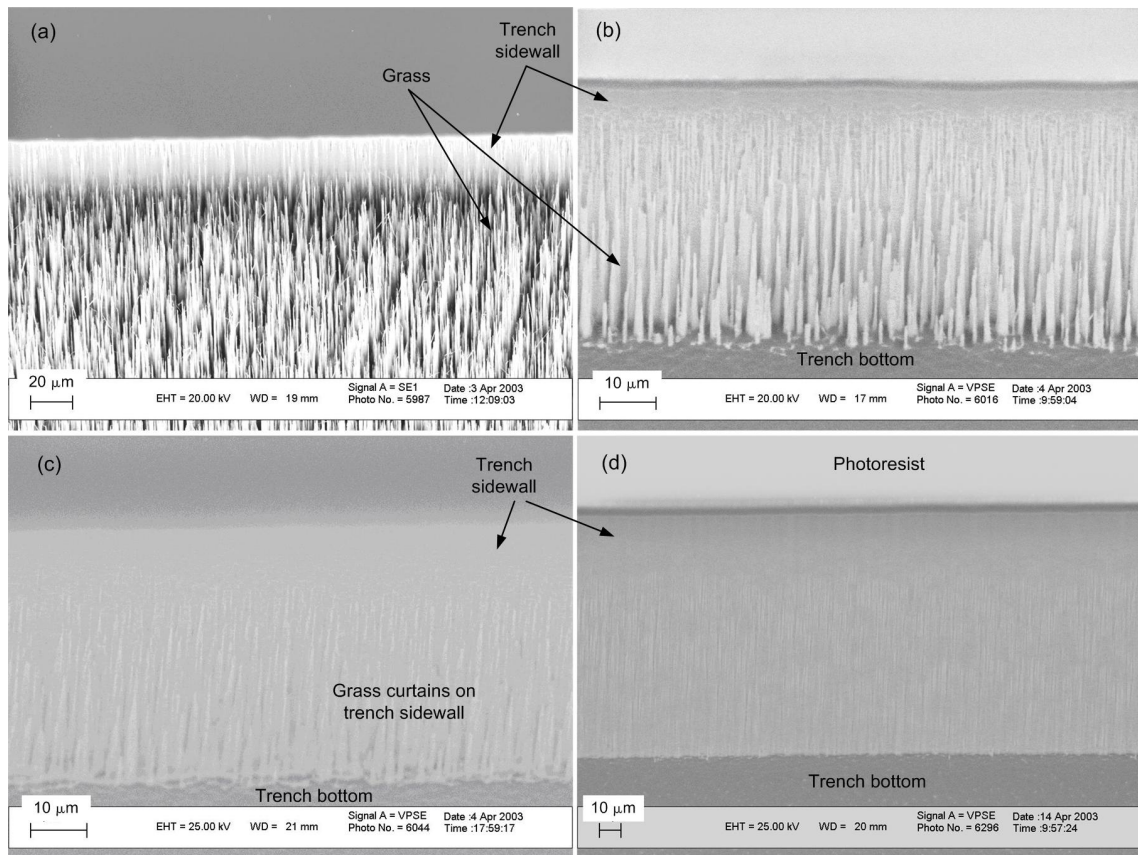


Figure 4.11 Reduced grass formation under increasing platen power, (a) 12W: trench is completely covered with grass, (b) 14W: the centre of the trench bottom is clear but grass is still forming along the sidewall, (c) 16W: clear trench bottom but the sidewalls have grass curtains, (d) 20W: the trench bottom and the sidewall is etched cleanly without any grass formation.

4.5.2 Etch lag

Larger areas etch faster than smaller areas [4.21, 26] due to the presence of higher etchant species density in the larger area, Figure 4.12(a). The etch rate variation increases with etch depth as ions find it harder to go down narrow thin channels ending up somewhere on the sidewall due to slight deviation from vertical directionality of the ion, Figure 4.12(b). Trenches of similar dimension also have etch rate difference depending on their location on the wafer. Areas close to wafer edge etch faster than similar regions in the center of wafer.

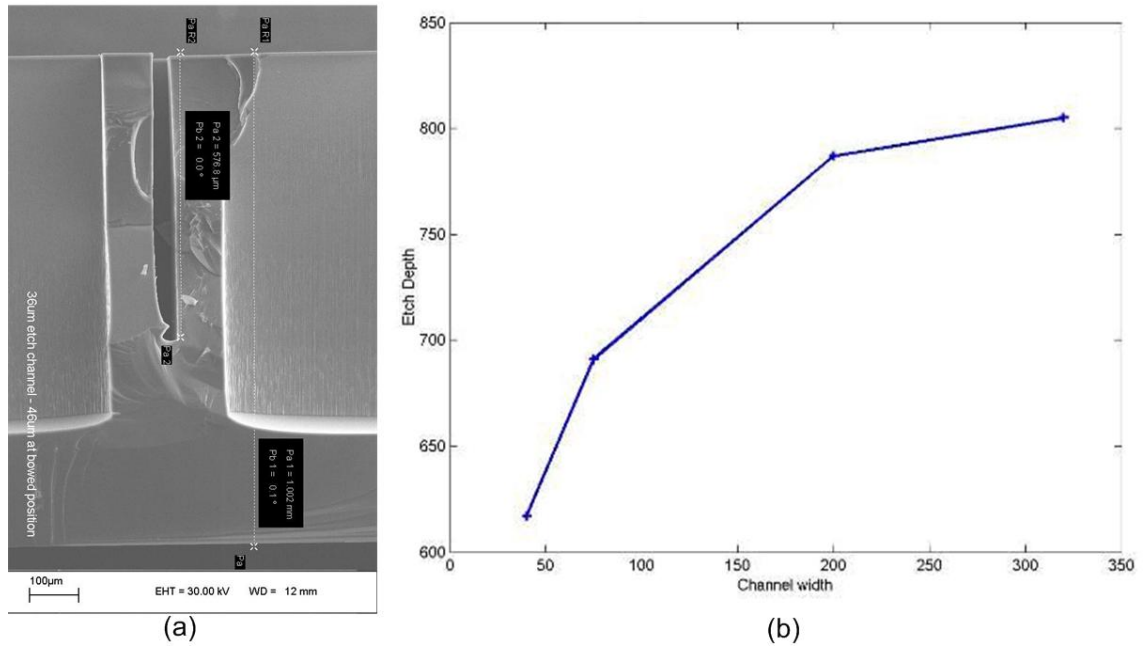


Figure 4.12 (a) SEM of etch cross section showing etch lag between small and large trench, (b) Etch depth vs. channel width (all dimensions in μm) for etch 5 hours long using process parameters from Table 4.4.

In through-wafer etching “etch lag” results in slower etch rates for smaller trenches compared to larger trenches causing over-etching at the bottom of larger channels. In SOI and through-wafer etching this detrimental artifact can lead to lateral silicon etching at the trench bottom, also known as footing damage or notching.

Etch lag can be reduced by using halo mask technique to get a uniform etch area, thus allowing the process designer to only develop a process for specific trench width.

Reducing the etch chamber pressure increases the mean free path of the ions allowing them to reach deeper trenches. SF_6 flow rate is seen to be the dominant process parameter affecting RIE lag.

Creating a process situation where the etchant density is optimized to be nearly similar for both large and small area will reduce etch lag but generally gives rise to grass formation in larger areas (Figure 4.13). This also requires process parameter ramping to control the etchant density with depth.

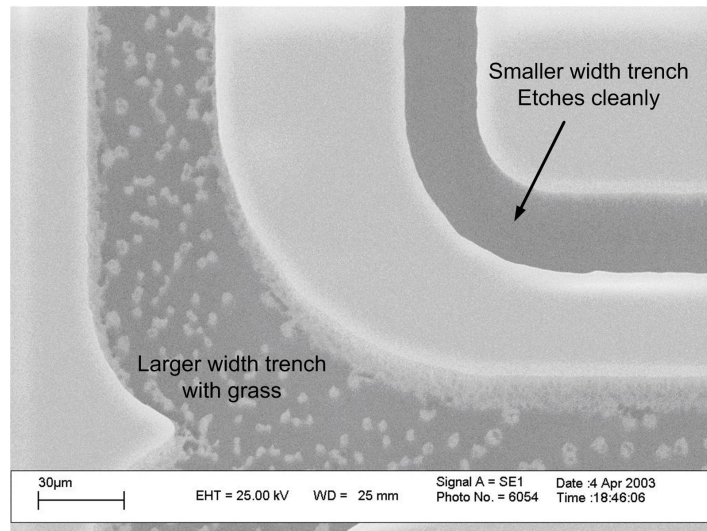


Figure 4.13 Process parameters optimized to reduce etch lag lead to grass formation in larger width trench while smaller trenches etch cleanly.

4.5.3 Loading effect

The loading effect is an interplay between the etch rate and the silicon exposure area. It is generally further classified into macroloading and microloading effects. In macroloading the effect leads to variation in etch rate for similar features at different positions on the wafer, the effect is due to the dependence of reaction rate on etching surface area [4.20]. There is better replenishment of etchant species towards the edge of the wafer than at the center resulting in higher etch rate at the edge of the wafer than the center. Due to macroloading the features on the edge of the wafer are overetched compared to features in the center, to achieve through-wafer etch. The overetch is demonstrated in a variation in sidewall roughness and profile shape.

Microloading is the relationship between local etch rate and pattern density. Features in high pattern density areas of a layout experience more competition for reactants leading to a negative gradient in reactant flux, and to a slower etch rate. As we saw in section 4.3.2, designing a halo mask geometry reduces microloading by reducing the silicon exposure disparity between larger and smaller etching regions.

4.5.4 Top edge cavitations

Another detrimental artifact common to DRIE is top edge damage or cavernous etch at the top of the structure (Figure 4.14). This effect is particularly prominent when the platen power is high. Experiments carried out at 12W platen power resulted in extremely small top edge damage whereas increasing the platen power to 20W resulted in significant damage to the top edge. The most probable cause of this artefact is charging of the mask which deviates the ions off the vertical axis and into the sidewall [4.31]. Exposing the sample to air after every hour of etch reduces the damage to the top edge, which suggests charging of the mask as a possible reason for this damage.

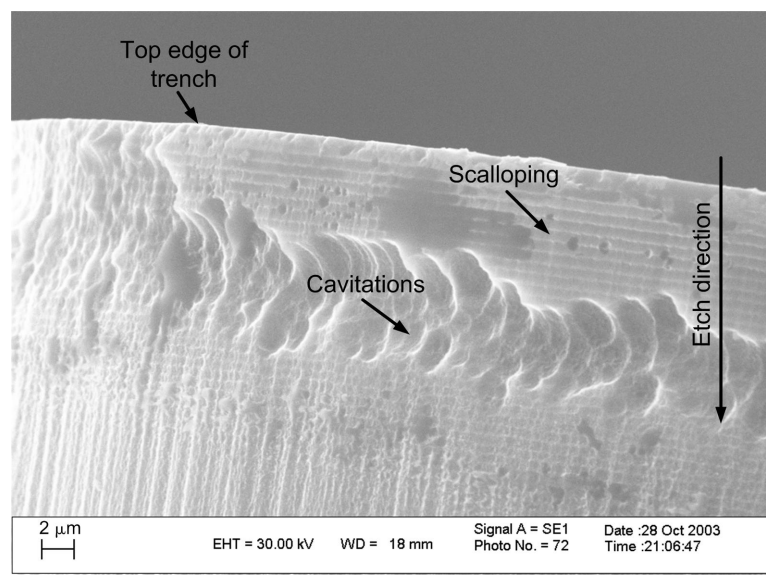


Figure 4.14 SEM of top edge damage.

4.5.5 Etch masking

Incomplete development of photoresist can lead to micro masking of silicon in the etch, which creates oxford spires in the etch channel (Figure 4.15). The micro-masking may lead to significant constriction of the etch channel resulting in a severe etch lag and incomplete through-wafer etching in that location. This causes packing pieces to be attached to the structures. Similarly, flaking of masking material or incomplete removal of etch end products from the etch chamber, leads to these materials redepositing on the wafer, masking further etching in that region.

To avoid micromasking due to incomplete photoresist development, an oxygen plasma de-scum is used after developing the photoresist. The dominant process parameters affecting micromasking are SF₆ flow rate and chamber pressure. Increasing in SF₆ flow rate or pressure leads to micromasking due to incomplete removal of residue.

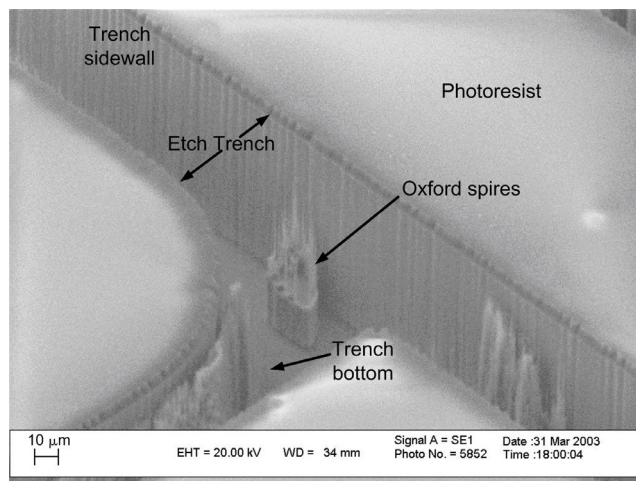


Figure 4.15 Micromasking in etch channel resulting in oxford spires.

4.5.6 Scalloping

Scalloping (Figure 4.16a) is a normal artifact produced by DRIE due to the time multiplexing of etch and passivate cycles. The size of the scallop depends on the etch cycle time and etch rate, the rms height of scalloping for a general processing conditions

is in the range of 5-50 nm. Figure 4.16b shows an AFM scan of scalloping on the trench sidewall giving an rms roughness of 8 nm for a process with 130 sccm SF₆ flow rate, 85 sccm C₄F₈ flow rate and a coil power of 600 W, platen power of 20 W and APC of 78%. Generally faster etch rates will lead to larger scallops (Figure 4.16c). Scalloping is not a major problem for most mechanical devices unless they need a mirror like surface. Scalloping can be removed or reduced by either increasing the etch rate or by performing a smoothing operation after the etch by oxidizing the surfaces and etching the oxide back to give a smooth surface.

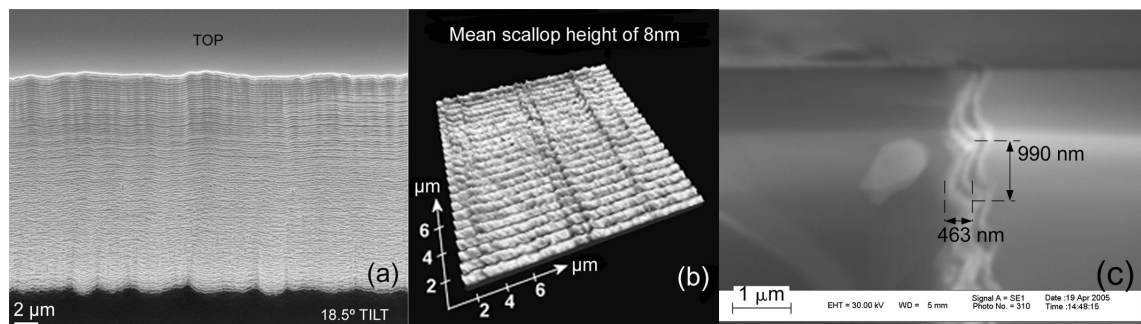


Figure 4.16 Scalloping (a) Scalloping on a sidewall, (b) AFM scan of top edge of sidewall shows scallops (courtesy: Sanjay Vijendran), (c) SEM of large scalloping on trench sidewall suggesting high etch rate.

4.5.7 Sidewall roughness

The quality of sidewalls resulting from through-wafer DRIE has a significant effect on the quality factor of the suspension as well as the reliability of the device (as structures with rough surfaces tend to have lower fracture strength). The sidewalls of the trench as shown in Figure 4.17 show a surface whose roughness increases with increasing depth of the trench. It becomes important to understand the process parameters affecting the sidewall quality to control the roughness. To do so we analyze the sidewall quality by fabricating test structures and observing them under SEM, interferometer and AFM. We also look at the relationship between etch gap and sidewall quality.

This work was done in collaboration and the full results are published in Pike et al.[4.32].

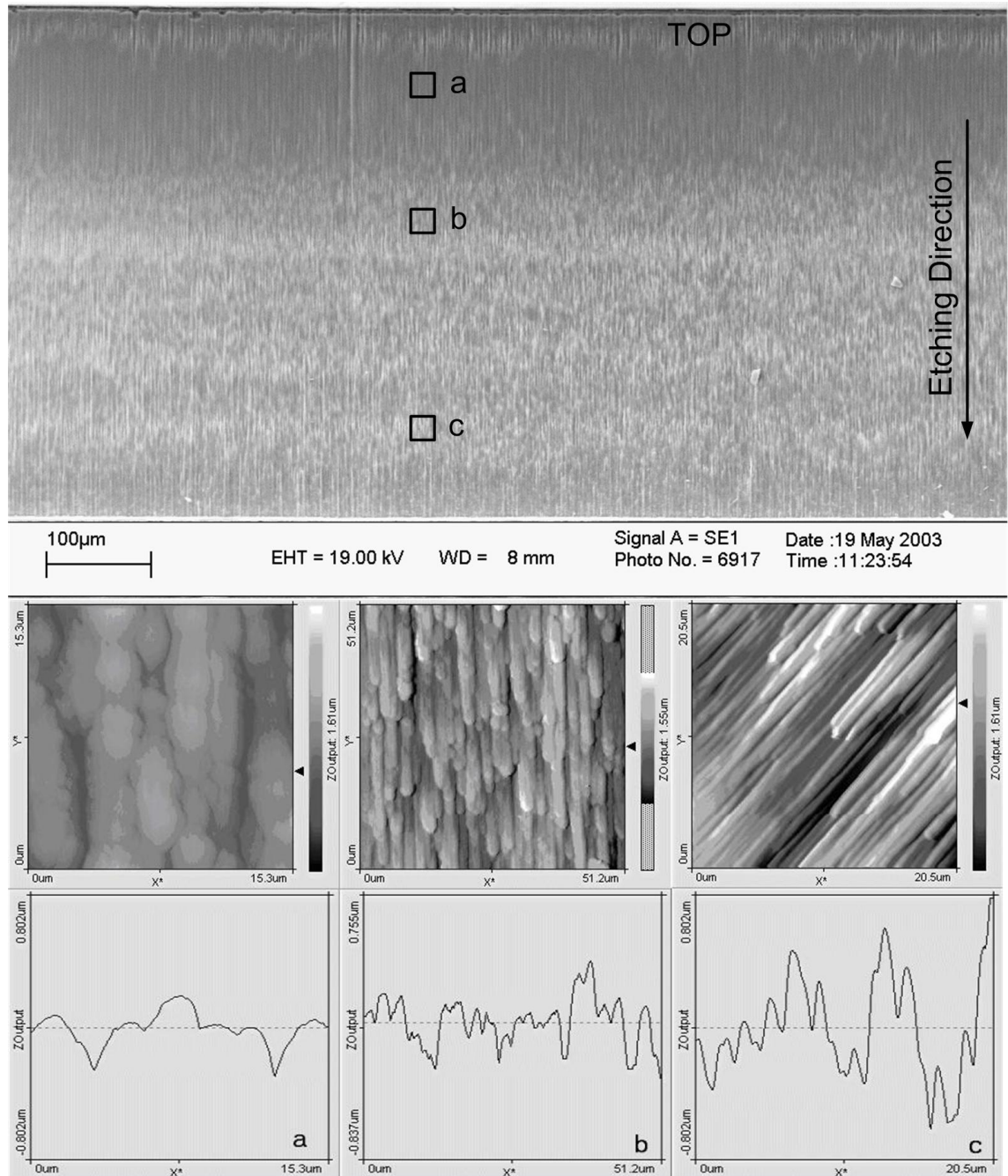


Figure 4.17 SEM image of sidewall quality of 500 μm high sidewall. a,b,c show tapping mode AFM scan of the top (a), middle (b) and bottom (c) of the trench sidewall. The roughness of the sidewall increases from peak-to-peak 0.4 μm at the top of the trench sidewall to 0.7 μm at the middle of the sidewall and 1.4 μm at the bottom of the sidewall.

4.5.7.1 Test structure with variable trench width

Test structures consisting of a series of beams separated by laterally tapered trenches were etched in 525- μm -thick Si (100) wafers (Figure 4.18). The etch pattern was developed in a 15 μm resist mask and the wafer mounted on a Silicon backing wafer using a thermal couplant (CoolGREASE, AI Technologies). The DRIE process parameters are the same as in section 4.6.1.

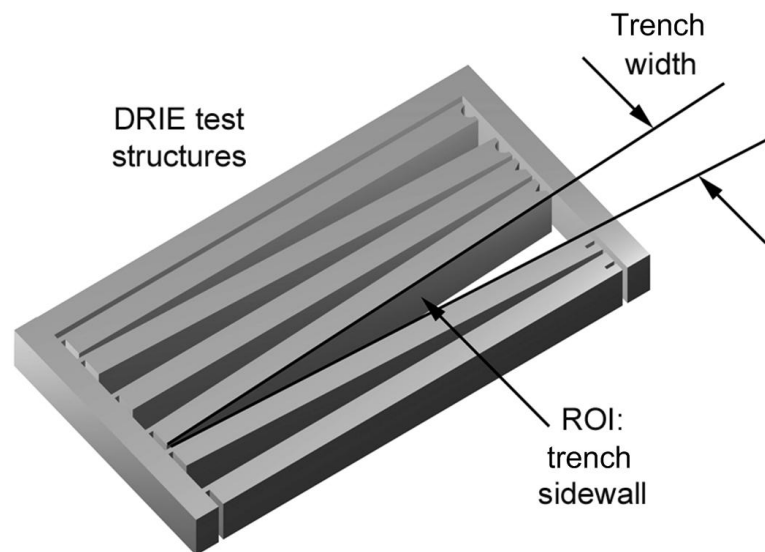


Figure 4.18 Schematic of test structure showing region of interest (ROI). A tapered trench was selected to examine sidewall surface quality with varying channel width. The individual structures (beams) can be separated for ease of measurement.

After through-wafer etching, the beams were cleaved out of the structure to allow for examination using SEM, AFM, and white-light interferometry.

The SEM is a LEO 1450 VP (Leica Electron Optics) operated at 30 kV, incorporating a Energy Dispersive X-ray (EDX) spectrometer (Oxford Instruments) for elemental analysis. A Nanosurf Easyscan AFM was used to image the sidewalls at selected points along the etched beams, particularly the scalloped regions visible within 15 μm of the

top surface. All measurements were done in dynamic mode AFM, with Silicon tips.

Scan areas were typically $50 \times 50 \mu\text{m}$, at scan speeds of 25 - 50 μm per second.

In order to examine the topography quantitatively over large areas, a scanning white-light interferometer (ZYGO Newview 200) was used for non-contact mapping of the etched surface.

4.5.7.2 Effect of trench width on sidewall roughness

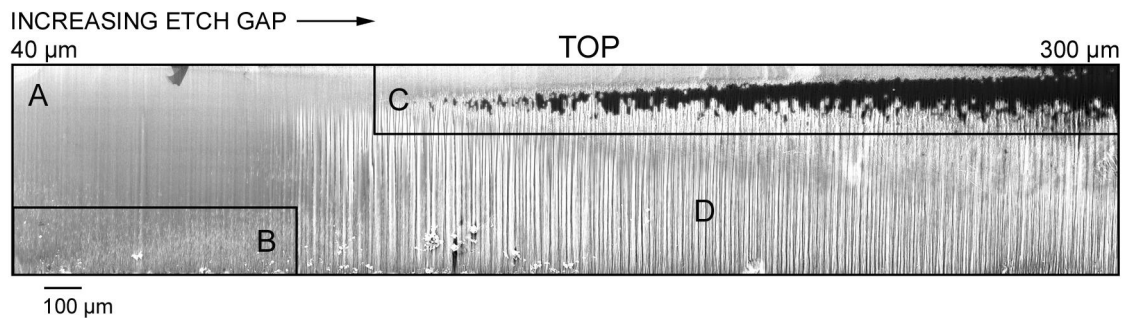


Figure 4.19 Sidewall SEM of through-wafer deep reactive-ion etched beam. Zones of varying sidewall morphology are labelled as: A. Overetched, B. Ion damaged, C. Overpassivated, and D. Striations.

Figure 4.19 shows the sidewall from one side of a low-angle laterally tapering trench etched completely through a 525- μm silicon wafer. The trench width in this image varies from 40 μm to 300 μm , with a taper angle of 6° . Overall, the sidewall is smoothest at the narrower end of the trench, although puncturing of the sidewall with micrometer-sized holes is evident towards the bottom. No scalloping is seen at the narrower end of the trench for the entire depth of the sidewall. As the trench widens to greater than 100 μm , vertical striations increasingly emerge, resulting in a columnar appearance for the lower portion of the sidewall. At wider trench width, areas of complete sidewall breakdown occur from about 50 μm and higher. Optical profilometry using white-light interferometry shows that at the narrower trench width, bowing of the

sidewall occurs (Figure 4.20). A cross section of the sidewall shows that the reentrant surface emerges towards the bottom. In contrast, for wider trenches, the profile is near vertical although the roughness of the sidewall towards the bottom prevents interferometric measurement.

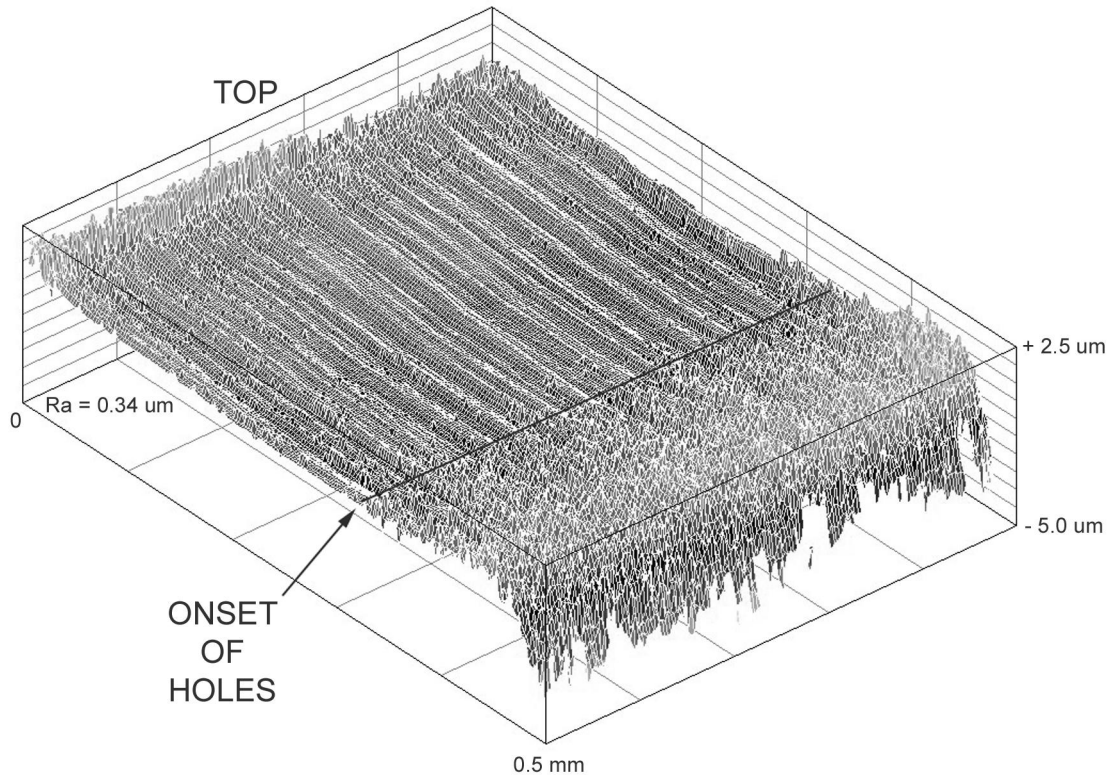


Figure 4.20 Interferometric measurement of sidewall topography near narrow trench end. The ion bombardment causes holes in the sidewall near the trench bottom where the re-entrant surface emerges above the top edge.

For good-quality DRIE, etching and passivation should remain in balance at the sidewalls throughout the etch, although etching should dominate at the trench floor. We will analyze these results in terms of this balance. For the sidewalls, if etching dominates, the sidewall polymer will be removed allowing subsequent Silicon etching with the slow erosion of the initial scalloping. If passivation dominates, the polymer layer will thicken with time, being thickest towards the top of the sidewall.

The loss of scalloping of the sidewalls for the smaller trench width can be seen as a result of over-etching. Bowing often accompanies such over-etching [4.33]. The major problem for this portion of the sidewall is the damage towards the bottom of the sidewall. Combining the SEM images of the distribution of this damage with the optical profilometer data shows that the onset of damage occurs as the reentrant surface emerges from under the top surface of the wafer. Low-angle SEM imaging shows these holes are circular as viewed vertically downwards (Figure 4.21). The probable cause of this damage is therefore low-angle ion-etching of the sidewall.

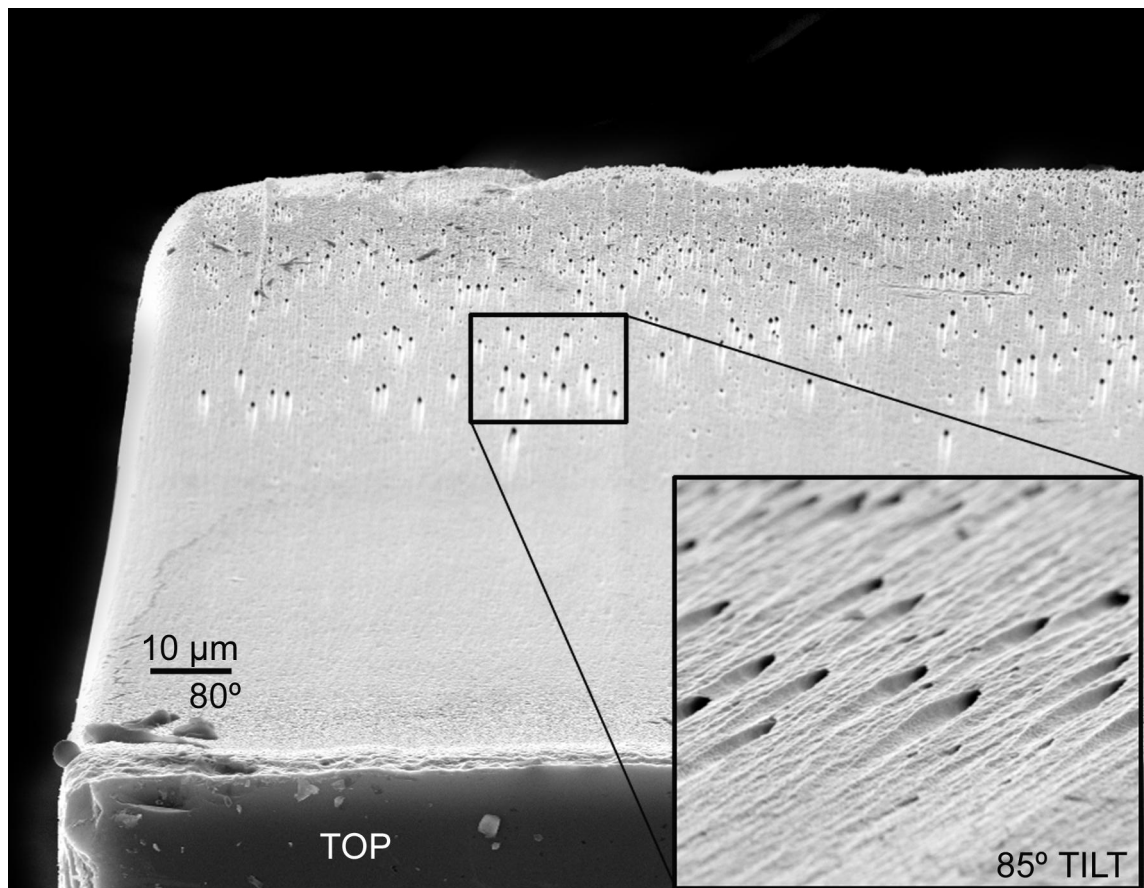


Figure 4.21 SEM picture showing the damage observed at narrow etch-gaps towards the trench bottom caused by ion bombardment (Inset: zoomed, rotated view at a tilt angle of 85°) (courtesy: Werner Karl).

At larger trench widths, passivation dominates. Figure 4.22 shows in detail the buildup of polymer at the top of the sidewall of the through-etched wafer. Energy dispersive X-ray micro-analysis confirmed the fluorine content of this layer, Figure 4.23. The scalloping is evident under the polymer, as is the onset of sidewall breakdown 100 μm from the top. A portion of polymer has detached from the sidewall, showing that the thicker passivation itself evolves into a non-uniform film. Sidewalls below passivation breakdown show the onset of vertical striations.

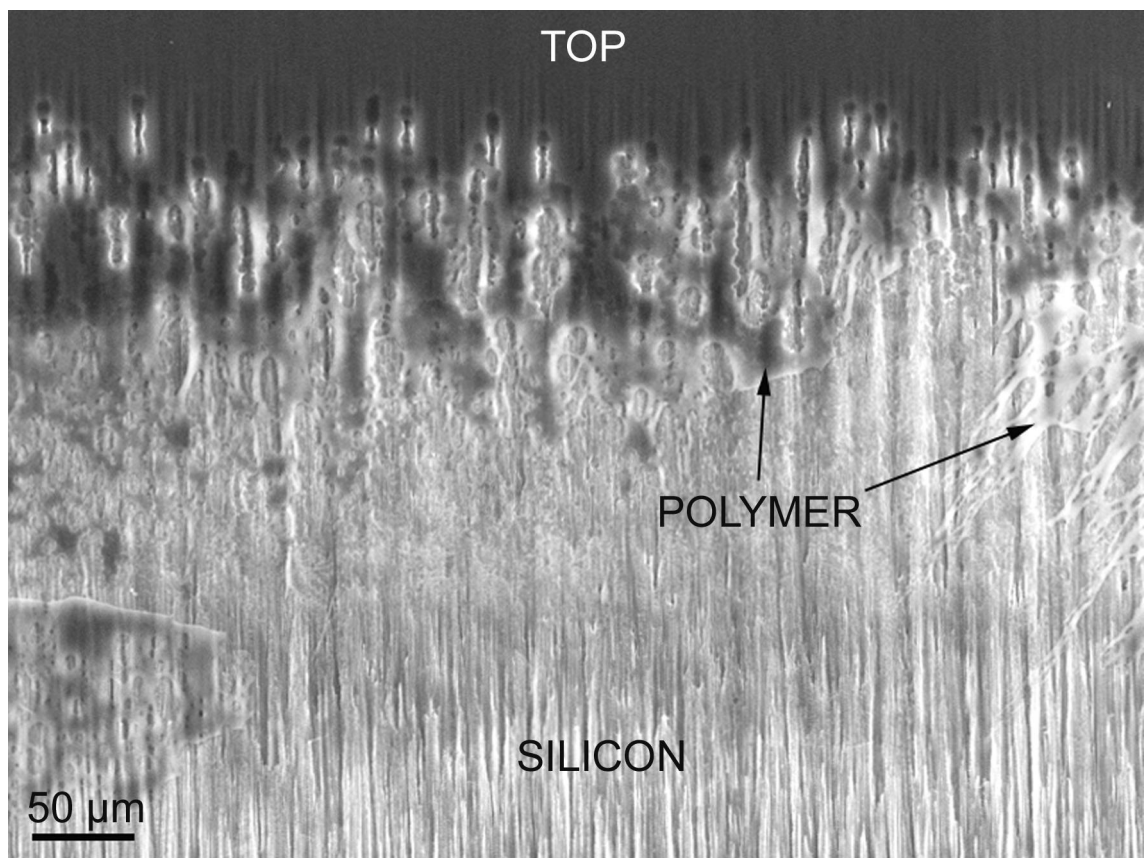


Figure 4.22 Passivation build-up observed at wide etch-gaps leading to striations and therefore to rough sidewalls.

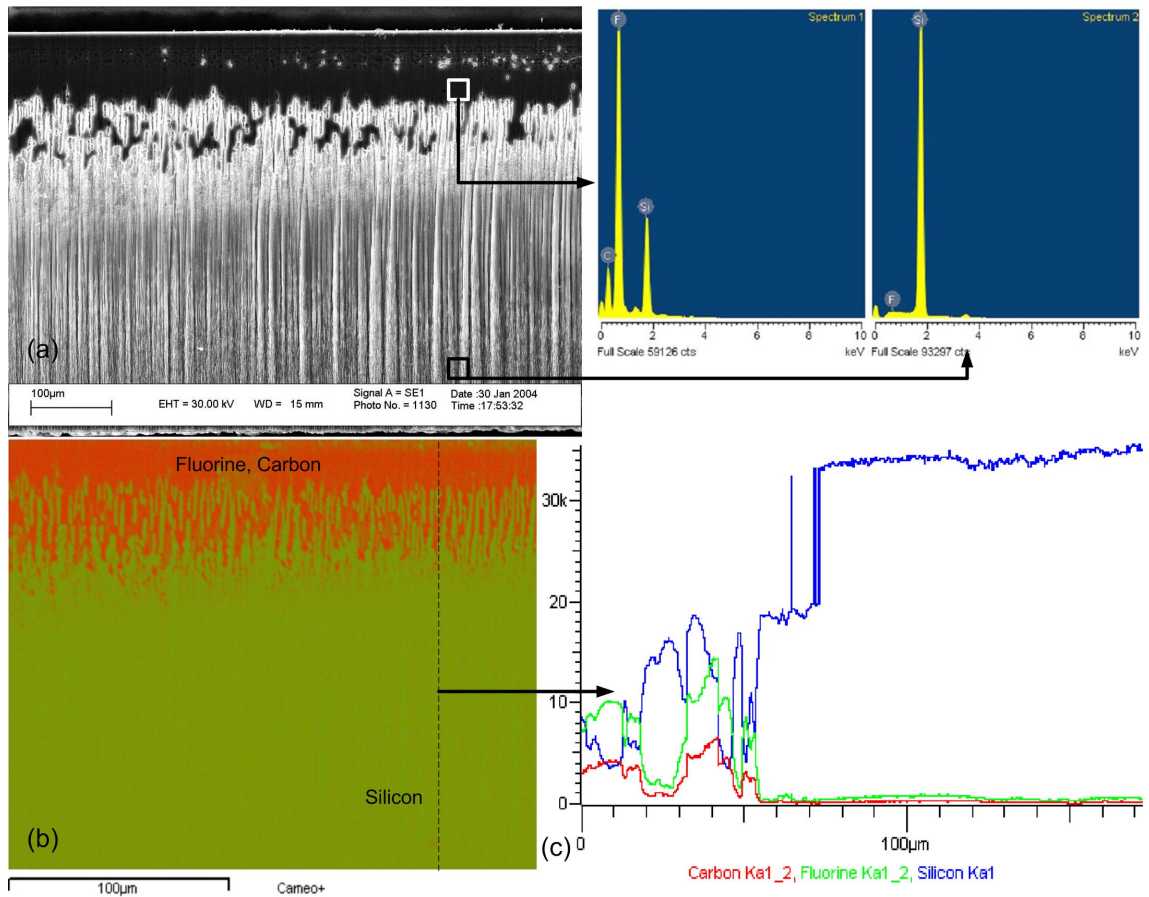


Figure 4.23 EDX analysis of the beam shows fluorine presence in the darker areas which were charging up in the SEM, proving the hypothesis of CF_2 deposition. (a) SEM image of the beam section analysed for Fluorine content showing a higher concentration of carbon and fluorine at the top darker region of SEM image than at the lighter part towards the bottom of the sidewall, (b) Elemental map of the sidewall highlighting (red) the carbon and fluorine dominated regions, and (c) Linescan from the top edge of the beam to the bottom edge showing the concentration of fluorine, carbon and silicon along the etch direction.

Charging in the SEM, evident as pale borders at the polymer edges, is suggestive of a potential cause for polymer-film breakdown in the DRIE: it is known that charging of the polymer film disrupts the ion flux during the etch step [4.34]. Polymer buildup disrupts the charging significantly leading to catastrophic failure of the lateral uniformity of the process. Hence overpassivation rather than overetching results in lower-quality sidewall.

4.5.7.3 Effect of passivation breakdown on sidewall smoothness

The passivation layer consists of single-chain carbon difluoride polymer. As the carbon-carbon and carbon-fluorine bonds are two of the strongest bonds in organic chemistry, considerable energy is required to either grow or shorten the polymer chains. For growth, a combination of ions and fluorine radicals is required to dislodge a fluorine atom from the chain. CF_2 radicals, essentially PTFE monomers, can then add to the chain, with the final addition of a terminating fluorine radical [4.30]. For reduction of the chain, the process is reversed, and the polymer is etched. High-energy vertically-directed ions are present during the etching steps, while during passivation, when the accelerating voltage is zero, lower-energy ions are scattered isotropically from the plasma. The equilibrium position of the growth/etch reaction is determined by the incoming flux of CF_2 radicals and ions.

At the floor of the trench, there will be an incoming flux of CF_2 radicals during the passivation step. Before any silicon etching can take place during the etching step all the polymer deposited on the floor during the passivation step must be removed, again as CF_2 radicals. Redeposition of the polymer from the trench bottom to the sidewalls has been identified as a substantial contribution to sidewall passivation in previous work [4.35-39]. Analyses and experimental data have indicated that the incoming flux of CF_2 radicals as etching products vary at different heights of the trench sidewall [4.39] and there will be a reduced, lower-incident-angle flux of CF_2 radicals towards the top of the sidewalls and less redeposition of polymer with increasing trench depth.

This provides an explanation for etching of the passivation towards the top of the sidewalls at narrower trench widths. The flux of redeposited CF_2 is reduced as the

trench is etched, causing the polymer thickness deposited on the sidewall over an entire cycle to be less than the thickness etched, inevitably leading to eventual overetching of the sidewall. Overpassivation of the sidewalls at wider channel widths can be explained by the increased flux of CF_2 radicals from the broader floor of the trench as more material is etched from the floors of the wider trench and wider range of deposition angle is available for the sputtered CF_2 radicals. The passivation in this case grows more than it is etched during each cycle, causing build-up of passivation beyond a critical level for uniform coverage.

Although redeposition of etched passivation provides an explanation consistent with observations, other effects could contribute. During the passivation step, the flux of activating ions at sidewalls might be expected to drop with trench depth. However, the flux at the top of the sidewalls would be the same for all trench widths, whereas a transition from overetching to overpassivation is observed for wider trenches. Therefore ion-flux variations during the DRIE cycles are unlikely to provide a complete explanation.

4.5.7.4 Sidewall smoothness

The sidewall quality of through-wafer DRIE structures is very dependent on the aspect ratio of the etched channels. Below about 100 μm etch width, sidewalls tend to be smooth, albeit overetched, with some bowing leading to ion damage towards the bottom of the sidewalls. For wider channels, buildup of passivation leads to an eventual breakdown in polymer coverage, causing vertical striations and a very rough surface.

This behaviour is analysed as a transition to overpassivation for increased channel width, and a transition to overetching with etch depth for the narrower channels.

Redeposition of passivation from the trench floor during the etch step is suggested as an explanation in both these regimes.

As the aspect ratio of the trenches changes during etching, no single set of process parameters can be expected to optimize the balance between sidewall passivation and etch for a through-wafer etch. Ramping of parameters may be one route to improved sidewall quality.

4.5.8 Etch profile evolution

In DRIE, the profile of the etched structure is controlled by successively varying the etching and passivation to achieve highly anisotropic features. As shown in Figure 4.24 the etch trench can be either sloping inwards (narrower at bottom than at top), which is characterized as negative profile, or sloping outwards (positive profile), or it can have a bow (the middle section is etched more laterally than the top or bottom).

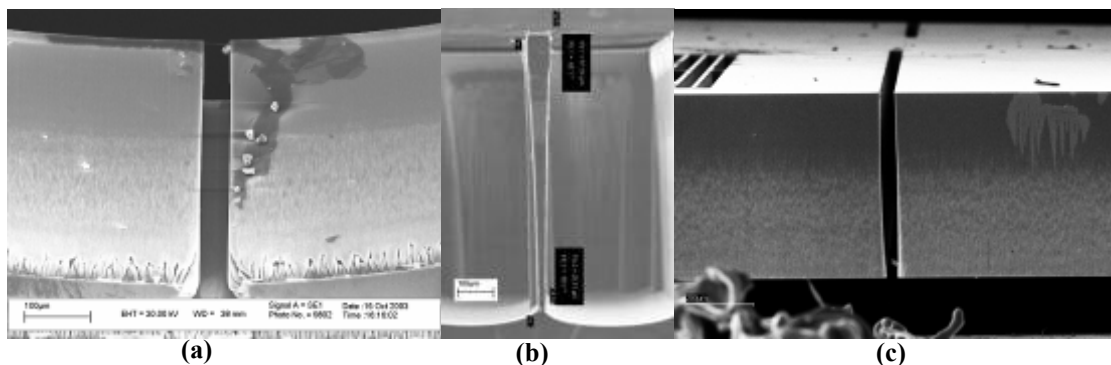


Figure 4.24 Profile shape of etched trench for various processing conditions in DRIE. (a) Negative profile, (b) Positive profile, (c) Bowed profile.

An ability to understand, measure and tailor profile shapes is extremely important from a mechanical standpoint as well as when the structure is used for devices with a strict profile shape requirement. For example, a deviation from the ideal vertical profile leads to a variation in the natural frequency of the lateral suspension (see section 5.3).

The profile evolving with time is dependent on the charge accumulation, ion energy distribution and etchant/passivant ratio in various parts of the trench, which are influenced by the incumbent etching conditions.

Channel profile and bowing has been discussed in Chen et al. [4.26] and Ayon et al. [4.40] and ways to control anisotropy and profile have been discussed. Singh et al. [4.41] presents a model for profile simulation in reactive ion etching. Previous works [4.9, 42] have mostly focused on how to achieve high anisotropy and control profile and reduce bowing, but as we present here, bowing can be a boon for some applications, and a better control and understanding of its mechanical significance and understanding of the process which causes it, will help designers use various profile shapes and bowing to their advantage. The effect of process conditions on DRIE etch shape is discussed.

4.5.8.1 Reason for etch profile

The relative density of etching and passivating species in each cycle decides the profile of the trench sidewalls. Etching and passivating time ratio, process cycle time, chamber pressure, SF₆ and C₄F₈ gas flow rate, coil power, and platen power affects the density of etching and passivating species in each cycle. The cause for the various profile shapes are:

Negative/Reentrant profile: A longer passivate cycle with respect to etching cycle results in non-complete removal of passivation from the bottom of the trench resulting in narrowing of the trench, Figure 4.24(a). This leads to a thicker beam cross section with depth of the etch. Chen et al. [4.26] mentions a shorter etch cycle leading to

insufficient removal of passivating film, producing significant surface roughness and other deleterious artifacts like micromasking and grass formation.

Positive profile: When the etch cycle is longer than the passivation cycle, the passivation is removed from the sidewall of the trench (towards the bottom of the trench) leading to a wider trench bottom as the etch progresses, Figure 4.24(b).

Bowing: Removal of passivation coating from the trench sidewall faster than it is formed causes and aggravates bowing, Figure 4.24(c). Ishihara [4.9], Sun [4.42] show bowing to be caused by charging of SiO₂ mask or a buried layer. In our HAR etching, we have seen bowing when using photoresist as a mask and the bowing is quite symmetric with a thin neck and wider top and bottom. Having a SiO₂ mask helps preserve the pattern size as photoresist is prone to edge erosion which changes the effective masked area to the etching species. Lii [4.37] investigated the bowing effect in a silicon trench under plasma etching and proposes two reasons for the undercutting of the sidewall: (a) etching by divergent ions scattered by ion-molecule collisions in the sheath, and (b) another mechanism involving the scattering of ions from the edge of the mask. Lii also shows that redeposition of passivation polymer during etching cycle plays an important role in profile evolution.

SF₆ plasma consists of positive and negatively charged ions, radicals and atoms (equation 4.1). The etching mechanisms are considered to be independent of each other but Lii [4.37] demonstrates an amplification in reaction between ions and reactive neutral radicals as the trench depth increases. The concentration of radicals is at least two orders of magnitude higher than ions and the radical flux ($\sim 10^{19} \text{ cm}^{-2}\text{s}^{-1}$) is also

much higher than the ion flux ($\sim 10^{15} \text{ cm}^{-2} \text{ s}^{-1}$)[4.5]. This could have a very prominent effect on the bowing of the sidewall as we notice an increase in the isotropic etch with increased etch depth. At about the middle of the wafer thickness the etching starts lagging behind the passivation and the profile starts turning negative or reentrant.

Chang et al. [4.43] discuss surface potential buildup due to flux imbalance of isotropic electrons and anisotropic ions leading to lateral etching of the sidewall (Figure 4.25).

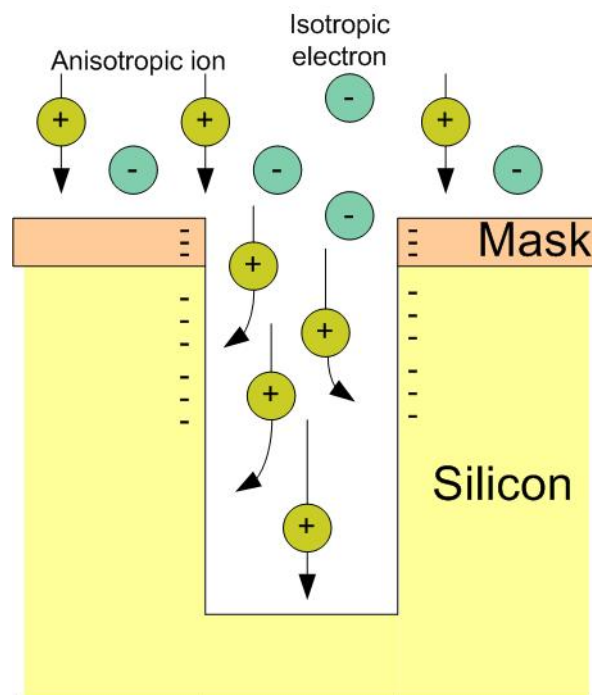


Figure 4.25 Surface potential build-up due to flux imbalance of isotropic electrons and anisotropic ions leading to lateral etching of the trench sidewalls.

Due to the isotropic nature of the electron and negative ions in the plasma, the top surface of the sidewall has more negative charge which deflects the positive ions laterally towards the sidewall causing lateral etching.

Most of the analysis of bowing in the literature has been for shallow trenches and SOI, so there is not a coherent theory that provides a complete explanation for the top edge

becoming positive, then a maximum undercut causing necking and then the trench developing a negative slope resulting in a narrower bottom.

4.5.8.2 Effect of process parameters on etch profile

APC angle or Chamber pressure: Chamber pressure has a strong effect on the etch profile. With higher APC angle, the trench gets narrower with depth; decreasing the APC angle improves the profile which converges towards vertical sidewalls, and reducing the pressure further leads to a wider trench bottom. At the same APC angle, larger areas etch to a wider floor than top, which could be due to an effective increase in etchant density at the floor of a large trench than a smaller trench at the same pressure.

Etch/Passivate ratio: Increasing the etch cycle compared to the passivation cycle leads to an increase in the isotropic nature of the etch which leads to a higher bowing of the profile. It also results in a wider trench bottom than a similar etch with lower etch/passivation ratio.

Platen Power: Platen power defines the energy of the ions, higher platen power accelerates the ions faster vertically leading to better profile control as a significant portion of bowing is attributed to the non-verticality of ions. The side-effect of high power ions is poor surface quality of the sidewalls.

4.5.8.3 Bowing of profile in deep etch

For tall structures such as features created by through-wafer etching, the process parameters were selected to avoid grass formation in the etch trench, which means the process is etch dominant. During the run the process is etch dominant as is evident from etching of larger trenches which tend to widen out towards the bottom.

Towards the start of the process, the trenches tend to have a wider bottom than top due to the process being etch dominant but after some depth the passivation polymer removed from the trench bottom is not completely removed from the trench which leads to it depositing back on the sidewall. As the trench etch depth increases more redeposition occurs on the sidewall thus shadowing the corner of the trench bottom from etch, this ultimately leads to a narrowing of the trench.

As the trench etch depth increases the etchant density starts reducing, and ultimately the overall process for that trench may turn from etch dominant to passivation dominated, which will also cause narrowing of the trench as the etch depth becomes large.

4.5.8.4 Advantages of bowed profile

A bowed profile can be advantageous where a large surface area is needed on the top of the feature for traces to run but the effect of bowing needs to be compensated to achieve the mechanical performance target (see section 5.3). Due to bowing the effective thickness of the beam will be much lower than for the ideal rectangular profile case. In the case of lateral suspension, the profile bowing is incorporated in the design to create springs with lower spring stiffness but larger top surface width. The larger top surface width provides more leeway for the metal traces to be thicker and further apart thus reducing processing complexity arising from a smaller feature size.

4.5.9 Notching

In through-wafer silicon etching using high-density low-pressure inductively coupled plasma, a notching (or footing) effect occurs towards the end of the etch at the bottom silicon-insulator interface. Such an interface will be present as the etched silicon wafer

will have either an oxide layer to avoid break through of the plasma or the wafer will be bonded to a handle wafer using either photoresist or other adhesives. Notching damage at the foot of micro-structures can lead to significant degradation of their mechanical performance and is unacceptable particularly when an optically flat surface is needed. A method to avoid notching, by eliminating charge buildup, through the use of a backside thin metal backside coating is developed.

4.5.9.1 Theoretical background on notching

In HDLP (high-density low-pressure) plasma processes like DRIE, surface charging is always a concern towards the end of a through-wafer etch at the bottom of the semiconductor-insulator interface [4.44, 45]. Without any modification to the process, surface charging can produce a final lateral undercut at this interface, Figure 4.26.

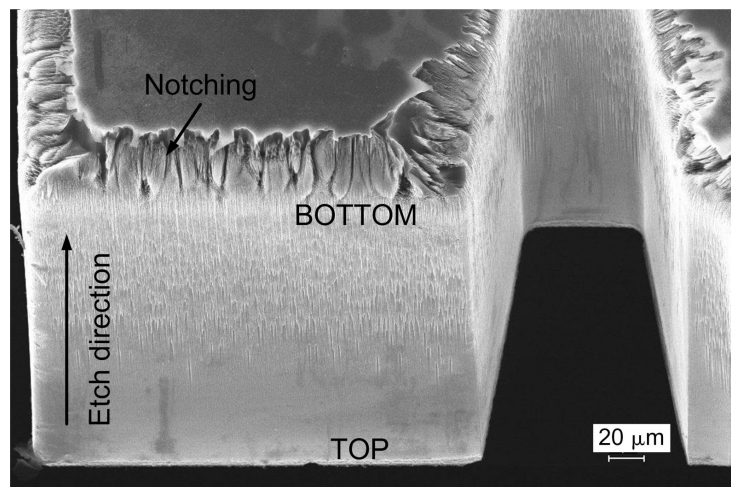


Figure 4.26 Notching damage at the bottom of a through-wafer etched feature. The wafer was bonded to a handle wafer using photoresist.

Due to the directional nature of the positive ions, a substantial proportion will travel to the foot of the trench where they positively charge the insulator layer. In contrast, electrons, due to their isotropic directionality, impinge on the top surface of the wafer but cannot get to the bottom of a high aspect ratio trench to neutralize any positive

charge build-up in the insulator layer. The positively charged insulator surface then deflects the ions towards the sidewall causing a lateral etch (Figure 4.27).

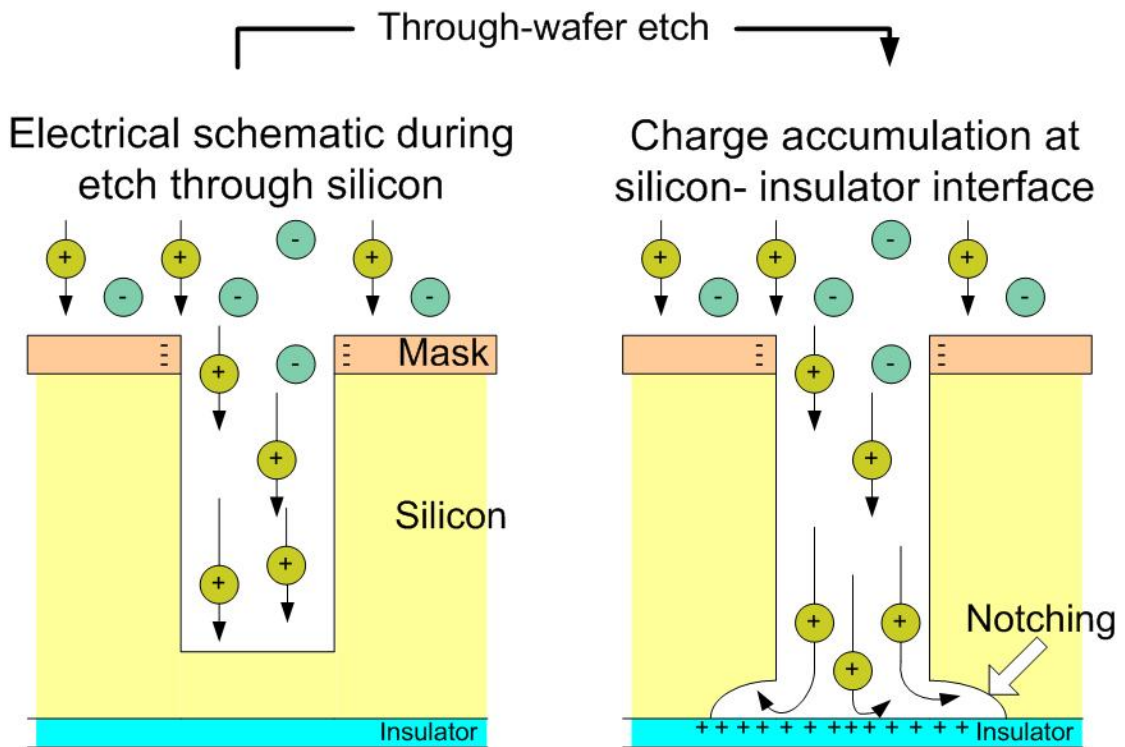


Figure 4.27 Charge distribution in deep trench and positive charge accumulation at Silicon-insulator interface resulting in lateral undercutting at the trench foot (notching).

4.5.9.2 Avoiding notching

Plasma tools and process conditions have been modified in the past to alleviate and remove notching. Previous works have focused on ways to engineer the ion distribution in order to reduce the charge accumulation or increase the ion directionality. Some of the mechanisms proposed are low temperature etching [4.2], increasing bias voltage to reduce ion deflection, decreasing chamber pressure [4.5] to improve ion directionality, increasing the electron irradiance angle to decrease the potential buildup [4.46] and pulsed plasma etching [4.47]. Most of these mechanisms have been demonstrated to be effective for shallow etching. Except for pulsed plasma etching, these techniques are not

directly applicable to etching hundreds of micrometres of silicon. All these techniques generally reduce the notching, but cannot completely eliminate it.

Surface Technology Systems (STS) has adapted the pulsed plasma etching for its time-multiplexed inductively coupled plasma etcher to reduce notching in SOI etching.

Running the plasma at low frequency generates more low energy low directionality ions which neutralize the charge build-up at the top of the trench. Reducing the negative potential at the top of the trench facilitates more electrons into the trench alleviating the positive charge build-up at the bottom of the trench. This technique has been successfully demonstrated to reduce notching in SOI etches [4.44]. The major limitation is the need for an endpoint detection to stop the normal etch mode and switch to the pulsed plasma etching mode.

Changing the ion angular distribution also affects the etch rate, anisotropy, etch profile evolution and mask selectivity. Methods employing ion distribution engineering are dependent on the aspect ratio (RIE lag), pattern factor (silicon exposure), and plasma uniformity. An ideal method for eliminating notching would be design independent, so that no further process modifications are required.

Hence an alternative that has been explored is the inclusion of a conductive layer which can form a path to neutralize the positive ions at the end of the etch. Fransilla et al [4.48], Rasmussen et al [4.49] have used a metal coating on the backside to work both as an etch stop and to eliminate notching. Chabloz et al. [4.50] and Kim and Kim [4.51] demonstrated using a metal layer on a glass wafer anodically bonded to the backside of the device wafer to reduce notching in silicon structures.

We examine the use of metal coating on wafer backside as a method to avoid notching in through-wafer silicon etching [4.52]. This is achieved by changing the process flow so that the root cause of charging at the silicon-insulator interface is eliminated. By creating a silicon-conductor interface the charge is allowed to dissipate into a metal layer. The silicon-conductor interface is realised by deposition of a thin metal layer on the wafer backside. The etch rate and etch characteristics are not affected, as the process parameters remain unchanged and the etching is done while operating the plasma at high frequency (HF).

4.5.9.3 Experimental Setup

Test structures to quantify notching were fabricated by through-wafer DRIE etching silicon wafers. The process flow schematic is shown in Figure 4.28. The silicon wafers are 525 μm thick. The silicon wafer was coated with a thin backside metal layer using either an evaporator or sputterer. The front side of the wafers was coated with a 9 μm thick AZ 9260 photoresist mask. The wafer was etched for 3 hours and then attached to a silicon handle wafer using thin Shipley S-1813 resist. Subsequently it was etched until the trenches were visibly clear. The wafer was then overetched for an additional 15 minutes to assure a complete through-wafer etch across the entire wafer.

To investigate the mode of charge dissipation which eliminates notching at the bottom of through-wafer etched trenches, various experiments were designed.

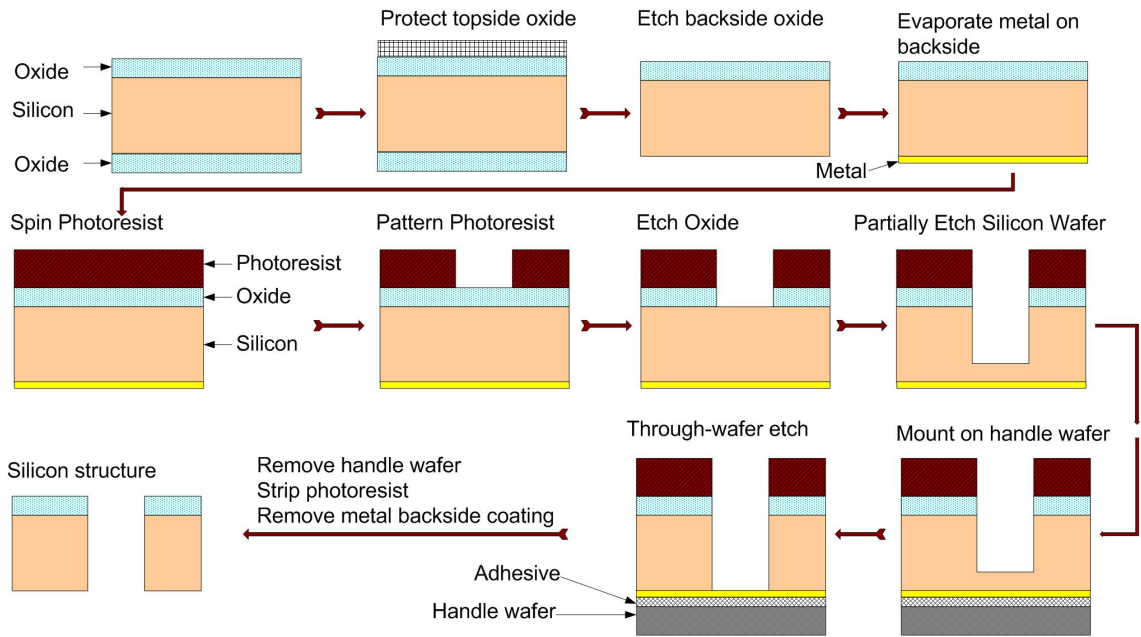


Figure 4.28 Process flow schematic for through-wafer etching using a metal backside coating to eliminate notching.

4.5.9.4 Metal coating directly on etched wafer backside

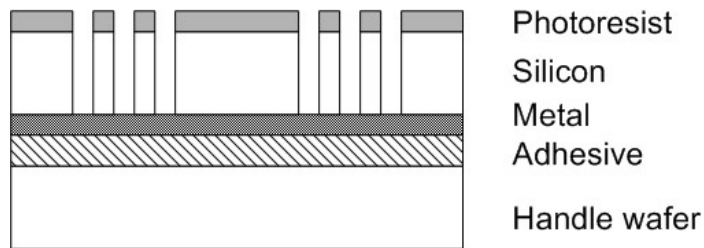


Figure 4.29 Schematic of etch setup with metal coating directly on the wafer backside and then bonded to a handle wafer.

Notching was compared for two silicon wafers etched using identical DRIE etch parameters. One wafer had no backside metal layer; the other wafer had an Aluminum (Al) backside metal layer as shown in Figure 4.29. The silicon wafers were then bonded to a handle wafer using photoresist. The wafer without any metal coating had extensive notching as seen in Figure 4.30a whereas the wafer with Aluminium coating on the backside showed no signs of notching (Figure 4.30b) after the etch. This experiment

demonstrated that by using the metal directly on device wafer backside one can completely eliminate the notching effect.

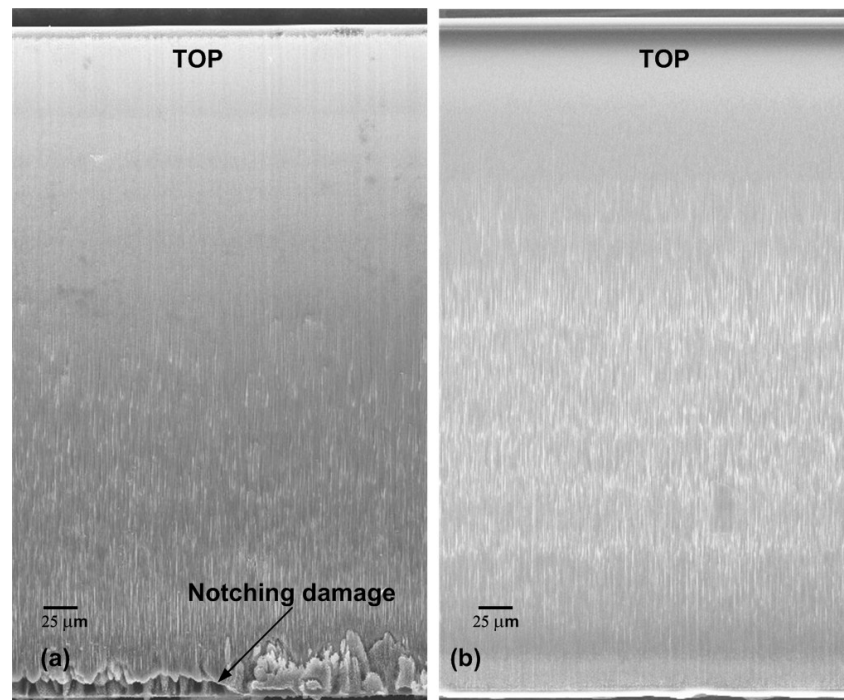


Figure 4.30 (a) Notching damage observed at the foot of a through-wafer etched structure; the wafer was bonded to a handle wafer using thin photoresist. (b) The same structure on a wafer with a thin metal coating on the backside; no damage at the foot of the sidewall is visible.

Similar notching damage was encountered for silicon wafers without backside metal layers bonded to the handle wafer using thermally conductive pastes such as cool-grease. Both photoresist and cool-grease are electrically insulating. It was observed that for a thermally insulating adhesive (like photoresist), the damage was more extensive.

Trenches with similar dimensions were etched in a silicon wafer with and without backside metal coating. The wafer without metal coating showed extensive lateral etching at the etch foot, Figure 4.31a. The same trench shows a much cleaner surface towards the bottom of the wafer, if a thin aluminium backside layer is used, Figure 4.31b.

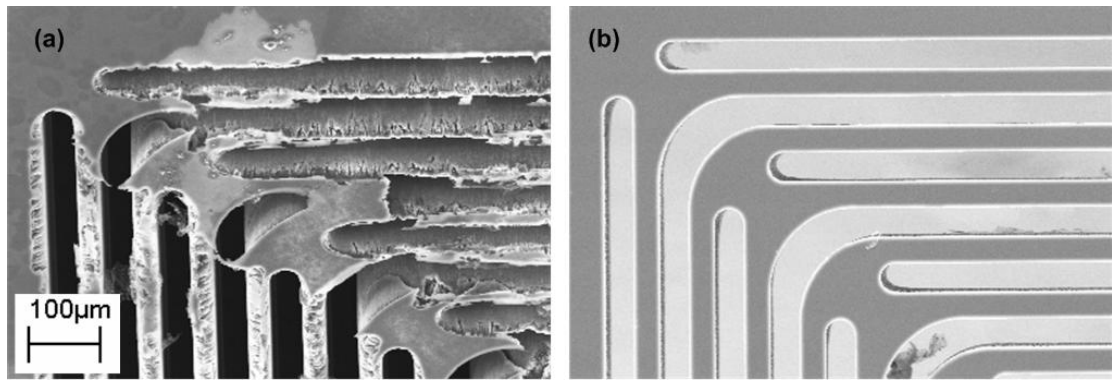


Figure 4.31 Backside of an etched wafer. (a) Etched trenches with no backside metal coating, showing extensive notching. (b) Etched trenches with backside metal coating, showing no visible notching.

The absence of an insulator interface eliminates any charge accumulation at the foot of the trench. During overetching of the structures which is necessary to compensate for etch lag, the positive charges of the reactive ions impinging on the metal layer are neutralized. This is evident from no observable silicon damage due to a deviation of the ion trajectory towards the sidewall, Figure 4.32.

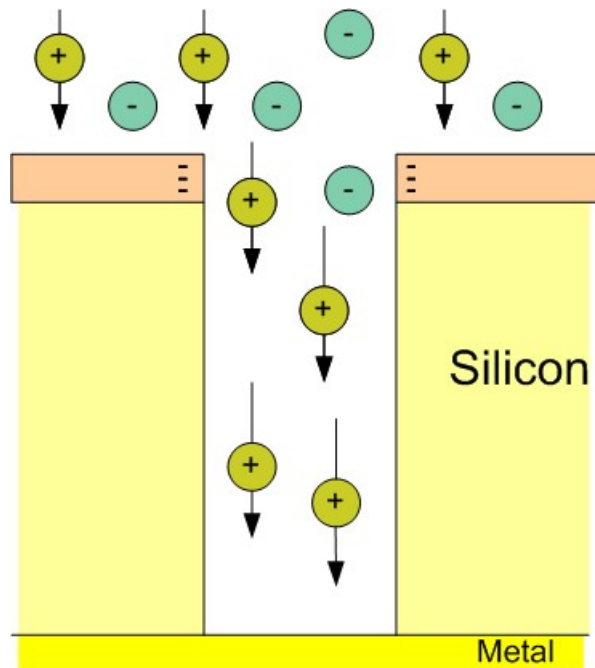


Figure 4.32 Charge dissipation at metal surface in a silicon trench with a metal coating on the wafer backside.

4.5.9.5 Metal layer on handle wafer

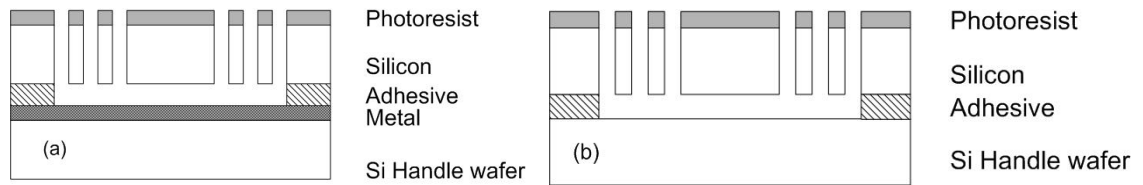


Figure 4.33 (a) Schematic of test setup with metal coated handle wafer glued to the device wafer at the outside edges, (b) Schematic of the test setup with silicon handle wafer bonded to the device wafer at the outside edge using photoresist.

To investigate whether the metal layer needs to be connected to the device wafer to avoid notching, the handle wafer was coated with metal and the device wafer bonded to it using photoresist patterned in a periphery-ring (Figure 4.33). Once the etch proceeds through the wafer thickness the handle wafer's metal layer is exposed.

We observed no notching at the bottom of the structures. This leads us to believe that charges from any impinging ions dissipated through the metal layer into the handle wafer. In another setup the device wafer was attached to a silicon handle wafer with photoresist patterned in a periphery-ring. Notching was eliminated in this case as well. This method would be suitable for cases where metal exposure to plasma is prohibited.

4.5.9.6 Floating metal layer

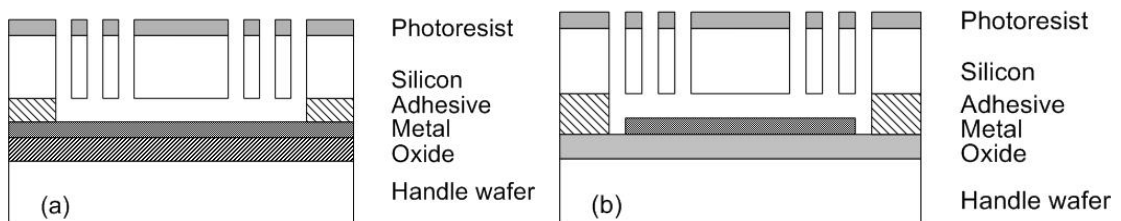


Figure 4.34 Schematic of experimental setup, (a) metal layer connected to the plasma at edges, (b) metal layer completely isolated.

To investigate whether a metal layer not connected to either the device or handle silicon wafer is sufficient to eliminate notching, a metal coated oxidized silicon handle wafer is bonded to the device wafer using an adhesive (Figure 4.34).

When the metal layer was extending all the way to the wafer edge and exposed to some plasma at the edges, we did not see any significant notching but there was some evidence of isotropic etching of the bottom surface of the structures.

To clarify whether connectivity of the metal to plasma is sufficient to reduce notching we patterned the metal layer on the handle in a circle smaller than the wafer so it is completely inscribed inside the handle wafer. In this case we saw notching damage of the structures (Figure 4.35). This leads us to believe that connectivity of metal layer to plasma/silicon wafer is important.

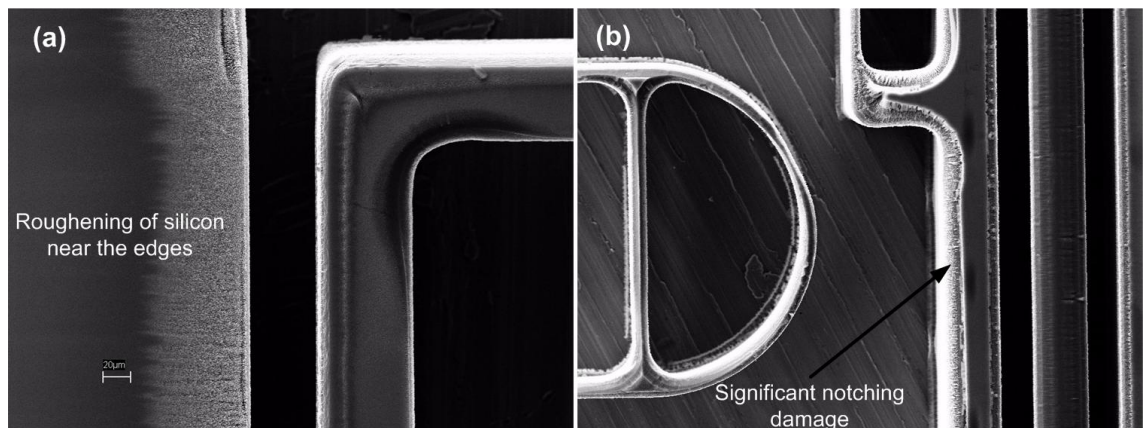


Figure 4.35 (a) Damage due to partially floating metal layer, (b) Notching damage due to completely floating metal layer.

4.5.9.7 Electroplated metal for dry release

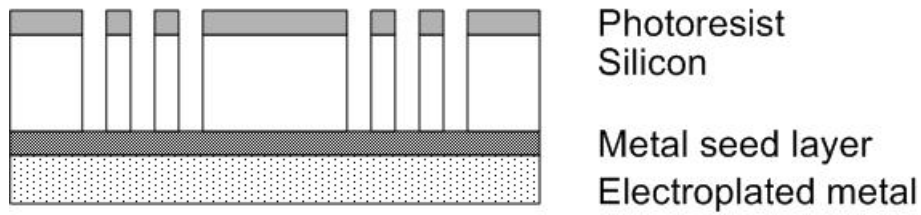


Figure 4.36 Schematic of test setup with electroplated metal on device wafer backside.

To eliminate the need for a handle wafer, we electroplated nickel on a Cr/Au seed layer to 5 μm thickness (Figure 4.36). This was sufficient to act as a mechanically strong layer to constraint any of the structures released on completion of etch. The method also avoids any possible thermal sinking problem caused by using a thermally-insulating adhesive. The process is cleaner and more economical as it avoids the wastage of another silicon wafer (handle wafer).

Additionally we can dry release the structures by peeling off the metal layer as shown in Figure 4.37.

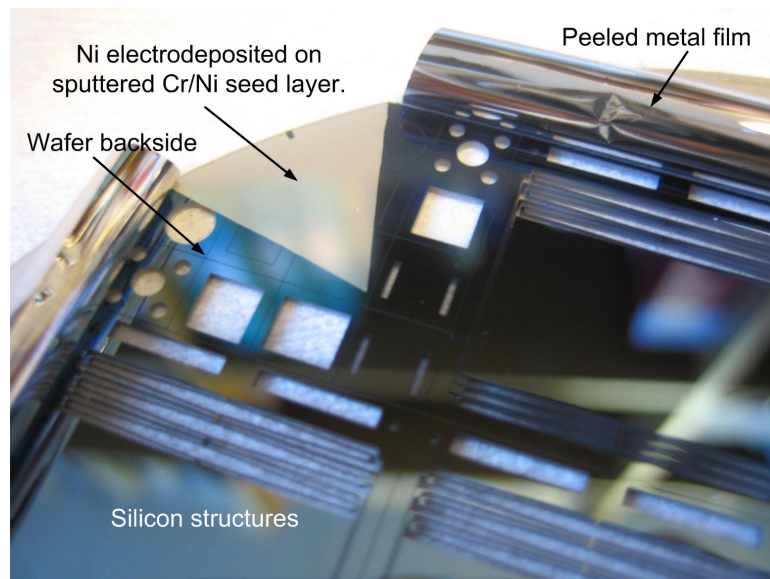


Figure 4.37 Optical image of dry release process by peeling the metal layer from the wafer backside.

4.5.9.8 Other metals besides Aluminium

Various backside metals like Cr [4.50], Ti/Au [4.51], Cr/Cu, Cr/Ni, Cr/Au, Al have been tested, with identical results. Aluminium has the advantage of being easy to remove using any alkaline solution such as photoresist developer. Unless used as a mechanical layer to constraint island geometries falling out upon completion of etch, it is not critical for the metal layer to adhere well to the backside of the device wafer.

4.5.9.9 Pulsed plasma mode for notching reduction

Pulsed plasma mode was investigated to quantify the effect of low-frequency (LF) etching conditions on the profile shape of the structures.

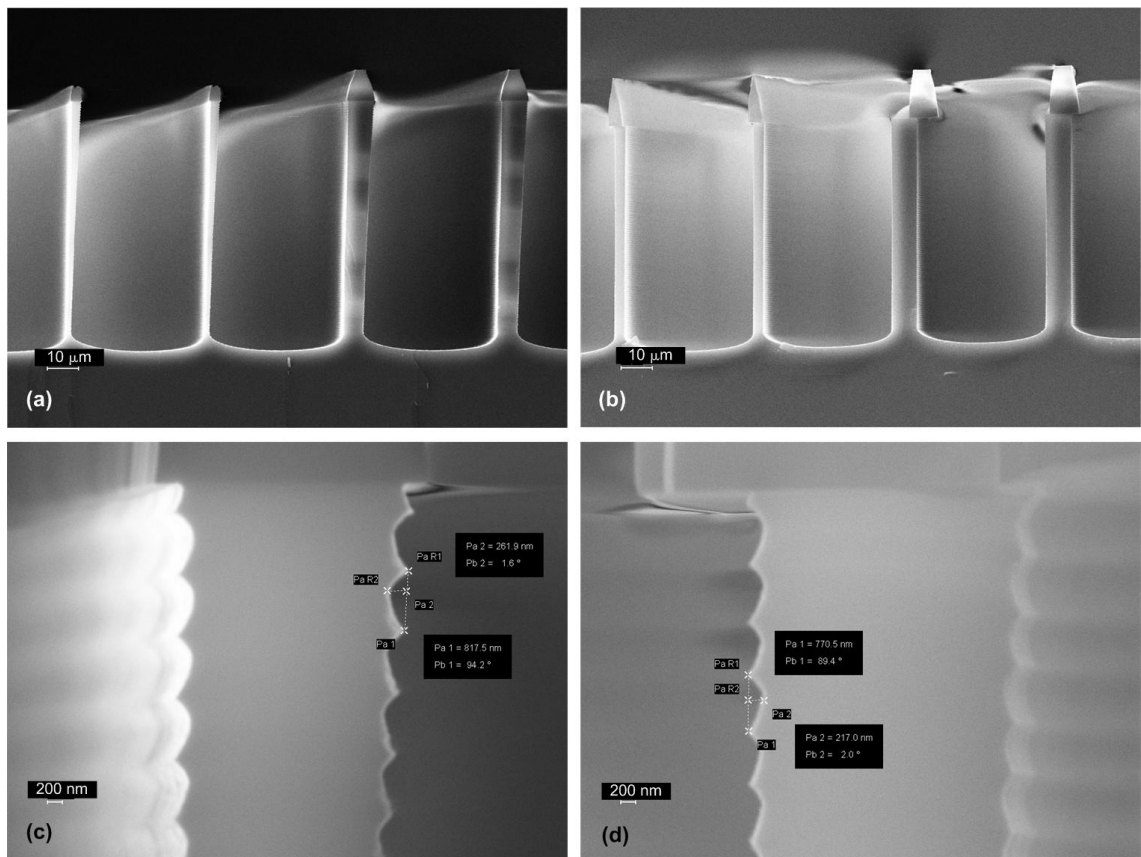


Figure 4.38 SEM image of trench profile etched for 30 minutes using (a) LF plasma mode showing thinning down of the structures towards the bottom as compared to, (b) HF plasma mode which maintains profile anisotropy better and (c) scallop size for LF mode is 260 nm × 818 nm compared to, (d) HF mode scalloping which is 217 nm × 770 nm.

We used the process parameters optimized for through-wafer etching in HF mode and switched the process to LF mode to investigate the effect of LF on the etching characteristics. Even though the etch rate was identical for both LF and HF etching at 3 $\mu\text{m}/\text{min}$, the profile shape of the etched trench at LF is markedly diverging compared to HF plasma (Figure 4.38a,b). This is due to an increase in isotropic etching in each etch cycle as seen by the increase in the size of the scalloping during LF compared to HF (Figure 4.38c,d). So LF mode etching is not a quick solution to reducing notching and requires an overall optimization of process parameters to get good results.

4.5.9.10 Thermal sinking problem

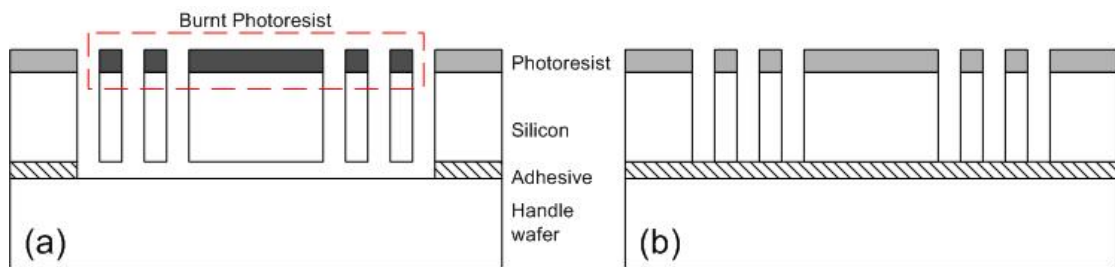


Figure 4.39 Schematic of experimental setup to investigate effect of good thermal contact between the device and handle wafer, (a) Wafer bonded on the periphery such that when the structures are etched through-wafer, the structures are thermally isolated from the handle wafer, and (b) the device wafer is completely bonded to the handle wafer allowing the isolated structures thermal connectivity to the handle wafer.

To achieve repeatable etch conditions a stable control of the wafer temperature is most important. Photoresist and wax have low thermal conductance, so other temporary bonding agents such as cool-grease [4.53] with high thermal conductivity were investigated for attaching the handle wafer. In another experiment, the backside metal coating itself was electroplated. The plated metal was chosen to be a few micrometres thick in order to create a mechanically stable layer, reducing the need for a separate

handle wafer. A qualitative comparison of the various examined conditions is presented in Table 4.2.

In cases where the complete wafer is bonded to the handle wafer using a thin layer of photoresist, the thermal sinking seems to be sufficient to achieve repeatable etching. For cases where the device wafer was bonded to the handle by a thin photoresist periphery-ring, we saw photoresist burn (Figure 4.40) which is indicative of bad thermal path between the device and chuck. Improper thermal sinking of the wafer causes the temperature of the wafer to rise to almost 150 °C within 5 minutes causing the resist to be less resilient to the plasma leading to fast degradation appearing as a burnt (grey) layer. Once the resist is burnt, the plasma attacks the silicon.



Figure 4.40 (a) Optical image of burnt photoresist due to thermal sinking problem – the reflective surface shows normal photoresist, (b) photoresist is burnt in this case on the proof-mass which has bad thermal connectivity through the long springs – the grey non-reflective surface is burnt resist.

4.5.9.11 Analysis of methods for avoiding notching

The effect of notching in through-wafer silicon DRIE has been discussed. Charging of an insulator layer is believed to be the root cause for a lateral undercut observed at the silicon-insulator interface. Coating the backside of the silicon wafer with a thin metal layer completely eliminates this notching effect. In the presented case an evaporated aluminium layer was successfully used. Ultimately the choice of metal to prevent notching will depend on its compatibility with an existing process flow.

Compared to other previously presented techniques used to reduce notching, which are mainly based on tweaking the actual DRIE etch parameters, the method presented here is independent of the chosen DRIE settings. This is a very important difference, as it allows the uncompromised optimization of the DRIE process avoiding the danger of introducing notching. With the backside metal layer the notching is completely eliminated and is no longer dependent on the aspect ratio or etch pattern.

4.6 Process Engineering

Table 4.3 presents the trends in silicon etch rate, sidewall smoothness, trench profile control, across wafer uniformity, grassing and etch lag for the various parameters of the DRIE process. The effect of increase or decrease in the level of the process parameter is assumed to be from an etchant rich environment. For passivation dominant conditions the effects of some of the parameters would be very different. A case in point is the SF₆:C₄F₈ flow rates, for etchant dominant conditions, the sidewall smoothness deteriorates if the etchant concentrations are increased by increasing the gas flow ratio, but if it is a passivation dominant environment, an increase in the etchant condition will

lessen the chances of a passivation deposition and breakdown on the sidewall thus improving the sidewall quality.

Table 4.3 Effect of process parameters on the etch characteristics.

Etch effect → Parameter ↓	Change	Silicon etch rate	Sidewall quality	Profile shape	Etch uniformity	Photoresist etch rate	Etch lag
Etch:Passivate	↑	↑↑	↓	↑	↓	↑	↑
SF ₆ :C ₄ F ₈ flow	↑	↑↑	↓	↑	↑↑	↑	↓↓
Cycle time	↑	↑↑	↓	↑	↓	↑	↑
APC	↓	↑	↑↑	↑↑	↑	↑	↓
Coil power	↑	↑	↑	↑	↑	↑	↓
Platen power	↑	↑	↑	↑↑	↑	↑↑	↓

The arrow ↑ shows the increase and ↓ shows decrease. Double arrow ↑↑ show the dominant process parameter for that specific etch characteristics. Profile shape refers to the profile anisotropy and an increase in it means an increase in the verticality of the sidewall.

For a through-wafer etch using a halo mask, etch lag is not a concern as the trench width is constant across the features. Similarly, etch uniformity across the wafer is not a critical effect as the trenches can be over-etched at the edges of the wafers, the side-effect of the over-etch is increased notching of structures at the wafer edge, but this has been completely eliminated through the application of a metal layer at the backside of the wafer. Due to the availability of thicker photoresist it is not critical to tune the process parameters to improve photoresist selectivity; platen power is the dominant process parameter which affects the selectivity.

This effectively reduces the process engineering to finding the right combination of process parameters which affect the silicon etch rate, sidewall quality, and profile shape in the desired way for a given silicon exposure area. It is an iterative process and generally there is sufficient process window to change one parameter to affect a certain etch characteristic without worsening any other etch characteristics. For etchant dominant conditions, both sidewall quality and verticality of the profile shape are strongly dependent on the chamber pressure. Reducing the chamber pressure improves both the sidewall quality and makes the profile shape vertical; this is due to the increased directionality of the ions.

After considering the various issues with DRIE and multiple iterations of parameters to achieve the desired etch characteristics, we have developed a process recipe for etching 525 μm silicon wafer with etch gaps of 40 μm .

4.6.1 Process description

A process recipe (Table 4.4) has been developed to achieve through-wafer etching without parameter ramping and with an overall silicon etch rate of 2 $\mu\text{m}/\text{minute}$. The process flow is as shown in Figure 4.28. The complete etch is divided into two parts, the first run etches the wafer without handle wafer then the device wafer is mounted on a handle wafer. The second run etches the wafer through the full thickness.

Table 4.4 Etch Parameters for through-wafer etching.

Parameter	Value
Total cycle time	17 second
Etch:Passivation step time	10:7
SF ₆ flow rate (etch step)	130 sccm
O ₂ flow rate (etch step)	13 sccm
C ₄ F ₈ flow rate (passivation step)	85 sccm
Platten power (etch step)	20 Watt
Platten power (passivation step)	0 Watt
Coil Power (etch and passivation step)	600 Watt
Pressure (etch step)	20 mTorr
Pressure (passivation step)	11 mTorr
APC Angle (etch and passivation step)	74%
Etch rate	2.04 $\mu\text{m}/\text{min}$
Etch:Passivation ratio	1.375
SF ₆ :C ₄ F ₈ flow rate ratio	1.53

4.6.2 Fabricated devices

The mask was designed using Nemetschek Vectorworks [4.54] and laser printed by Delta Mask [4.55] with a resolution of $1.5\ \mu\text{m}$ linewidth and $0.2\ \mu\text{m}$ address grid. The mask design (Figure 4.41) included suspension designs for horizontal (Figure 4.42) and Galperin configuration (Figure 4.43).

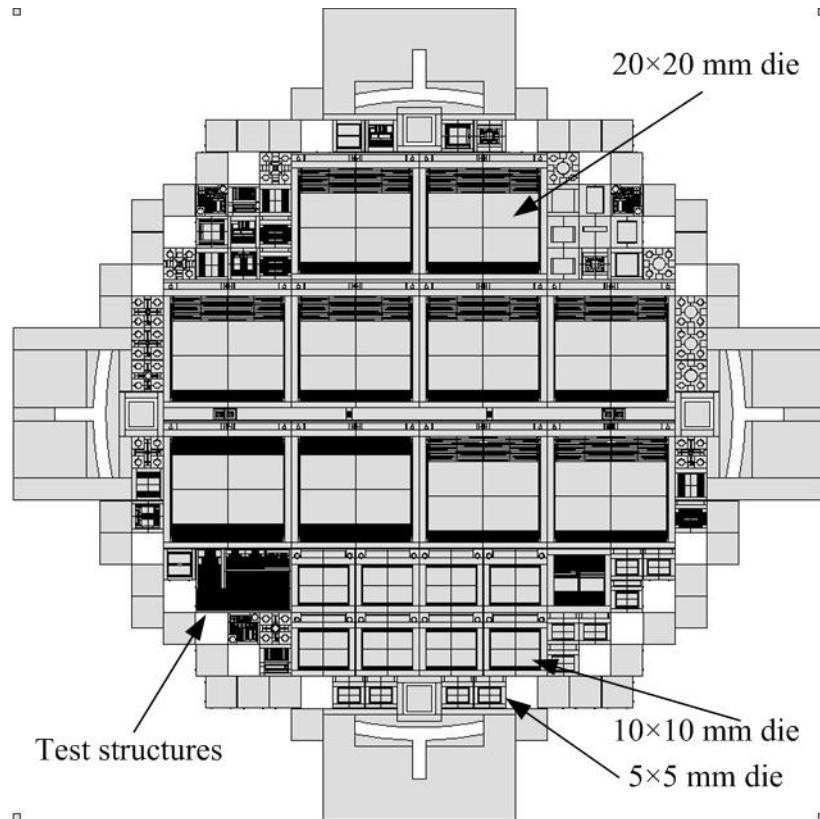


Figure 4.41 Full wafer mask design included 20×20 mm dies as well as 10×10 mm and 5×5 mm dies with lateral suspensions.

The $\{100\}$ single crystal silicon wafer was aligned at 45° to the mask plate to enable (100) plane along the suspension compliant direction. (100) plane of silicon crystal has the lowest Young's modulus [4.56] which reduces the stiffness of the spring in the compliant direction thus lowering the resonant frequency of the suspension.

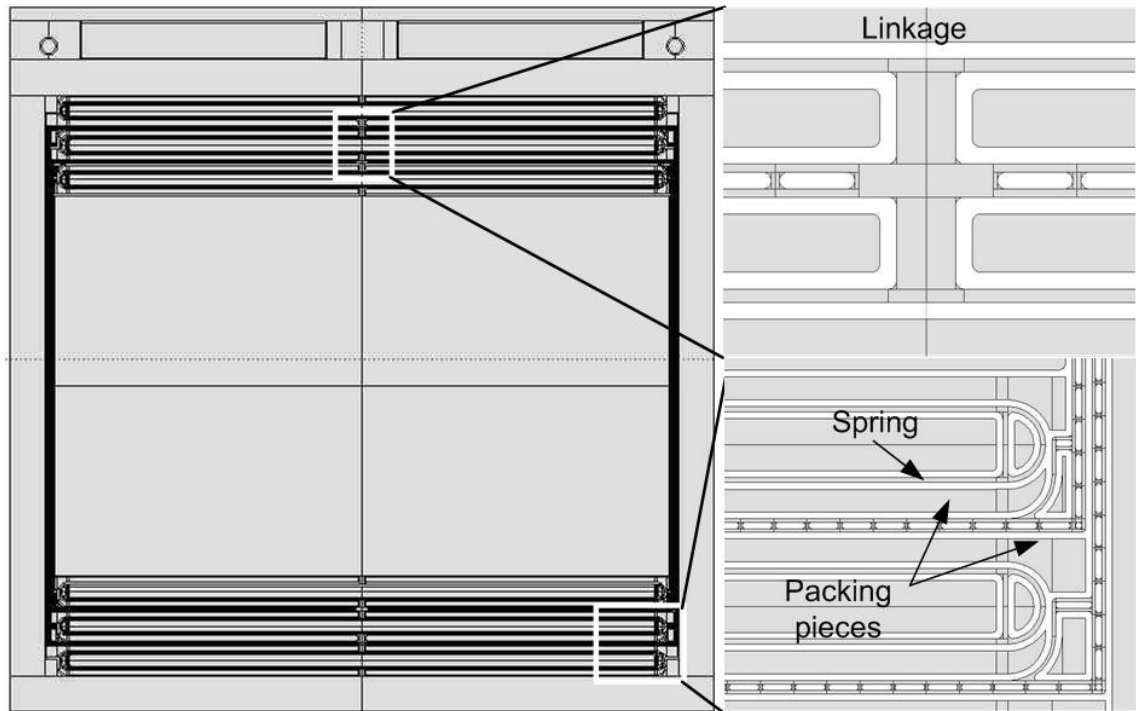


Figure 4.42 Mask layout of the horizontal lateral suspension, the inset shows the spring connector and the linkages with the filleting along with the packing pieces.



Figure 4.43 Mask layout of the Galperin configuration lateral suspension, the insets show the spring and linkage along with the packing pieces.

A n-type {100} silicon wafer is used as substrate wafer, 200 nm thick oxide was grown in a dry thermal furnace. The oxide on one side of the wafer is reactive ion etched using CHF_3 plasma, this side is henceforth referred as the backside of the wafer. A 200 nm layer of Aluminium is evaporated on the backside in a thermal evaporator. A 9 μm thick AZ9260 photoresist is spin-coated on the wafer frontside, pre-baked at 110°C and lithographically patterned using a mask aligner. The photoresist is then developed in AZ400K developer. The underlying 200 nm oxide on the frontside of the wafer is then etched using CHF_3 plasma in RIE. The wafer is loaded into the STS ICP DRIE etcher to etch for 3 hours using the process parameters mentioned in Table 4.4. The process flow is shown in Figure 4.28. The complete recipes for the through-wafer etch is presented in Appendix C. After the first etch the wafer was unloaded and bonded onto a silicon handle wafer using a thin photoresist. The wafer was then etched for another 1 hour 20 minutes in the STS ICP DRIE etcher. Upon visual confirmation of the completion of the etch – by noticing the bright Al layer at the bottom of the trench, the wafers were unloaded and the handle wafer was released using acetone. The backside Al coating was stripped in MF219 developer. The dies were separated by breaking the tabs.

Figure 4.44 shows a fully functional lateral suspension, various configurations were designed and fabricated. The suspension shown in Figure 4.44 has a set of six springs and three intermediate frames. Tabs were used to keep the devices together while etching the wafer; the remnants of the tab are visible alongside the die. A silicon lateral suspension with reduced mass frame and springs with cross-bars is shown in Figure 4.46, the close-up shows the sidewall of the spring end connector. All etch gaps were 40

μm wide including the rectangular cavities etched in the intermediate frames to reduce mass.

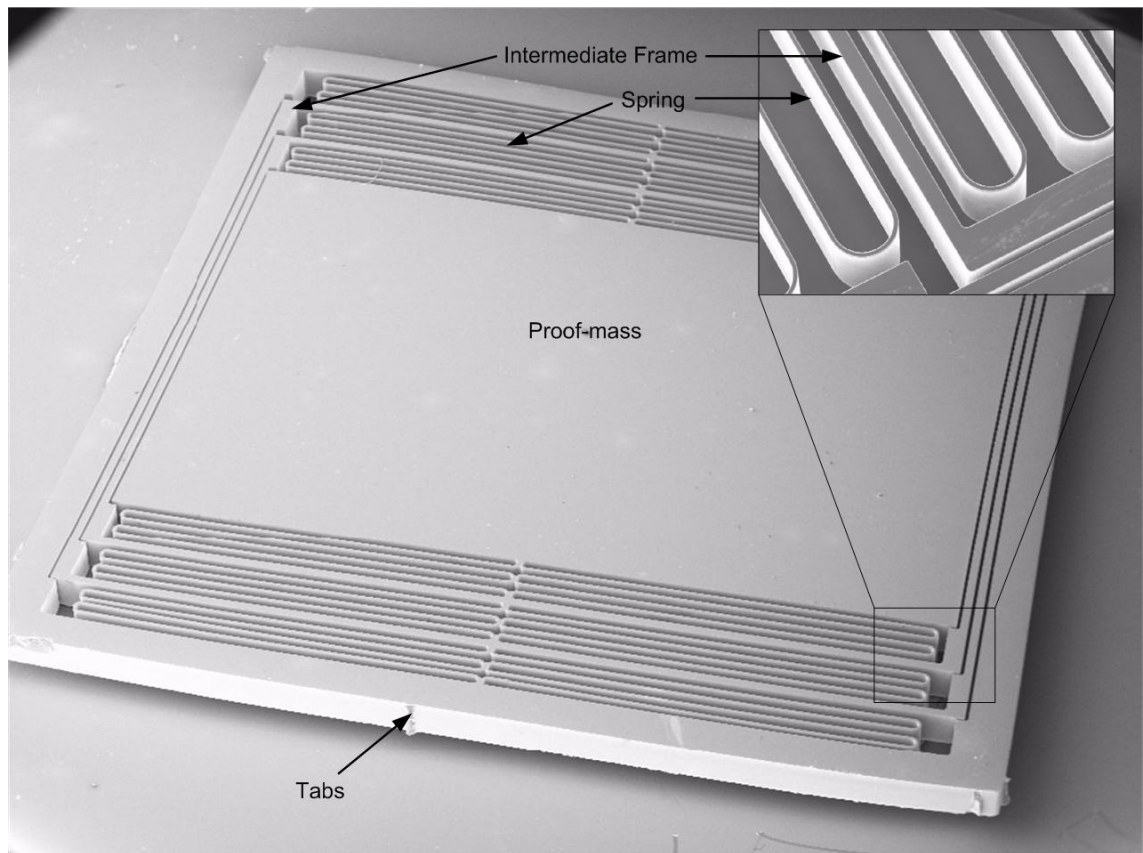


Figure 4.44 Silicon lateral suspension with six sets of springs and three intermediate frames fabricated by DRIE.

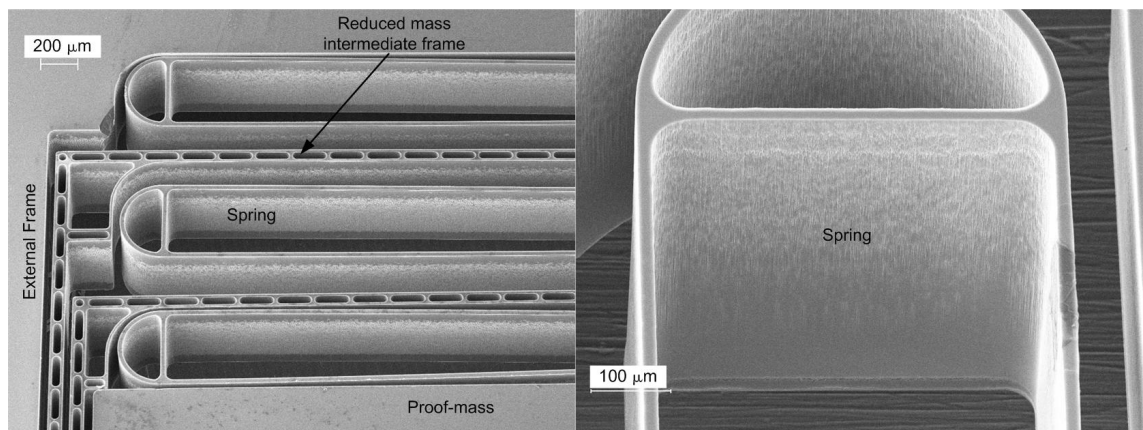


Figure 4.45 Close-up of silicon lateral suspension with reduced mass frame and spring with cross-bar.

Figure 4.46 shows a SEM micrograph of the spring beam sidewall. The sidewall smoothness varies from 8 nm rms roughness at the top edge to nearly 1 μm rms roughness at the bottom edge. The rough portion of the sidewall starts at approximately a quarter way through the etch which is around the time when the lateral etch starts increasing as seen in the profile SEM (Figure 4.47a).

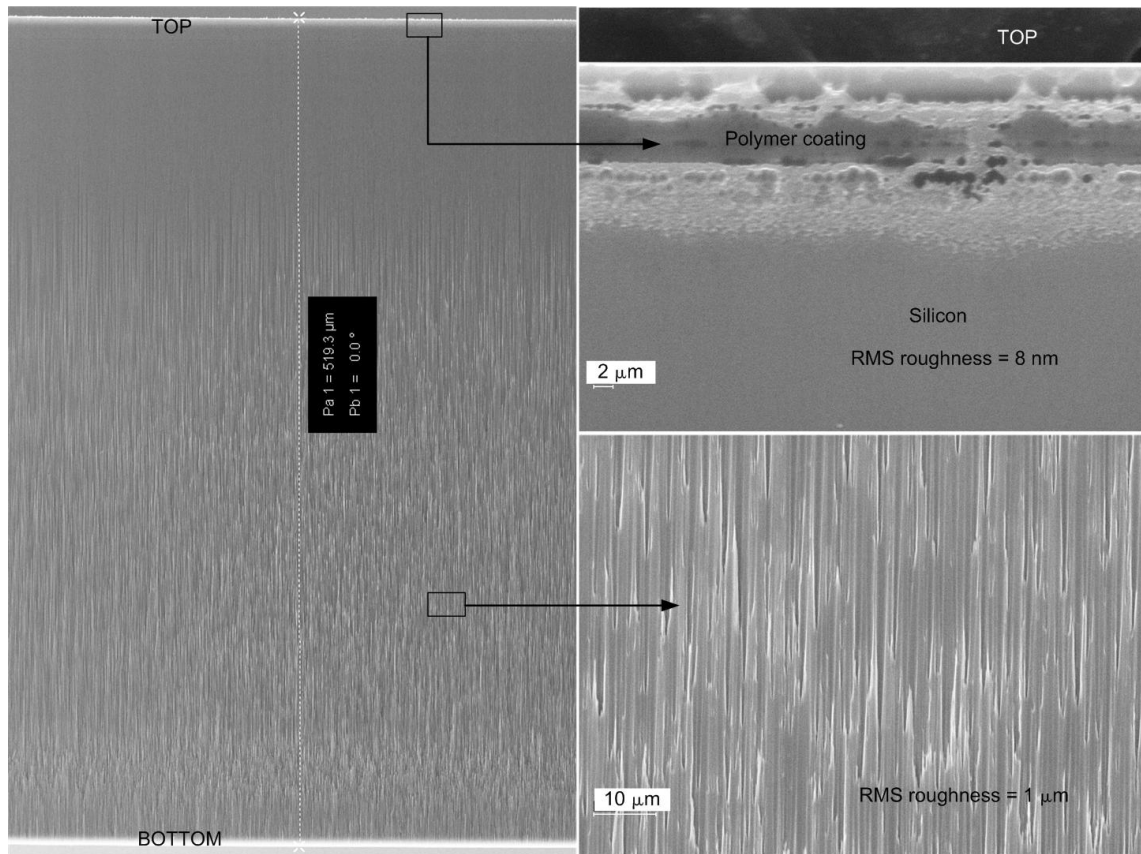


Figure 4.46 Close-up of spring sidewall.

The profile SEM shows bowing of the spring beam (Figure 4.47a), intermediate frame (Figure 4.47b), and the trench cross-section (Figure 4.47c). We will investigate the effect of bowing on the dynamics of the suspension in next chapter. An advantage of the shape of the bowed profile is the higher rigidity in the z direction while reducing the rigidity in the x direction. The bowed shape also leads to a lower mass of the beam compared to a rectangular profile.

Suspension: Fabrication

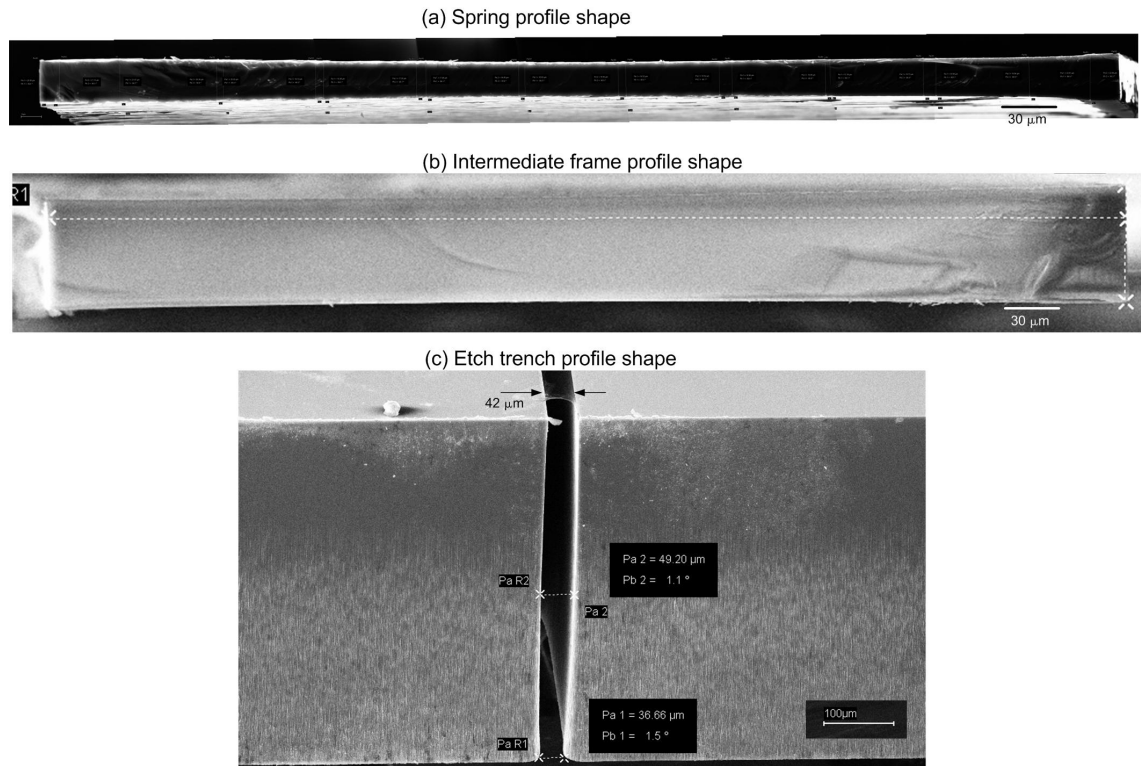


Figure 4.47 Etch profile shape, (a) spring beam cross-section showing an etch profile which is slightly bowed towards the centre, and (b) the profile shape of a cross-section of an intermediate frame showing a similar bow like the spring beam.

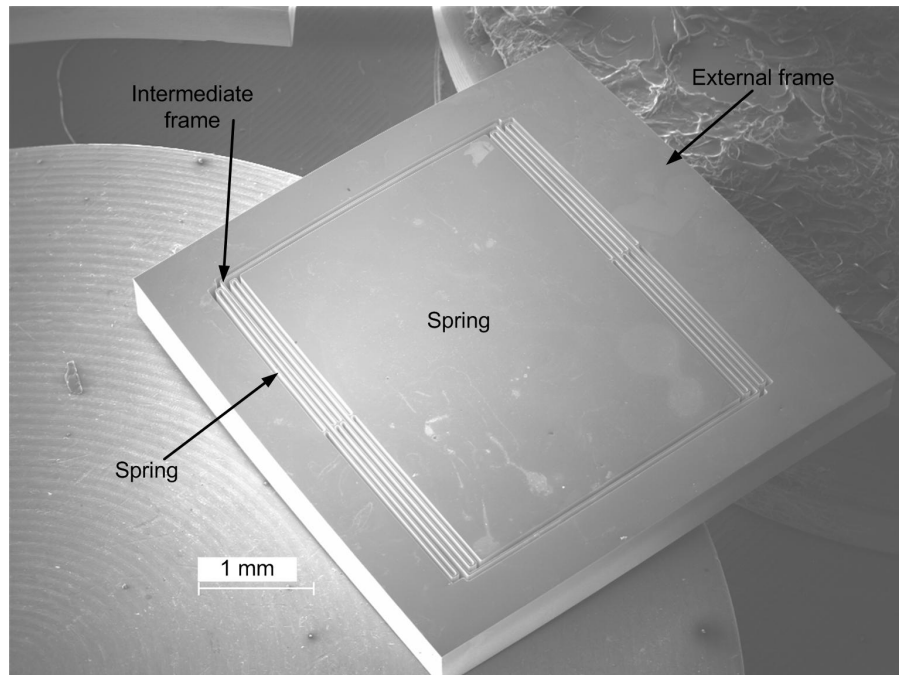


Figure 4.48 SEM of a silicon lateral suspension within a 5 mm×5 mm die.

As we mentioned in Figure 4.41, the mask contains a silicon suspension fabricated within $10\text{ mm} \times 10\text{ mm}$ and $5\text{ mm} \times 5\text{ mm}$ die. Figure 4.48 shows a $5\text{ mm} \times 5\text{ mm}$ lateral suspension die. The gaps between the springs are $40\text{ }\mu\text{m}$, thus eliminating the need for spacers.

4.7 Summary

DRIE based on Bosch time-multiplexed etching and passivation cycles was selected as the processing technique for fabricating thick suspensions by through-wafer etching of single crystal silicon wafer.

The etch trenches are designed with uniform width across the wafer to enable etch uniformity, so the features on the wafer are enclosed within a “halo” geometry.

Through-wafer etching necessitates either a handle wafer or a protective layer to safeguard the substrate holder from exposure to plasma and also to restraint the packing pieces of “halo” geometries from falling in the process chamber. Various bonding techniques are tried and the suggested technique is to coat the backside of the device wafer with metal and then bonded to a handle wafer using thin photoresist.

Plasma processes suffer from a range of deleterious artifacts like grassing, top edge cavernous damage, micro-masking, sidewall roughness, profile shape and notching, which were discussed in detail. Various process and design modifications are incorporated to reduce or eliminate the deleterious side effects of DRIE. Grassing and micro-masking are completely removed by increasing the platen power and decreasing

the processing pressure and introducing O₂ plasma de-scum prior to silicon etch.

Scalloping is a side-effect of the time-multiplexed etching and passivation cycle and is reduced by decreasing the etch cycle time.

Sidewall roughness is analyzed in detail and re-deposition of polymers as a reason for increased roughness with increasing channel width is proposed and validated through experimental results. Profile shape is shown to be an effect of sidewall charging and ion angular distribution; decreasing the chamber pressure increased the anisotropy of the etch leading to improved verticality of the trench sidewalls. Notching caused due to charge accumulation at the silicon-insulator interface is successfully eliminated by coating the wafer backside with a thin metal layer.

A process recipe is developed to attain the desired sidewall quality and etch profile shape. A variety of suspensions were fabricated with varying spring and frame designs. The sidewalls vary in roughness from 8 nm RMS to 1 μm RMS. The profile shape of the spring beams is nearly vertical with some bowing midway through the thickness.

All work covered in this chapter was carried out by the author alone with the exception of sidewall characterization which was done in collaboration.

4.8 Conclusion

The ability to micromachine thick structures out of single crystal silicon using DRIE is successfully demonstrated. This is possible by controlling the process parameters to achieve the desired etch characteristics while reducing or eliminating the deleterious artifacts of plasma processing.

For through-wafer etching the important characteristics to optimize the process were the sidewall quality and profile shape. By engineering a set of process conditions which related the sidewall quality to the etch trench width, we are able to find a suitable etch width for reduced sidewall roughness and silicon etch rates exceeding $2 \mu\text{m}/\text{min}$.

Notching, which can significantly ill-affect the mechanical characteristics of the device, is completely eliminated by a proposed scheme to coat the wafer backside with a thin metal layer; this also improved the thermal uniformity across the wafer while etching, improving the sidewall quality.

Through-wafer DRIE is demonstrated as a reliable and repeatable process for creating silicon suspensions where the suspension is a vertical extrusion of the 2D design. The developed process can be used to fabricate other high-aspect ratio through-wafer silicon micro-mechanical structures.

The next chapter looks at the experimental determination of the suspension dynamics and analyzes the effects of the fabrication process on the suspensions.

4.9 Bibliography

- [4.1] A. Schilp and F. Laermer, Method of anisotropically etching silicon, US Patent US5501893: Robert Bosch GmbH, March 26, 1996
- [4.2] S. Tachi, K. Tsujimoto, S. Arai, and T. Kure, "Low-temperature dry etching," *Journal of Vacuum Science & Technology A: Vacuum, Surfaces, and Films*, vol. 9, pp. 796-803, 1991.
- [4.3] B. E. Volland, *Profile simulation of gas chopping etching processes*, Ph.D. Thesis, Institute of Physics, University of Kassel, 2004
- [4.4] F. Becker, I. W. Rangelow, and R. Kassing, "Ion energy distributions in SF₆ plasmas at a radio-frequency powered electrode," *Journal of Applied Physics*, vol. 80, pp. 56-65, 1996.
- [4.5] S. Rauf, W. J. Dauksher, S. B. Clemens, and K. H. Smith, "Model for a multiple-step deep Si etch process," *Journal of Vacuum Science & Technology A: Vacuum, Surfaces, and Films*, vol. 20, pp. 1177-1190, 2002.
- [4.6] S. Tachi and S. Okudaira, "Chemical sputtering of silicon by F⁺, Cl⁺, and Br⁺ ions: Reactive spot model for reactive ion etching," *Journal of Vacuum Science & Technology B: Microelectronics and Nanometer Structures*, vol. 4, pp. 459-467, 1986.
- [4.7] H. Hayashi, S. Morishita, T. Tatsumi, Y. Hikosaka, S. Noda, H. Nakagawa, S. Kobayashi, M. Inoue, and T. Hoshino, "Mechanism of C₄F₈ dissociation in parallel-plate-type plasma," *Journal of Vacuum Science & Technology A: Vacuum, Surfaces, and Films*, vol. 17, pp. 2557-2571, 1999.
- [4.8] P.-A. Clerc, L. Dellmann, F. Gretillat, M.-A. Gretillat, P.-F. Indermuhle, S. Jeanneret, P. Luginbuhl, C. Marxer, T. L. Pfeffer, G.-A. Racine, S. Roth, U. Stauer, C. Stebler, P. Thiebaud, and N. F. d. Rooij, "Advanced deep reactive ion etching: a versatile tool for microelectromechanical systems," *Journal of Micromechanics and Microengineering*, vol. 8, pp. 272-278, 1998.
- [4.9] K. Ishihara, C. F. Yung, A. A. Ayon, and M. A. Schmidt, "An inertial sensor technology using DRIE and wafer bonding with interconnecting capability," *Journal of Microelectromechanical Systems*, vol. 8, pp. 403-408, 1999.

- [4.10] J. W. Weigold, K. Najafi, and S. W. Pang, "Design and fabrication of submicrometer, single crystal Si accelerometer," *Journal of Microelectromechanical Systems*, vol. 10, pp. 518-524, 2001.
- [4.11] C. Acar and A. M. Shkel, "Structurally decoupled micromachined gyroscopes with post-release capacitance enhancement," *Journal of Micromechanics and Microengineering*, vol. 15, pp. 1092-1101, 2005.
- [4.12] J. Li, Q. X. Zhang, and A. Q. Liu, "Advanced fiber optical switches using deep RIE (DRIE) fabrication," *Sensors and Actuators a-Physical*, vol. 102, pp. 286-295, 2003.
- [4.13] A. Lipson, *A Tunable Micro-Electro-Mechanical Optical Filter in Silicon*, Ph.D. Thesis, Department of Electrical and Electronic Engineering, Imperial College, London, UK, 2006
- [4.14] P. D. Mitcheson, P. Miao, B. H. Stark, E. M. Yeatman, A. S. Holmes, and T. C. Green, "MEMS electrostatic micropower generator for low frequency operation," *Sensors and Actuators A: Physical*, vol. 115, pp. 523-529, 2004.
- [4.15] Y. Hanein, C. G. J. Schabmueller, G. Holman, P. Lucke, D. D. Denton, and K. F. Bohringer, "High-aspect ratio submicrometer needles for intracellular applications," *Journal of Micromechanics and Microengineering*, vol. 13, pp. S91-S95, 2003.
- [4.16] R. R. A. Syms, M. M. Ahmad, I. R. Young, Y. Li, J. Hand, and D. Gilderdale, "MEMS Helmholtz coils for magnetic resonance imaging," *Journal of Micromechanics and Microengineering*, vol. 15, pp. S1-S9, 2005.
- [4.17] S. J. Ok, C. Kim, and D. F. Baldwin, "High density, high aspect ratio through-wafer electrical interconnect vias for MEMS packaging," *IEEE Transactions on Advanced Packaging*, vol. 26, pp. 302-309, 2003.
- [4.18] "Surface technology systems," <http://www.stssystems.com>.
- [4.19] A. M. Hynes, H. Ashraf, J. K. Bhardwaj, J. Hopkins, I. Johnston, and J. N. Shepherd, "Recent advances in silicon etching for MEMS using the ASE(TM) process," *Sensors and Actuators A: Physical*, vol. 74, pp. 13-17, 1999.
- [4.20] C. J. Mogab, "The Loading Effect in Plasma Etching," *Journal of The Electrochemical Society*, vol. 124, pp. 1262-1268, 1977.
- [4.21] J. W. Coburn and H. F. Winters, "Conductance considerations in the reactive ion etching of high aspect ratio features," *Applied Physics Letters*, vol. 55, pp. 2730-2732, 1989.

- [4.22] R. Khanna, X. Zhang, J. Protz, and A. A. Ayon, Microfabrication Protocols for Deep Reactive Ion Etching and Wafer-Level Bonding, *Sensors*, 18, pp 51-60, 2001
- [4.23] Clariant AZ 9260 Resist,
http://www.azresist.com/products/na/photoresists/thick_film.html.
- [4.24] M. J. Madou, *Fundamentals of microfabrication*, 1 ed: CRC Press LLC, 1997.
- [4.25] Shipley SPR1813 resist,
http://appserver.microe.rit.edu/classes/emcr666_676/reference/photoresists/S1813_MSDS.pdf.
- [4.26] K. S. Chen, A. A. Ayon, X. Zhang, and S. M. Spearing, "Effect of process parameters on the surface morphology and mechanical performance of silicon structures after deep reactive ion etching (DRIE)," *Journal of Microelectromechanical Systems*, vol. 11, pp. 264-275, 2002.
- [4.27] A. A. Ayon, R. Braff, C. C. Lin, H. H. Sawin, and M. A. Schmidt, "Characterization of a time multiplexed inductively coupled plasma etcher," *Journal of The Electrochemical Society*, vol. 146, pp. 339-349, 1999.
- [4.28] H. Jansen, M. d. Boer, R. Legtenberg, and M. Elwenspoek, "The black silicon method: a universal method for determining the parameter setting of a fluorine-based reactive ion etcher in deep silicon trench etching with profile control," *Journal of Micromechanics and Microengineering*, vol. 5, pp. 115-120, 1995.
- [4.29] D. C. Gray, H. H. Sawin, and J. W. Butterbaugh, "Quantification of surface film formation effects in fluorocarbon plasma etching of polysilicon," *Journal of Vacuum Science & Technology A: Vacuum, Surfaces, and Films*, vol. 9, pp. 779-785, 1991.
- [4.30] M. Inayoshi, M. Ito, M. Hori, T. Goto, and M. Hiramatsu, "Surface reaction of CF₂ radicals for fluorocarbon film formation in SiO₂/Si selective etching process," presented at International workshop on basic aspects of nonequilibrium plasmas interacting with surfaces (BANPIS'97), Shirahama, Japan, 1998.
- [4.31] S. Ohki, M. Oda, H. Akiya, and T. Shibata, "Cavernous undercuts appearing in reactive ion etched submicron-wide deep trenches," *Journal of Vacuum Science & Technology B: Microelectronics and Nanometer Structures*, vol. 5, pp. 1611-1616, 1987.

- [4.32] W. T. Pike, W. J. Karl, S. Kumar, S. Vijendran, and T. Semple, "Analysis of sidewall quality in through-wafer deep reactive-ion etching," *Microelectronic Engineering*, vol. 73-74, pp. 340-345, 2004.
- [4.33] I. W. Rangelow, "Critical tasks in high aspect ratio silicon dry etching for microelectromechanical systems," presented at 49th International Symposium of the American Vacuum Society, Denver, USA, 2003.
- [4.34] A. Grigonis, R. Knizikevicius, Z. Rutkuniene, and M. Puceta, "Kinetics of composition of polymeric layer during silicon etching in CF_2Cl_2 plasma," *Applied Surface Science*, vol. 199, pp. 270-277, 2002.
- [4.35] J.-H. Min, S.-W. Hwang, G.-R. Lee, and S. H. Moon, "Redeposition of etch products on sidewalls during SiO_2 etching in a fluorocarbon plasma. I. Effect of particle emission from the bottom surface in a CF_4 plasma," *Journal of Vacuum Science & Technology A: Vacuum, Surfaces, and Films*, vol. 20, pp. 1574-1581, 2002.
- [4.36] H. Hubner, "Calculations on Deposition and Redeposition in Plasma Etch Processes," *Journal of the Electrochemical Society*, vol. 139, pp. 3302-3309, 1992.
- [4.37] Y.-J. T. Lii and J. Jorne, "Redeposition during deep trench etching," *Journal of Electrochemical Society*, vol. 137, pp. 2837-2845, 1990.
- [4.38] I. W. Rangelow, P. Thoren, and R. Kissing, "Computer simulation of pattern profiles through physical etching with shadow, trenching, and redeposition," *Microelectronic Engineering*, vol. 3, pp. 631-638, 1985.
- [4.39] B.-O. Cho, S.-W. Hwang, G.-R. Lee, and S. H. Moon, "Angular dependence of the redeposition rates during SiO_2 etching in a CF_4 plasma," *Journal of Vacuum Science & Technology A: Vacuum, Surfaces, and Films*, vol. 19, pp. 730-735, 2001.
- [4.40] A. A. Ayon, X. Zhang, and R. Khanna, "Anisotropic silicon trenches 300-500 μm deep employing time multiplexed deep etching (TMDE)," *Sensors and Actuators A: Physical*, vol. 91, pp. 381-385, 2001.
- [4.41] V. K. Singh, E. S. G. Shaqfeh, and J. P. McVittie, "Simulation of profile evolution in silicon reactive ion etching with re-emission and surface diffusion," *Journal of Vacuum Science & Technology B: Microelectronics and Nanometer Structures*, vol. 10, pp. 1091-1104, 1992.

- [4.42] Y. Sun, B. J. Nelson, D. P. Potasek, and E. Enikov, "A bulk microfabricated multi-axis capacitive cellular force sensor using transverse comb drives," *Journal of Micromechanics and Microengineering*, vol. 12, pp. 832-840, 2002.
- [4.43] J. P. Chang and J. W. Coburn, "Plasma-surface interactions," *Journal of Vacuum Science & Technology A: Vacuum, Surfaces, and Films*, vol. 21, pp. S145-S151, 2003.
- [4.44] S. A. McAuley, H. Ashraf, L. Atabo, A. Chambers, S. Hall, J. Hopkins, and G. Nicholls, "Silicon micromachining using a high-density plasma source," *Journal of Physics D: Applied Physics*, vol. 34, pp. 2769-2774, 2001.
- [4.45] T. Kinoshita, M. Hane, and J. P. McVittie, "Notching as an example of charging in uniform high density plasmas," presented at The 3rd International Workshop on Advanced Plasma Tools for Etching, Chemical Vapor Deposition, and Plasma Vapor Deposition: Sources, Process Control, and Diagnostics, San Jose, California (USA), 1996.
- [4.46] G. S. Hwang and K. P. Giapis, "Electron irradiance of conductive sidewalls: A determining factor for pattern-dependent charging," *Journal of Vacuum Science & Technology B: Microelectronics and Nanometer Structures*, vol. 15, pp. 1741-1746, 1997.
- [4.47] S. Samukawa and T. Mieno, "Pulse-time modulated plasma discharge for highly selective, highly anisotropic and charge-free etching," *Plasma Sources Science and Technology*, vol. 5, pp. 132-138, 1996.
- [4.48] S. Franssila, J. Kiihamaki, and J. Karttunen, "Etching through silicon wafer in inductively coupled plasma," *Microsystem Technologies*, vol. 6, pp. 141-144, 2000.
- [4.49] F. E. Rasmussen, J. Frech, M. Heschel, and O. Hansen, "Fabrication of high aspect ratio through-wafer vias in CMOS wafers for 3-D packaging applications," presented at The IEEE 12th International Conference on Solid-State Sensors, Actuators and Microsystems, Boston, MA, USA, 2003.
- [4.50] M. Chabloz, J. Jiao, Y. Yoshida, T. Matsuura, and K. Tsutsumi, "A method to evade microloading effect in deep reactive ion etching for anodically bonded glass-silicon structures," presented at The IEEE 13th Annual International Conference on Micro Electro Mechanical Systems, Miyazaki, Japan, 2000.

- [4.51] C.-H. Kim and Y.-K. Kim, "Prevention method of a notching caused by surface charging in silicon reactive ion etching," *Journal of Micromechanics and Microengineering*, vol. 15, pp. 358-361, 2005.
- [4.52] S. Kumar and W. T. Pike, "Technique for eliminating notching in through-wafer etching," presented at 16th MME Micromechanics Europe Workshop, Gothenburg, Sweden, 2005.
- [4.53] Coolgrease CGR7016, <http://www.aitechnology.com/thermal.html>.
- [4.54] Vectorworks Designer, Nemetschek AG, Konrad-Zuse-Platz 1, 81829 Munich, Germany <http://www.nemetschek.net/>.
- [4.55] Delta Mask V.O.F, Nijmansbos 56, 7543 GJ Enschede, The Netherlands <http://www.deltamask.nl>.
- [4.56] N. Maluf, *An Introduction to Microelectromechanical Systems Engineering*, Artech House, Inc., 2000.

five

5 Suspension: Characterzation

In this chapter, we use experimental methods to determine the dynamics of the fabricated suspension. Any deviation of the suspension resonant frequency and rejection ratio from the analytical and numerical estimates of chapter 3 are analysed and the causes for them are discussed. The analytical and numerical models are then updated to incorporate the effect of fabrication process variation [5.1]. A compensation design for the suspension is developed to attain the target resonant frequency.

5.1 Measurement Techniques

The normal modes of the suspension along the major axes are determined from slow-scan imaging in a variable pressure scanning electron microscope [5.2]. For measuring the resonant frequency the suspension is mounted on a SEM stub such that it is free to move. The electron-beam is rastered parallel to the compliant direction of excitation.

The raster time is set to a few tens of seconds for measuring the resonant frequency. The same system is used to measure the damping of the suspension with rastering times of few minutes. The suspension is excited by applying a force in the appropriate direction by either moving the positioning stage or tapping the SEM chamber from outside. It is expected that for future measurements an internal piezoactuator will be mounted on the positioning stage to vibrate the suspension along the direction of interest.

5.1.1 Resonant frequencies

The scan time is adjusted so that several time periods of oscillation correspond to the frame acquisition time. Figure 5.1 is a typical slow-scan of the oscillation. The electron beam (e-beam) in the SEM is rastered parallel to the direction of the movement of the spring and proof mass. The scan allows us to take a snapshot of the suspension while it is oscillating. The time taken for scanning the complete frame is known from the SEM scan software. We count the number of oscillations ($n_{oscillations}$) in a fixed length of the frame ($frame_{oscillations}$). Since we know the time taken for the complete frame ($time_{frame_full}$), we can calculate the time taken for the oscillations counted. Dividing the number of oscillations counted by the time taken for the e-beam to raster over them gives the number of oscillations per unit time. In Figure 5.1, total time for the full frame acquisition ($time_{frame_full}$) is 5.1 s, the length of the whole frame ($frame_{full}$) is 5.505 mm,

the length of frame ($frame_{oscillations}$) containing 40 oscillations is 3.911 mm. The resonant frequency for the lateral suspension can be calculated as:

$$\omega_o = \frac{frame_{full} \times n_{oscillations}}{frame_{oscillation} \times time_{frame_{full}}} = \frac{5.505mm \times 40}{3.911mm \times 5.1s} = 11.03Hz \quad (5.1)$$

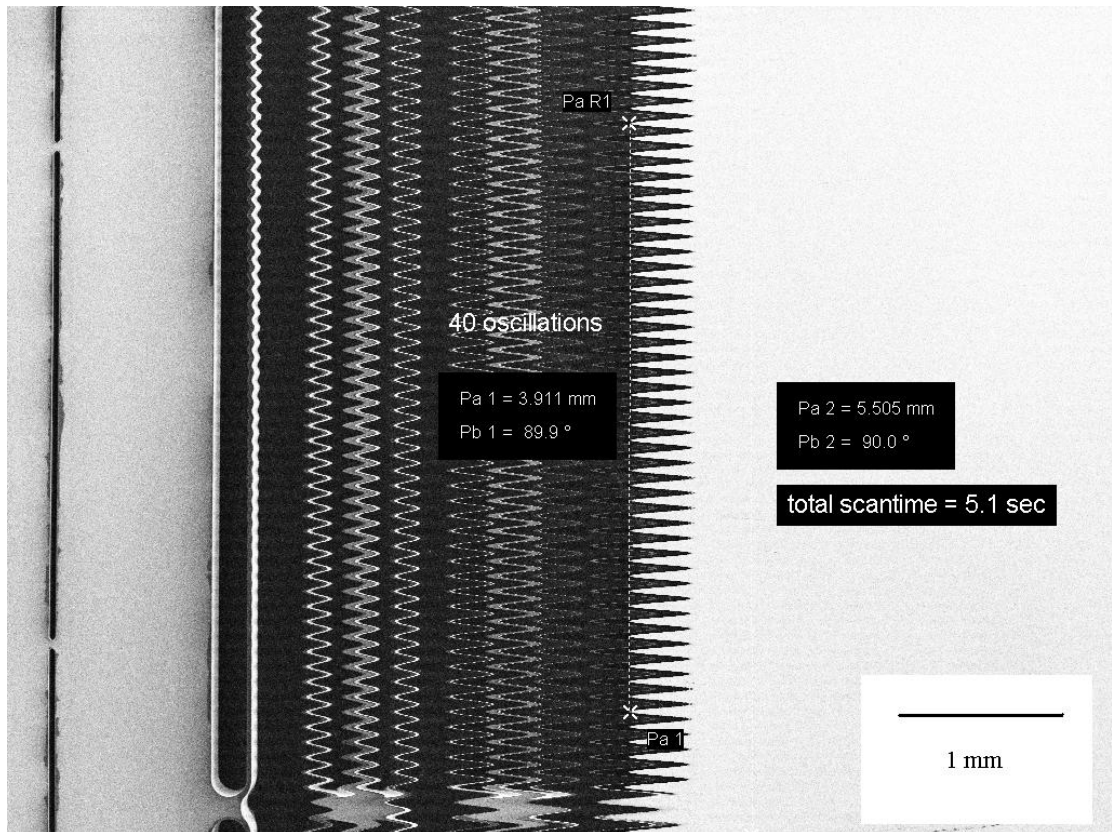


Figure 5.1 Slow-scan image of suspension under excitation, the edges of the spring and proof mass appear as a sinusoid due to the rastering of the electron beam parallel to the direction of motion of the proof mass. The sinusoidal edges show the fundamental mode of the suspension.

On closer inspection we can see the higher-order modes overlapped on-top of the normal modes. Figure 5.2 shows the overlap of the xI mode (the first in-plane spurious mode along X -axis) on the normal x mode, the xI mode is higher frequency than the x mode and is visible in the SEM as a higher-frequency oscillation on the springs whereas the proof-mass and the overall springs have a low-frequency oscillation shape from the

x mode. Similarly both the rotational modes and other translational modes can be visualized by carrying out a slow scan along the various axes. The modes are excited by orienting the stage in a way that an externally applied tap on the chamber walls gets directly translated to the suspension along the direction of interest.

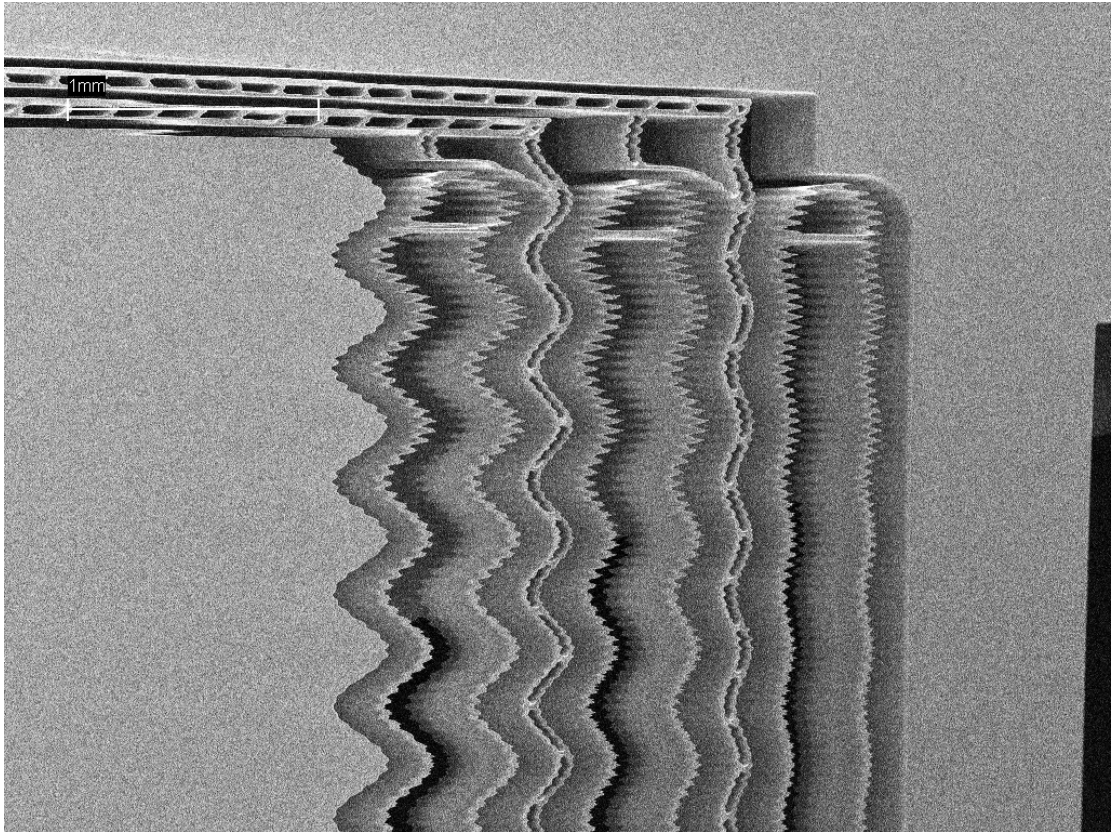


Figure 5.2 Overlap of the first spurious mode along the x -axis (ω_{x1}) on top of the normal x -axis mode (ω_x). The $x1$ mode is visible as the higher frequency mode on the springs. The x mode is visible as the low-frequency sinusoid of the proof mass and the springs.

To visualize the out-of-plane z mode, the suspension is tilted so that the beam is parallel to the Y -axis of the suspension. The constant oscillation of the centre of the proof mass (Figure 5.3 inset 2) shows the out-of-plane z mode (ω_z) whereas the see-saw oscillation of the proof mass at the corners (Figure 5.3 inset 1) gives the rotation mode about Y -axis (ω_β).

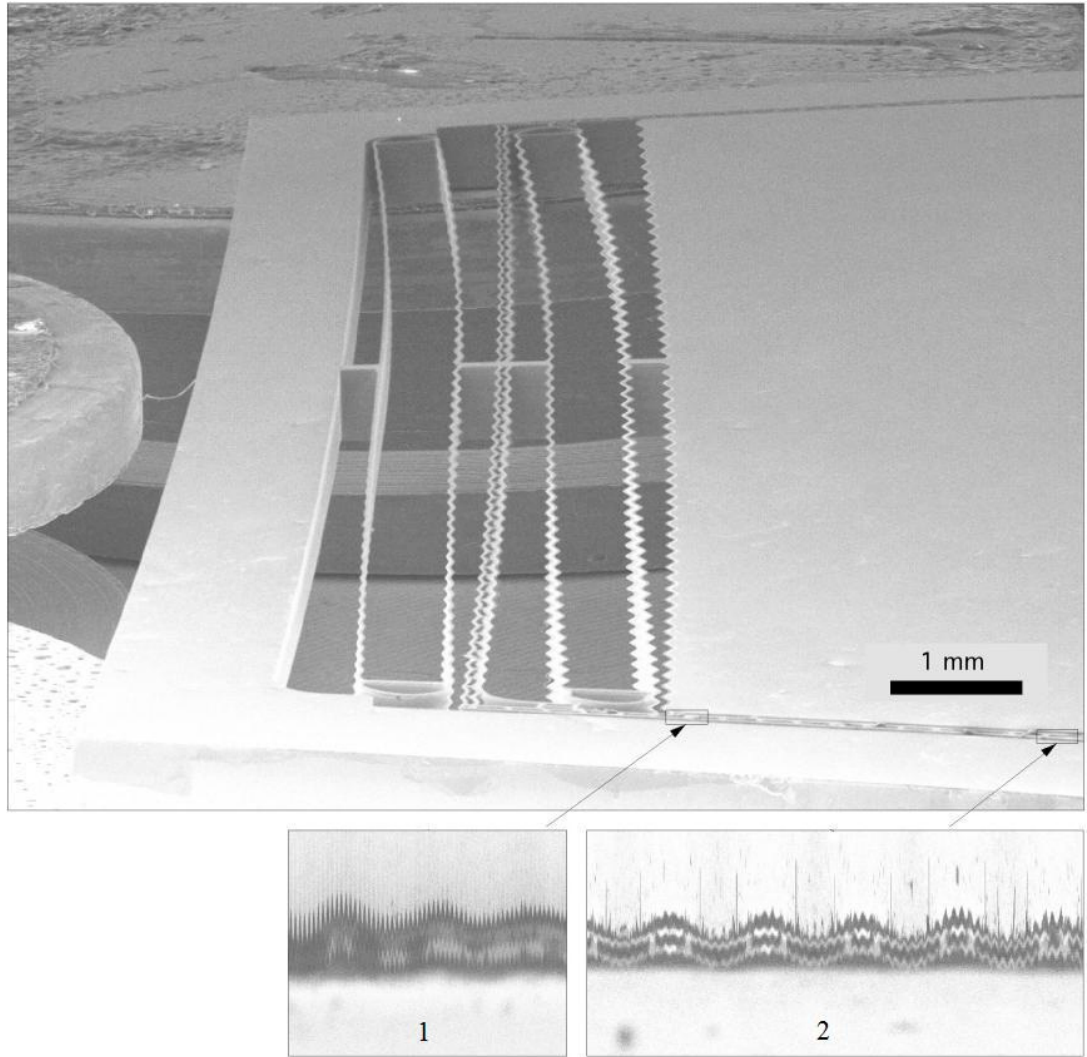


Figure 5.3 SEM of the suspension with the electron beam scanning along the Y -axis of the suspension, the insets show the ω_z and ω_β modes. Inset 1 shows the see-saw motion of the proof mass due to the rotational mode (ω_β) about Y -axis of the suspension. The out-of-plane mode (ω_z) is clearly visible at the center of the proof mass in inset 2 as a constant amplitude oscillation.

We calculate the normal mode frequencies from the SEM measurement in a similar way as the x mode by calculating the time taken for a specific number of oscillations showing that specific mode.

The SEM based measurement of resonant frequencies is suitable for measuring only low-frequency systems due to the loss of resolution for images with scan acquisition

time of less than 0.1 second as the SEM's e-beam rastering is slow. This restricts the technique to the measurement of suspensions with modes below few hundred hertz.

5.1.2 Quality factor

The quality factor (Q) of the suspension is calculated by carrying out a ringdown test in a SEM. The Q is determined by the time taken for the amplitude to reduce by $1/e$ which is the decay time constant, τ of the suspension. The expression for calculating the Q for a suspension with resonant frequency ω_0 is given by

$$Q = \pi\omega_0\tau \quad (5.2)$$

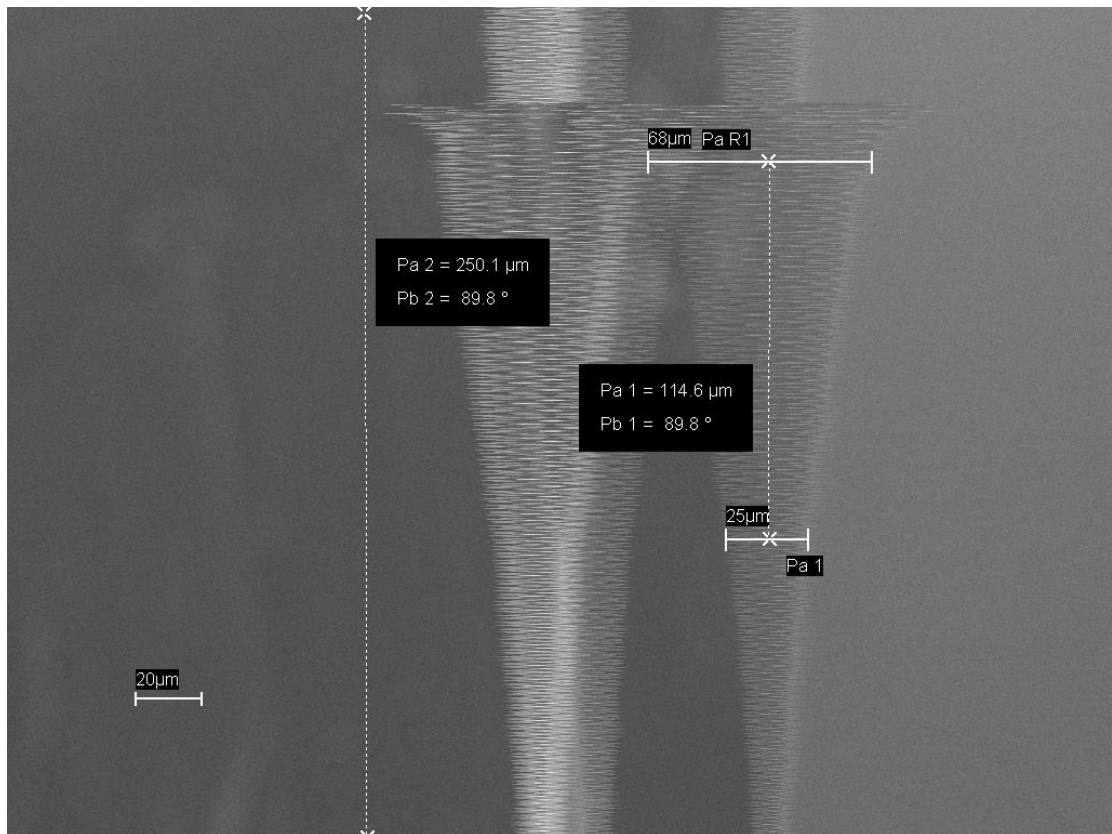


Figure 5.4 Ringdown of suspension in SEM slow-scan. Measuring the time taken for the amplitude of oscillations to drop to $1/e$ of its initial value gives the decay time constant (τ) of the system.

Figure 5.4 shows the ringdown test for the suspension in UHV where the rastering time is 24 minutes. Availability of a variable pressure SEM allows ringdown tests to be performed at various pressure levels including ultra high vacuum (UHV).

For the ringdown in Figure 5.4 the initial amplitude of oscillation is 68 μm , so decay time constant (τ) is given by the scan time taken for the amplitude to decay to 1/e of initial amplitude which is 25 μm . The total time for the scan ($time_{frame_full}$) is 24 minutes, the length of the frame ($frame_{full}$) is 250.1 μm and the length of frame ($frame_{oscillation}$) between the initial oscillation and when it decays to 1/e of its initial value is 114.6 μm .

The decay time is thus calculated as

$$\tau = \frac{frame_{oscillation} \times time_{frame_full}}{frame_{full}} = \frac{114.6 \mu\text{m} \times 24 \text{ min} \times 60 \text{ sec/ min}}{250.1 \mu\text{m}} = 664.3 \text{ sec} \quad (5.3)$$

Q can be calculated using equation 5.2,

$$Q = \frac{2 \times \pi \times 10.9 \times 664.3}{2} \approx 22000 \quad (5.4)$$

With such high Q values it was important to stabilize the suspension before imparting the ringdown impulse. This is achieved by raising the chamber pressure to few hundred pascals for a few minutes prior to the impulse to dampen out the background oscillations. The chamber pressure is then reduced to the required level just before the scan.

5.2 Experimental Work

The resonant frequency and mode visualization is carried out in the SEM using the method described in section 5.1. The quality factor (Q) of the suspensions is determined by carrying out a ringdown test and calculating the decay time constant.

5.2.1 Resonant frequencies

The resonant frequency of the fabricated suspension is measured and compared to the analytical model developed in chapter 3. Table 6.1 presents the analytically and numerically calculated resonant frequencies and compares it to the experimentally determined values. The tolerance on the measured values is due to measurement error when using a SEM image; some modes are harder to visualize leading to higher errors when calculating the resonant frequency values.

Table 6.1 Vibration modes of silicon suspension with 24 μm wide springs. The suspension has two set of springs with one intermediate frame.

Mode	Model Analysis	Model FEA	Measured	Error (Analytical)	Error (FEA)
ω_x	12.2	12.2	7.9 \pm 0.1	-35.2%	-35.2%
ω_{x1}/ω_x	17.5	14.4	15.7 \pm 0.2	-10.2%	+9.0%
ω_y/ω_x	9.3	8.9	9.4 \pm 0.3	+1.0%	+5.6%
ω_z/ω_x	11.5	11.1	11.9 \pm 0.2	+3.5%	+7.2%
ω_α/ω_x	12.4	14.0	-	-	-
ω_β/ω_x	23.5	20.4	19.2 \pm 0.2	-18.3%	-5.9%
ω_γ/ω_x	9.1	9.6	10.5 \pm 0.5	+15.4%	+9.4%

As we see in Table 6.1, fabricated devices demonstrate significantly different resonant frequencies compared to the simulated device. Even though the suspension is designed to have a resonant frequency of 12.2 Hz, the first mode is only 7.9 Hz for the fabricated suspension, a drop of 35%. The analytical model is more accurate than the FEA model for calculating the translational resonant frequencies of the suspension. This can be due to the fact that the FEA model is much simplified and the spring end connector rigidity

is much higher for the actual device which is accounted for in the analytical model. FEA model is overall quite accurate and predicts all the modes within 10% of their measured values and is much more accurate than the analytical model for rotational modes. This is due to the FEA taking care of the bending and torsional components of the stiffness more accurately than the analytical model.

The drop in the fundamental in-plane mode along X -axis (ω_x) is due to the thinning of the spring during fabrication since a thin spring will reduce the second area moment I_x and ω_x is linearly dependent on square root of I_x . As we discussed earlier in section 4.5.8 the etched features do not have vertical walls and this could cause a significant change in the stiffness of the springs. An analysis of the spring shape thus becomes important to understand the difference in the model and actual device.

The first spurious mode along X -axis (ω_{x1}) is nearly 9% higher than the model estimate; this is due to the decrease in mass of spring and frames due to reduction in spring and frame width from bowing compared to the ideal rectangular profile.

The slight variation in the lateral in-plane mode (ω_y) and out-of-plane mode (ω_z) could be due to variation in I_x and I_z for the spring and frame due to bowing of the profile shape.

We are unable to visualize the rotational mode about X -axis (ω_α) as the best place to visualize it is by looking down the X -axis of the suspension and seeing the oscillation of the edges of the proof mass. This is hard to achieve due to the distance and the almost

latched condition of the proof-mass under maximum deflection due to gravity causing the proof-mass to rest on the bottom springs restricting mechanical movement.

The rotational modes agree within 10% of the FEA values, which is a good agreement given that there is higher measurement error in these modes compared to the translational modes.

Even though the fundamental resonant mode is significantly different from the predicted value from the analytical and numerical model, the rejection ratio of the higher order modes to the fundamental is nearly similar to the model. This is due to the dependence of the modes predominantly on I_x which defines ω_x . Modes which are dependent on J also are independent of the profile shape as J is proportional to I_x for thin springs (section 5.3.3) and so the rejection ratio is independent of I_x . The slight difference in some modes can be attributed to their dependence on I_z which is not proportional to I_x .

To analyze the performance of a fabricated device and correctly predict the mechanical characteristics of a new design, it is important to consider the profile shape in the analytical and numerical models. We use an analytical model in section 5.3 for designing lateral suspensions taking into account the non-ideal etch profile. Numerical models become complex when the profile shape needs to be taken into consideration. To avoid complexity associated with meshing bowed beam cross section of high aspect ratio beams, we use the analytical models to calculate an effective thickness of the spring and used it in the FEA model with rectangular spring profile so we can obtain some information on the modes and their shapes. Silicon suspensions are then fabricated and their mechanical characteristics compared to analytical calculations.

5.2.2 Quality factor at varying pressure

The SEM allows controlling the pressure of the test chamber from 1 to 400 Pa, which is suitable for seeing the effect of viscosity on the Q , though for measuring the Q at atmospheric pressure we use an optical microscope. The Q variation with pressure is shown in Figure 5.5 for a suspension. The Q at standard atmospheric pressure (1 atm = 1 bar = 10^5 Pa) is 1000, decreasing the pressure below 1 atm does not result in significant change in Q until the pressure is lower than 600Pa. The Q -factor at UHV (Ultra-high vacuum, 0.001 Pa) is 40,000.

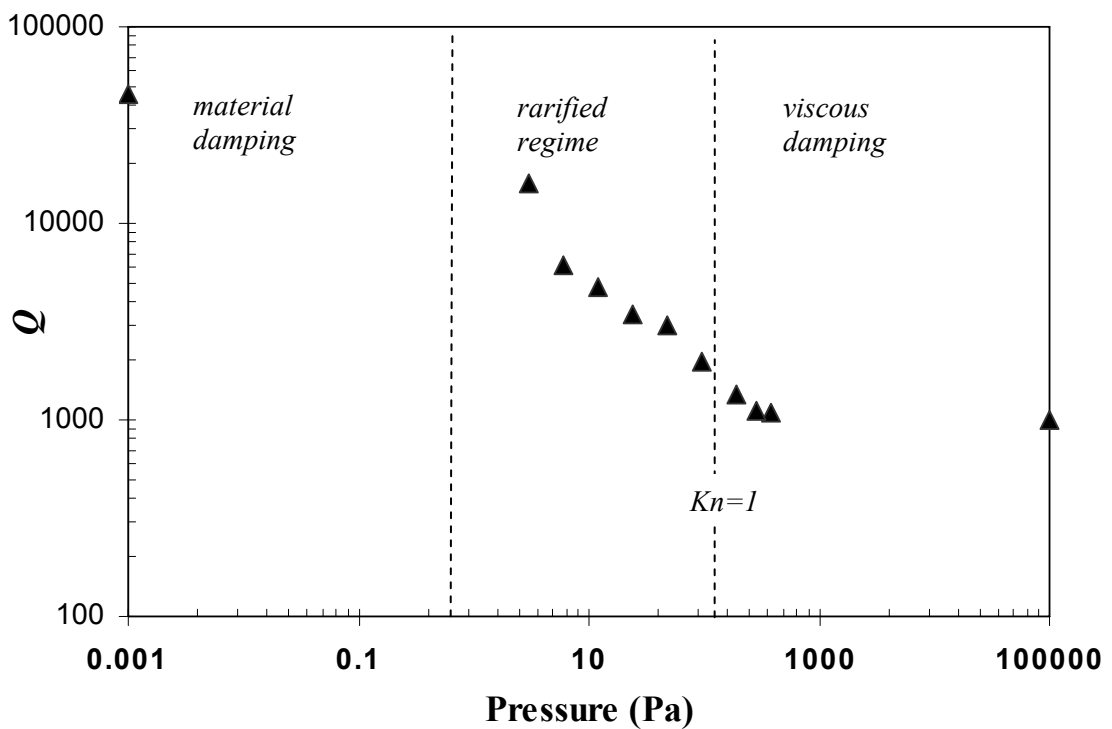


Figure 5.5 Plot of measured quality factor as a function of pressure for 10 Hz silicon suspension.

The variation in quality factor at various pressures can be classified into three regimes of gas and material damping of structures. In the first two regimes: high pressure and rarefied regime, gas damping dominates. When the pressure is very low gas damping is smaller than material damping of the silicon suspension. At high pressure the dominant

gas damping is due to the closing and opening of the springs with oscillation leading to squeeze-film damping. Squeeze-film damping is dependent on the viscosity of the gas which does not vary with pressure in the high-pressure regime so the damping is quite high but constant in high-pressure regime. In rarefied/molecular regime, viscosity is a function of pressure and damping reduces with reducing pressure. The transition between the two gaseous damping regimes is determined by the Knudsen number, Kn , which is given by the ratio of the mean free path of the gas molecules to the size of the damping gap – in this case the separation between the springs. The Knudsen number is given by

$$Kn = \frac{\lambda}{L} = \frac{k_B T}{\sqrt{2\pi\sigma^2 PL}} \quad (5.5)$$

where,

λ is the mean free path (m), L is the representative physical length scale (m), k_B is the Boltzmann's constant (1.38×10^{-23} J/K), T is the temperature (K), σ is the particle diameter (m) and P is the total pressure in Pascal (Pa).

The rarefaction of flow based on Knudsen number is generally divided into four flow regimes: Continuum regime (<0.001), slip flow ($0.001 - 0.1$), transition flow ($0.1 - 10$) and free molecular (>10). For the silicon suspension with spring gaps of $410 \mu\text{m}$, Kn is unity at a pressure of 330 Pa, and the transition is expected for pressure range of 3.3 Pa to 3.3 kPa. Below 3.3 Pa the material damping will dominate and above 3.3 kPa the Q does not change with pressure but is much reduced.

In the environmental SEM, the quality factor for low pressure between 1 Pa and 0.001 Pa is extrapolated from the rarefied regime as the chamber is not capable of varying pressure in this range.

The suspension used in this case was etched silicon with a 200 nm oxide on the top surface and a thin coating of polymer (passivation layer) on its sidewall from DRIE. Cleaning the passivation layer increase the Q even further at UHV to 250,000. Even though it is possible to attain such high Q for a bare silicon suspension, it is not realistic to attain similar Q for the complete device as the presence of other metal and polymer insulator layers dictate the Q of the device (as metal and polymer have much higher material loss leading to a low Q) and preempt any aggressive chemical etch required to get rid of the Teflon coating on the suspension sidewalls.

In the SEM, the suspensions are mounted such that the regions above and below the die is unconstrained so at high pressure (>400 Pa until 1 bar) the only damping that occurs is due to the air flow between the springs. The analytical formula for calculating the squeeze flow damping coefficient in the high pressure regime (non-varying viscosity) is given by

$$\alpha_{squeeze} = \frac{14\eta l t^3}{Nd^3} \quad (5.6)$$

where l is the length of the spring, t is the thickness of the spring, N is the number of spring sets, d is the gap between the parallel sides of a spring and η is the viscosity of the surrounding media.

For a suspension with two set of springs and one intermediate frame $N = 4$, $t = 525 \mu\text{m}$, $\eta = 1.98 \times 10^{-5} \text{ kg m}^{-3} \text{ s}^{-1}$, $l = 8032 \mu\text{m}$, $d = 410 \mu\text{m}$. The coefficient of squeeze flow damping is calculated by using equation 5.5, $\alpha_{squeeze} = 1.16 \times 10^{-6} \text{ kg m}^{-2} \text{ s}^{-1}$.

Q-factor due to squeeze flow damping is given by

$$Q_{squeeze} = \frac{m\omega_0}{\alpha_{squeeze}} \quad (5.7)$$

Using equation 5.6, we calculate the quality factor for the suspension due to squeeze flow damping as, $Q_{squeeze} \approx 14000$, which is much higher than the experimentally determined Q of 1000 at high pressure. This shows other effects besides squeeze film damping affect the Q -factor at high pressure. Viscosity is directly proportional to the ambient pressure in the rarefied regime so with decreasing pressure viscosity also decreases which reduces $\alpha_{squeeze}$ in turn increasing $Q_{squeeze}$.

5.3 Effect of Etch Profile Shape on Suspension

Dynamics

The experimentally measured value of resonant frequency was much lower than the model estimated value as we discussed in section 5.2.1. The DRIE etch causes a deviation of the spring profile from the ideal rectangular shape.

As discussed in section 4.5.8 the profile shape of an etched channel can be either tapering (towards or away from the centre line), vertical, bowing or a combination of these effects. It is generally difficult to maintain a vertical profile shape particularly for high aspect ratio structures as in this case. For these conditions it is important to

quantify and model the influence of the profile shape on the mechanical performance of the resulting device.

Previous works have analyzed the bending of folded cantilevers in the compliant direction if the deviation from the rectangular profile is small [5.3, 4] or trapezoidal [5.5], but the approximations made are not applicable to the more pronounced etch profiles observed in this work and elsewhere [5.6].

We quantify the profile shape for through-wafer etched beams and present an analytical model to evaluate the effect of profile shape on silicon lateral suspensions. A design methodology is developed to compensate for the non-rectangular spring cross-section and to achieve the requisite mechanical performance targets.

5.3.1 DRIE etch profile

Lateral undercutting of the sidewall resulting in bowing of the profile is attributed to various etching and plasma conditions. The time multiplexing of etching and passivation cycles in DRIE can be tuned to tailor the overall profile shape by varying various process parameters such as gas flow rate, chamber pressure, RF coil power and platen power. It becomes increasingly difficult to control the overall profile shape of the etched structures for deep etches, as various effects relating to changes in reactivity and charging come into play and change the etching characteristics with etch depth. With increasing etch depth, the sidewalls accumulate charge distorting the electric field lines causing the ions to deflect laterally towards the sidewall resulting in lateral etching [5.7, 8]. Also, with increasing etch depth, the reaction between ions and reactive neutral radicals increases causing accelerated lateral etching by the isotropic radicals [5.9].

Even though it is possible to tailor the overall profile shape of a HAR structure, the cross-section (CS) is almost never completely linear. This is not much of a concern for larger mechanical structures but can significantly affect the mechanical properties of slender structures where the undercut depth becomes a significant proportion of the structure width.

This is the reason why fabricated suspensions demonstrate significantly different resonant frequencies compared to the simulated device (Table 6.1). Detailed discussion on DRIE etch profile is presented in section 4.5.8.

5.3.2 Spring profile characterization

Spring cross-sections from various etch runs are analyzed to quantify the undercut. The beam cross-section is quantified using a scanning electron microscope (SEM) and white light interferometer. Figure 5.6 shows the SEM of the cross-section of the spring beam. The mask width of the beam was $24\ \mu\text{m}$ which is reduced to $22\ \mu\text{m}$ in the actual fabricated structure. Additionally the beam cross-section narrows in the middle to $16\ \mu\text{m}$ before reverting back to $22\ \mu\text{m}$ giving a bowed profile.

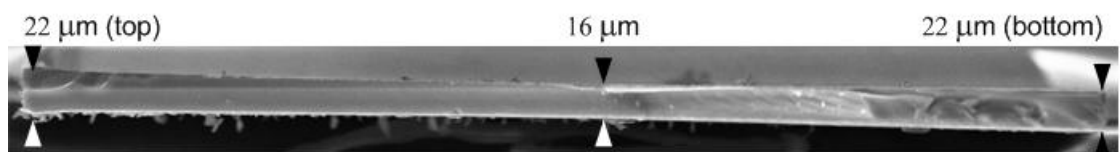


Figure 5.6 SEM image of beam cross-section. The mask design was for a spring width of $24\ \mu\text{m}$ which is reduced to $22\ \mu\text{m}$ at top edge of the spring during the etch and the middle section of the beam is thinner than the top and bottom.

The bowing is further characterised using interferometer as shown in Figure 5.7. The linescan shows the bowing on an exaggerated scale.

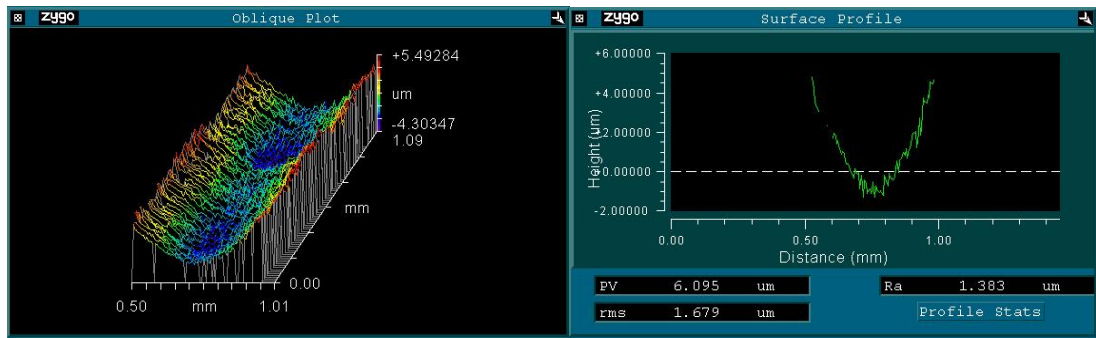


Figure 5.7 Undercut measurement using Zygo white light interferometer of spring cross-section.

A set of suspensions with $24\ \mu\text{m}$ and $31\ \mu\text{m}$ wide springs are etched to verify the consistency of the etch profile. Figure 5.8 shows that the undercut is similar for both the spring thickness, which means the undercut is independent of the feature size and is solely dependent on the process parameters (as discussed in section 4.5.8).

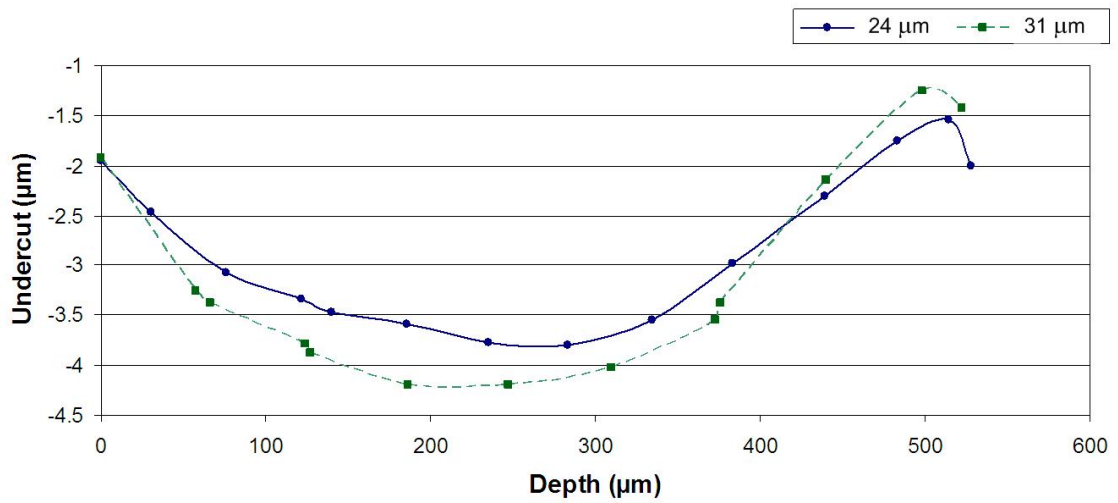


Figure 5.8 Measured lateral undercut for $24\ \mu\text{m}$ and $31\ \mu\text{m}$ wide beam.

The advantage of a feature size independent undercut is that one needs to measure the undercut for any one feature on the wafer and then the effect of undercut on the mechanical performance of all feature widths can be compensated using the data from the initial structure. This assumes that the etch trenches are same across the wafer, it is expected that for varying trench widths the undercut will also vary.

5.3.3 Analytical model

The non-rectangular beam cross-section (Figure 5.9) has an effect on the bending and torsion constants I_x , I_z and J . I_x and I_z are area moment of inertia along X and Z axes respectively. J is the torsional rigidity about the Y -axis. The profile can be quantified by a depth-dependent beam width, $w(t)$ which can be assumed symmetric about the yz -plane of the beam. The bending constant for a beam with thickness t is then given by

$$I_x = \frac{1}{12} \int_0^t w^3(t') dt' \quad (5.8)$$

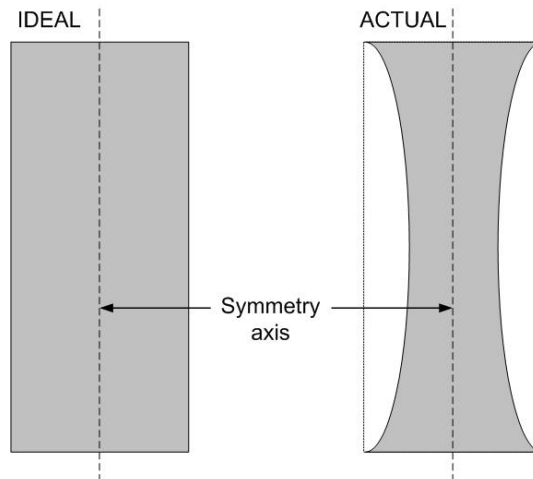


Figure 5.9 Beam cross section of an anisotropically etched beam, (a) rectangular cross-section, (b) bowed cross-section.

As the beam profile will normally be measured at a series of discrete points, for example from a SEM cross section, it is more useful to consider the numerical approximation for beam-width data $(w_n, t_n; n = \{1, N\})$, taken at a series of depths which need not be regularly spaced as shown in Figure 5.10.

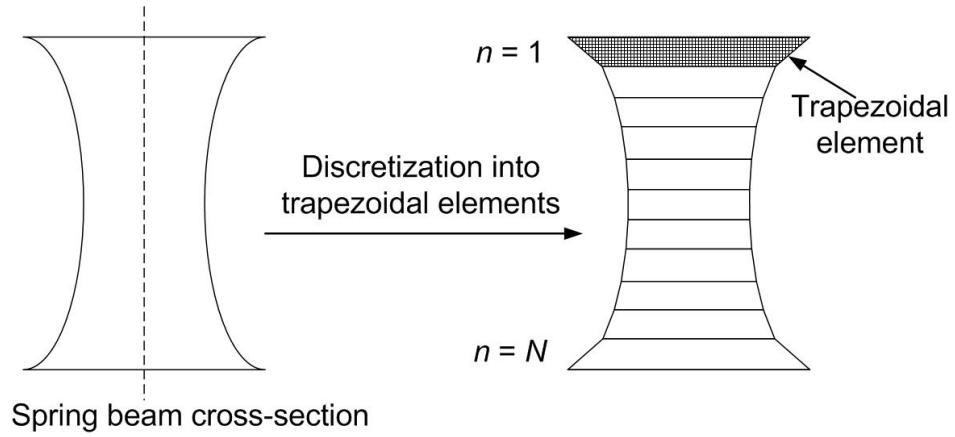


Figure 5.10 Discretization of the spring cross-section into trapezoidal elements to calculate the bending and torsional constants.

Approximating the profile as a series of trapezoids, the X -axis bending constant is given by

$$I_x \approx \frac{1}{24} \sum_{n=0}^{N-1} w_n^2 (t_{n+1} - t_n) (3w_{n+1} - w_n) \quad (5.9)$$

Similarly, for I_z approximating the profile to a series of rectangles:

$$I_z \approx \frac{1}{12} \sum_{n=0}^{N-1} w_n (t_{n+1} - t_n) \{3(t_n + t_{n+1} - t)^2 + (t_{n+1} - t_n)\} \quad (5.10)$$

The neutral axis of the beam is assumed to be at half the wafer thickness (t). The torsion constant can be derived with the help of membrane analogy [5.10]: the torsional rigidity of a cross section is directly proportional to the total volume swept by a pressurized membrane stretched over an opening the shape of the cross section. From this analogy the solution for a long thin beam, $J = w^3 t / 3$ can be decomposed for a long thin beam of varying width into contributions from thin slices of width dt' , giving

$$J = \frac{1}{3} \int_0^t w^3(t') dt' \quad (5.11)$$

which is proportional to the expression for I_x in equation 5.9. This proportionality is coincidental, applying only to thin beams, but has the important effect that the ratio of deflections due to torsion and bending in the compliant direction is unchanged by cross-sectional shape of the beam as we observed earlier in section 5.2.1. Hence, although the etch profile can have a large effect on the values of the normal modes of the suspension, ratios between modes will tend to be little affected, as the modes of the suspension are mostly dependent on I_x and J of the beams. For the analysis, an effective beam width, w_{eff} is given by

$$w_{\text{eff}}^3 = \frac{1}{3t} \int_0^t w^3(t') dt' \quad (5.12)$$

w_{eff} can be used in the expressions for a rectangular, high-aspect-ratio suspension geometry to give the correct values of I_x and J , although the value of I_z will not be valid. So the ratio of the modified natural frequency to the frequency for a rectangular spring cross-section is given by:

$$\frac{\omega_x}{\omega_{x0}} = \sqrt{\frac{I_x}{I_{x0}}} \quad (5.13)$$

where ω_{x0} , I_{x0} refer to the resonant frequency and second area moment for the nominal profile.

The various resonant modes for the suspension can be derived by using expressions from Table 3.5 with updated I and J values for the springs.

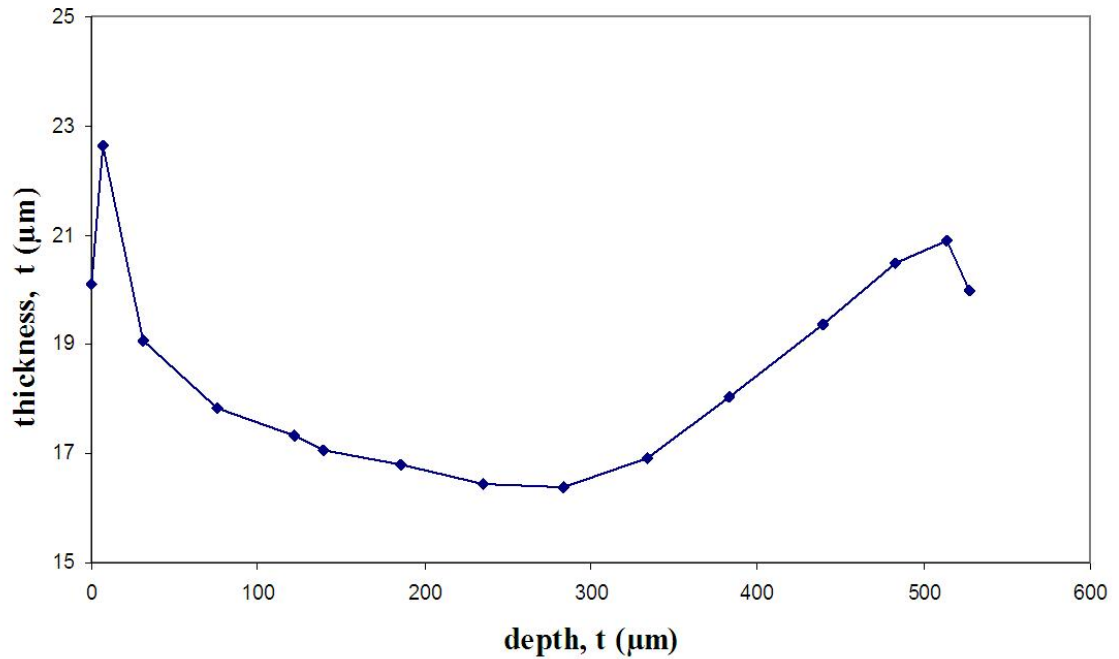


Figure 5.11 Etch profile of the spring - total spring thickness vs. etch depth.

By measuring the profile shape of a 24 μm wide spring (Figure 5.11) we have numerically calculated the new $I_x = 263821 \mu\text{m}^4$, $I_z = 236 \times 10^6 \mu\text{m}^4$ and $J = 105 \times 10^4 \mu\text{m}^4$. The effective width (w_{eff}) is calculated as 18.16 μm . I_x and J are just 43% of their nominal values assuming a rectangular profile with the spring width of 24 μm . I_z is less sensitive to the etch profile being only 80% of nominal, as the bending constant along the z-axis is mostly determined by the thickness of the spring which is constant and is only linearly dependent on the width of the spring cross-section.

Table 6.2 compares the model estimated values incorporating the profile shape to the initial model estimates based on ideal rectangular profile and experimentally measured values. The FEA model was developed using an effective spring width of 18 μm with a rectangular profile which gives the same I_x and J as the analytical values. However, it is

not possible to simultaneously match I_z , which causes an error in the FEA calculation of ω_z as compared to the analytical model which is closer to the measured value.

Table 6.2 Resonant modes for a 24 μm wide spring suspension. Comparison between analytical, numerical and experimental data incorporating beam profile shape.

	Analytical (ideal)	Analytical (profile)	FEA	Observed
ω_x	12.2	8.1	8.0	7.9±0.1
ω_{x1}/ω_x	17.5	17.5	14.2	15.7±0.1
ω_y/ω_x	9.4	9.3	8.8	9.4±0.3
ω_z/ω_x	10.1	11.5	10.2	11.9±0.2
ω_{α}/ω_x	12.4	12.4	13.6	not measured
ω_{β}/ω_x	20.6	23.5	20.5	19.2±0.2
ω_{γ}/ω_x	9.2	9.1	9.5	10.5±0.5

The agreement between analytical and FEA model incorporating profile shape with observed values provide confidence in the lateral suspension models. Analyses of other suspensions show excellent agreement of FEA and analytical results for a broad range of geometrical designs.

5.3.4 Compensation for a non-ideal etch profile

To compensate for the reduction in frequency, the width of the spring has to be increased so that the second area moments I_x , I_y and torsional rigidity, J for the spring with the bowed profile is similar to the values required for achieving the correct resonant frequencies. The compensation strategy for achieving the performance target is as shown in Figure 5.12. The addition of a rectangular area to the existing spring profile

to achieve the effective thickness for the required resonant frequency is possible due to the profile shape being independent of the feature width as demonstrated in Figure 5.8.

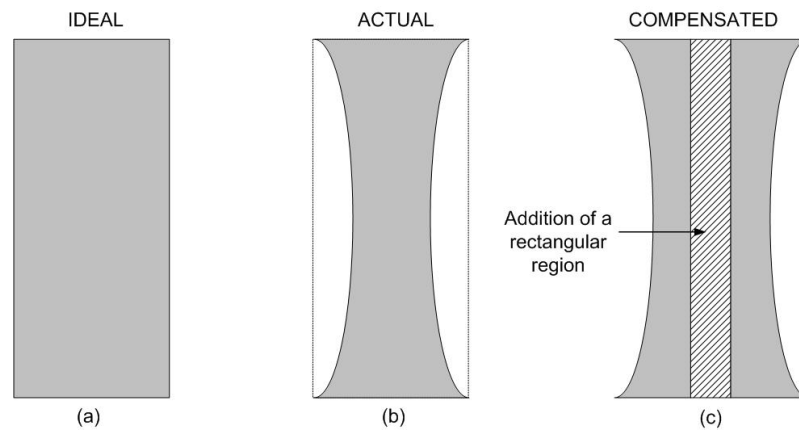


Figure 5.12 Compensation for spring etch profile. (a) Ideal, (b) Actual after fabrication, and (c) Compensated beam cross-section showing the addition of a rectangular area of width Δw to increase the second moment of area I_x for the fabricated spring beam to specification.

The additional width of the spring (Δw) is calculated by solving the equation for the moment of area I_x for spring with nominal thickness required for achieving the specified resonant frequency (10 Hz in this case).

$$I_{nominal} = I_{fill} + I_{actual} + 2\left(\frac{\Delta w}{2}\right)^2 \frac{A_{spring}}{2} \tag{5.14}$$

$$I_{nominal} = \frac{\Delta w^3 t}{12} + \frac{\Delta w^2 A_{spring}}{4} + I_{actual}$$

where A_{spring} is the cross-sectional area of the spring (Figure 5.12b), $I_{nominal}$ is second area moment for spring with effective width required for achieving the specified resonant frequency, I_{actual} is the second area moment for the spring which is fabricated and is the basis for the next set of designs, I_{fill} is the second area moment for the added rectangular area to increase the I and J components of the spring, and t is the thickness of the spring (same as thickness of the wafer). To calculate Δw we need to solve a cubic equation of the form:

$$\frac{\Delta w^3 t}{12} + \frac{\Delta w^2 A_{spring}}{4} - (I_{nominal} - I_{actual}) = 0 \quad (5.15)$$

For the current design specification with 24 μm spring width,

$$I_{nominal} = \frac{1}{12} \times 24^3 \times 500 = 576000 \mu\text{m}^4$$

$$I_{actual} = \frac{1}{12} w_{eff}^3 t = \frac{1}{12} \times 18^3 \times 500 = 243000 \mu\text{m}^4$$

$$A_{spring} = 9535 \mu\text{m}^4 \text{ and } t = 500 \mu\text{m}.$$

Solving equation 5.12, we get $\Delta w = 6 \mu\text{m}$.

The compensated spring would have a thickness of 30 μm (24 μm + 6 μm) to achieve the specified resonant frequency of 10 Hz. We fabricated suspensions with 30 μm wide spring and measured its resonant frequencies, which is presented in Table 6.3 along with the original 24 μm wide spring suspension. For the analytical model we numerically calculated the values of I_x , I_z and J from the SEM of the cross-section of the spring (Figure 5.13).

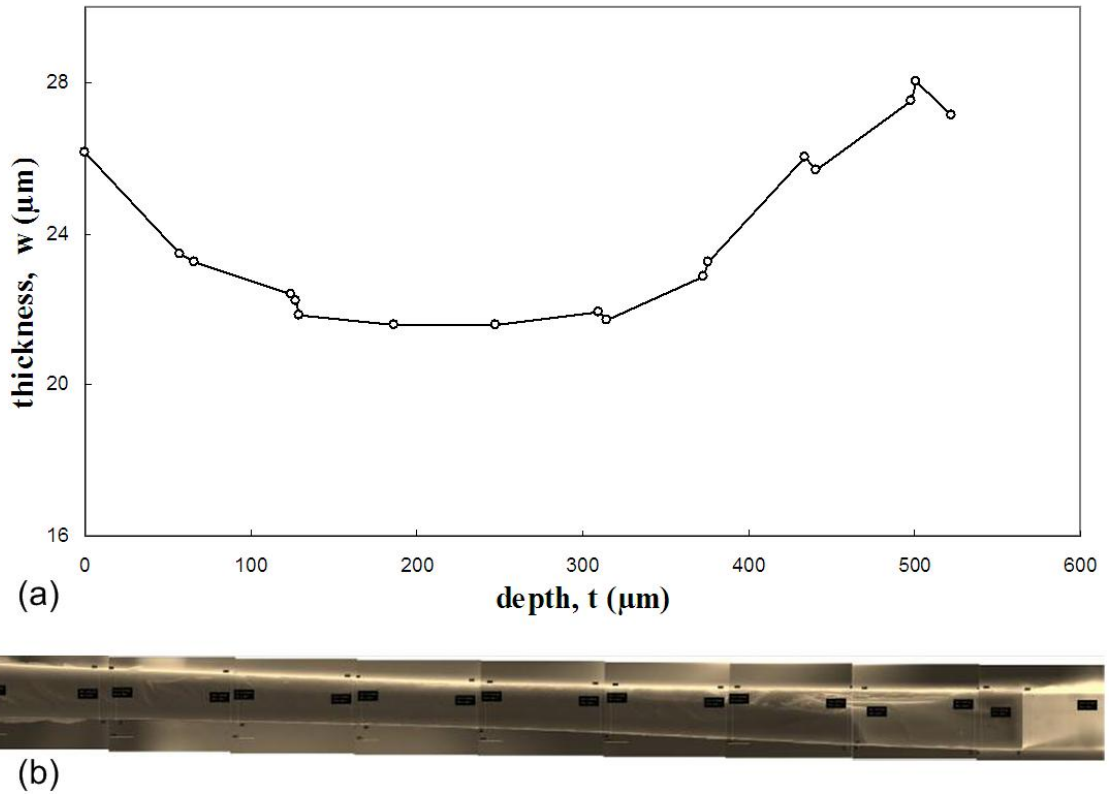


Figure 5.13 Spring profile for 30 μm wide beam, (a) total spring thickness vs. etch depth, (b) SEM of the beam cross-section.

As we can observe from Table 6.3, the suspension with 30 μm wide spring is close to our initial specification of 10 Hz. The cross-axis sensitivity also improves as the wider spring in addition to being compliant along X -axis also increases the stiffness along Z -axis.

The analytical model developed is further verified by calculating the resonant frequencies and comparing it against measured values for a one spring set suspension with spring width of 24 μm . The analytical, FEA and measured values of the resonant frequencies are presented in Table 6.4.

Table 6.3 Modal frequency for suspension with 24 μm spring which is increased to 30 μm to compensate for the reduction in resonant frequency due to etch profile shape.

Resonant frequency	Initial Suspension design 24 μm springs			Compensated spring design 30 μm spring		
	Analytical (ideal)	Analytical (profile)	Measured	Analytical (ideal)	Analytical (profile)	Measured
ω_x	12.2	8.1	7.9 \pm 0.1	14.3	9.9	10.3 \pm 0.2
ω_{x1}/ω_x	17.5	17.5	15.7 \pm 0.2	14.9	14	12.5 \pm 0.5
ω_y/ω_x	9.4	9.3	9.4 \pm 0.3	11.1	11.1	11.3 \pm 0.2
ω_z/ω_x	10.1	11.5	11.9 \pm 0.2	9.3	11.1	19.0 \pm 0.2
ω_α/ω_x	12.4	12.4	-	10.8	14.3	-
ω_β/ω_x	20.6	18.8	19.2 \pm 0.2	17.6	17.1	13.0 \pm 0.2
ω_γ/ω_x	9.2	9.1	10.5 \pm 0.5	10.9	10.9	11.5 \pm 0.3

Table 6.4 Resonant modes for 1 spring set suspension with 24 μm wide spring.

	Analytical	FEA	Observed
ω_x	11.4	11.4	10.7 \pm 0.2
ω_{x1}/ω_x	20.4	36	42 \pm 2
ω_y/ω_x	7.7	7.2	6.8 \pm 0.4
ω_z/ω_x	10.1	8.3	9.5 \pm 0.5
ω_α/ω_x	14.9	10.4	not measured
ω_β/ω_x	19.3	15.7	not measured
ω_γ/ω_x	7.5	8.3	8.5 \pm 0.3

The analytical, FEA and observed values are in good agreement for the one spring suspension. The largest error is in the analytical result for the first on-axis spurious mode (ω_{x1}), where the observed value is double the model predicted value. This error is

not surprising as the assumption for the analytical calculation that the suspension has a constant mass density is least valid for a single spring. For the two spring suspension the agreement improves as the spatial periodicity of the suspension becomes closer to the assumed constant mass density of the suspension.

The design compensation scheme developed in this section allows for the estimation of resonant modes for a wide variety of lateral suspension designs prior to fabrication. The good agreement between the analytical and numerical model provides confidence in using the model to predict the dynamical performance of suspensions pre-fabrication.

5.4 Summary

The resonant frequency and quality factor of the suspension is measured using a variable pressure SEM. The Q of the suspension is measured to be 1000 at atmospheric pressure and about 40,000 at UHV. The resonant frequency measured for the suspensions are much below the model estimates. The rejection ratios however are similar to the estimates.

The discrepancy in the measured and model estimates is attributed to the non-ideal profile of the spring beams cross-section. The analytical and FEA models used an ideal rectangular geometry for the spring beam cross-section whereas SEM and interferometer scans confirmed the spring beam cross-section to be bowed. The difference in resonant frequency of the suspension is therefore due to the reduced area moment of the spring beam.

The analytical model is updated to incorporate the effect of the spring beam profile by using a numerically calculated area moment for the spring beam. The analytical model is then used to determine an effective spring thickness for the FEA analysis. Both analytical and FEA model are closer to the measured values after incorporating the etch profile shape.

A compensation scheme is devised to calculate the spring beam width to attain the specified resonant frequency. This enabled the design and fabrication of a new set of suspensions which are able to reach the desired resonant frequency of 10 Hz. The cross-axis rejection ratios are improved due to thicker springs.

The author's major contributions covered in this chapter are the characterization of fabricated suspensions. Some measurements were performed by other members in the microseismometer team for suspensions that were fabricated by the author, since such measurements are part of complete data sets presented in this chapter, they have not been individually recognized. The profile compensation scheme was implemented by the author in collaboration with Tom Pike. The spring beam profile characterization and updated numerical models are also performed by the author.

5.5 Conclusion

The lateral suspension demonstrated a Q of 1000 in air and 40,000 at UHV and removing the polymer coating from the spring sidewalls increased the Q to 250,000 – higher than anything reported for bulk fabricated single crystal suspension. The suspension satisfies the criteria set in chapter 2 to achieve $Q \geq 330$ to satisfy the NEA (Noise equivalent acceleration) requirement of $0.35 \text{ ng}/\sqrt{\text{Hz}}$.

After incorporating the effect of the etch profile shape, the analytical and numerical estimates are in excellent agreement with the measured resonant frequencies providing a high level of confidence on the lateral suspension models and their applicability to other designs.

As far as the dynamics of the suspension are concerned, a non-ideal etch profile, if properly incorporated into the design, causes few problems. Bowing reduces I_x and J so to increase it back to nominal value for the required resonant frequency, the spring is increased in width which increases I_z thus increasing the cross-axis separation of modes. Bowing also reduces the mass of the spring which improves the rejection ratio for the first on-axis spurious mode (ω_{x1}).

For fabricating metal traces on the springs, the bowed profile of the spring provides a larger top surface area for traces.

5.6 Bibliography

- [5.1] W. T. Pike and S. Kumar, "Effect of profile shape on mechanical performance of silicon lateral suspension," presented at 16th MME Micromechanics Europe Workshop, Gothenburg, Sweden, 2005.
- [5.2] W. T. Pike and I. M. Standley, "Determination of the dynamics of micromachined lateral suspensions in the scanning electron microscope," *Journal of Micromechanics and Microengineering*, pp. S82-S88, 2005.
- [5.3] R. Liu, B. Paden, and K. Turner, "MEMS resonators that are robust to process-induced feature width variations," *Journal of Microelectromechanical Systems*, vol. 11, pp. 505-511, 2002.
- [5.4] T. Harness and R. R. A. Syms, "Characteristic modes of electrostatic comb-drive X-Y microactuators," *Journal of Micromechanics and Microengineering*, vol. 10, pp. 7-14, 2000.
- [5.5] K. W. Lee, *Electromechanical modelling of trapezoidal microstructures*, Ph.D. Thesis, Department of electrical and electronic engineering, Imperial College, London, 2003
- [5.6] A. A. Ayon, R. Braff, C. C. Lin, H. H. Sawin, and M. A. Schmidt, "Characterization of a time multiplexed inductively coupled plasma etcher," *Journal of The Electrochemical Society*, vol. 146, pp. 339-349, 1999.
- [5.7] J. C. Arnold and H. H. Sawin, "Charging of pattern features during plasma etching," *Journal of Applied Physics*, vol. 70, pp. 5314-5317, 1991.
- [5.8] J. P. Chang and J. W. Coburn, "Plasma-surface interactions," *Journal of Vacuum Science & Technology A: Vacuum, Surfaces, and Films*, vol. 21, pp. S145-S151, 2003.
- [5.9] Y.-J. T. Lii and J. Jorne, "Redeposition during deep trench etching," *Journal of Electrochemical Society*, vol. 137, pp. 2837-2845, 1990.
- [5.10] W. Weaver, S. P. Timoshenko, and D. H. Young, *Vibration problems in engineering*, 5 ed: John Wiley & Sons, 1990.

Six

6 Microseismometer: Prototype

This chapter presents a brief description of the microseismometer prototype and its various components. Fabrication processes required to build each of the modules are also detailed along with some overall experimental results for the microseismometer. The work in this chapter has been a team effort with contributions from the author on each of the aspects covered. The overall design of the microseismometer is covered in Pike et al. [6.1, 2].

6.1 Seismometer

Seismometers measure the ground motion arising from a seismic event by determining the motion of the ground (reference frame) relative to the suspended proof-mass (inertial frame of reference). The relative motion can be measured as displacement, velocity or acceleration by various methods like strain gauges, magnetometers, electron tunnelling, piezoresistive sensing, piezoelectric sensing, interferometer and capacitive (or electrostatic) sensing. A description of these methods is provided in Kovacs [6.3].

Differential capacitive position transducer is the most widely used precision sensing mechanism and is employed in the most sensitive seismometers. Differential capacitive position transducer can be implemented as a distance (gap) changing or overlap area changing system (Figure 6.1). Gap changing systems have a non-linear transfer function whereas for systems where the overlap area of the plates is varied with position the change in capacitance is more linear (limited by fringing field effects) [6.4].

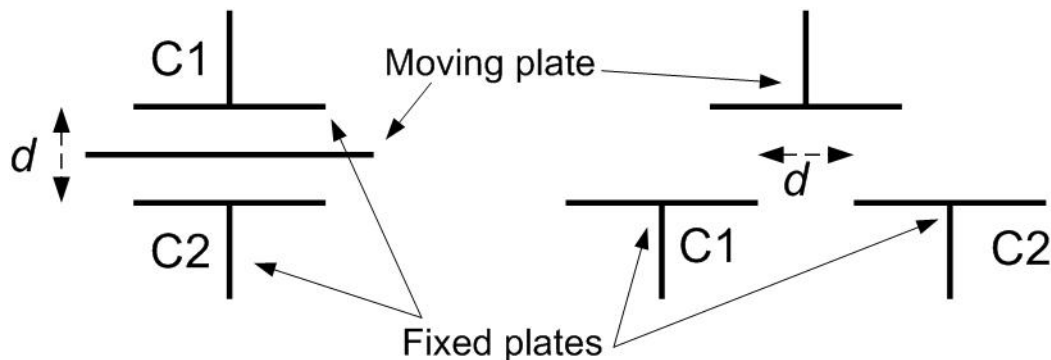


Figure 6.1 Two implementation of capacitive sensing, (a) distance (gap) changing: the distance between the plates is varied and (b) overlap area changing: the overlap area between the plates is varied with position.

The microseismometer can be operated in open-loop or closed loop configuration, in open-loop the voltage output of the capacitive transducer is the final output whereas in

closed-loop the output of the feedback controller is the final output. Operating a system with feedback provides the ability to shape the frequency response of the microseismometer and produce a linear signal. In addition, feedback increases the dynamic range, and sensitivity of the system. Feedback control is further discussed in section 6.3.

Conventional seismometers produce a velocity output, preferable in terrestrial seismology, since the background-seismic-velocity noise is evenly spread in its power spectrum and so the output allows the greatest dynamic range of the seismic signal over the band of interest. For an electromagnetic seismometer the proof-mass has a coil attached to it which moves in a magnetic field. The current induced in the coil is proportional to the velocity thus allowing a velocity output from the sensor.

The feedback actuation can be implemented as an electrostatic parallel plate or comb drive actuator or can be electro-magnetic in design with an actuation coil in an external magnetic field. The magnetic actuator provides much lower noise than the electrostatic counterpart as it does not require high voltages. Figure 6.2 shows the various subsystems of the microseismometer.

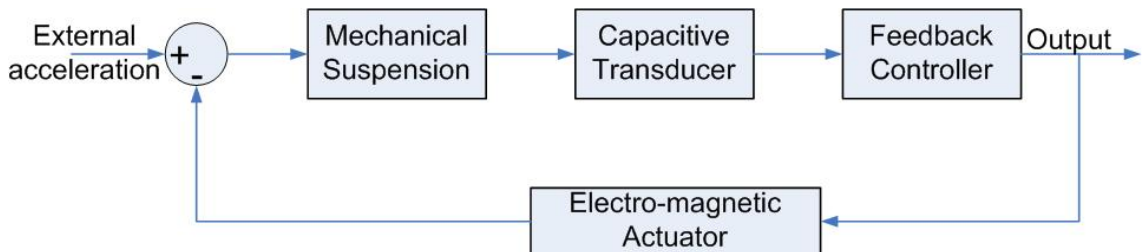


Figure 6.2 Block diagram of the microseismometer. The four major functional units are the mechanical suspension, capacitive transducer which converts the mechanical motion of the proof mass to electrical signal, feedback controller which drives the electro-magnetic actuator to keep the proof-mass at equilibrium.

Section 6.4 provides details of the electro-magnetic actuator designed for the microseismometer. In section 6.5 we will look at the fabrication aspects of the various mechanical components of the microseismometer. Section 6.6 provides a brief introduction to the assembly of the complete device; section 6.7 looks at damping of the packaged suspension and experimental test results are presented in section 6.8.

6.2 Lateral Differential Capacitive Array Transducer

The microseismometer employs a lateral capacitive array transducer (LCAT) [6.1] to sense the lateral motion of the proof mass (see section 6.2). This transducer determines the displacement between the fixed plate (pickup) and the parallel moving plate (drive) attached to the suspended proof mass by measuring the change in capacitance between the periodic electrode array on the drive and pickup plates. The sensitivity of differential capacitive transducer increases as the nominal gap between the fixed and moving plate is reduced. Increasing the sensitivity requires smaller electronic gain leading to smaller contribution of electronic noise to the overall noise of the system. However, decreasing the gap between the fixed and moving plates increases the coquette-flow damping of the suspension leading to higher mechanical noise. Hence optimum performance is a compromise between increasing the sensitivity and reducing the damping.

Figure 6.3 shows the cross-sectional view of the microseismometer assembly for the capacitive transducer. The suspension die is bonded to the fixed (capping) die at the edges while the central portions are separated by a micro-machined cavity. The suspension and capping die contain an array of drive and output electrodes, the direction of periodicity of the arrays aligned to the allowed motion of the proof mass. The drive

and output electrodes have the same periodicity (Figure 6.4a). The signal from the output electrodes are transmitted using traces over the springs.

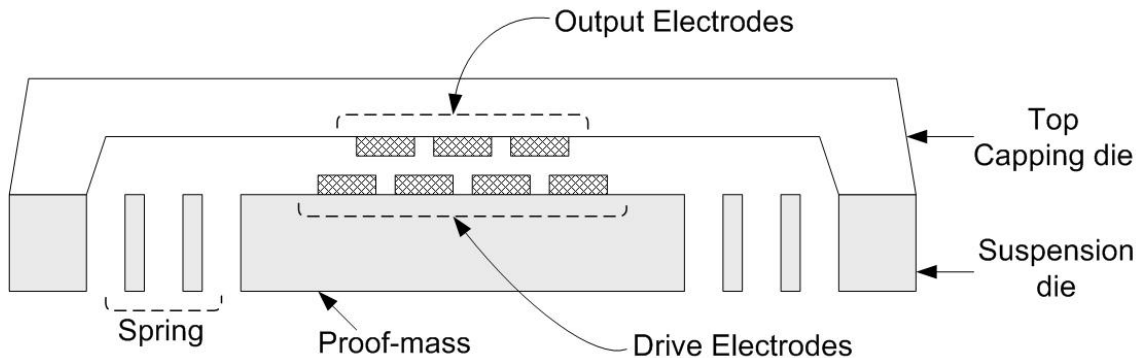


Figure 6.3 Cross-sectional view of the microseismometer showing the Capacitive array transducer with the drive electrodes on the proof-mass and a set of overlapping output electrodes on the top capping die.

Displacement of the proof mass under acceleration changes the relative position of the proof mass electrodes and the capping die electrodes. A small change in the relative position of these electrodes change the overlap between the proof mass electrodes and the fixed capping die electrodes and so can be transduced as a change in capacitance between the fixed and moving plates through suitable drive and pick-up electronics.

The LCAT's output electrodes are deposited on the silicon proof mass and the drive electrodes are deposited on the fixed glass layer aligned directly above the silicon substrate. The drive electrodes (Figure 6.4a) are driven with out-of-phase voltages, and two sets of output electrodes provide a differential output signal. Figure 6.4b shows the drive and output signals, the frequency of the drive signal is high enough to minimize low-frequency (so called $1/f$) noise common to analog electronics. There are 36 electrodes on each of the +/- DRIVE and +/- OUTPUT transducers. The gap between

the drive and output electrodes is 40 μm resulting in a capacitance of ~ 14 pF in equilibrium when there is an equal overlap between all the electrodes.

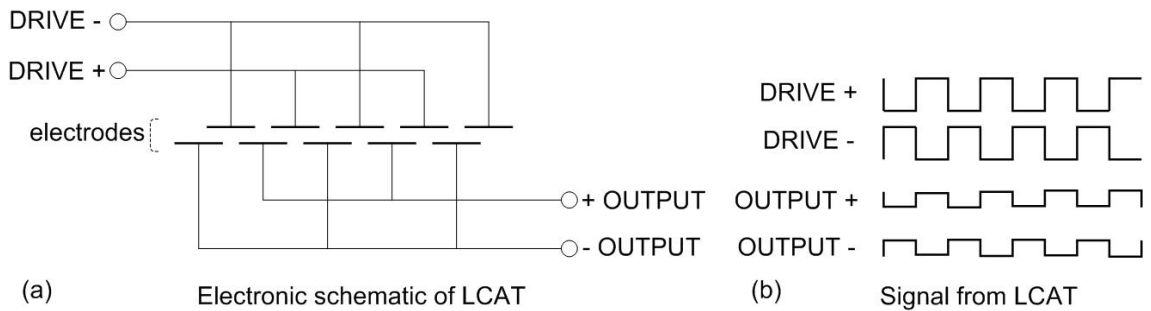


Figure 6.4 (a) Configuration of the drive and output electrodes, and (b) alternate drive electrodes are driven out-of-phase by a +DRIVE and –DRIVE square-wave pulse train. The output electrodes provide a differential output signal.

To reduce the parasitic capacitive coupling between the electrodes on the proof mass and the underlying silicon, a metal ground plane is used under the electrodes on the proof mass.

6.3 Feedback Controller

A seismic acceleration can, in general, be decomposed into two parts: a steady-state or “DC” signal due to the Earth’s gravity and a varying, or “AC” signal due to seismic activity. Only the “AC” signal is of interest with regards to a seismometer. The “AC” seismic signals are 160dB smaller than the “DC” gravitational signal. When a feedback is used in such circumstances, the actuator is unable to exert a large enough force to counteract the DC force and move the suspended proof mass to approximately a null position without severely degrading the sensor self-noise as the noise generated by the large actuator will dominate the instrument performance.

To enable the use of a low-force actuator thus maintaining the low-noise of the system, the feedback controller is supplemented with an open-loop DC operation also known as limit control. The limit control electronics allows the electrode arrays to transition between null points. When the suspension is under a steady force, such as a gravitational field, the proof mass is allowed to be displaced by many array periods of electrodes to a new null position under open-loop operation. The feedback is then reapplied.

The feedback drives the proof mass to the nearest null point. The preset limit is only slightly more than the signal range required to drive the proof-mass between the adjacent null points. Hence the actuator needs to be only strong enough to drive the proof mass over a little more than one period of the electrodes.

The feedback force is proportional to the current through the feedback coil. By passing the feedback signal through a capacitive differentiating circuit, the feedback force is proportional to the derivative of the sensor output voltage thus generating ground-velocity proportional output.

6.4 *Electromagnetic Actuator*

Electromagnetic actuators produce much higher force than their electrostatic equivalents. A current can be driven through a coil with less noise than a high voltage can be put on the electrostatic plates. Hence an electromagnetic actuator has less noise than its electrostatic equivalent.

The magnetic circuit is composed of two sets of external magnets of flattened horseshoe geometry on each side of the assembled dies. A set of rectangular spiral coils metallized on the proof mass are connected to the external electronics. As current flows through the coil, the proof mass experiences a lateral force ($F_{feedback}$) from both arms of the magnetic coil as given by Lorenz equation:

$$F_{feedback} = BIL \quad (6.1)$$

where B is the magnetic flux density, I is the current in ampere and L is the length of the coil under the magnetic field.

The magnets are so designed that the two arms of the spiral coil are within the linear portion of the magnetic field for most of their movement. The design of the magnet yokes have a significant effect on the magnetic flux density and numerical simulation is used to optimize the design (see section 6.5.3).

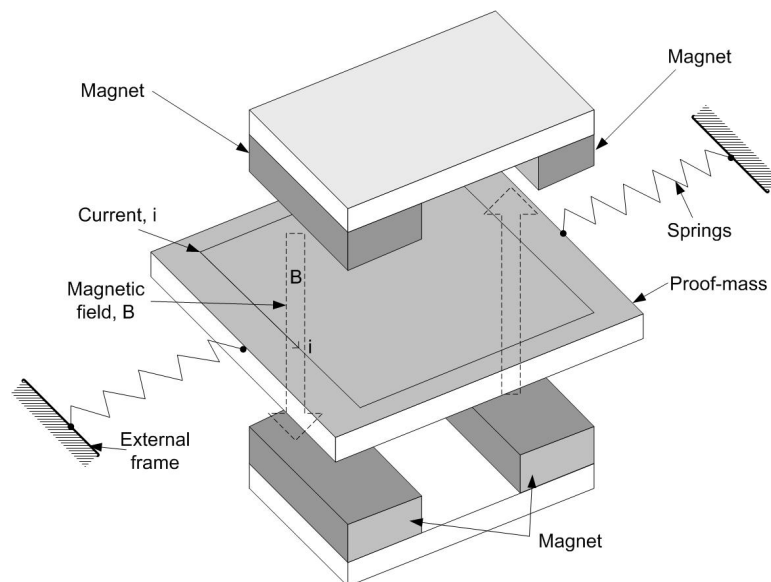


Figure 6.5 Perspective view of the magnetic circuit. The planar coil on the proof mass is enclosed by magnetic field from the pair of magnets on either arm of the coil. The feedback force is generated by running a current through the coil.

The dies are sealed at the edges using solder, so the traces are deposited under an insulator bridge through the seal to avoid shorting.

6.5 Components of Microseismometer

The microseismometer is composed of three main mechanical sub-units – the proof-mass die, the capping dies and the magnetic units. These three mechanical sub-units are fabricated separately and then assembled together as described in section 6.6.

6.5.1 Proof-mass wafer

The proof-mass wafer contains the proof-mass dies which comprises of the suspension and the circuit fabricated on the suspension. Figure 6.6 shows the complete proof-mass die with the mechanical suspension and the integrated circuitry for control and measurement of the suspension. The close-ups show the electrical traces running on the springs and the coil fabricated on the proof-mass.

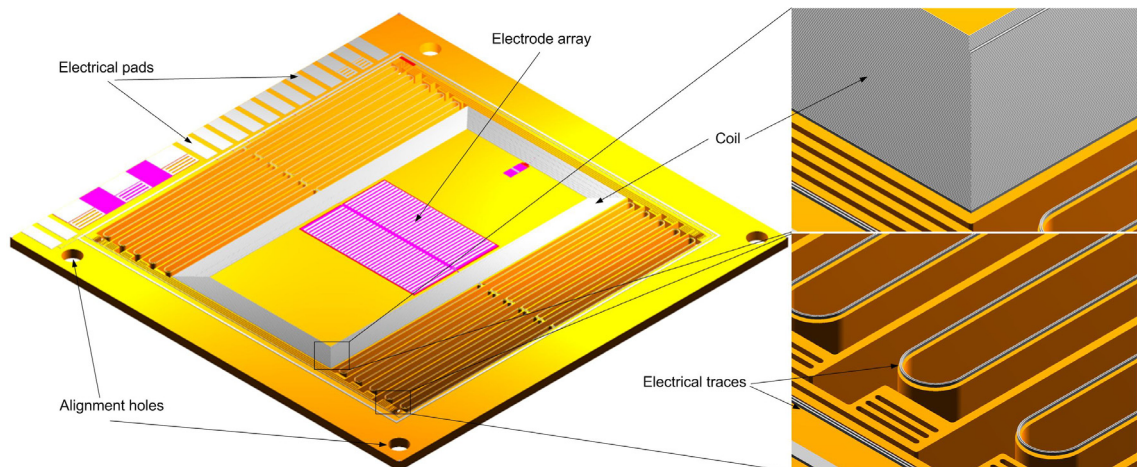


Figure 6.6 Proof-mass die showing the mechanical suspension with the circuit fabricated on top of the suspension to control and measure the displacement of the proof-mass.

The proof-mass die consists of the mechanical resonating unit, a coil to drive the suspension electromagnetically, a set of capacitive electrodes to pickup the

displacement of the proof-mass and a metal layer around the edge of the die (edge seal layer) to connect and hermetically seal the proof-mass die to the capping die.

The key requirements for fabricating the features on the proof-mass wafer are:

1. First Insulator layer: to electrically isolate the metal traces on top of the proof-mass and springs from the silicon substrate.
2. First Metal layer: to deposit a ground-plane under the drive electrodes on proof-mass to eliminate capacitive coupling with the silicon substrate and for metal links for coil and under edge seal (proof-mass capping wafer seal).
3. Second Insulator layer: to form a multiple loop coil for the electro-magnetic actuator and forming a bridge over the metal link going under the edge seal.
4. Second Metal layer: to form the coil, traces along the springs and pads for solder reflow.

Microseismometer: Prototype

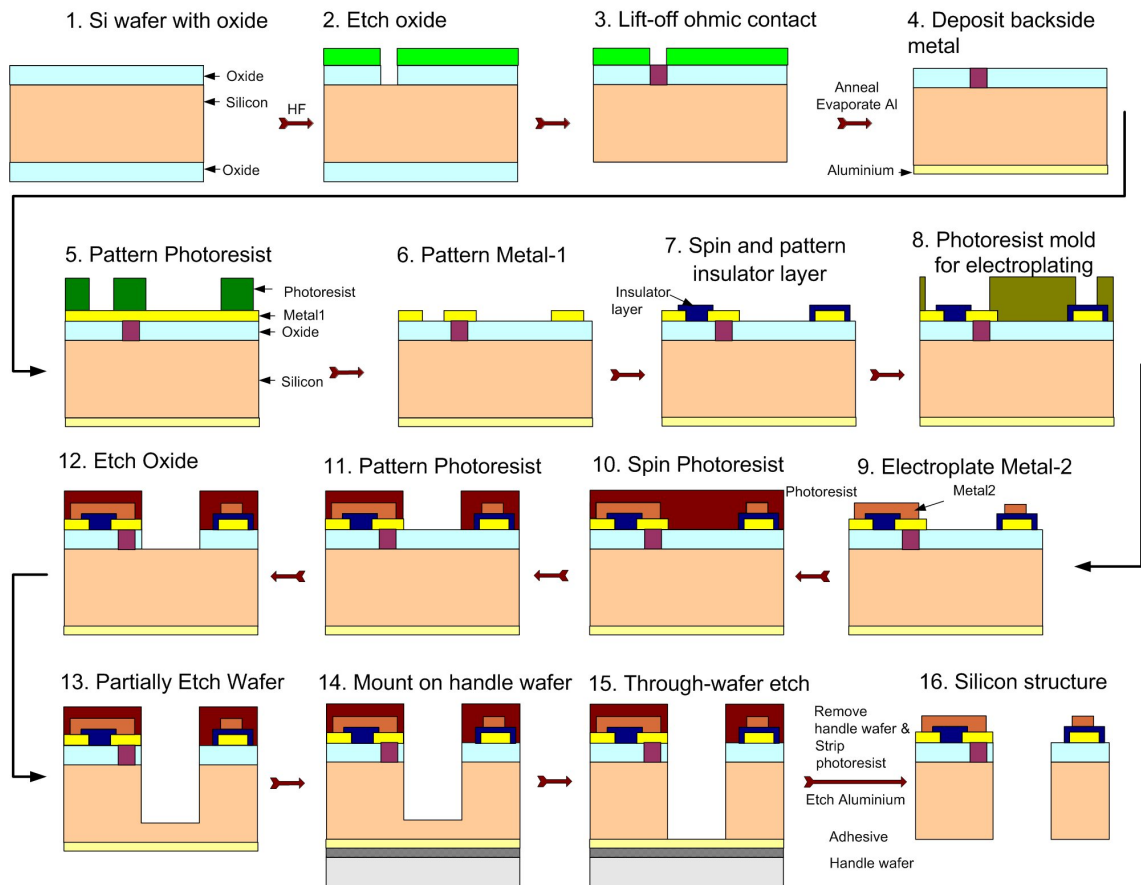


Figure 6.7 Process schematic for the complete suspension fabrication with metal and insulator layers.

Process flow for the full suspension fabrication is shown schematically in Figure 6.7.

The processing of the proof-mass wafer starts with a double sided polished single crystal silicon wafer. 200nm of oxide is grown thermally in a dry furnace (step 1, Figure 6.7). A 1 μm thick layer of SPR1813 is spun on one side of the wafer and it is patterned using the ohmic contact mask (step 2, Figure 6.7). The contact pads and the backside oxide is etched in 49% buffered HF for 6 minutes. To form the ohmic contact, metal lift-off process is used, a 75 nm layer of AuSb(1% Antimony) is evaporated followed by a 25 nm NiCr(80/20 weight percent Ni/Cr) layer and then a 200 nm Au cap layer (step 3, Figure 6.7). The wafer is then taken out of the evaporator and the resist is stripped before annealing it at 395°C for 1 minute. The contacts are then checked to confirm

whether they are ohmic, Figure 6.8 shows a typical I-V curve for ohmic contact pre-anneal and post-anneal. The resistance of the ohmic contact is 200 ohms. An issue with the ohmic contact pads is the formation of granular islands on the contact pad as seen in Figure 6.9, even though the pads appears non-shiny the contact resistance was consistent and the layer was mechanically stable.

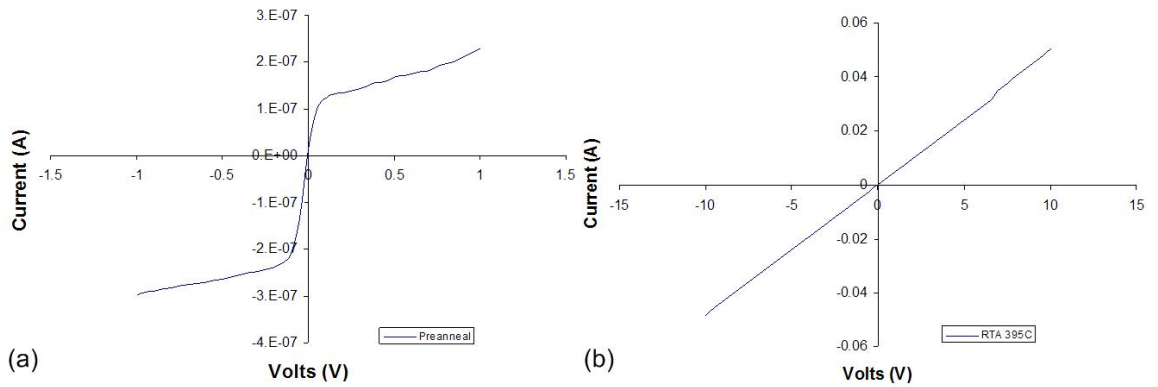


Figure 6.8 (a) Contact resistance of pads prior to anneal, and (b) Post-anneal I-V curve for contact pads showing a contact resistance of 200 ohms.

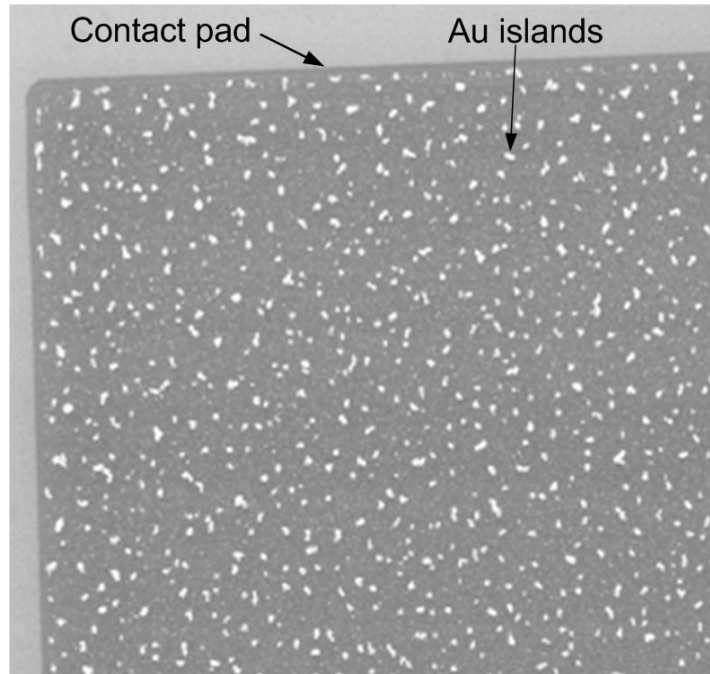


Figure 6.9 Contact pad post-anneal showing a rough surface, the brighter islands is the Au layer which dissolves in the underlying NiCr layer.

Next a 30nm Cr adhesion layer and 200nm Au Metal-1 layer is sputter deposited on the oxide layer(step 4, Figure 6.7). Subsequently a 0.5 μm thick layer of photoresist (Shipley SPR 1813) is spun and patterned lithographically (step 5, Figure 6.7). The metal layer is wet etched (step 6, Figure 6.7) to form the ground-plane for capacitive shielding of the capacitive electrodes for pickup, interconnect for making multiple loop coils and interconnects for connecting the traces to pads which are outside the edge seal layer. The patterned metal-1 is shown in Figure 6.10. Figure 6.11 shows metal-1 interconnect for making the connection across the edge seal layer underneath the insulator layer.

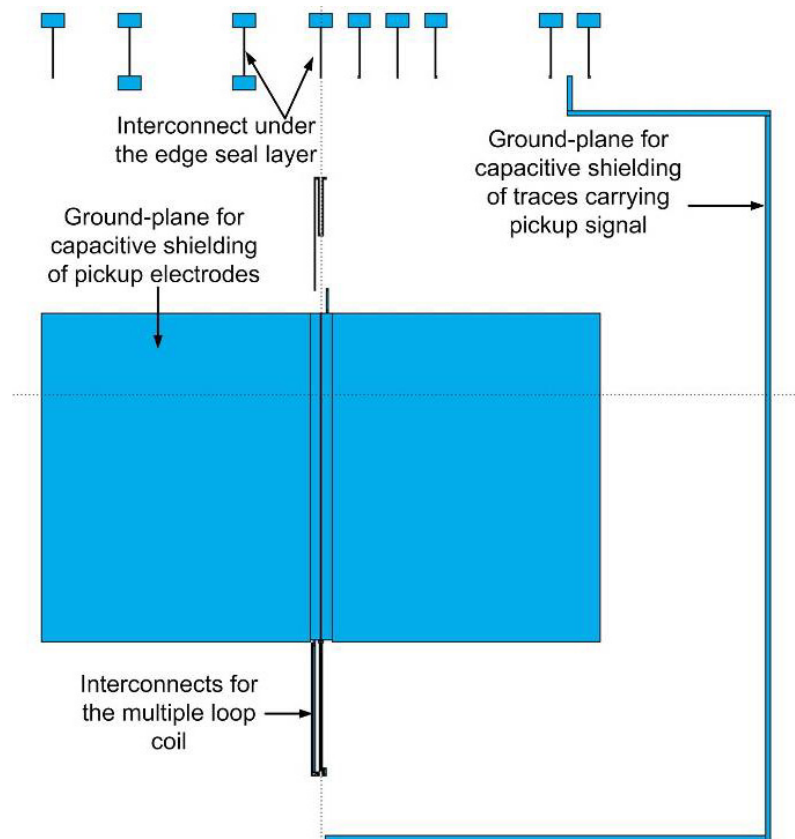


Figure 6.10 Mask layout of the metal-1 layer showing the ground-plane, interconnects for the coil and traces. Metal 1 is 30nm Cr and 200nm Au and is patterned by wet chemical etching.

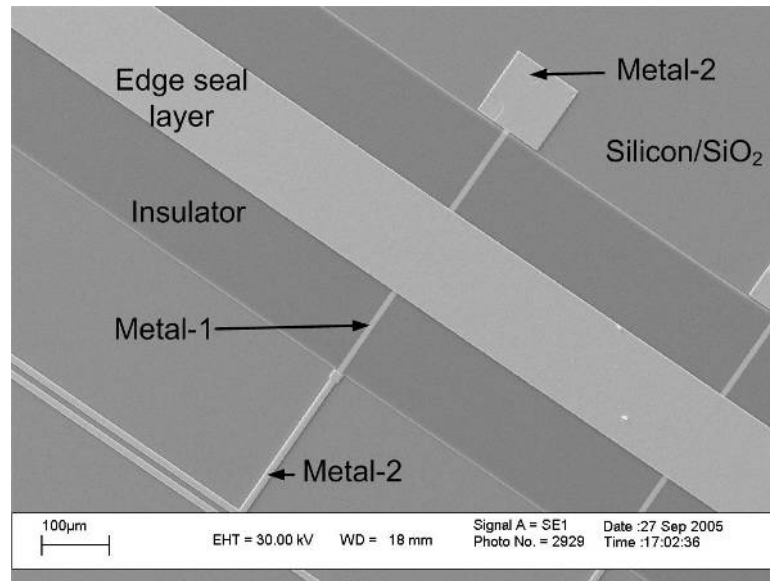


Figure 6.11 Metal-1 interconnect underneath the insulator layer for making the connection between two segments of metal-2 across the edge seal layer.

The next step in the process is the deposition of the insulator layer which in conjunction with metal-1 makes bridging under metal-2 layers possible. The insulator layer is photo-definable Photoneece [6.5], which is a positive polyimide. Photoneece is spun coated on the wafer, cured temporarily and then lithographically patterned (step 7, Figure 6.7). After developing the patterned photoneece, it is cured at high temperature to form a mechanically strong layer with sloping sidewalls suitable for running thin traces across the edge of the insulator (Figure 6.12).

The photoneece insulator layer is used to cover the ground-plane for subsequent fabrication of capacitive pickup electrodes on top. It also covers the metal-1 interconnects to bridge the metal-2 layer across the edge seal layer as seen in Figure 6.11.

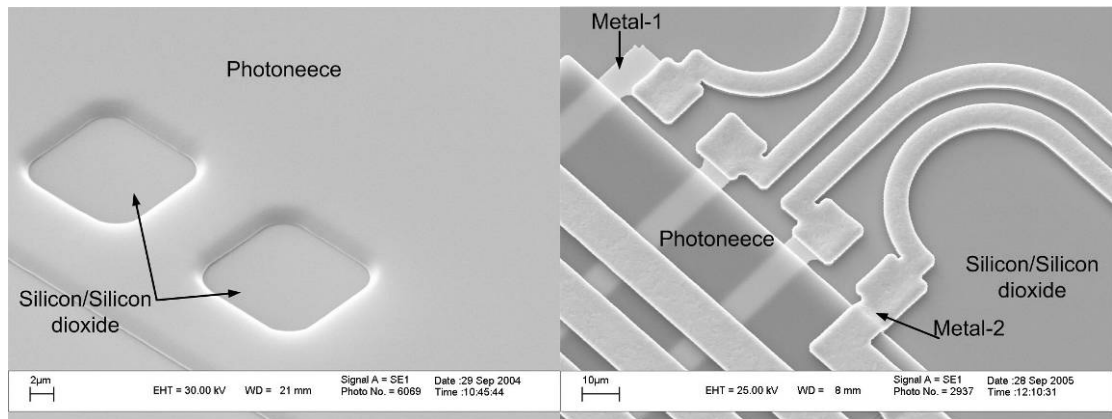


Figure 6.12 Photoneece, a photo-definable positive polyimide is spin coated on the wafer and lithographically patterned. The developed and cured photoneece layer has sloping sidewalls suitable for running thin metal traces across the edge of the insulator pads (courtesy: Werner Karl).

The topmost layer is the metal-2 layer which forms the coil, traces, edge seal layer, pickup electrodes and the pads for interconnectivity between the proof-mass die and capping die (Figure 6.13). To fabricate the metal-2 layer, a thin layer of Cr/Cu (30 nm/200 nm) is first sputtered on the full wafer. The Cr/Cu layer is then spin coated with a 10 μm photoresist (AZ9260) which is lithographically patterned to form the mold for subsequent electroplating (step 8, Figure 6.7). The mold is then immersed in an electroplating bath for plating Cu to a thickness of 5 μm (step 9, Figure 6.7) and then a 100 nm of Au is electroplated to protect the surface of Cu from oxidation (Figure 6.14a). The photoresist is then stripped and the initial seed layer is preferentially etched from areas where there is no electroplated Cu/Au (Figure 6.14b).

Microseismometer: Prototype

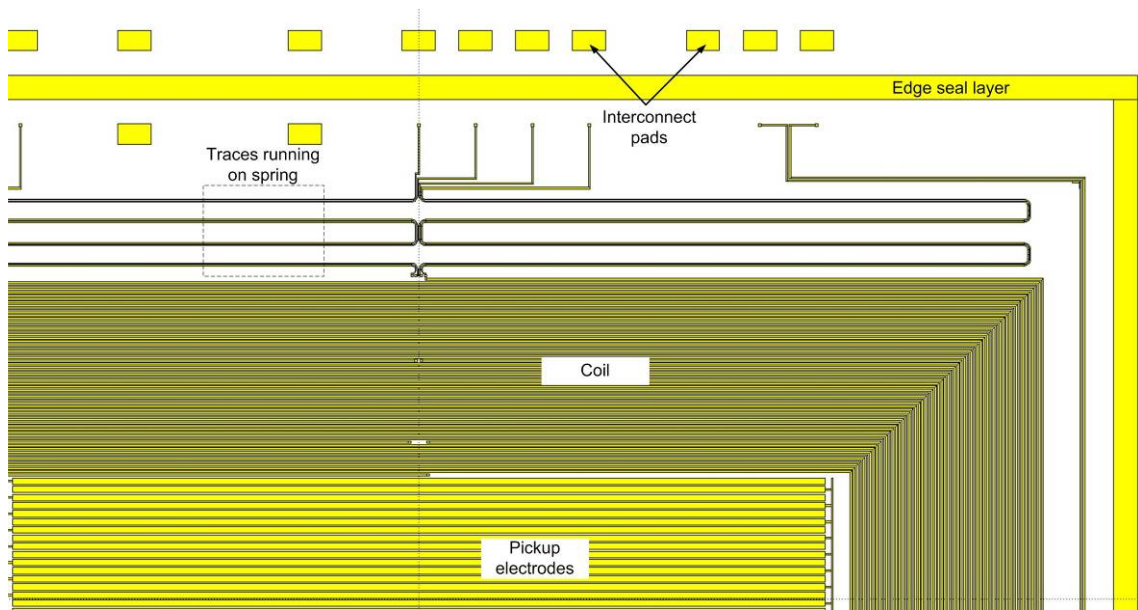


Figure 6.13 Metal-2 mask layout showing the coil, traces, edge seal layer, pickup electrodes and the interconnect pads for connectivity between the proof-mass die and capping die.

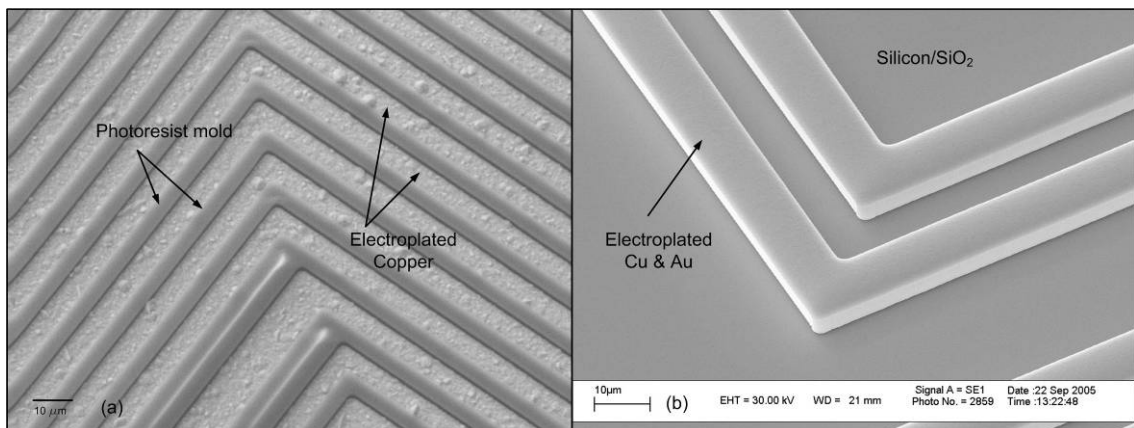


Figure 6.14 (a) Electroplated Cu in the photoresist mold, and (b) Electroplated Cu/Au after removal of the photoresist mold and etching of the initial Cr/Cu seed layer.

Figure 6.15 shows the complete metal-1, insulator and metal-2 layers fabricated on the proof-mass wafer prior to DRIE. After all the functional metal and insulator layers are processed, the backside of the wafer is coated with 500 nm thick Al layer in a thermal evaporator. The frontside of the wafer is then spun coated with a 14 μm thick layer of photoresist (AZ9260) which is lithographically patterned and developed for etching the

suspension (step 11, Figure 6.7). The wafer is first etched in CHF_3 plasma in RIE (Reactive Ion Etching) system to etch the oxide layer (step 12, Figure 6.7). After oxide etch the wafer is transferred to STS ICP Etcher for DRIE. The DRIE process is carried out in two steps. The first step etches the wafer partially to a depth of approximately 350-400 μm (step 13, Figure 6.7). The wafer is then removed from the etching chamber and mounted on a handle wafer using photoresist (step 14, Figure 6.7). The sandwich is then etched further in the DRIE etcher for the full thickness of the wafer (step 15, Figure 6.7). Due to the etch lag between the edge and center of the wafer, the complete wafer is overetched to etch all the trenches on the wafer to full wafer thickness.

On completion of the etch, the wafer is released from the handle wafer by dissolving the photoresist in a suitable solvent. The backside aluminum layer is wet etched and the packing pieces fall off the wafer. The dies are separated by breaking the tabs which hold them together.

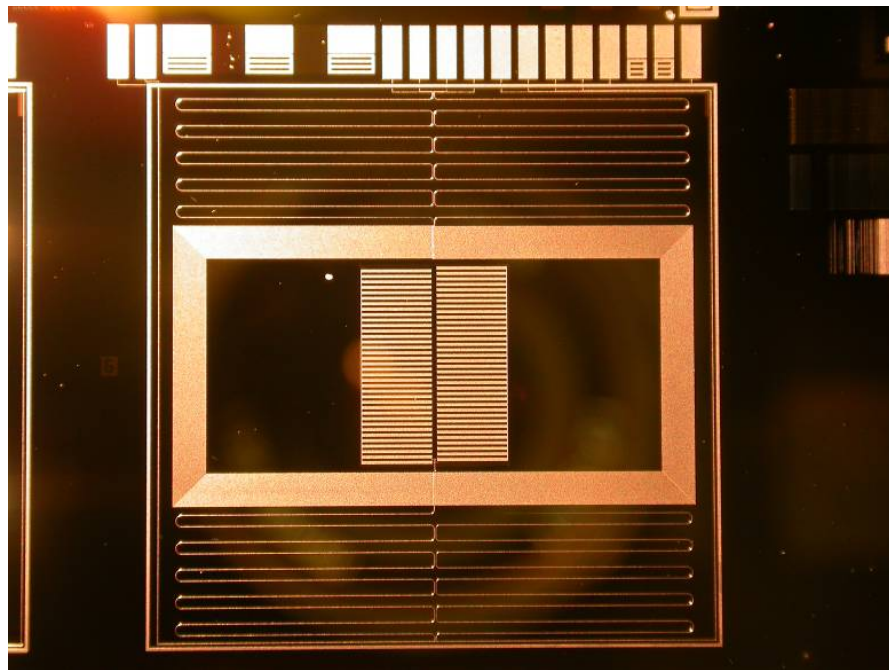


Figure 6.15 Optical micrograph of the circuit on top of the proof-mass die prior to DRIE.

Figure 6.16a shows the proof-mass die with all the layers. The traces run on the top surface of the springs (Figure 6.16b).

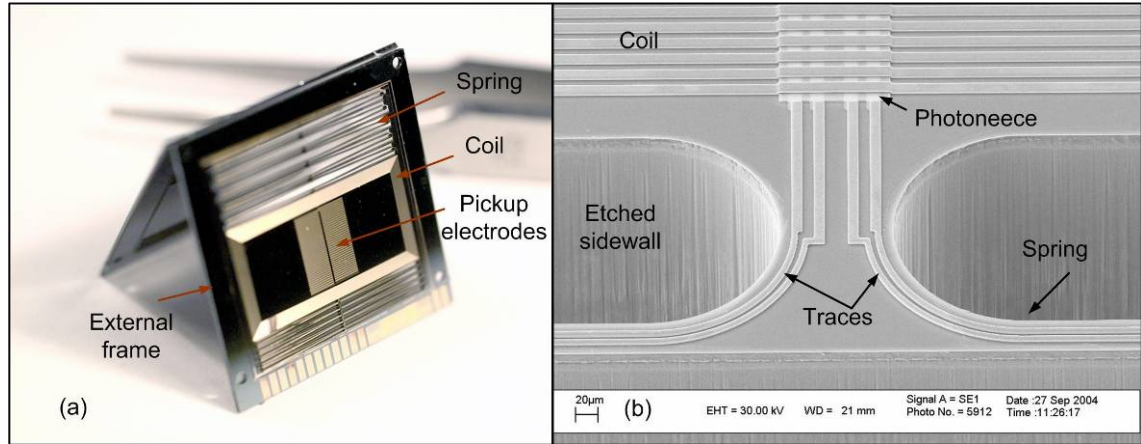


Figure 6.16 (a) A complete proof-mass die, and (b) Closeup of the metal traces on a spring (courtesy: Werner Karl).

Assembly of the final device is undertaken by reflowing solder to create a seal around the device die and to form an interconnect between the electrodes on capping wafer and device wafer, this is discussed in section 6.6.

6.5.2 Capping wafer

The suspension die is enclosed between two capping dies (Figure 6.17) made of borosilicate glass, the top one contains the pickup electrodes and the bottom die has a cavity to reduce damping. The suspension die is bonded to the pickup die using solder reflow, the bottom die is bonded to the suspension die using glass frit.

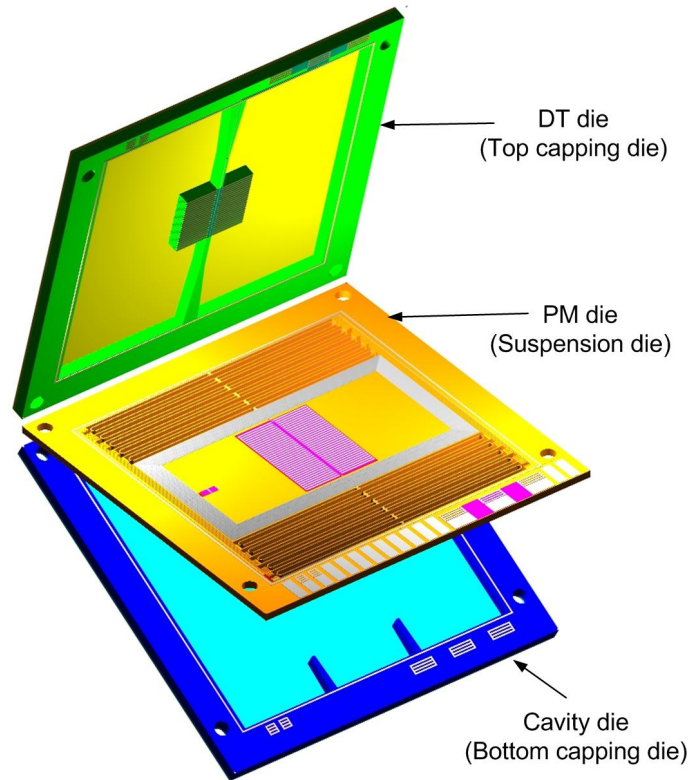


Figure 6.17 Exploded view of the capping and proof mass dies. The DT (Differential transducer) die contains the drive LCAT electrodes. The cavity die is underneath the suspension die and is required for vacuum encapsulating the suspension.

Process steps for the fabrication of the capping wafer is shown in Figure 6.18. The steps are similar for both top and bottom capping wafer except the presence of metal electrodes, and traces on the top capping wafer whereas the bottom capping wafer has no metallization. Both the top and bottom capping wafers are then sand powder blasted to form the cavities for decreasing the damping.

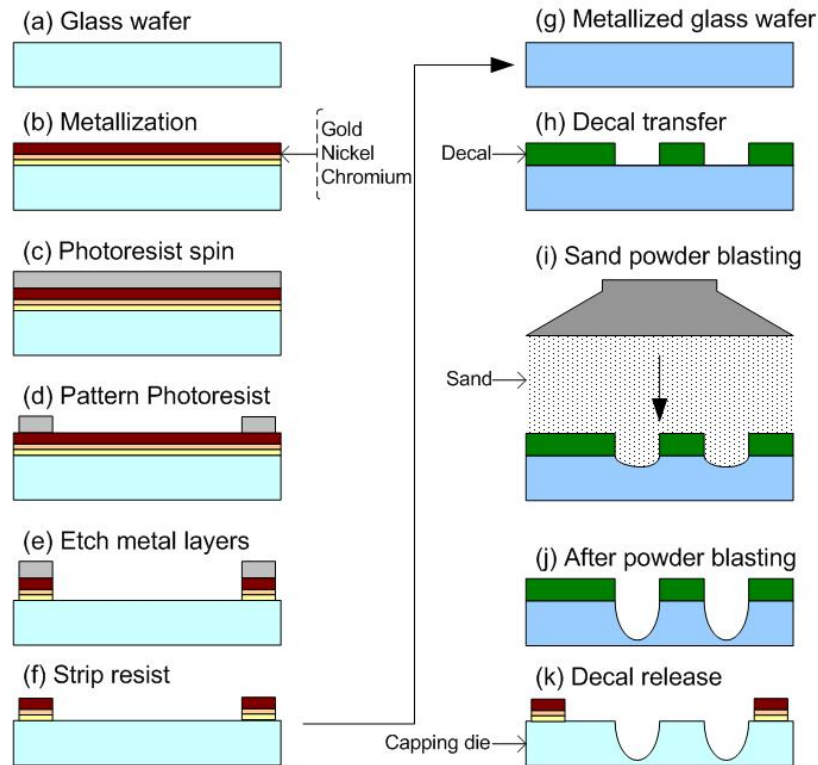


Figure 6.18 Schematic steps for metallization of the glass wafer and the subsequent sand powder blasting to etch the cavities.

The top capping die contains the capacitive pickup electrode array for measuring the displacement of the proof-mass. In addition it contains a seal ring on its edge. The seal ring has solder deposited on it by either electroplating, jetting or manual solder ball placement. The solder is then reflowed to form the seal and electrical contact between the capping die and the proof-mass die (discussed in section 6.6.1).

To form the capacitive electrodes, traces and the seal ring on the top capping die, a layer of 30nm Cr adhesion layer followed by a 200nm Ni and then 100nm Au are sputter deposited on the glass wafer. Subsequently a 500nm thick photoresist layer (Shipley SPR 1813) is spun coated on the wafer and lithographically patterned. The metal layers are then wet etched to pattern the features. Figure 6.19a shows the mask layout for the

metallization on the top capping die and Figure 6.19b shows the glass die with full metallization.

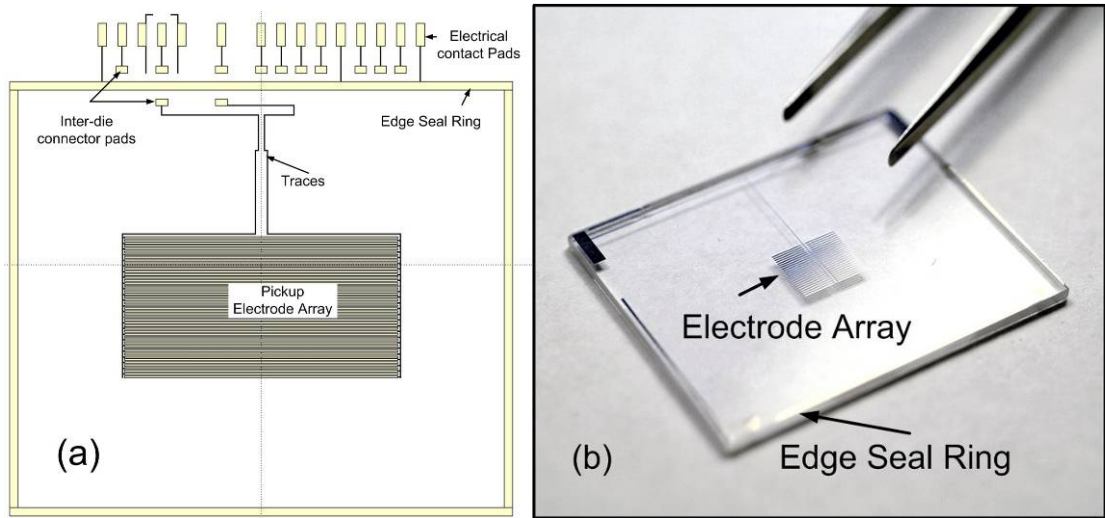


Figure 6.19 (a) Mask layout for the top capping wafer metal layer, and (b) Top capping die with the metal layer.

Subsequent to the metallization the wafer is powder sand blasted to form the cavity. The powder sand blasting is done by Crystal Mark [6.6]. Powder sand blasting is a fast low-cost, anisotropic glass etching process with aspect ratios of 1:6. A nozzle shoots a stream of fine sand onto the substrate, the etching is done by the physical removal of glass by the fine sand particles. A laser-cut pre-patterned polymer decal is stuck onto the wafers to protect the regions of glass wafer which are not etched. The decal also protects the underlying metal layers from exposure to the sand blasting.

Powder sand blasting creates sloping sidewalls which are quite suitable for creating cavities to reduce gas damping. 0 shows a powder sand blasted top capping wafer, the cavities are etched to the specified depth (800 μm) on the metal side of the capping wafer and then the wafer is turned over and the opposite side is sandblasted with an appropriate decal to create dicing lines for separating the capping dies. Figure 6.20

shows the etched cavity on one side of the wafer and the dicing etch from the other side. Powder sand blasting is used to create the cavities in the top capping wafer for reducing the gas damping.

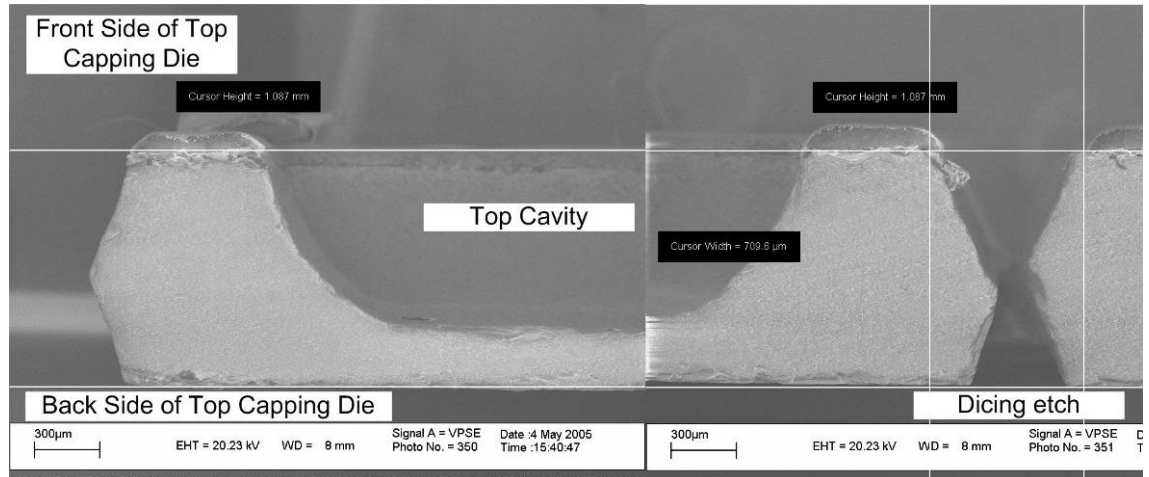


Figure 6.20 On the top capping wafer, the side containing the circuit is powder sand blasted first to etch the cavities, then the wafer is turned over and with a different decal dicing lines are etched through the glass wafer. This allows for easy release of the dies (*courtesy: Trevor Semple*).

The bottom capping die is primarily to decrease damping by having a large cavity. The bottom capping wafer is sand powder blasted to create the cavity to the desired depth on one side and then sand powder blasted from the backside to create the dicing channels. Glass frit is then screen printed on the wafer. The seal between the bottom capping wafer and proof mass die is formed by glass frit bonding which is discussed in section 6.6.2.

6.5.3 Magnetic unit

The magnetic actuator comprised a yoke piece, on each yoke two Samarium Cobalt (SmCo) rare earth magnets are mounted and on each magnet a pole piece is used to focus the field. Figure 6.21 shows the schematic of the magnetic actuator components.

The coil on the proof mass lies within the magnetic flux lines and a current running in the coil generates the feedback force as seen in Figure 6.22.

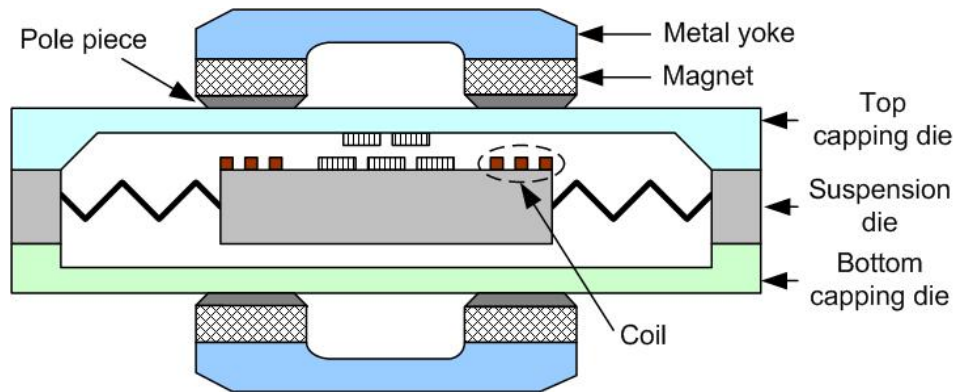


Figure 6.21 Magnetic circuit for the microseismometer comprising of magnets, yoke and coil. The yoke closes the circuit between the set of magnets on either side of the die sandwich. The yoke under the magnet smoothes the magnetic flux lines and creates a larger linear region for the coil to move within.

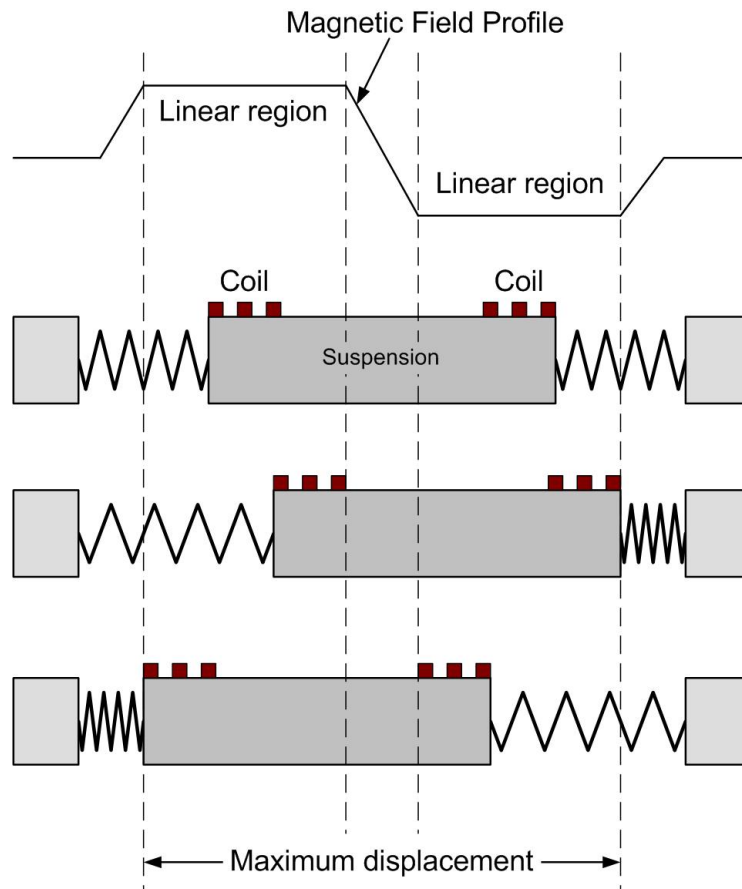


Figure 6.22 Location of the coil within the magnetic field. For maximum deflection force the coil should be in the linear region of the magnetic field.

Ansyz electromagnetic simulation is used to calculate the magnetic flux density at the coil on the proof-mass. The magnetic flux density is better concentrated when using pole pieces on the magnets. The bevelling of the pole piece also affects the strength and linearity of the magnetic flux density as seen in Figure 6.23.

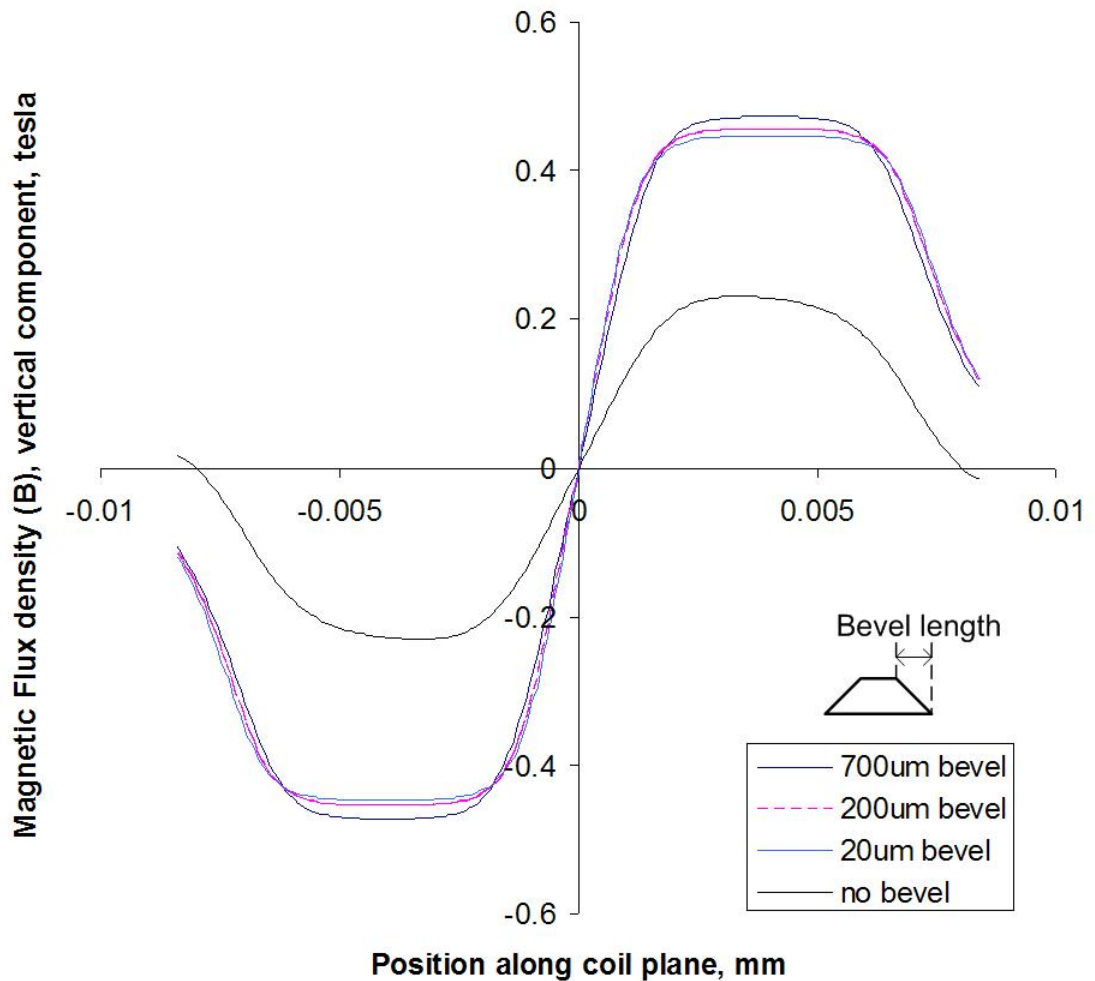


Figure 6.23 Magnetic flux density at the coil for varying level of bevelling on the yoke. As expected a sharper bevelling leads to a higher magnetic flux density but the linear range is reduced.

The magnetic components are glued to the device assembly. The soft iron yoke is coated to prevent corrosion. The magnets used are SmCo rare earth magnets.

6.6 Device Assembly

Figure 6.24 shows the schematic cross-section of a fully assembled microseismometer die, the proof mass and capping die is sandwiched between a set of magnets. The magnetic circuit consists of four magnets and iron yokes.

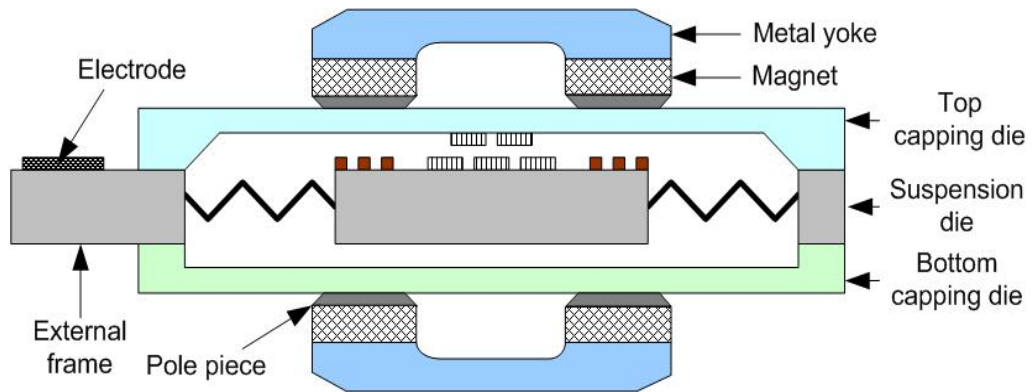


Figure 6.24 Cross-sectional view of the microseismometer assembly showing the yoke, magnets, top and bottom capping dies, proof mass die and electrode pads for signal readout and feedback.

The top capping die is attached to the proof-mass die using solder as discussed in section 6.6.1. The bottom capping die is attached to the proof mass die using glass frit, details of which are presented in section 6.6.2. The magnets are glued onto the yoke and the pole pieces are held to the magnets by the magnetic field. The magnetic actuator assembly is then glued on the outside surface of the top capping and bottom capping die.

6.6.1 Solder reflow

Solder reflow is used to form a contact between the pads on proof mass die and top capping die as the external pads are located on only proof mass die. In addition a solder ring all around the proof mass die and top capping wafer die is reflowed to form a hermetic seal. Figure 6.25 shows the schematic of the contact and solder seal between the top capping die and proof mass die.

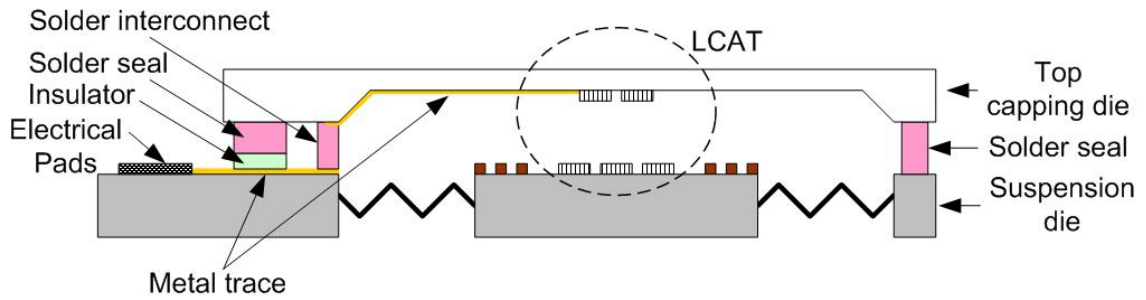


Figure 6.25 Schematic of the contact and seal between the top capping die and the proof mass die.

Solder reflow for bonding needs two wetting surfaces, one each on the two dies being bonded together. Solder wetting is the ability of solder to stick to a specific metal otherwise it will ball up to reduce its surface energy. Metals such as gold, copper and nickel have good wetting property and are used for making the pads where solder is initially deposited and also the pads which are ultimately bonded during solder reflow. For the microseismometer, the top capping wafer contains a layer of Cr/Ni/Au on top of which the solder is deposited. On the proof-mass wafer, the bonding pads are made of Cr/Cu/Au.

Various methods have been investigated for solder reflow like solder printing, solder paste screen printing, solder electroplating and solder ball placement either manually or using deep etched grooves.

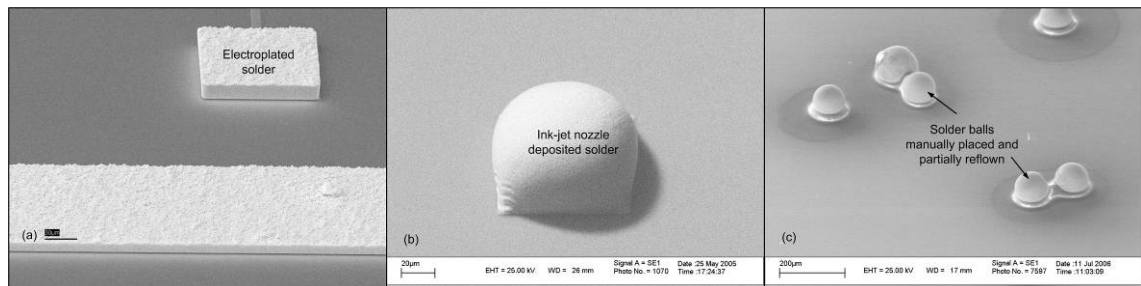


Figure 6.26 (a) Solder electroplating, (b) Solder jetting, and (c) Solder ball placement (courtesy: Trevor Sample).

Solder ball placement using grooves etched in silicon by DRIE is one of the promising methods where holes in a silicon wafer are etched which hold the solder balls. The balls are transferred onto the main wafer (glass top capping wafer with reflow pads) by application of flux to the reflow pads which are then reflow in-place. Figure 6.27 shows the schematic of the transfer of solder balls using a wafer with grooves for defining the location of the solder balls.

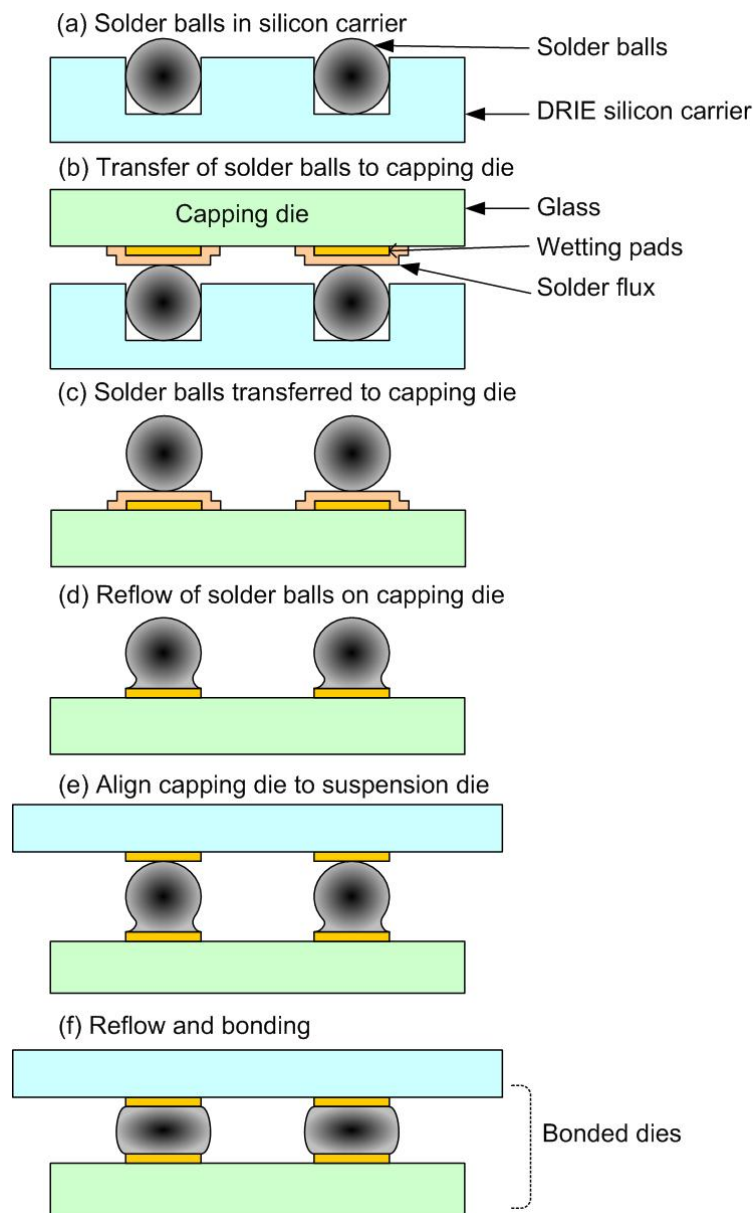


Figure 6.27 Mechanism of solder ball transfer using grooves on wafers, the grooves are etched using DRIE. The solder balls are transferred to the top capping die. The top capping and proof-mass dies are then aligned and bonded.

6.6.2 Glass frit bonding

Glass frit is screen printed on the bottom capping wafer, the bottom capping die and proof mass die are then aligned and heated to 350°C at which temperature the frit melts and forms a seal between the two dies (Figure 6.28).

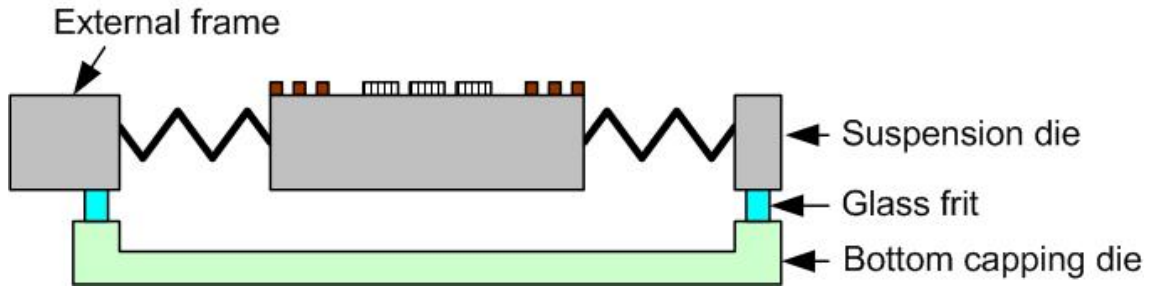


Figure 6.28 Glass frit bonding to form seal between the bottom capping die and the proof mass die.

The glass frit bonding is done at a higher temperature than solder reflow temperature so glass frit bonding step is performed prior to the solder reflow step.

6.6.3 Vacuum encapsulation

To encapsulate the mechanical resonator in vacuum the solder and glass frit bonding need to be hermetic. The vacuum encapsulation is performed during the solder reflow which is subsequent to the glass frit bonding. The top capping die and the proof-mass die are aligned and placed in the reflow chamber. A reducing gas is then introduced inside the chamber to remove oxide from the surface of the solder. The chamber is then evacuated and the temperature of the assembly is raised so that the solder reflows and wets the pads on the proof-mass die. Figure 6.29 shows the schematic of the vacuum encapsulation. The region marked by the red square represents the hermetically sealed cavity which contains the suspension.

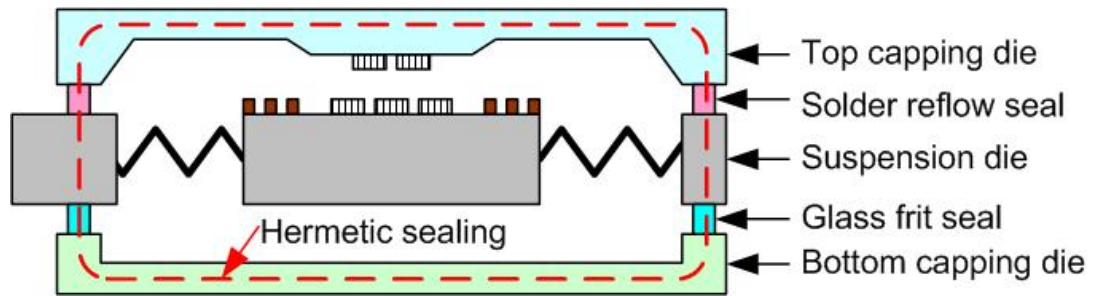


Figure 6.29 Schematic of the hermetically sealed cavity enclosing the mechanical resonator.

6.7 Microseismometer Damping

The thermal noise of the suspension increases with the damping of the suspension.

Damping in these suspensions is a sum of materials damping in the spring itself and gas damping, which at atmospheric pressures is dominated by viscous forces and is independent of pressure. The material damping will consist of damping in the silicon itself, expected to be very small, and losses in the surface layers resulting from the DRIE, potentially a much larger contribution. As we measured in section 5.2.2 Q was increased from 40,000 to 250,000 a 6 fold increase by removing the polymer coating from the spring sidewall.

The overall quality factor of the suspension depends on the sum total of the loss associated with the mechanical anchors, squeeze film, Couette flow, and Poiseuille flow damping as well as bulk losses associated with material defects and thermo-elastic damping (TED). The quality factor of the device due to gas damping is given by

$$\frac{1}{Q_{gas}} = \frac{1}{Q_{squeeze}} + \frac{1}{Q_{couette}} + \frac{1}{Q_{poiseuille}} \quad (6.2)$$

Analytical model to calculate squeeze film, Couette flow, and Poiseuille flow damping are discussed in [6.7-9]. Table 6.5 contains the dimensional parameters used to calculate the gas damping for the fully assembled microseismometer.

Table 6.5 Suspension dimensional parameters for damping calculation for microseismometer.

Parameters	Value
Air viscosity, η	$1.87 \times 10^{-5} \text{ kg/m}^3/\text{s}$
Silicon density, ρ	$2.33 \times 10^3 \text{ kg/m}^3$
Suspension resonance frequency, f_0	10 Hz
Cross-sectional area of the spring, A_{spring}	$24 \mu\text{m} \times 525 \mu\text{m}$
Length of spring, l_{spring}	8.032 mm
Number of spring, N	4
Thickness of springs, t	525 μm
Temperature, T	25°C
Mean free path λ at 1 atm	$70.0 \pm 0.7 \text{ nm}$
Spacing between springs, d_{spring}	410 μm
Gap between coil and pickup electrodes, d_{gap}	40 μm
Depth of cavity over proof-mass, h_{cavity}	800 μm
Depth of cavity under proof-mass, h_{frit}	150 μm
Area of proof-mass, $A_{proof-mass}$	187.55 mm^2
Area of electrode array, $A_{electrode}$	63.76 mm^2
Mass of proof-mass, $m_{proof-mass}$	$2.66 \times 10^{-4} \text{ kg}$

The theoretical Q -factor related to squeeze flow damping is given as

$$Q_{squeeze} = \frac{2\pi f_0 A_{spring} \rho N d_{spring}^3}{14\eta l_{spring} t^2} \quad (6.3)$$

Using equation 6.3 $Q_{squeeze} \approx 14000$ for a suspension with two set of springs.

Couette flow damping for a gap with thickness d is given by

$$Q_{couette} = \frac{d_{gap}}{\eta A_{proofmass}} 2\pi f m_{proof-mass} \quad (6.4)$$

where d_{gap} is the distance between the proof mass and the capping wafers and is divided into two components, one for the couette damping over the electrode array which is much closer to the proof-mass and the other between the proof-mass and the top and bottom cavities. Using equation 6.4, $Q_{couette} \approx 500$.

Poiseuille flow damping due to transfer of fluid between volumes is given by

$$Q_{poiseuille} = \frac{h^2}{12\eta A_{proofmass}} \sqrt{km} \quad (6.5)$$

where $h^2 = (d_{gap}^2 + (h_{cavity} + h_{fril})^2)$. Using equation 6.5, $Q_{poiseuille} \approx 700$.

The Q for the assembled device is then calculated from equation 6.2, $Q_{gas} \approx 290$.

Calculating the noise equivalent acceleration (NEA) for the device in air using equation 1.4, $NEA = 3.65 \times 10^{-9} \text{ ms}^{-2}/\sqrt{\text{Hz}}$. The NEA of the device is lower than the targeted NEA for the suspension. Couette flow damping is the dominant term in determining the overall Q of the suspension, so reducing the damping by increasing the gap between the proof-mass and the capping dies will lead to a higher overall Q enabling the suspension to meet the target noise level.

6.8 Experimental Result

The fully assembled device is then mounted on a single axis tilt holder. The output of the coil on the proof-mass is measured using a network analyzer. Figure 6.30 shows a fully assembled device.

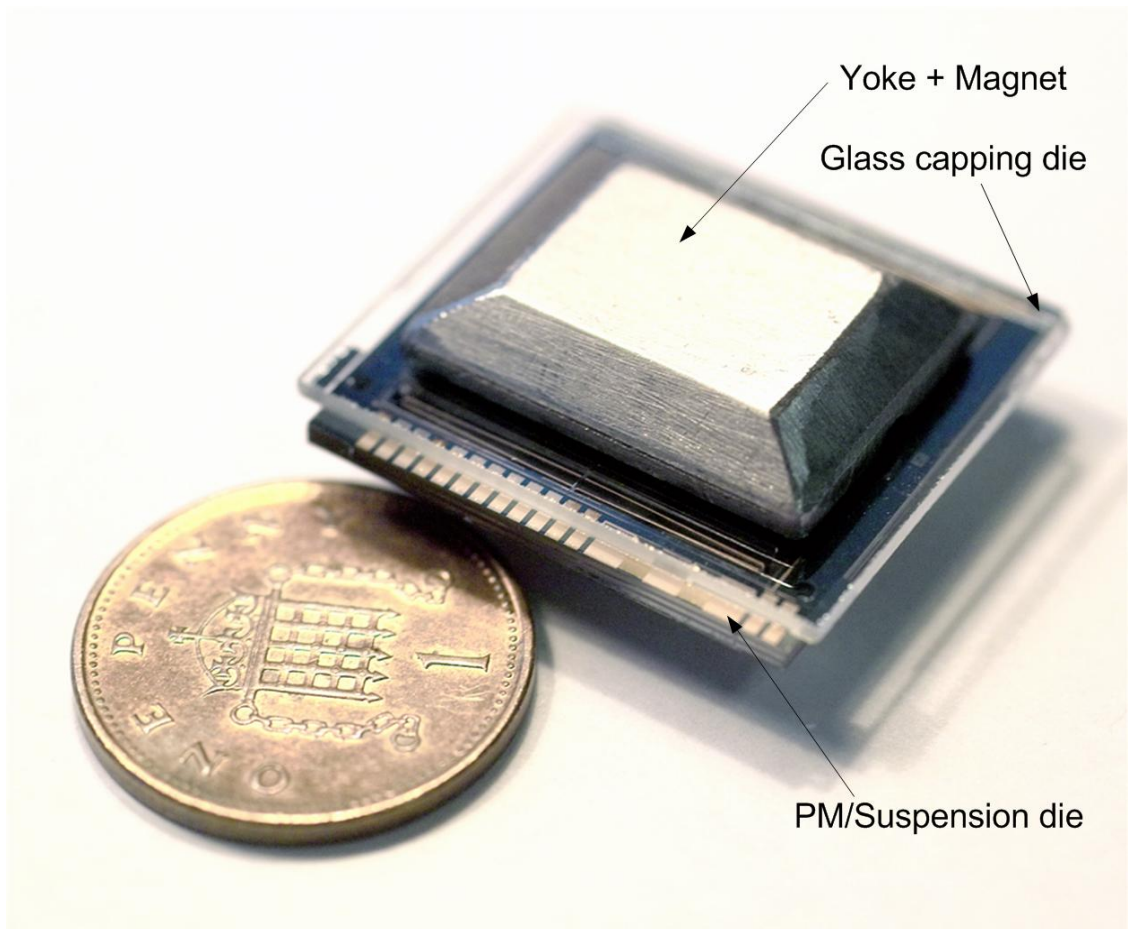


Figure 6.30 A fully assembled microseismometer, for size reference a British penny is placed next to it (*courtesy: Werner Karl*).

6.8.1 Experimental measurement setup

The microseismometer evaluated here is a single-axis Galperin design. The output from the coil is measured using a network analyzer. White noise is fed into one of the coils on the suspension and the response from the other coil is measured by the network spectrum analyzer. Figure 6.31 shows the measurement setup and schematic of the measurement. The microseismometer is mounted on a tilting platform which is tilted to 54.74° as shown in a close-up of the conditioning unit in Figure 6.32; the conditioning unit contains the analog to digital converter and feedback circuit.

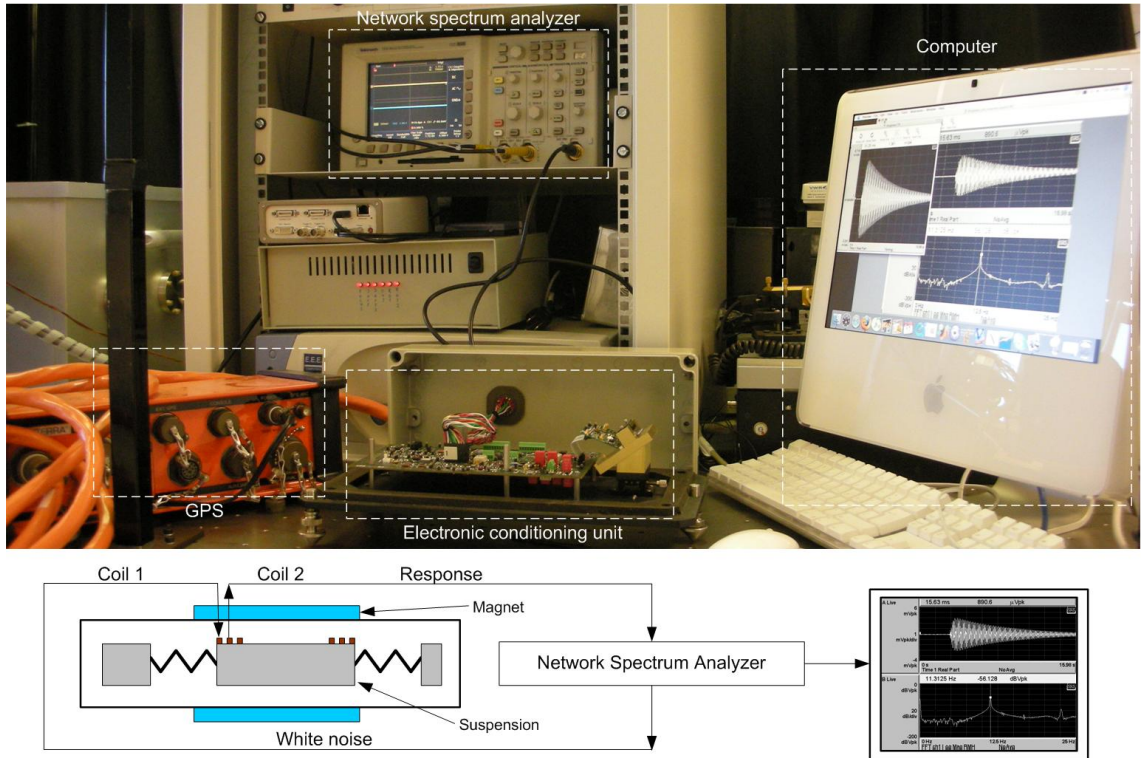


Figure 6.31 Experimental measurement setup for measuring the resonant frequency and Q-factor of the prototype microseismometer.

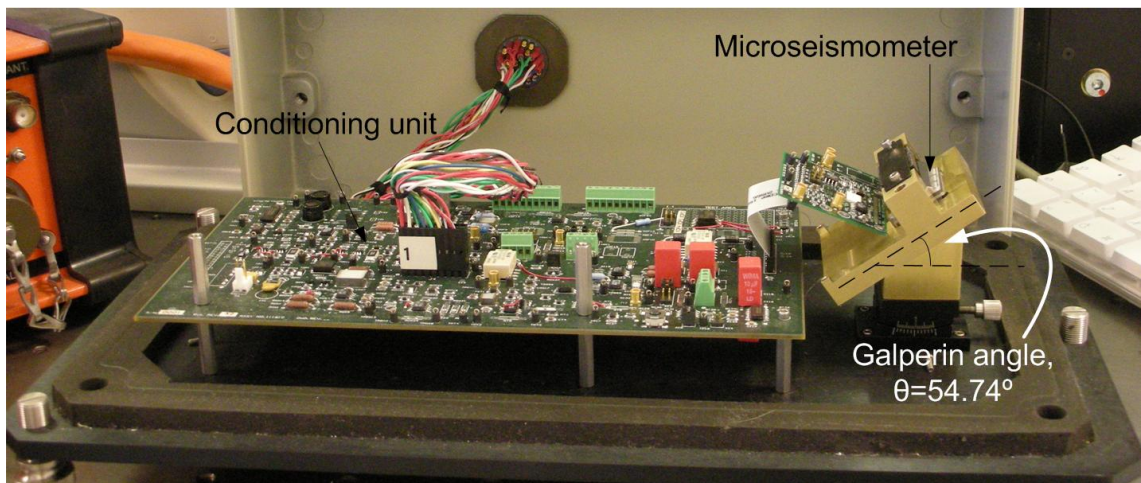


Figure 6.32 Close-up of the electronic conditioning unit containing the microseismometer.

6.8.2 Microseismometer dynamics measurements

Measurement of the resonant frequency and quality factor is carried out for an assembled microseismometer. Under the external magnetic field the coil on the

suspension generates a current which we measure to find the response of the suspension.

The resonant frequency for the suspension is calculated to be 12.35 Hz from the response plot (Figure 6.33) which shows the current output of one of the coils under an external magnetic field.

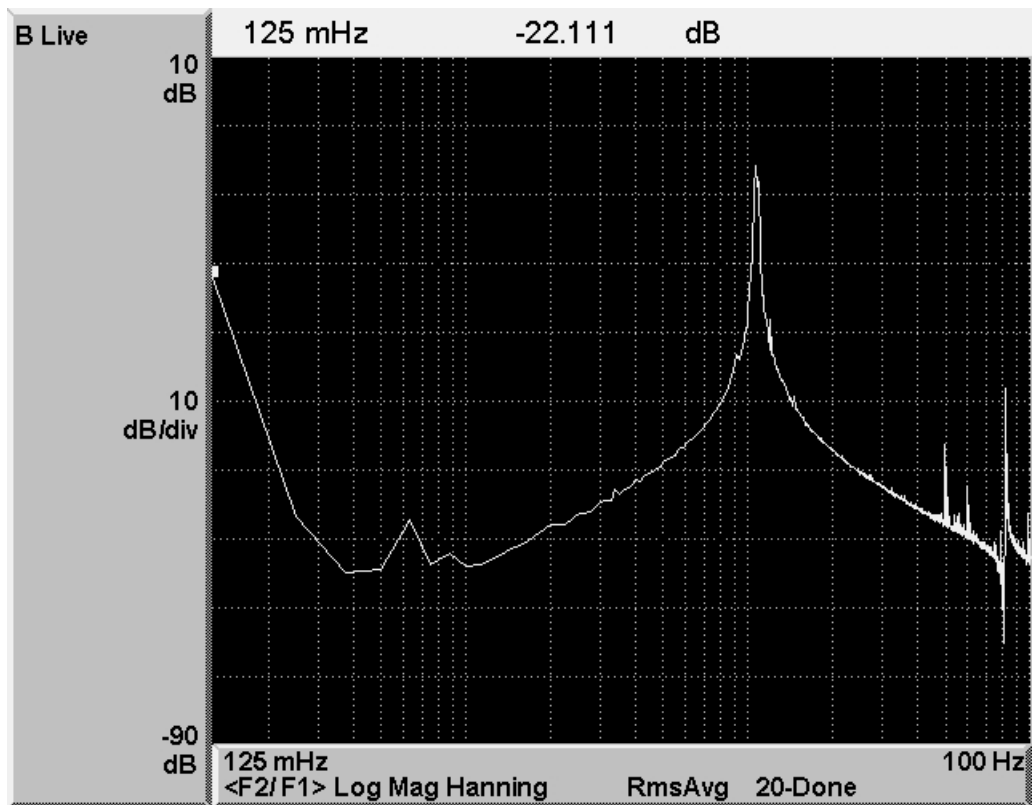


Figure 6.33 Response plot for the suspension. The coil generates a current when driven under the external magnetic field. The peak in the response curve corresponds to the normal resonant modes. The first peak is at a frequency of 12.35 Hz.

The Q-factor of the suspension is measured by doing a ringdown test on the suspension (Figure 6.34). The current from the coil reduces as the vibration dies down. We calculate the decay time for the amplitude and calculate the Q-factor using equation 2.5.

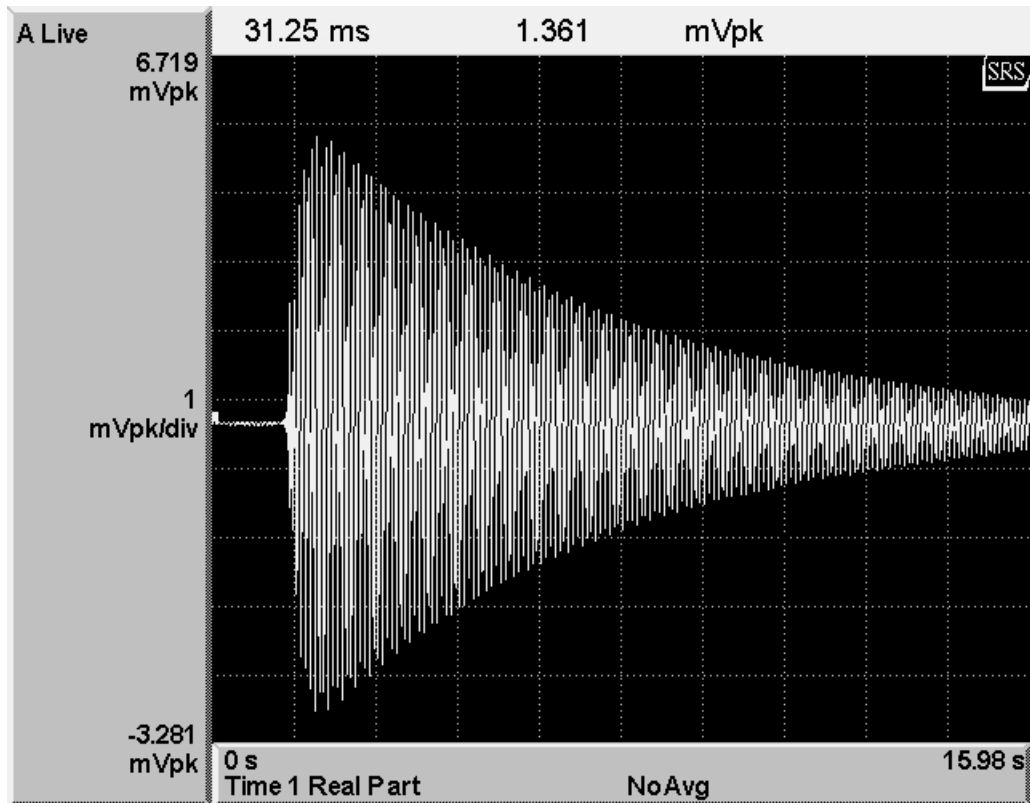


Figure 6.34 Ringdown test of the suspension. The current generated in the coil reduces as the vibration decays.

The Q-factor for the microseismometer is calculated to be $Q = 250$ from a time decay constant $\tau = 6.5$ seconds. The NEA for the device is calculated using equation 1, $NEA = 3.89 \times 10^{-9} \text{ ms}^{-2}/\sqrt{\text{Hz}}$.

6.8.3 Vibration and shock test

The robustness of the silicon suspension to either vibration or shock is a critical parameter in device performance. We look at the failure modes in response to vibration and shock. As the silicon suspension is part of the microseismometer sensor assembly, we need to set shock and vibration to satisfy the following conditions:

1. Transport of the microseismometer sensor assembly using ground and air transport for final assembly as a system.
2. Transport of the complete system to the deployment destination.

3. Launch shock and vibration involved in transporting the system in space.

When the sensor assembly is part of a full fledged microseismometer (system), the suspension can be actively damped to avoid shock and vibration, in which case only vibration and shock test on the complete assembly is of concern. Testing of the complete system is to be undertaken by the assembler (Kinometrics for terrestrial microseismometer) and is not considered here. Far more important for this work is the shock and vibration response of a bare die or a packaged die (with capping dies and magnets) to transportation vibrations and shock level. The bare die is not transported out of the MEMS facility without the capping dies and the magnetic assembly so the transportation of packaged die for final assembly is the point of highest vulnerability.

Using US Department of Defence guidelines for vibration levels in transportation specified in MIL-STD-810F section 514.5[6.10], a composite vibration envelop is designed [6.11], shown as transportation exposure in Figure 6.35. The transportation composite includes the worst vibration environments for truck, rail, and air transportation. Truck transportation provides the worst vibration environment at lower frequency levels, while air transportation is worst at higher frequencies.

The composite transportation vibration envelop starts at 6 Hz (the lowest level the testing equipment can attain) and is flat at $0.015 \text{ g}^2/\text{Hz}$ to 65 Hz at which point it increases at approximately 6dB/Octave till it gets to $0.025 \text{ g}^2/\text{Hz}$ at 100 Hz. The vibration envelop is flat at $0.025 \text{ g}^2/\text{Hz}$ till 500 Hz and then drops at -6dB/Octave to $0.0016 \text{ g}^2/\text{Hz}$ at 2000 Hz. The total RMS g level for the transportation composite is around 5g.

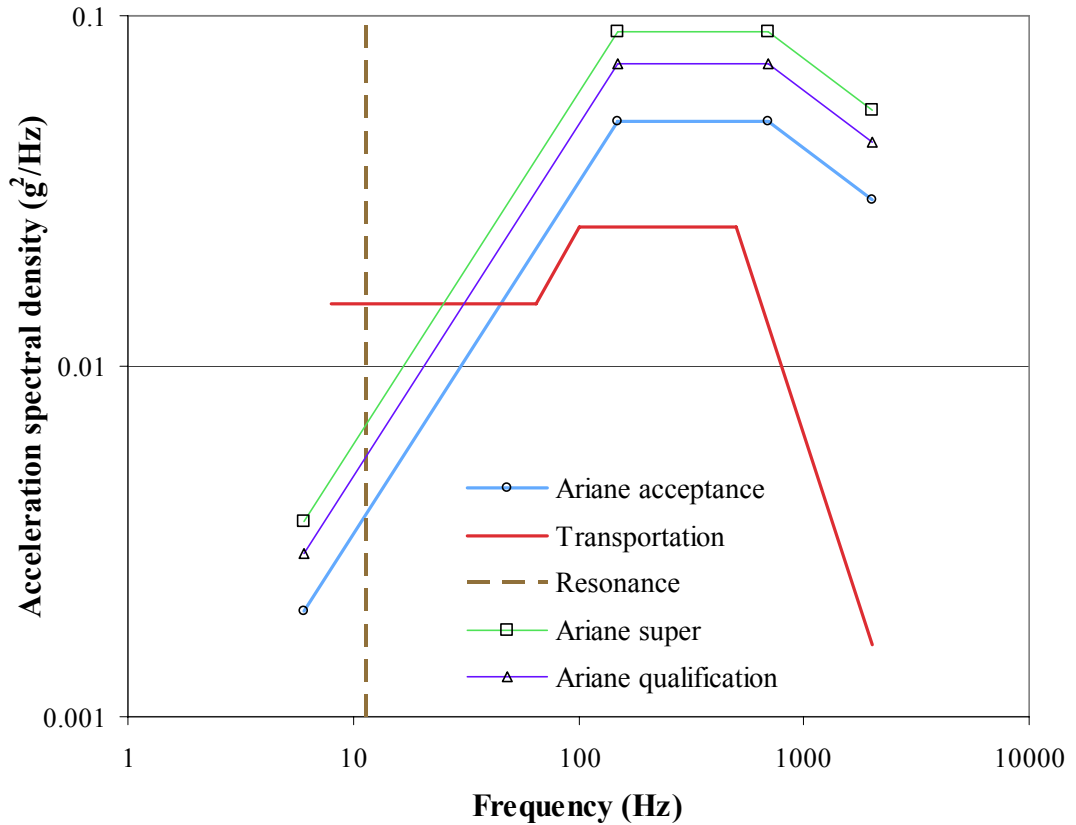


Figure 6.35 Minimum intensity exposure for transportation of packaged die using a combination of truck, rail and air transport.

The suspension die was clamped between the DT and cavity die for the vibration and shock measurements. The packaged suspension was then placed on a Ling Dynamic Shaker [6.12] (Figure 6.36) at AOPP [6.13], University of Oxford. The vibrator has a maximum force rating of 8 kN (up to 16 kN with additional modules), the vibration and shock profiles can be customized. To test the response of packaged sensor, it was placed in the Galperin configuration on the test bench and the vibrator was programmed using the Transportation composite vibration profile. The suspension failed around the spring linkages and also on the frame –listing and picture of the failures are:

1. Fracture at spring linkages (Figure 6.37).

2. Damage at the corners of the intermediate frames and proof-mass due to the corners colliding with each other (Figure 6.38).

The two classes of failures can be classified as complete fracture and surface spallation. The packaged suspensions were able to sustain shock up to 75g laterally and 35g vertically.

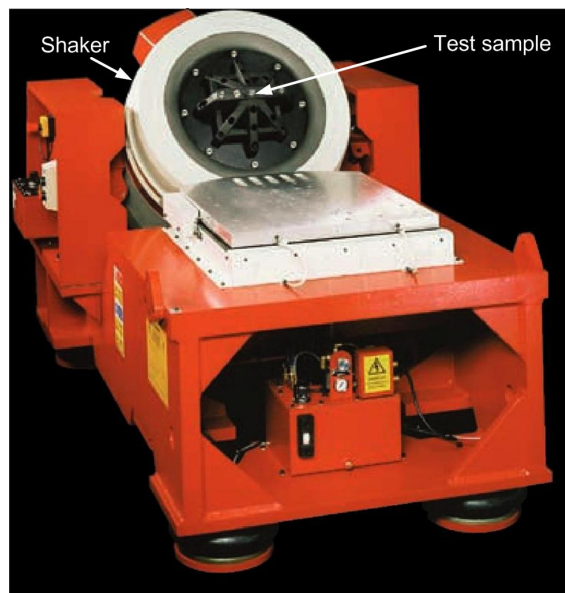


Figure 6.36 Ling Dynamic Shaker at AOPP, University of Oxford used for doing shock and vibration analysis of packaged suspension.

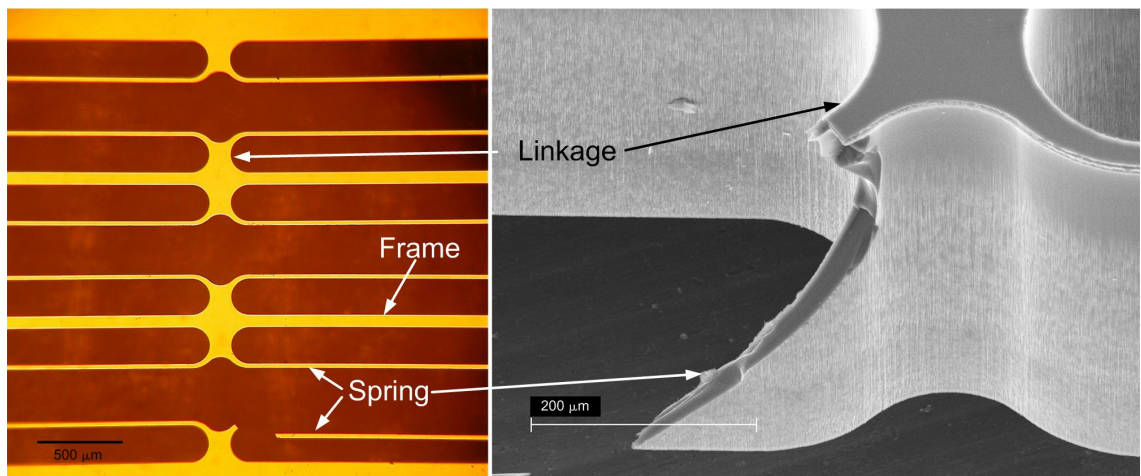


Figure 6.37 Fracture of the spring at the linkage.

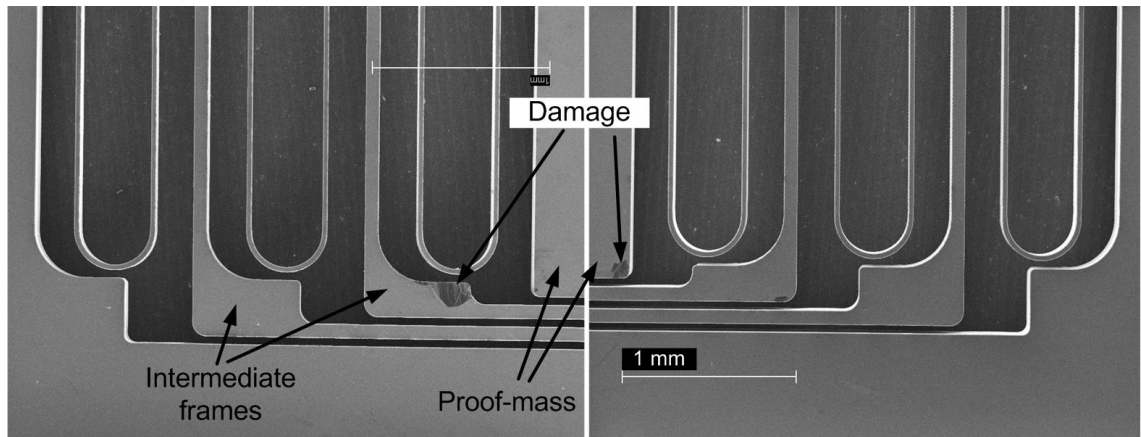


Figure 6.38 Frame and proof-mass damage due to collision at the corners.

To avoid failures at the linkages, the geometry was modified and the filleting was improved. Figure 6.39 shows the new designs for the linkage. The designs were based on the FEA analysis carried out in section 3.5.

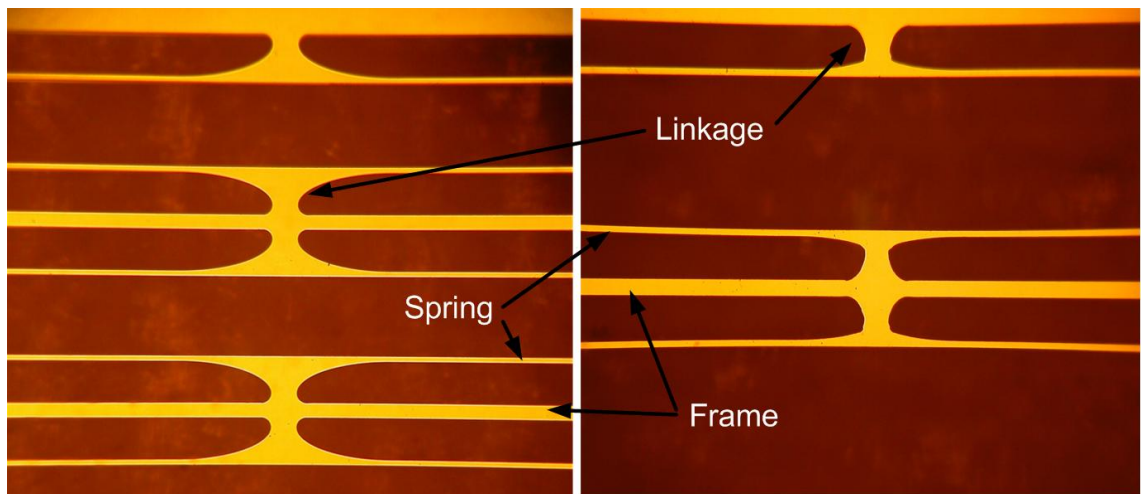


Figure 6.39 Redesigned linkages to reduce the stress concentration.

To avoid the frames and proof-mass colliding, a variety of damping structures were designed as shown in Figure 6.40. The design philosophy behind cavity and comb finger dampers is an increase in viscous damping as the protrusion enters the etched cavity thus increasing the damping to frame motion. In the spring constraining tabs, the

frames are restricted in motion by being inside an envelop which stops the springs from colliding with the frames. The frame spring damper places a spring at the end of the frames thus dissipating some of the vibration energy.

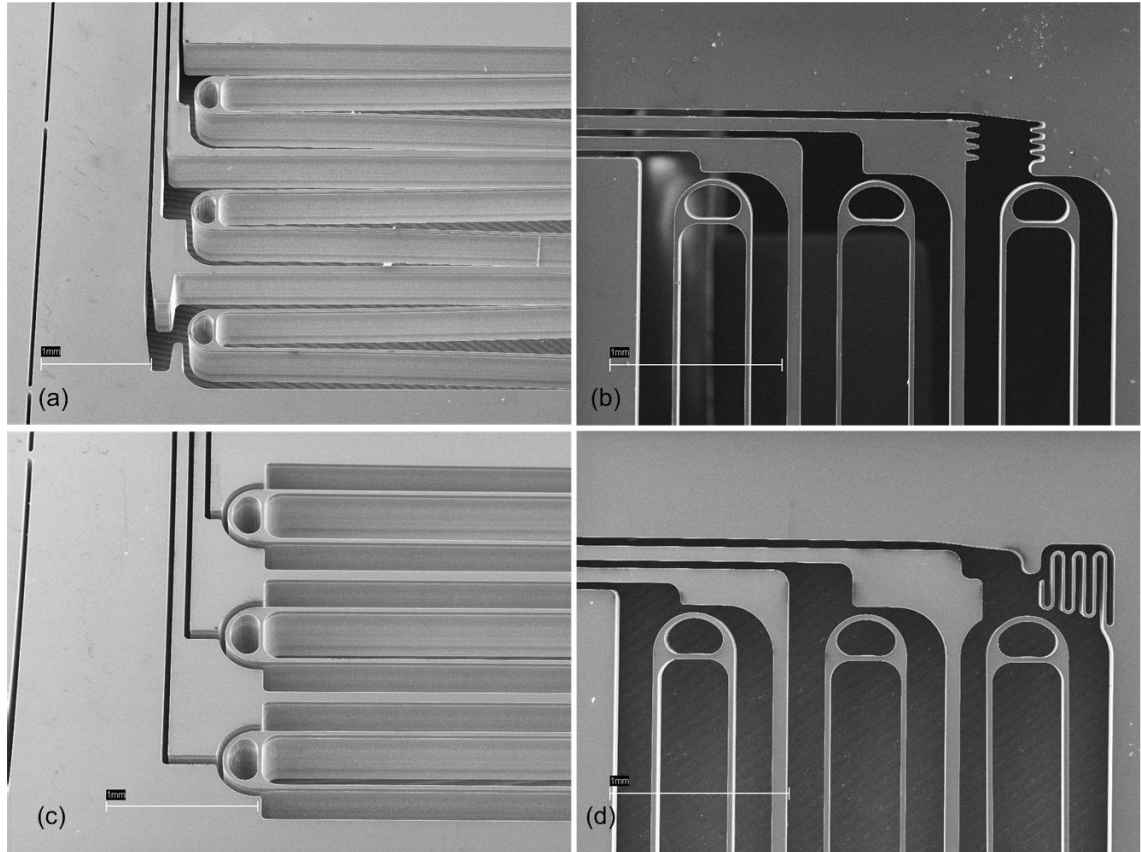


Figure 6.40 Damper designs to avoid frames and proof-mass collision, (a) Cavity damper, (b) Comb finger dampers, (c) Spring constraining tabs, and (d) Frame spring damper.

A new set of suspensions were fabricated incorporating the redesigned linkage geometry and the various damping structures. The packaged suspension was then exposed to transportation composite vibration levels without any failure. The vibration level was then increased to Ariane acceptance levels (Figure 6.35) which is the minimum vibration characteristics for a launch using ESA's Ariane rockets. The packaged suspensions survived the vibration levels without any failure. The vibration level was then increased to Ariane qualification and subsequently to Ariane super which is higher vibration levels than is required for a space launch mission. The linkages did

not undergo any failure. The damping structures had some failures as shown in Figure 6.41 which is mostly fractured pieces of silicon on the proof-mass and frames. The frame springs work well at reducing the damage.

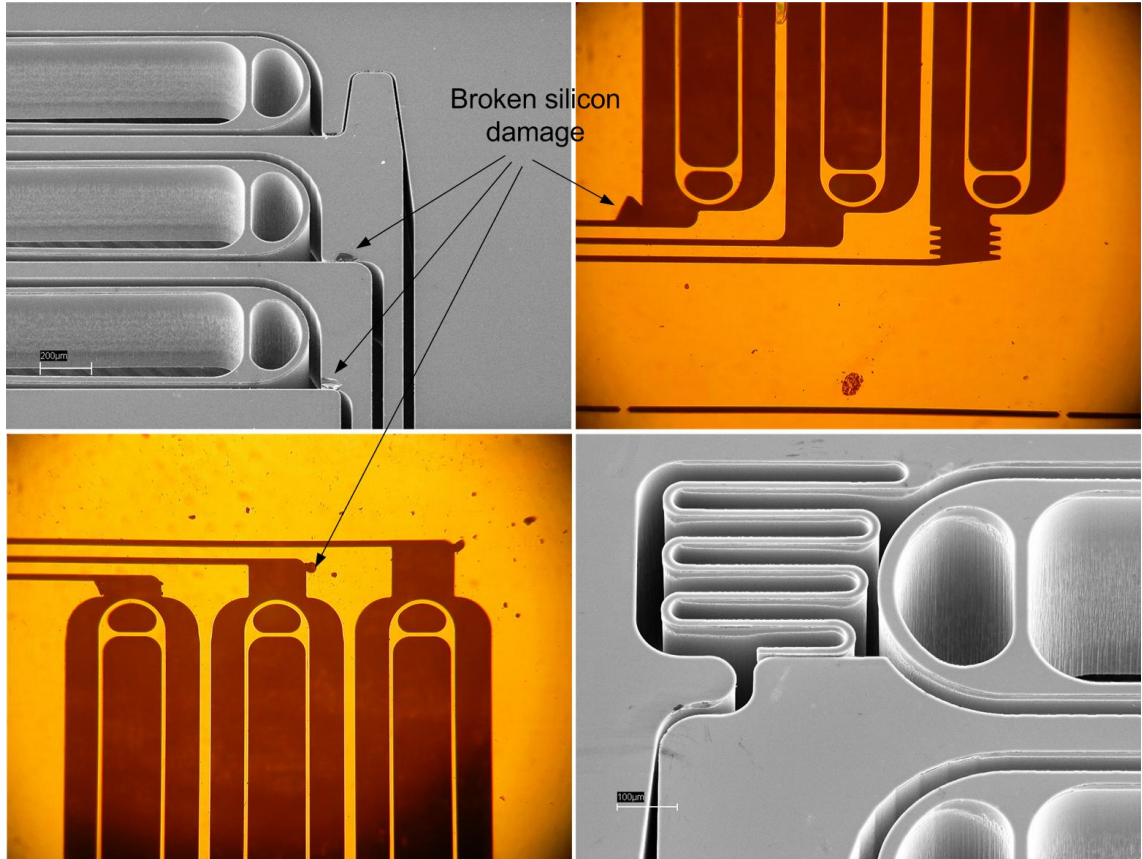


Figure 6.41 Damage to the frames and proof-mass at Ariane super vibration levels for packaged suspension.

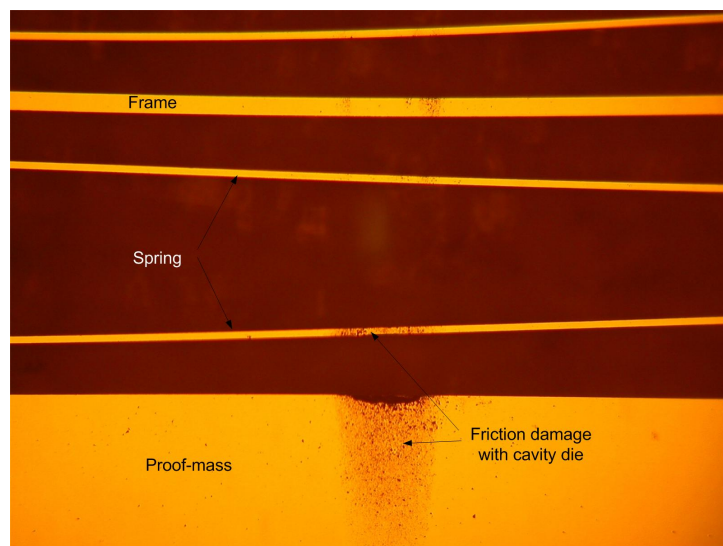


Figure 6.42 Friction damage on proof-mass due to cavity die support fingers.

There was additionally some frictional damage to the proof-mass from the cavity die (Figure 6.42). This will not affect the device performance and can be fixed by changing the cavity die.

6.9 Other Issues

A seismometer is most affected by tilt, temperature and pressure. Tilt is a major issue for a horizontal seismometer but does not pose significant problems for the Galperin configuration. The equilibrium between gravity and spring force is disturbed when the temperature changes so the seismometer needs to be compensated for it. Pressure causes variable buoyancy on the proof mass when it is not sealed and even when sealed it can cause temperature difference as well as deformation of the complete assembly. As we saw in chapter 5, the Q for the proof mass changes with pressure. For low self-noise it is desirable to have a very high Q which is attained at low-pressure, this requires the mechanical unit to be vacuum encapsulated. The small size of microseismometer is suitable for vacuum encapsulation.

6.10 Summary

A complete seismometer sensor unit comprises of the motion sensing and feedback circuit besides the mechanical suspension. For the microseismometer a lateral differential capacitive array transducer (LCAT) is used to measure the motion of the suspension. The feedback circuit keeps the proof-mass centred, thus increasing the dynamic range of the sensor. In the microsesimometer an electromagnetic actuator, consisting of a coil on the proof-mass, and a pair of permanent magnets, placed on either side of the proof-mass, is used to provide the feedback force.

The full fabrication steps for the proof-mass die are presented. Besides the silicon lateral suspension fabricated using DRIE, the suspension contains metallization and insulator layers to form the LCAT pickup electrodes and the coil for the electromagnetic feedback actuator. A full fledged Metal-Insulator-Metal-DRIE process flow is presented. The recipe for the complete process is presented in Appendix C.

Fabrication steps for the DT capping wafer and Cavity capping wafer are summarized. Sand blasting is used to etch glass to create the cavities and dice the dies.

The magnetic unit contains a pair of magnets either side of the PM die. The magnets are Samarium Cobalt (SmCo) rare earth magnets. The yoke pieces are soft iron and the pole pieces are bevelled to focus the magnetic field. FEA is used to determine the bevelling angle for the pole pieces to improve the linearity of the magnetic flux density over the coil.

A microseismometer prototype is assembled by bonding the cavity die to the PM die by glass frit reflow. The DT die is bonded to the PM-cavity sandwich by solder reflow. Solder balls or electroplated solder is used to form the pads used to bond the dies together.

The dynamics of the microseismometer prototype are then determined by measuring the current off one of the coils while the other coil is used to actuate the suspension using white noise electrical signal. The suspension is measured to have a resonant frequency of 12.35 Hz and a quality factor of 250.

The packaged dies also undergo vibration and shock testing. The linkages and frame dampers are modified to build suspensions that can withstand rocket launch and multiple modes of ground and air transportation. The suspension also withstood 75g of lateral and 35g of vertical shock.

The silicon suspension fabrication was done by the author. The metal layers and insulator layers were processed by Werner Karl with contributions from the author, Trevor Semple and Sanjay Vijendran. The solder and glass frit assembly was performed by Trevor Semple with contributions from Tom Pike, Werner Karl and the author. The characterization was done by the author with contributions from Tom Pike and Werner Karl.

6.11 Conclusion

We demonstrate a fully functional microseismometer sensor assembly. The packaged suspension has a Q of 250 in air with a NEA of $0.4 \text{ ng}/\sqrt{\text{Hz}}$ which is higher than the target NEA of $0.35 \text{ ng}/\sqrt{\text{Hz}}$. The couette flow damping dominates and would need to be reduced to increase the Q for the suspension in air. This is achieved by increasing the gap between the pickup electrodes but at the expense of reducing the sensitivity of the device. Ultimately the suspension is planned to be vacuum packaged which will completely eliminate viscous damping and allow the suspension to have lower noise than the target.

Shock and vibration tests demonstrate suspension that is suitable for terrestrial and space deployment. The practicality of building a microseismometer around the suspensions looks even more lucrative given the robustness of the suspensions.

6.12 Bibliography

- [6.1] W. T. Pike, I. M. Standley, and A. Trnkoczy, Micro-machined accelerometer, US Patent US6776042: Kinemetrix, Inc,
- [6.2] W. T. Pike, I. M. Standley, and R. R. A. Syms, Improved micro-machined suspension plate with integral proof mass for use in a seismometer or other device, US Patent US7036374: May 2, 2006
- [6.3] G. T. A. Kovacs, *Micromachined transducers sourcebook*, McGraw-Hill, 1998.
- [6.4] B. Li, D. Lu, and W. Wang, "Micromachined accelerometer with area-changed capacitance," *Mechatronics*, vol. 11, pp. 811-819, 2001.
- [6.5] Photoneece, "Toray,"
http://www.toray.co.jp/english/electronic/products/pro_b001.html.
- [6.6] Crystal Mark Inc., 613 Justin Ave., Glendale, CA 91201, USA
<http://www.crystalmarkinc.com/>.
- [6.7] M. Andrews, I. Harris, and G. Turner, "A comparison of squeeze-film theory with measurements on a microstructure," *Sensors and Actuators A: Physical*, vol. 36, pp. 79-87, 1993.
- [6.8] Y.-H. Cho, A. P. Pisano, and R. T. Howe, "Viscous damping model for laterally oscillating microstructures," *Journal of Microelectromechanical Systems*, vol. 3, pp. 81-87, 1994.
- [6.9] T. Corman, P. Enoksson, and G. Stemme, "Gas damping of electrostatically excited resonators," *Sensors and Actuators A: Physical*, vol. 61, pp. 249-255, 1997.
- [6.10] MIL-STD-810F, "Environmental Engineering Program Guidelines,"
<http://www.dtc.army.mil/navigator/>, 2002.
- [6.11] I. M. Standley, "NEMS Devices Shock and Vibration Levels," Internal Document, Kinemetrix, Inc., Pasadena, CA USA 2006.
- [6.12] Ling Dynamic Shaker, LDS-Group, <http://www.lds-group.com>.
- [6.13] Vibration testing, Atmospheric, Oceanic and Planetary Physics, University of Oxford, http://www.atm.ox.ac.uk/main/facilities/vibration_testing.html.

Seven

7 Conclusions and Future Work

This thesis describes the design, analysis and fabrication of single crystal silicon lateral suspensions. The suspensions are designed to have a low resonant frequency and a large proof-mass. The suspension is made from single crystal silicon (SCS) which is a popular semiconductor material with extremely high Young's modulus, yield strength and a very low material defect and a wide repertoire of standard fabrication tools. The availability of high aspect ratio micromachining tools like STS DRIE etcher enables us to fabricate thick lateral suspensions out of silicon.

The suspension so designed is for use as a seismic mass in a seismometer.

Seismometers are able to detect extremely low level vibration signals. The fundamental limit to a sensors ability to resolve a vibration signal is set by the overall noise of the sensor which comprises the electronic and mechanical noise of the sensor. In this thesis our primary concern is with reducing the mechanical noise of the sensor. The mechanical noise floor is determined by the Brownian noise of the suspension given as noise equivalent acceleration (NEA) which is inversely proportional to the mass, time period and quality factor of the suspension. This is the reason why the suspension designed here has low resonant frequency (long period), relatively large mass (compared to MEMS vibration sensors) and high quality factor through use of SCS.

The lateral suspensions are fabricated by through-wafer DRIE of SCS wafers. The suspensions have resonant frequencies of around 10 Hz, a proof-mass weighing 0.22 grams and a quality factor that varies from 1000 at atmospheric pressure to 40,000 in UHV and as high as 250,000 with proper post processing to remove any lossy materials from the suspension.

To understand the suspension dynamics and explore the design space to maximize cross-axis rejection ratio while keeping the fundamental mode low, an analytical and FEA model is used. The models were extended to include the effect of DRIE on profile shape of the spring beams. The model estimates of the suspension modes were in excellent agreement with the observed values thus providing an invaluable tool for designing lateral suspensions.

A prototype microseismometer is assembled with electrostatic motion sensing and electromagnetic feedback circuit. The microseismometer demonstrates a noise floor of 0.4 ng/ $\sqrt{\text{Hz}}$ at atmospheric pressure. The packaged suspensions are also robust to vibration exposure for transportation and space launch and to shock levels of 75g laterally and 35g vertically. Vacuum packaging the suspension should lower the noise floor by an order of magnitude. Some of the other topics that need to be addressed in future are discussed in the subsequent sections of this chapter.

7.1 Microseismometer Characterization

The fully integrated microseismometer is still under fabrication and the complete device when ready needs to be characterized to find its overall self-noise, bandwidth, temperature sensitivity, power consumption, and linearity.

Vibration and shock testing of a vacuum packaged suspension needs to be performed as the Q for the suspension is extremely high in vacuum and can lead to substantial damage particularly near the resonant frequency.

7.1.1 Alternate designs

In the current design, magnetic actuation was used for feedback control of the proof-mass, and capacitive pickup was used to read the displacement of the proof mass. Alternate system designs should be investigated that have fully electrostatic actuation and pickup or with optical pickup to see if they have any benefits over the current design.

7.1.2 Fully electrostatic geophone

Geophones are low-cost devices and so the assembly required for the current device is not suitable for such a systems. An electronically actuated system is proposed which can be further developed into a commercial system. Figure 7.1 shows the design layout and a fabricated device.

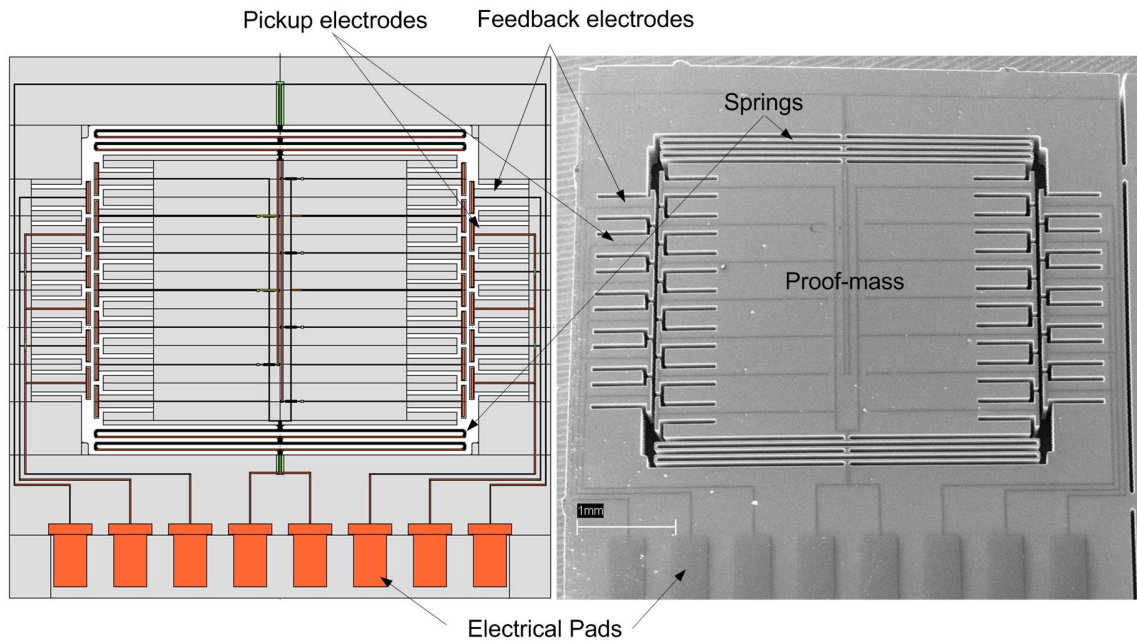


Figure 7.1 (a) 2D model of a fully electrostatic inertial sensor, (b) a fabricated geophone.

The fabrication process uses the same processing used for fabricating the PM die but without the additional processing of capping wafers or packaging concerns.

7.2 Modelling Extension

The analytical and numerical models used for the suspension in the thesis show good correlation with experimental results. They can be further expanded and applied to design and analyze other systems.

The numerical model can be developed further to include fluid flow for damping estimation. This will allow better understanding of the damping mechanism in the lateral suspension. Further work can also be carried out on electrostatic simulation both analytically and numerically of capacitive pickup electrodes.

Damping structures like fingers and springs (Figure 7.2) to engage and increase damping when the suspension is undergoing its maximum throw were tried though there is still a need for optimization of these structures.

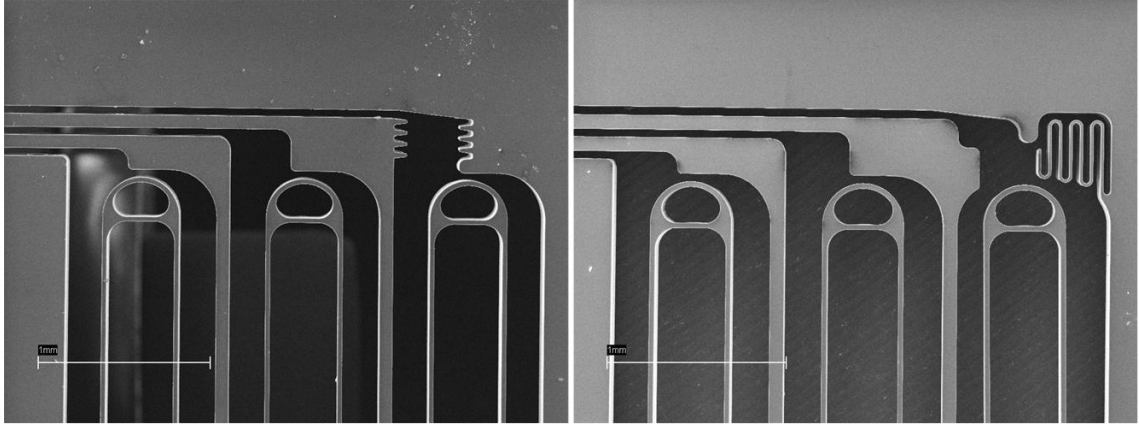


Figure 7.2 Damping structures to increase damping when the suspension is at its maximum deflection.

Another method to reduce the incidences of failure is by metal plating near the contact points and self-caging of the resonant structure. These methods will work by increasing energy dissipation using the metal structures and reducing the impact energies.

The shock tests reported in this thesis were all done at atmospheric pressure thus the suspension was viscously damped. The microseismometer is expected to use a vacuum packaged suspension which will have extremely high Q of the order of 10,000 – 40,000 or even higher. Feedback based damping will most likely be required to passively damp the suspension by shorting the coils on the suspension through a large resistor.

7.2.1 Application to other inertial sensors

Resonating mass systems are popular with inertial sensor designers and the model, and fabrication technique can be easily expanded into making other inertial sensors like tilt meters, gyroscopes, stress sensors etc.

7.2.2 Application to other devices

Another area where lateral suspensions can be expanded is actuators; the design is suitable for making long range motion actuators which have extensive use in optical systems, biological sample handling etc.

7.3 Applications of Through-Wafer DRIE

A major contribution of the thesis is the demonstration of a reliable fabrication method via through-wafer etching. In addition metallization and insulation deposition methods developed as part of the work can be used for making a wide range of devices.

7.3.1 Other through-wafer devices

Figure 7.3 shows some other through-wafer devices fabricated using the process developed for the microseismometer. This shows the universality of the processing mechanism. Through-wafer etching is not only suitable for creating very thick single crystal silicon inertial sensors but in many cases can replace devices created on SOI. The cost advantage of a single wafer and no release can outweigh the advantages of SOI.

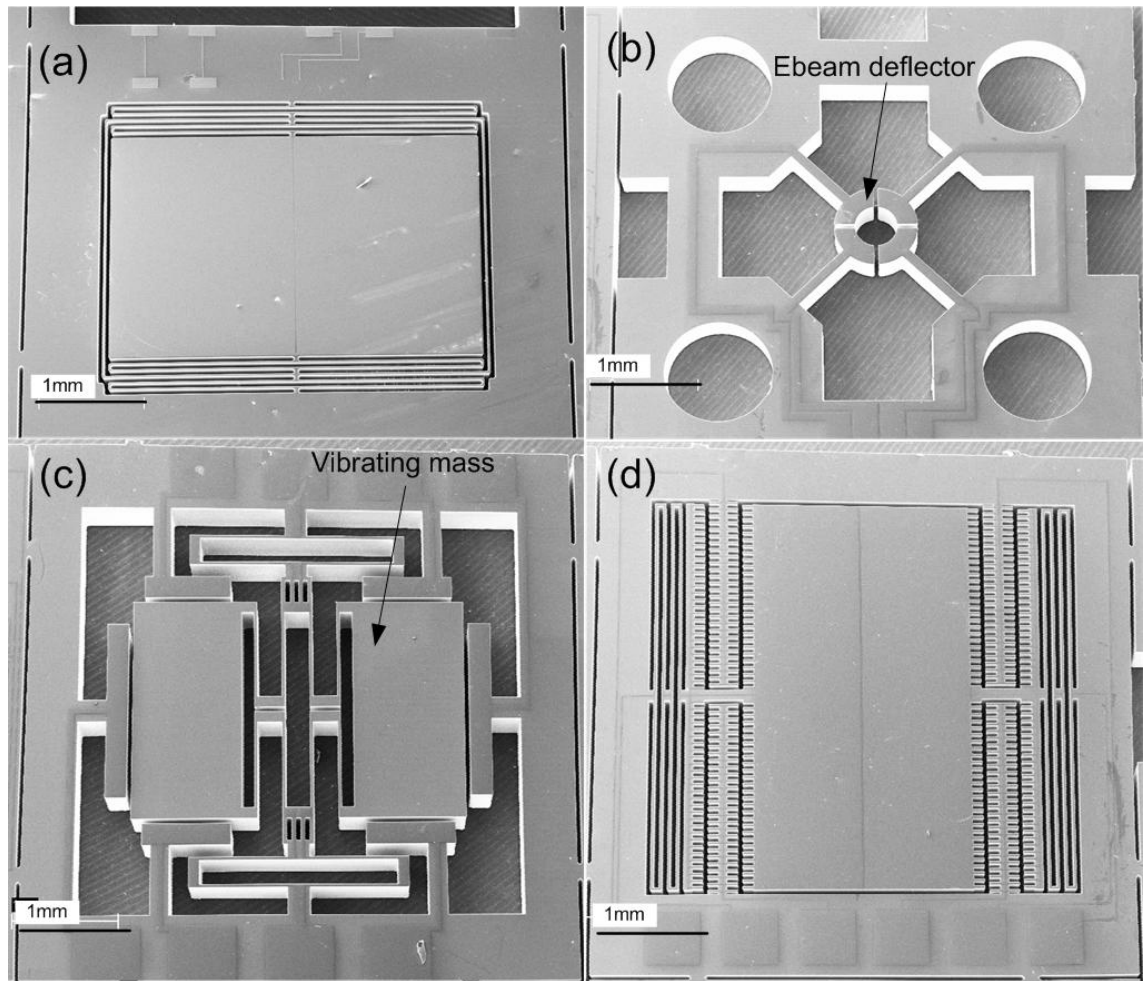


Figure 7.3 Some prototype devices fabricated using the MIMD (Metal-Insulator-Metal-DRIE) process, (a) geophone sensor, $5\text{mm} \times 5\text{mm}$, (b) μSEM components, (c) a tuning-fork gyroscope, (e) comb drive based suspension.

7.3.2 Silicon molding

This work is done by the author in collaboration with Michael Larsson. We have developed a new method for electroforming tall metal structures using high aspect ratio (HAR) silicon molds. Mold fabrication is realized by through-wafer deep reactive ion etching (DRIE). DRIE has been used for forming molds for making polymer [7.1, 2], polysilicon [7.3, 4] and electroplating metal structures [7.5] The advantage of the current technique is the ease of mold separation and an extremely high life of the mold.

The method is further extended to create metal structures suspended from the substrate. The technique is particularly conducive to low-cost fabrication of tall structures, similar to those possible with LIGA. Replica release is facilitated by an insulating conformal polymer release layer deposited on mold sidewalls. Structures hundreds of micrometers tall have been electroformed exhibiting extremely smooth sidewalls. The latter is comparable with typical sidewall quality achievable by LIGA and significantly better than that achievable with other known molding techniques.

The method described here employs through-wafer silicon etching to realize HAR molds. Tall metallic structures can be electroplated within through-wafer etched inserts, passivated by a conformal polymer release layer. The layer smoothes mold sidewall roughness and facilitates replica release.

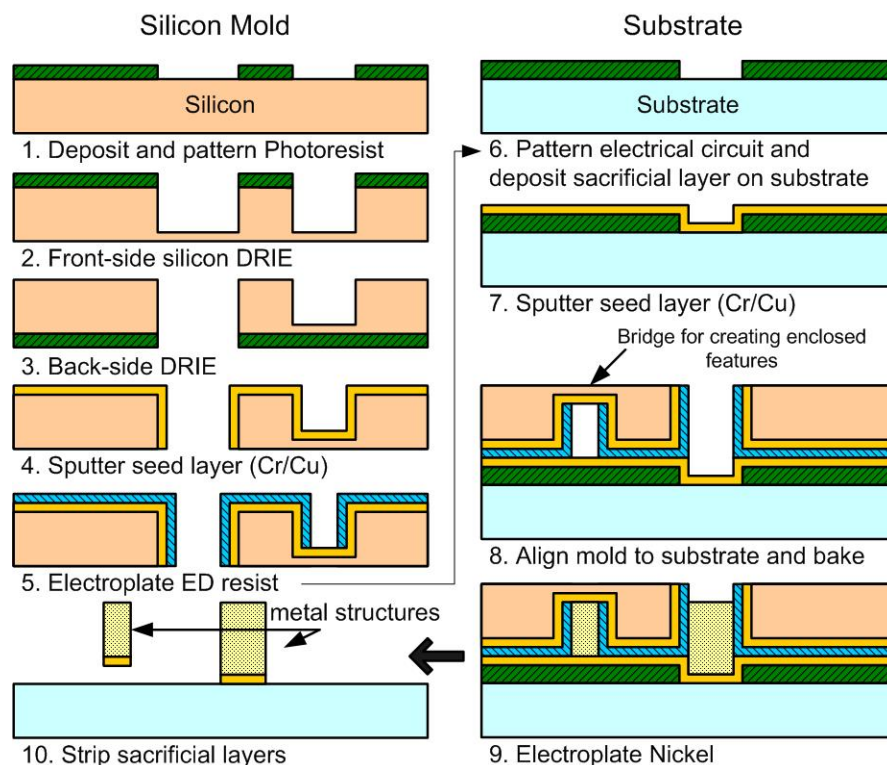


Figure 7.4 Fabrication sequence for the silicon mold, substrate preparation, electroplating, and release.

Conclusions and Future Work

Mold fabrication and electroforming steps are shown in Figure 7.4. The silicon mold is formed via through-wafer DRIE, with mask design and process parameters optimized for vertical or slightly outward tapering smooth sidewalls. To make structures completely enclosed within other structures, bridges are designed, allowing the fabrication of shapes such as rotors with hubs without the need for assembly (Step 3 in Figure 7.4). The silicon mold is subsequently sputtered with a thin coating of Cr/Cu, allowing a conformal coating of polymethylmethacrylate (PMMA) to be applied via electrodeposition from a heated solution of Shipley Eagle ED2100 (Figure 7.5). The coating is baked at 50 °C for 30 minutes to achieve coalescence and improve adhesion with the underlying seed layer. Low temperature baking reduces reflow along feature edges and promotes leak-free sealing with the substrate. After electroplating, the mold is removed by dissolving the release layer in an organic solvent. Metal structures as tall as 230 μm are electroplated (Figure 7.6) and the sidewall rms surface roughness is measured to be between 15-25 nm. Suspended structures are created in a similar manner by electroplating on a substrate with the sacrificial layer defining a gap beneath the structures. Figure 7.7 shows 50 μm thick suspended structures separated from the substrate by a gap of 14 μm .

The technique of electroplating metal structures using a reusable silicon mold enables low-cost, mass production of metal microstructures. Mold lifetime is prolonged through the presence of a release layer, which additionally smoothes mold sidewalls. The use of bridges and the possibility of fabricating suspended microstructures reduce the need for manual assembly. Even taller structures can be created by stacking multiple anodically bonded molds. The process will be developed to create reliable tall micro-structures.

Conclusions and Future Work

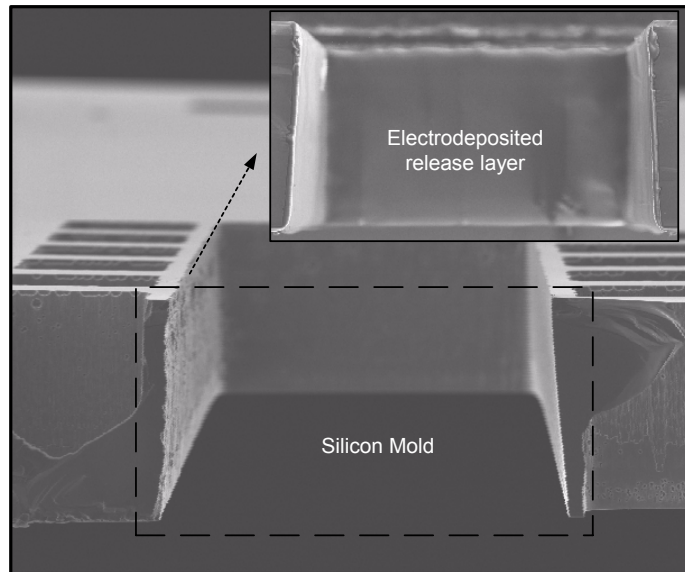


Figure 7.5 SEM image of a silicon mold after DRIE (inset shows the mold with a 10 μm thick PMMA release layer).

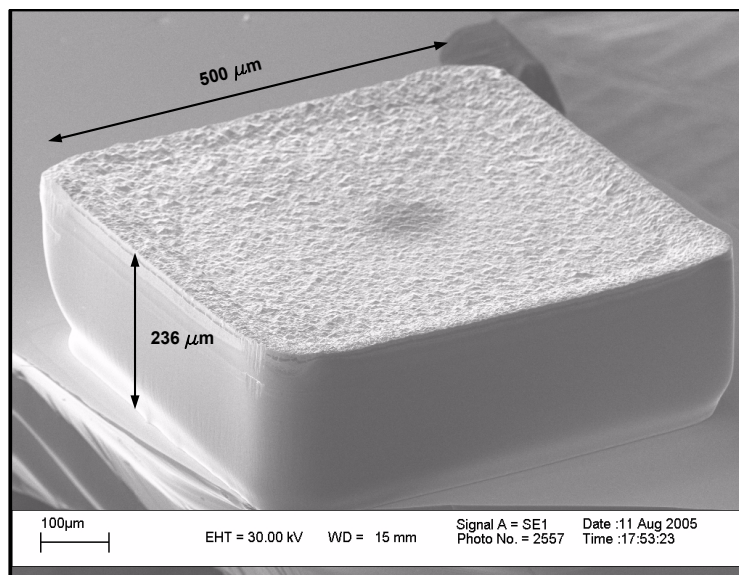


Figure 7.6 SEM image of a molded metal test structure electroplated to 236 μm height. The sidewall is vertical except where the structure is anchored to the substrate. Reflow of the release layer forms a hump at the mold-substrate interface leading to profile variation.

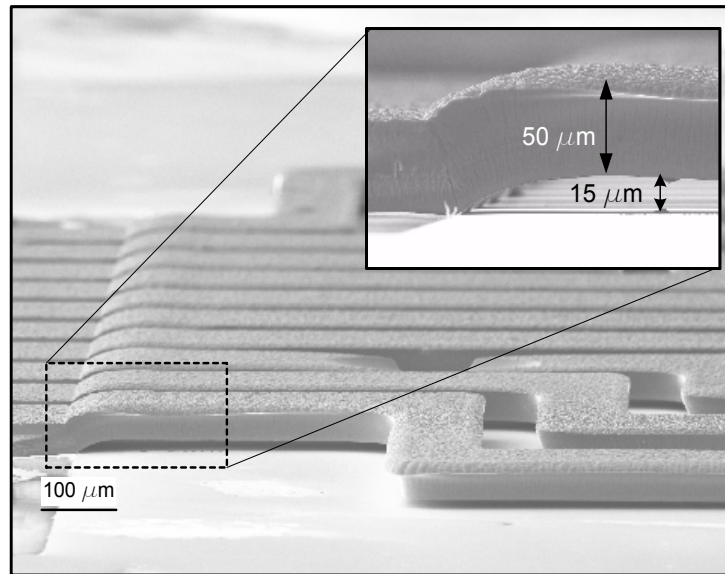


Figure 7.7 Suspended metal structures molded using the fabrication steps depicted earlier. The plated structure is 50 μm high and is suspended 14 μm over the base plate.

The technique can be developed into a reliable process for making tall metal structures.

7.3.3 Single mask through-wafer devices

Through-wafer etching can be used to make single mask devices where the mechanical element is fabricated by through-wafer etching and the metal is deposited on the device using a shadow mask which is made by through-wafer etching.

The process steps are shown in Figure 7.8. The mechanical structure is fabricated by through-wafer etching the device wafer using a single mask. The corresponding shadow mask for depositing the metal layers is also prepared by through-wafer etching another wafer (can be thinned for better resolution). The shadow wafer is placed on top of the device wafer and then placed in a sputter coater where the metal layers are deposited through the holes in the shadow mask onto the device wafer. The sputtered layer due to its isotropic nature deposits on all the surfaces exposed through the shadow mask. This

is especially useful in devices like lateral comb drives where a metallic layer on the whole surface of the finger improves the electrical characteristics.

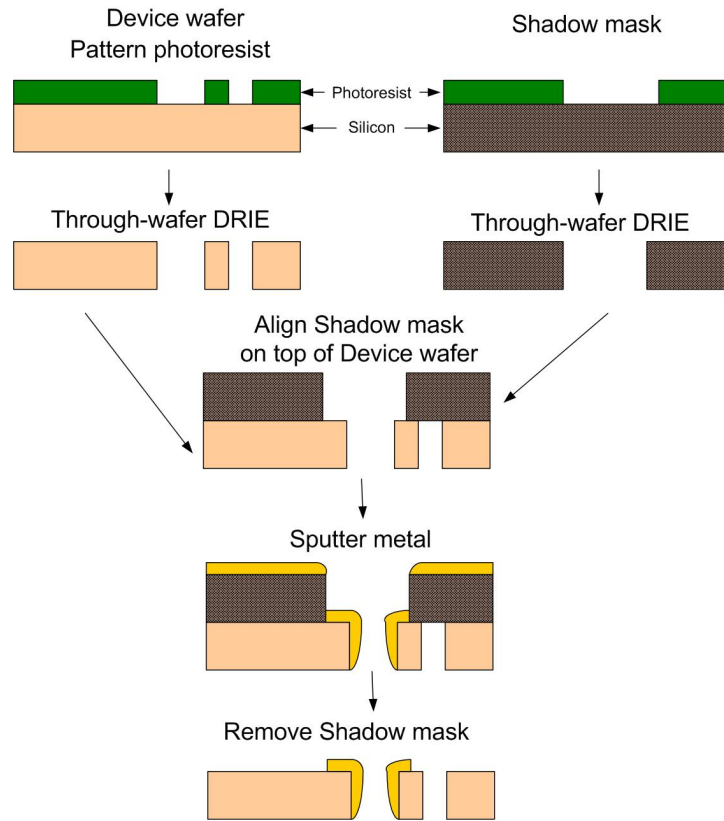


Figure 7.8 Process schematic for single-mask DRIE device fabrication.

7.3.4 SOI replacement through-wafer devices

Thermal isolation is many times very desirable in small-scale devices to reduce the effect of temperature variation. Zhang and Najafi [7.6] demonstrated a silicon oxide isolation trench formed by DRIE etching of thin trenches and oxidation to form a thermally isolating mechanically strong bridge. A processing system can be developed to make the microseismometer suspension on a similar thermally isolated island. The method can also be expanded to form structures that are electrically isolated from the substrate by channels which are anchored mechanically but are electrically insulating from the substrate.

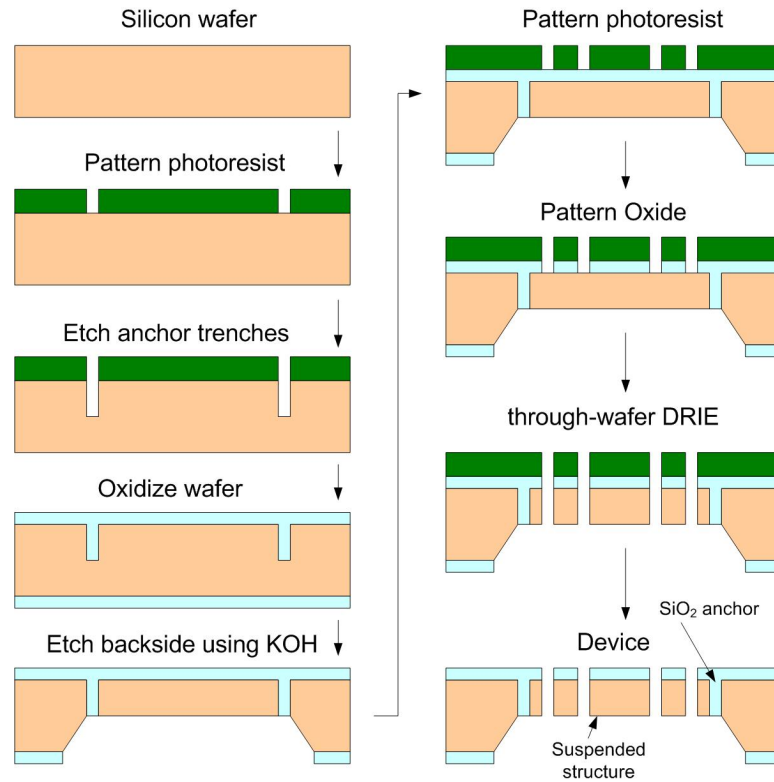


Figure 7.9 Process schematic of a SOI replacement through-wafer process.

This scheme can be used for creating devices which has several different modules which need to be electrically isolated. The ability to electrically isolate them which still lithographically aligned eliminates any manual alignment. An example would be a in-plane actuator composed of several moving arms all actuated by its own set of comb drives.

7.4 Bibliography

- [7.1] Y. J. Zhao and T. H. Cui, "Fabrication of high-aspect-ratio polymer-based electrostatic comb drives using the hot embossing technique," *Journal of Micromechanics and Microengineering*, vol. 13, pp. 430-435, 2003.
- [7.2] L. P. Yeo, S. L. Poh, Y. C. Lam, and M. B.-E. Chan-Park, "Plasma polymerization of C₄F₈ thin film on high aspect ratio silicon molds," *Innovation in Manufacturing Systems and Technology (IMST)*, 2005.
- [7.3] A. Selvakumar and K. Najafi, "High Density Vertical Comb Array Microactuators Fabricated Using a Novel Bulk/Polysilicon Trench Refill Technology," presented at 1994 Solid-State Sensor and Actuator Workshop, Hilton Head, South Carolina, pp. 138-141, June 13-16, 1994.
- [7.4] C. Keller and M. Ferrari, "Milli-Scale Polysilicon Structures," presented at 1994 Solid-State Sensor and Actuator Workshop, Hilton Head, South Carolina, pp. 132-137, June 13-16, 1994.
- [7.5] D. Sander, R. Hoffmann, V. Reiling, and J. Muller, "Fabrication of metallic microstructures by electroplating using deep-etched silicon molds," *Microelectromechanical Systems, Journal of*, vol. 4, pp. 81-86, 1995.
- [7.6] C. Zhang and K. Najafi, "Fabrication of thick silicon dioxide layers using DRIE, oxidation and trench refill," presented at 15th IEEE International Conference on Micro Electro Mechanical Systems MEMS 2002 (code 59062), Las Vegas, NV, United States, pp. 160-163, 2002.

Appendix A: Analytical model

Derivations of Analytical Expressions for suspension spring stiffness.

(The derivations were originally done by William T. Pike and are presented here after being re-derived by the author.)

A1. Translational Modes

A1.1 On-axis compliant stiffness (k_x):

The suspension spring unit can be decomposed into a set of beams with rigid end connectors as shown in figure a1.

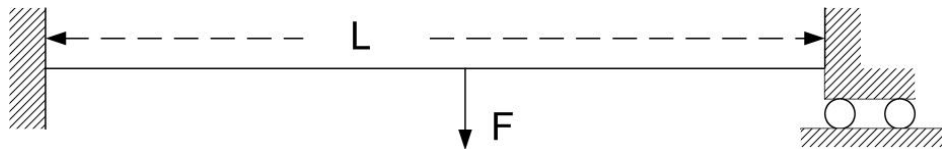


Figure a1: Fixed-fixed beam.

The maximum deflection of the beam is given for fixed-fixed beam by Roark [A.1]

$$\delta x = \frac{FL^3}{192EI_x} \quad (\text{a.1})$$

where E is the Young's modulus of rigidity, and I_x is the area moment of inertia of the beam about X -axis.

Spring stiffness for the fixed-fixed beam is then

$$k = \frac{F}{\delta x} = \frac{192EI_x}{L^3} \quad (\text{a.2})$$

The two beams in each spring are in parallel, so the effective spring stiffness for the spring unit is half the stiffness of one of the beams.

$$k_{spring} = \frac{k}{2} \quad (\text{a.3})$$

The two spring units on either side of the proof-mass is in series, doubling up the spring stiffness for the complete suspension.

$$k_x = 2 \times \frac{k}{2} = k = \frac{192EI_x}{L^3} \quad (\text{a.4})$$

$L = 2l$, length of a beam from the linkage to the end connector, so the spring stiffness is

$$k_x = \frac{24EI_x}{l^3} \quad (\text{a.5})$$

For suspension with n spring sets, the spring constant along X-axis will be k_x/n .

A1.2 Cross-axis spring constant along Y-axis (k_y):

A force acting along Y-axis is taken to derive the deflection of a folded cantilever beam as shown in figure a2.

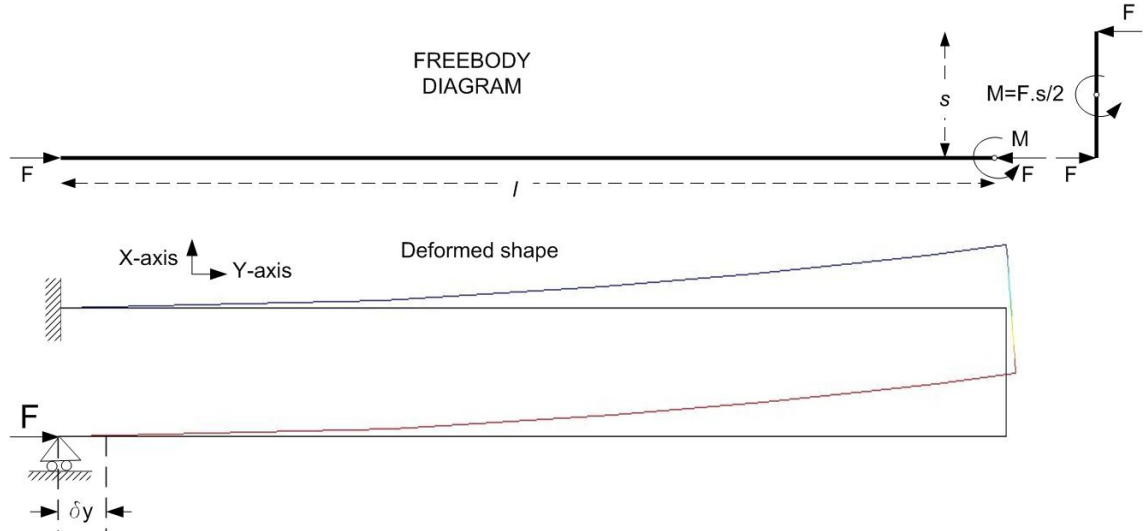


Figure a2: Free body diagram of the spring elements for calculating spring constant along Y-axis.

From Roark [A.1], the angular displacement for a cantilever is given by

$$\theta = \frac{ML}{EI_x} = \frac{Fls}{2EI_x} \quad (\text{a.6})$$

where E is the Young's modulus of rigidity, and I_x is the area moment of inertia of the beam about X-axis and $M = Fs/2$ is the moment acting on the beam.

The lateral deflection along the Y-axis for the folded cantilever beam is then calculated as

$$\delta y = s\theta = \frac{Fls^2}{2EI_x} \quad (\text{a.7})$$

The spring stiffness for the folded cantilever beam is then calculated as

$$k = \frac{F}{\delta y} = \frac{2EI_x}{ls^2} \tag{a.8}$$

For the mirrored pair of folded cantilever beam, the springs are in series so the spring stiffness for a single spring unit is $2k$. The suspension has two units of spring on either side of the proof-mass, the spring units are in series leading to a total spring stiffness in the y direction for the suspension to be

$$k_y = 4k = \frac{8EI_x}{ls^2} \tag{a.9}$$

For suspension with n spring sets, the spring stiffness will be k_y/n .

A1.3 Cross-axis spring constant along Z-axis (k_z):

The spring stiffness for a folded cantilever spring is made of two components: twisting of the beam due to the moment generated in the elbow and bending of the beam under the vertical force loading. The boundary conditions are shown in the free body diagram in figure a3.

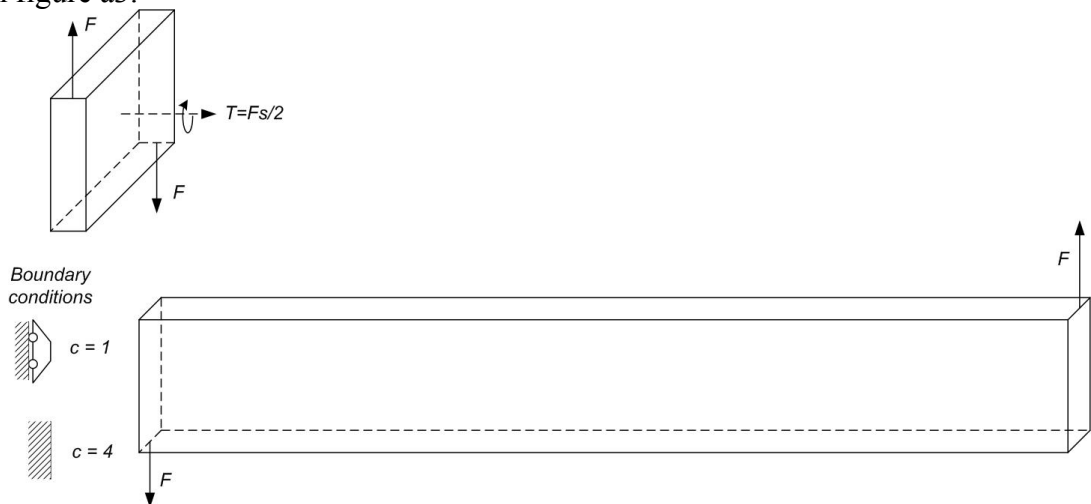


Figure a3: Free body diagram for vertical deflection of the folded cantilever beam.

Under vertical loading the beams will bend depending on the end boundary conditions, table 3.1 in Judy's Ph.D. thesis [A.2] gives the deflection as:

For fixed-free cantilever beam, the deflection is –

$$\Delta z = \frac{Fl^3}{3EI_z} \tag{a.10}$$

For fixed-guided end beam, the deflection is –

$$\Delta z = \frac{Fl^3}{12EI_z} \quad (\text{a.11})$$

The deflection is proportional to the rigidity of the end connector, given by a factor c which is numerically determined. After incorporating c the end deflection then is given as

$$\delta z_{bending} = \frac{cFl^3}{12EI_z} \quad (\text{a.12})$$

where $c = 1$ is a guided end boundary condition, and $c = 4$ is a fixed boundary condition.

The elbow undergoes an angular deflection under the torque caused by the opposing directions of the vertical loading on the elbow given by

$$\theta_{elbow} = \frac{Tl}{GJ} = \frac{Fs}{2} \frac{l}{GJ} = \frac{Fls}{2GJ} \quad (\text{a.13})$$

where G is the shear modulus of rigidity, and J is the area moment of inertia about Z-axis.

The angular deflection causes a twisting of the beam given by

$$\delta z_{twist} = s\theta_{elbow} = \frac{Fls^2}{2GJ} \quad (\text{a.14})$$

The total vertical deflection of the beam under vertical loading is thus

$$\delta z_{total} = \delta z_{bending} + \delta z_{twist} = \frac{cFl^3}{12EI_x} + \frac{Fls^2}{2GJ} \quad (\text{a.15})$$

The spring constant for the folded cantilever beams is then

$$k = \frac{F}{\delta z_{total}} = 1 / \left(\frac{cl^3}{12EI_x} + \frac{ls^2}{2GJ} \right) \quad (\text{a.16})$$

Spring constant for a spring unit is twice the spring constant of the folded cantilever beams as they add in series. Spring on either side of the proof-mass add in series giving a spring constant for the suspension as

$$k_z = 4k = 1 / \left(\frac{cl^3}{48EI_x} + \frac{ls^2}{8GJ} \right) \tag{a.17}$$

For a suspension with n spring sets, the spring constant is k_z/n .

A2. Rotational Modes

A2.1 On-axis rotational mode (k_α):

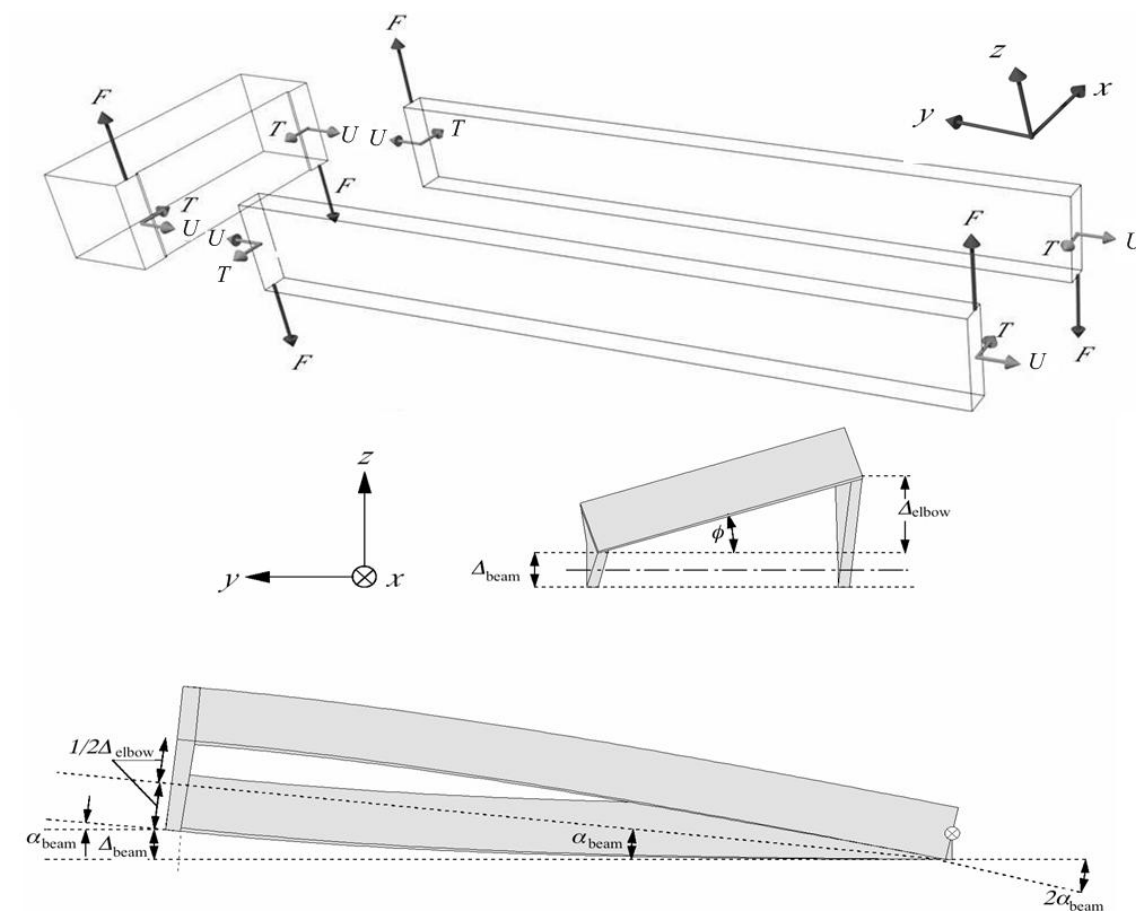


Figure a4: Free body diagram of spring beams under torsion about X-axis.

The angular deflection about X-axis consists of a contribution from the twisting occurring about the X-axis of the linkages and a more complex contribution from a combination of twisting and bending of the beams. Taking the twisting of the linkages first, as there are two linkages for each spring unit of the suspensions on each side of the suspended mass, each of length $(s-w)/2$, the torsional spring constant $k_{\alpha,link}$ will be

$$k_{\alpha,link} = \frac{2GJ_s}{s-w} \tag{a.18}$$

where J_s is the torsion constant of the linkage.

The torsional compliance of the linkages can be made very low by increasing the width of the linkage. The compliance due to the distortion of the beams will then dominate. The forces and torques producing this distortion are analysed in the free-body diagram of figure a4. For a total external torque of τ , each beam will experience a torque $T = \tau/4$ on its connecting face to the linkage to the proof mass. This torque will be opposed by a combination of a torque U and moment Fl provided by the elbow. Considering the balance of forces and torques on the elbow, the forces will produce an overall moment $Fs/2$ which must be opposed by torques $Fs/2$. The resulting axial torques will cause a twist of each beams. Hence the overall deflection of each beam will be due to a combination of a torque U and force F producing a bend in the z direction and a twist about the y axis due to the torque $Fs/2$.

The external torque can therefore be regarded as being distributed between the bending torque U and force F so that the resulting deflection and twist of the beams cause a pure rotation of the suspension unit about X-axis. The force F will be opposed by the other half of the suspension unit but will slightly reduce the effect of the external torque by an negligible amount Fw_s , due to the forces acting on the linkage, it is neglected for the derivation. Equating the torques acting on the beam, we get

$$T = Fl + U \quad (a.19)$$

The angular deflection for the overall beam is $2\alpha_{\text{beam}}$ as shown in fig a4(c), the two beams comprising the folded cantilever pair undergo double the deflection due to forces acting at the ends and an angular deflection of the elbow. α_{beam} can thus be calculated as:

$$\Delta_{\text{beam}} + \frac{\Delta_{\text{elbow}}}{2} = l\alpha_{\text{beam}} \quad (a.20)$$

where the deflection of the beam, Δ_{beam} , is given by Roark [A.1] table 3, expressions 1a and 3a as:

$$\Delta_{\text{beam}} = \frac{Fl^3}{3EI_z} + \frac{Ul^2}{2EI_z} \quad (a.21)$$

the deflection of the elbow, Δ_{elbow} , is given by

$$\Delta_{\text{elbow}} = \phi_{\text{elbow}}s = \frac{Fs}{2} \frac{l}{GJ} s = \frac{Fl s^2}{2GJ} \quad (a.22)$$

The deflection angle of the beam ends is given by Roark table 3, expression 1 as:

$$\alpha_{\text{beam}} = \frac{Fl^2}{2EI_z} + \frac{Ul}{EI_z} \quad (a.23)$$

Substituting equation (a.21) and (a.22) in equation (a.20) and solving it with (a.23) gives

$$\alpha_{beam} = \frac{Fl^2}{2EI_z} + \frac{Ul}{EI_z} = \frac{Fl^2}{3EI_z} + \frac{Ul}{2EI_z} + \frac{Fs^2}{4GJ} \quad (a.24)$$

reducing to:

$$U = F \left(\frac{s^2}{4GJ} - \frac{l^2}{6EI_z} \right) \cdot \frac{2EI_z}{l} \quad (a.25)$$

Substituting equation (a.25) in equation (a.19) to get F in terms of T , and substituting F and U in equation (a.23) in terms of T derived from (a.25) and (a.19) leads to an expression relating α_{beam} and T . T is $\tau/4$, so the compliance for rotation about X -axis due to beam distortion is given by

$$\frac{1}{k_{\alpha,beam}} = \frac{l}{4EI_z} \left(1 - \frac{3}{4 + 3 \frac{EI_z s^2}{GJ l^2}} \right) \quad (a.26)$$

The total compliance will be sum of the compliances due the torsion of the linkages derived from (a.18) and (a.26):

$$\frac{1}{k_{\alpha}} = \frac{1}{k_{\alpha,link}} + \frac{1}{k_{\alpha,beam}} \quad (a.27)$$

For a mass moment of inertia about the X -axis of

$$I_{xx} = \frac{1}{3} mg^2 \quad (a.28)$$

The square of the rejection ratio for this mode is given by

$$\left(\frac{\omega_{\alpha}}{\omega_x} \right)^2 = \left\{ \frac{4EI_x(s-w)g^2}{GJ_s l^3} + \frac{4I_x g^2}{I_z l^2} \left[1 - \frac{3}{4 + \frac{3s^2 EI_z}{l^2 GJ}} \right] \right\}^{-1} \quad (a.29)$$

A2.2 Cross-axis rotational mode about Y-axis (k_{β}):

The torque about the Y -axis can be considered as two opposing forces acting along Z -axis on either side of the proof-mass (figure a5). This means the spring constant for rotation about Y -axis is proportional to the spring constant for motion along Z -axis (k_z).

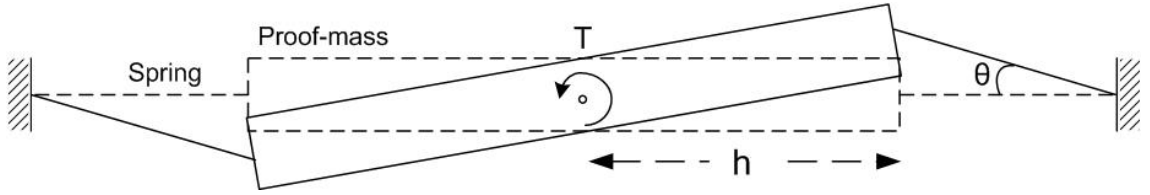


Figure a5: Rotational torque about Y -axis can be decomposed into an out-of-plane force acting on the springs.

The torque acting about Y -axis is then given in terms of the force acting along Z -axis on the springs as:

$$T_y = F_z \times h \quad (\text{a.30})$$

where h is the distance from the center of the proof-mass to the spring linkages.

The angular deflection can be calculated from the vertical deflection as:

$$\theta_\beta = \frac{\Delta z}{h} \quad (\text{a.31})$$

where Δz is the vertical deflection of the springs under a vertical force F_z .

Spring constant for rotation about Y -axis can therefore be calculated using a.29 and a.30 as:

$$k_\beta = \frac{T_y}{\theta_\beta} = \frac{F_z h^2}{\Delta z} = k_z h^2 \quad (\text{a.32})$$

As we can see from the FEA derived value for mode ratio ω_β/ω_x and ω_z/ω_x in figure a6, the rejection ratio for the rotational mode about Y -axis follows the rejection ratio for the out-of-plane mode. The analytical expression neglects the torsional effects which will tend to increase the rejection ratio for the rotational mode about Y -axis. The analytical expression thus gives the lower limit for the rejection ratio for rotation about the Y -axis which is useful when trying to increase the rejection ratios.

The modal frequency for rotational mode is given by

$$\omega_\beta = \sqrt{\frac{k_\beta}{I_{yy}}} = \sqrt{\frac{k_z h^2}{\frac{1}{3} m h^2}} = \sqrt{\frac{3k_z}{m}} = \sqrt{3} \omega_z \quad (\text{a.33})$$

where $I_{yy} = \frac{1}{3} m h^2$ is the mass moment of inertia.

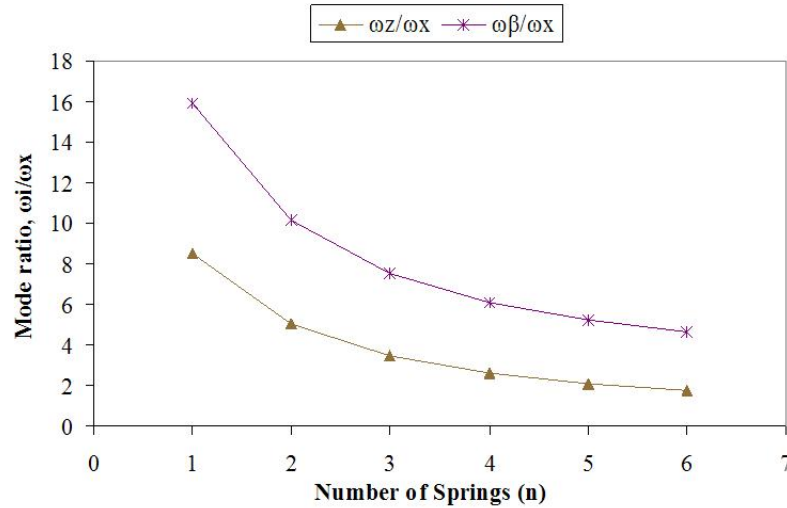


Figure a6: FEA derived results of ω_β/ω_x and ω_z/ω_x .

The error between the analytical and FEA calculated rejection ratio for β and z mode are exactly the same, showing a complete dependence of β mode on z mode.

A2.3 Cross-axis rotational mode about Z-axis (k_y):

The torque about Z-axis is comprised of two opposing lateral force acting along Y-axis on either side of the proof-mass (fig. a7).

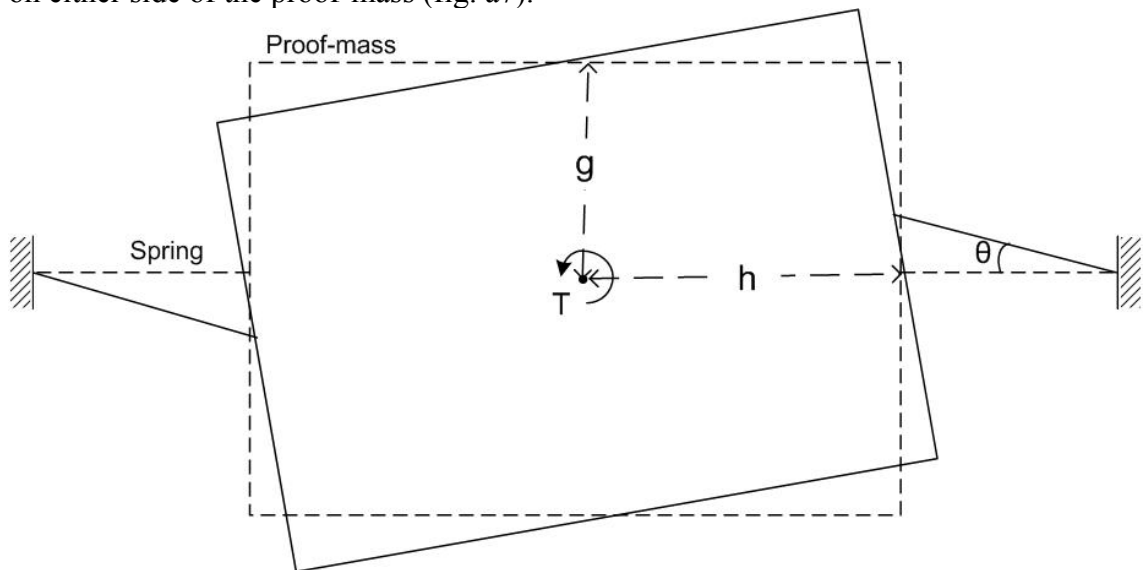


Figure a7: Torque about the Z-axis causes an angular deflection θ .

The torque acting about Z-axis is then given in terms of the force acting along Y-axis on the springs as:

$$T_z = F_y \times h \tag{a.34}$$

where h is the distance from the center of the proof-mass to the spring linkages.

The angular deflection can be calculated from the vertical deflection as:

$$\theta_\gamma = \frac{\Delta y}{h} \quad (\text{a.35})$$

where Δy is the total deflection of the springs under a lateral force F_y .

Spring constant for rotation about Z-axis can therefore be calculated using a.33 and a.34 as:

$$k_\gamma = \frac{T_z}{\theta_\gamma} = \frac{F_y h^2}{\Delta y} = k_y h^2 \quad (\text{a.36})$$

The modal frequency for rotational mode is then given by

$$\omega_\gamma = \sqrt{\frac{k_\gamma}{I_{zz}}} = \sqrt{\frac{k_y h^2}{\frac{1}{3} m (h^2 + g^2)}} = \frac{\sqrt{3}}{\sqrt{1 + g^2/h^2}} \omega_y \quad (\text{a.37})$$

where $I_{zz} = \frac{1}{3} m (h^2 + g^2)$ is the mass moment of inertia about Z-axis..

This simplified approach to calculating the rejection ratio neglects the effect of torsion on the beams and gives the lower estimate of the rejection ratio consistently so is useful for quickly exploring the design space.

A3. Bibliography

- [A.1] R. J. Roark, *Roark's formulas for stress and strain*, 6 ed: McGraw-Hill, 1989.
- [A.2] J. W. Judy, Batch Fabricated Ferromagnetic Microactuators with Silicon Flexures, Ph.D. Thesis, Electrical Engineering, University of California, Berkeley, 1996

Appendix B: Numerical model

B1. Finite Element Analysis (FEA)

A numerical method and a computer can be used to evaluate the mathematical model and estimate the characteristics of the process. Two common numerical methods are the finite difference method and variational method like Rayleigh-Ritz and Galerkin. In finite difference method [B.1] the derivatives are replaced by difference quotients (or Taylor series expressions), the resulting algebraic equation is solved by imposing the boundary conditions for the values of the solution at mesh points.

To solve differential equations using variational method, the equation is converted to an equivalent weighted-integral form and the approximate solution over the domain is assumed to be a linear combination ($\sum_i c_i \phi_i$) of suitable approximation function ϕ_i and undetermined coefficients c_i . The coefficients c_i are determined such that the integral statement equivalent to the original differential equation is satisfied. Various variational methods like Rayleigh-Ritz, Galerkin, least-squares vary in the choice of integral form, weight functions and approximation functions. Finite element method overcomes the limitations of variational method by employing a systematic procedure for derivation of the approximation functions over subregions of the domain.

The finite element method can be broken down into three basic schemes. First a geometrically complex domain of the problem is decomposed into simpler subdomains, the finite elements. Next for each finite element the approximation function is derived using continuous functions which are a combination of linear algebraic polynomials. Finally the algebraic relation between the undetermined coefficients are obtained by satisfying the weighted-integral governing equations for each element. Thus, the finite element method can be thought of as element-wise application of Rayleigh-Ritz or weighted-residual methods. The approximation function is normally an algebraic polynomial and the coefficients are the value of solution at some pre-selected points on the boundary and within the elements, called nodes.

Various commercial and academic numerical analysis tools are available. For mechanical static, dynamic and transient analysis FEM tools give detailed result on stress gradients within the geometry.

Numerical modeling of various spring-frame configurations were performed in Ansys to validate analytical results as well as to extract and view the modes. Ansys [B.2] is a software package for finite element analysis of structural, thermal, electrostatic and coupled-field problems.

B2. Isotropic vs. Anisotropic model

Silicon is an anisotropic model, the analytical models used in chapter 3 consider silicon an isotropic material with a modulus of rigidity of 129 GPa. To develop an analytical model which takes into account anisotropic nature of silicon is non-trivial. It is much easier to incorporate the anisotropic nature of silicon in numerical model.

Brantley [B.3] gives the numerical values for the elastic constants along the various crystal planes of silicon as $E_{11} = E_{22} = E_{33} = 165.7 \times 10^9 \text{ N/m}^2$, $E_{12} = E_{13} = E_{23} = 63.9 \times 10^9 \text{ N/m}^2$, and $E_{44} = E_{55} = E_{66} = 79.56 \times 10^9 \text{ N/m}^2$. Hooke's law is expressed for silicon as:

$$\begin{bmatrix} \sigma_x \\ \sigma_y \\ \sigma_z \\ \tau_x \\ \tau_y \\ \tau_z \end{bmatrix} = \begin{bmatrix} E_{11} & E_{12} & E_{12} & 0 & 0 & 0 \\ E_{12} & E_{11} & E_{12} & 0 & 0 & 0 \\ E_{12} & E_{12} & E_{11} & 0 & 0 & 0 \\ 0 & 0 & 0 & E_{44} & 0 & 0 \\ 0 & 0 & 0 & 0 & E_{44} & 0 \\ 0 & 0 & 0 & 0 & 0 & E_{44} \end{bmatrix} \begin{bmatrix} \varepsilon_x \\ \varepsilon_y \\ \varepsilon_z \\ \gamma_x \\ \gamma_y \\ \gamma_z \end{bmatrix}$$

The analytical calculations for the resonant modes are compared against numerical simulations with isotropic and anisotropic silicon property. The isotropic model is much more similar to the analytical model than the anisotropic model. The deviation of the resonant modes between the isotropic analytical model and anisotropic numerical model is pronounced in modes which are a function of the out-of-plane stiffness of the spring.

B3. Modal analysis using ANSYS

Mode-Frequency Analysis (ANTYPE, MODAL) is used for natural frequency and mode shape determination. The equation of motion for an undamped system, expressed in matrix notation using the above assumptions is:

$$[\mathbf{M}]\ddot{\mathbf{u}} + [\mathbf{C}]\dot{\mathbf{u}} + [\mathbf{K}]\mathbf{u} = \mathbf{0} \quad \text{b.1}$$

$[\mathbf{M}]$ is the structure mass matrix, $[\mathbf{K}]$ is the structure stiffness matrix and \mathbf{u} is the nodal displacement vector and $\ddot{\mathbf{u}}$ is the nodal acceleration vector.

For a linear system, free vibration will be harmonic of the form:

$$\{\mathbf{u}\} = \{\phi\}_i \cos(\omega_i t) \quad \text{b.2}$$

$\{\phi\}_i$ is the eigenvector representing the mode shape of the i^{th} natural frequency, ω_i the i^{th} natural circular frequency (radians per unit time) and t is time.

Substituting Equation b.2 in equation b.1 gives:

$$(-\omega_i^2 [\mathbf{M}] + [\mathbf{K}])\{\phi\}_i = \{0\} \quad \text{b.3}$$

The solutions to this equality are either $\{\phi\}_i = \{0\}$, which is trivial or

$$[K] - \omega^2 [M] = 0 \tag{b.4}$$

This is an eigenvalue problem which may be solved for up to n values of ω^2 and n eigenvectors $\{\phi\}_i$, where n is the number of DOF. Equation b.4 can be written as an eigenvalue and eigenvector problem as:

$$[K]\{\phi\}_i = \lambda_i [M]\{\phi\}_i \tag{b.5}$$

where, $\{\phi\}_i$ is the eigenvector and λ_i is the eigenvalue.

ANSYS uses an eigensolver like Black Lanczos to solve the eigenvalue and eigenvector matrices for the model. Grimes et al [B.4] gives the theoretical basis of the Block Lanczos solver.

The 3D element used for meshing the model is SOLID45 which has six degrees of freedom at each of its eight nodes. The element is shown in figure b1.

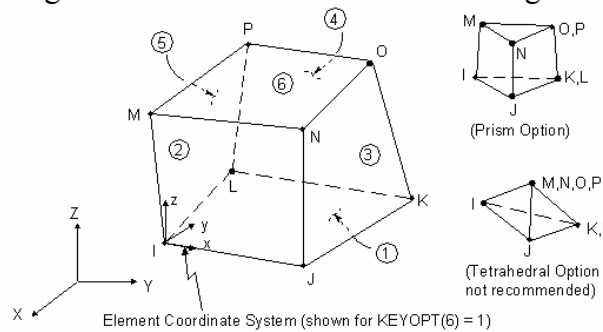


Figure b1: SOLID45 element used for meshing the suspension model for modal and stress analysis (*source:* Ansys manual).

B4. Input files for FEA using ANSYS

I. Multiple spring set suspension

! Parametric input file for lateral suspension

! Multiple spring model (no frame) – set parameter ‘ns’ to the number of spring sets

! Rectangular end connector

! Sunil, 10/10/2003

! Sunil, last update 25/10/2006

! Units set to umKsV (micrometers)

/PREP7

/TITLE, LATERAL SUSPENSION
MODAL ANALYSIS

/unit, SI

! Parameters nomenclature

! linkage [I] - connector between spring and frame

! spring [s]

! proof-mass [m]

! Wafer

wt = 525 !wafer thickness

! Spring parameters

Appendix B

ns = 2 !number of spring (on one side)	al, ln, ln+1, ln+2, ln+3 !linkage
sl = 8320 !spring length	k, kn+4, x0+ll, y0+lw+sw, z0
sw = 24 !spring width	k, kn+5, x0, y0+lw+sw, z0
sg = 492 !spring pitch (s in schematic figure 3.2)	l, kn+2, kn+4, swd
! Link parameters	l, kn+4, kn+5, lld
ll = 70 !link half length	l, kn+5, kn+3, swd
lw = sg/2 !link width (thickness in previous versions)	al, ln+2, ln+4, ln+5, ln+6 !link- spring connector
! Proof mass parameters	k, kn+6, x0+ll+sl, y0+lw, z0
ml = 8960 !half proof mass length	k, kn+7, x0+ll+sl, y0+lw+sw, z0
mw = 6030 !half proof mass width	
! Mesh size control settings	l, kn+2, kn+6, sld
sld = 100 !divisions spring length	l, kn+6, kn+7, swd
swd = 3 !divisions spring width	l, kn+7, kn+4, sld
lld = 5 !divisions linkage length	al, ln+7, ln+8, ln+9, ln+4 !spring horizontal - beam 1
lwd = 10 !divisions linkage width	
mld = 5 !divisions proof-mass length	k, kn+8, x0+ll+sl+sw, y0+lw, z0
mwd = 5 !divisions proof-mass width	k, kn+9, x0+ll+sl+sw, y0+lw+sw, z0
sgd = 10 !divisions spring end connector	l, kn+6, kn+8, swd
wtd = 5 !divisions wafer thickness (vertical extrusion)	l, kn+8, kn+9, swd
! Draw Model	l, kn+9, kn+7, swd
! Set starting point for the suspension	al, ln+10, ln+11, ln+12, ln+8 !spring vertical-horizontal connector (1)
x0 = 0	k, kn+10, x0+ll+sl+sw, y0+lw+sw+sg, z0
y0 = 0	
z0 = 0	k, kn+11, x0+ll+sl, y0+lw+sw+sg, z0
kn = 3	l, kn+9, kn+10, sgd
ln = 1	l, kn+10, kn+11, swd
! Draw one half of spring	l, kn+11, kn+7, sgd
k, kn, x0, y0, z0	al, ln+12, ln+13, ln+14, ln+15 !spring vertical segment
k, kn+1, x0+ll, y0, z0	
k, kn+2, x0+ll, y0+lw, z0	k, kn+12, x0+ll+sl+sw, y0+lw+sw+sg+sw, z0
k, kn+3, x0, y0+lw, z0	k, kn+13, x0+ll+sl, y0+lw+sw+sg+sw, z0
l, kn, kn+1, lld	
l, kn+1, kn+2, lwd	l, kn+10, kn+12, swd
l, kn+2, kn+3, lld	l, kn+12, kn+13, swd
l, kn+3, kn, lwd	

Appendix B

```

l, kn+13, kn+11, swd
al, ln+14, ln+16, ln+17, ln+18 !spring
vertical-horizontal corner (2)

k, kn+14, x0+ll, y0+lw+sw+sg+sw, z0
k, kn+15, x0+ll, y0+lw+sw+sg, z0

l, kn+15, kn+11, sld
l, kn+13, kn+14. sld
l, kn+14, kn+15, swd

al, ln+19, ln+18, ln+20, ln+21 !spring
horizontal segment (2)

k, kn+16, x0, y0+lw+sw+sg+sw, z0
k, kn+17, x0, y0+lw+sw+sg, z0

l, kn+17, kn+15, lld
l, kn+14, kn+16, lld
l, kn+16, kn+17, swd

al, ln+22, ln+21, ln+23, ln+24 !spring-
link connector (2)

k, kn+18, x0+ll, y0+lw+sw+sg+sw+lw,
z0
k, kn+19, x0, y0+lw+sw+sg+sw+lw, z0

l, kn+14, kn+18, lwd
l, kn+18, kn+19, lld
l, kn+19, kn+16, lwd

al, ln+23, ln+25, ln+26, ln+27 !linkage
(2)

! Define spring set as component
cm, spring1, area

! Mirror it number of spring (ns) times

*do, num, 2, ns, 1
wplane, -1, x0, y0+lw+sw+sg+sw+lw,
z0 !move WP to the start of next
spring
csys, 4
!use defined WP
arsym, y, spring1
!mirror about Y-axis
y0 = y0+lw+sw+sg+sw+lw

csys, 0
asel, s, loc, y, y0, y0+lw+sw+sg+sw+lw
cm, spring1, area
alls
*enddo

! Reset WP back to original CS
y0 = 0
wplane, -1, x0, y0, z0

! Draw a quarter of proof mass
y0 = y0 + ns*(lw+sw+sg+sw+lw)

rectng, x0, x0+ll, y0, y0+mw
rectng, x0+ll, x0+ml-ll, y0, y0+mw

! Mirror it about x and y axis to get the
complete suspension
! Mirroring about Y-axis
asel, all
wplane, -1, x0, y0+mw, z0
csys,4
arsym, y, all

! Mirroring about X-axis
arsym, x, all

! Glue everything together
nummrg, all

! Define material and elements
MP,DENS,1,2.329e-15 ! Density of
Silicon

! Isotropic material property
MP, EX, 1, 129e3 !Young's
modulus of silicon: 129 GPa
MP, PRXY, 1, 0.23 !Poisson's ratio
of silicon: 0.23

! Anisotropic silicon property –
comment out isotropic property to use
this
! C11=1.657e5 ! Stiffness Matrix
Components for Silicon
! C12=0.639e5 ! After W.A.
Brantley [1.34]
! C44=0.7956e5

```

```

! tb,ANEL,1,1 ! Stiffness Matrix for
Silicon
! tldata,1, C11,C12,C12,0,0,0
! tldata,7, C11,C12,0,0,0,C11
! tldata,13, 0,0,0,C44,0,0
! tldata,19, C44,0,C44

! Define Elements
ET,1,PLANE42      ! 2D Element
ET,2,SOLID64      ! 3D Anisotropic
Solid

! Area Mesh
! Settings for map mesh
ESIZE, ,5
TYPE, 1           !assigns element
number to elements defined
MSHAPE, 0, 2D    !use quads for
area
MSHKEY, 1        !mapped meshing

AMESH, ALL       !mesh all areas

! Extrude mesh to create volume
TYPE, 2
EXTOPT, ACLEAR, 1 !remove
area meshes
EXTOPT, ESIZE, wtd !number
of vertical divisions set by wtd
VEXT, all, , , , wt !extrume
area mesh to thickness wt

! Apply Boundary conditions
csys, 0
alls

asel, s, loc, y, 0 !selecting
starting face of first spring
asel, a, loc, y,
(ns*(lw+sw+sg+sw+lw)+mw)*2
!selecting end face

! Anchoring the suspension at both ends
da, all, ux, 0
da, all, uy, 0
da, all, uz, 0

alls
nummrg, all

```

```

! Solve the model for resonant modes
/SOLU
antype, modal, new
modopt, lanb, 10, 0, 1000,,off,,2
!select Block Lanczos solver
mxpand,10,,,0
!expand 10 modes
solve
!solve

```

! Use postprocessor (/POST1) to get the frequencies and mode shapes
! The layout is as seen in figure b2.

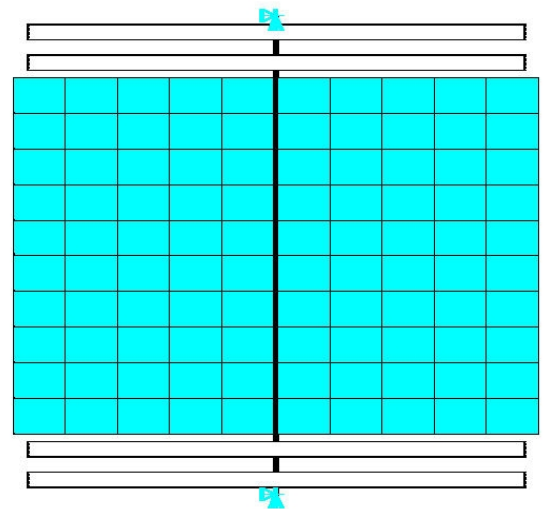


Figure b2: Suspension with two sets of springs.

II. Suspension with multiple springs and intermediate frames: Cross-bar spring end connector

```

! Parametric input file for lateral
suspension
! Multiple alternate intermediate frame
model (set parameter 'nFrame')
! Rounded cross-bar end connector
! Sunil, last update 25/10/2006

/PREP7
/TITLE, MULTIPLE INTERMEDIATE
FRAMES MICROSEISMOMETER
MODAL ANALYSIS
/unit, SI

```

! Units set to umKsV (micrometers)
! All length units in um (micrometer)

Appendix B

! Parameter nomenclature

! linkage - connector between spring &
frame - [l]
! spring [s]
! frame [f]
! proof-mass [m]

*afun, deg !set degrees as unit of
angle measurement

springL = 8370 ! 1/2 the spring
length - straight section
nFrame = 1+2 ! number of
internal frames + 1

ll = 50 ! 1/2 link length
lt = 315 ! link thickness
lang = 180/2 ! half of the angle
subtended by the 2 points
lr = 200/2
ld = 237/2*(1-cos(lang)) ! distance from
center of the kp joining line to kp on
center-curved portion of link

vst = 24 ! vertical spring
thickness
sl = springL-vst ! spring length of
straight section - one side
st = 24 ! spring thickness
sg = 530 ! spring gap
between two straight section of a spring
element
sang = 180/2
sr1d = sg/2*(1-cos(sang))
sr1 = sg/2 ! radius of curved
section of the spring - inside edge
sr2 = sr1+st ! radius of outer
curve for spring curved section

sfg = 176+sr1+st ! extra spring
frame gap besides fg for the spring
closest to the proof mass
fg = 40 ! etch channel
width between frames
ft = 60 ! frame thickness
- vertical (along x - ansys) segment
fth = 60 ! frame
horizontal (along y) segment thickness
!fl = springL + sfg + nFrame*(fg + ft) -
fg !largest frame length - outside

ml = 17760/2 ! proof-mass
length
fl = ml + (nFrame-1)*(fg + ft) -ll
mw = 11632 ! proof-mass
width

wt = 525 !wafer thickness

! Parameter check
! Check last spring is still smaller than
the last frame
! Check proof mass is smaller than last
frame

! Mapped mesh size settings
sldiv = 100 !spring segment
division
stdiv = 3 !spring thickness
divisions
scang = 10 !spring curved
section division
ldiv = 5 !linkage length
divisions
lvdiv = 10 !linkage width
divisions
fldiv = 100 !to keep the
element sized to 100 - will vary
depending on frame
ftdiv = 2 !frame thickness
divisions
fwdiv = 100 !frame width
divisions (frame segment linking two
sides of the PM frame)
mwdiv = 10 !proof mass
width divisions
mldiv = 5 !proof mass
length divisions
vdiv = 3 !vertical divisions
vsdiv = 10 !vertical spring
segment divisions

! Draw Model
! Going ccw from right-bottom for KP,
for lines from bottom side

! Define 2 keypoints for drawing the
curves using 2 KP and radius + a KP on
the side of curvature

Appendix B

```

k,1,-fl-1000,0,0
k,2,-fl-1000,0,wt

x0 = 0          !define starting point in
Global CSYS
y0 = 0
z0 = 0

! Move WP using wpofts, 0, yoff, 0 so
its always top centered wrt the area
! using *do - *enddo to develop all the
spring and frames

ini = 1
fin = nFrame

! draw spring and frames
! repeat loop for all spring and frames

k,3, x0-ll, y0, z0
k, 4, x0+ll, y0, z0
l, 3, 4, ldiv

kpnum = 4      !endingkeypoint number
lnum = 2        !line number

! starting number for keypoints at center
of the curved sections - as the larc
command is failing for 90deg arc

cpnum = (kpnum+28)*(nFrame-
1)+18+1000
vpnum = (cpnum+8)*(nFrame-1)+1000
!for vertical spring sections

*do, num, ini, fin, 1

! Draw linkage
k, kpnum+1, x0-ll, y0+lt, z0
k, kpnum+2, x0+ll, y0+lt, z0

*if, num, EQ, 1, then
l, 4, kpnum+2, lvdiv
l, kpnum+1, kpnum+2, ldiv
l, kpnum+1, 3, lvdiv
*endif

*if, num, GT, 1, then
l, kpnum-9, kpnum+2, lvdiv
l, kpnum+1, kpnum+2, ldiv
l, kpnum-8, kpnum+1, lvdiv
*endif

*if, num, EQ, 1, then
al, lnum-1, lnum, lnum+1, lnum+2
*endif

*if, num, GT, 1, then
al, lnum-14, lnum, lnum+1, lnum+2
*endif

! Draw spring-link contact
k, kpnum+3, x0+ll, y0+lt+st, z0
k, kpnum+4, x0-ll, y0+lt+st, z0

l, kpnum+2, kpnum+3, stdiv
l, kpnum+3, kpnum+4, ldiv
l, kpnum+4, kpnum+1, stdiv

al, lnum+1, lnum+3, lnum+4, lnum+5

! Draw spring straight sections
k, kpnum+5, x0+ll+sl, y0+lt, z0
k, kpnum+6, x0+ll+sl, y0+lt+st, z0

l, kpnum+2, kpnum+5, sldiv
l, kpnum+5, kpnum+6, stdiv
l, kpnum+6, kpnum+3, sldiv

al, lnum+6, lnum+7, lnum+8, lnum+3

! Spring vertical section
k, vpnum+1, x0+ll+sl+vst, y0+lt, z0
k, vpnum+2, x0+ll+sl+vst, y0+lt+st, z0

l, kpnum+5, vpnum+1, stdiv
l, vpnum+1, vpnum+2, stdiv
l, vpnum+2, kpnum+6, stdiv

al, lnum+9, lnum+10, lnum+11, lnum+7

! Spring curved section
k, vpnum+3, x0+ll+sl+vst,
y0+lt+st+sg+st, z0
k, vpnum+4, x0+ll+sl+vst, y0+lt+st+sg,
z0
k, cpnum+3+10*(num-1),
x0+ll+sl+vst+sr1, y0+lt+st+sg/2, z0

```

Appendix B

<p>k, cpnum+4+10*(num-1), x0+ll+sl+vst+sr2, y0+lt+st+sg/2, z0</p>	<p>l, kpnum+12, kpnum+11, stdiv</p>
<p>larc, vpnum+1, vpnum+3, cpnum+4+10*(num-1), sr2 l, vpnum+3, vpnum+4, stdiv larc, vpnum+4, vpnum+2, cpnum+3+10*(num-1), sr1</p>	<p>al, lnum+23, lnum+22, lnum+24, lnum+25</p>
<p>lesize, lnum+14, , scang lesize, lnum+12, , scang</p>	<p>! Spring straight section k, kpnum+14, x0-ll-sl, y0+lt+st+sg+st, z0 k, kpnum+13, x0-ll-sl, y0+lt+st+sg, z0</p>
<p>al, lnum+10, lnum+14, lnum+13, lnum+12</p>	<p>l, kpnum+13, kpnum+11, sldiv l, kpnum+12, kpnum+14, sldiv l, kpnum+14, kpnum+13, stdiv</p>
<p>! Vertical segment k, kpnum+8, x0+ll+sl, y0+lt+st+sg, z0 k, kpnum+7, x0+ll+sl, y0+lt+st+sg+st, z0</p>	<p>al, lnum+26, lnum+25, lnum+27, lnum+28</p>
<p>l, vpnum+3, kpnum+7, stdiv l, kpnum+7, kpnum+8, stdiv l, kpnum+8, vpnum+4, stdiv</p>	<p>! Spring vertical segment k, vpnum+6, x0-ll-sl-vst, y0+lt+st+sg+st, z0 k, vpnum+5, x0-ll-sl-vst, y0+lt+st+sg, z0</p>
<p>al, lnum+13, lnum+15, lnum+16, lnum+17</p>	<p>l, vpnum+5, kpnum+13, stdiv l, kpnum+14, vpnum+6, stdiv l, vpnum+6, vpnum+5, stdiv</p>
<p>l, kpnum+8, kpnum+6, vsdiv l, vpnum+2, vpnum+4, vsdiv</p>	<p>al, lnum+29, lnum+28, lnum+30, lnum+31</p>
<p>al, lnum+11, lnum+19, lnum+17, lnum+18</p>	<p>! Spring curved section k, vpnum+7, x0-ll-sl-vst, y0+lt, z0 k, vpnum+8, x0-ll-sl-vst, y0+lt+st, z0 k, cpnum+5+10*(num-1), x0-ll-sl-vst- sr1, y0+lt+st+sg/2, z0 k, cpnum+6+10*(num-1), x0-ll-sl-vst- sr2, y0+lt+st+sg/2, z0</p>
<p>! Spring straight section k, kpnum+10, x0+ll, y0+lt+st+sg+st, z0 k, kpnum+9, x0+ll, y0+lt+st+sg, z0</p>	<p>larc, vpnum+6, vpnum+7, cpnum+6+10*(num-1), sr2 l, vpnum+7, vpnum+8, stdiv larc, vpnum+8, vpnum+5, cpnum+5+10*(num-1), sr1</p>
<p>l, kpnum+9, kpnum+8, sldiv l, kpnum+7, kpnum+10, sldiv l, kpnum+10, kpnum+9, stdiv</p>	<p>lesize, lnum+34, , scang lesize, lnum+32, , scang</p>
<p>al, lnum+20, lnum+16, lnum+21, lnum+22</p>	<p>al, lnum+33, lnum+32, lnum+31, lnum+34</p>
<p>! Linkage-spring contact k, kpnum+12, x0-ll, y0+lt+st+sg+st, z0 k, kpnum+11, x0-ll, y0+lt+st+sg, z0</p>	
<p>l, kpnum+11, kpnum+9, ldiv l, kpnum+10, kpnum+12, ldiv</p>	

! Vertical spring segment
k, kpnnum+15, x0-ll-sl, y0+lt, z0
k, kpnnum+16, x0-ll-sl, y0+lt+st, z0

l, vnum+7, kpnnum+15, stdiv
l, kpnnum+15, kpnnum+16, stdiv
l, kpnnum+16, vnum+8, stdiv

al, lnum+35, lnum+36, lnum+37,
lnum+33

l, kpnnum+16, kpnnum+13, vsdiv
l, vnum+5, vnum+8, vsdiv

al, lnum+37, lnum+38, lnum+29,
lnum+39

! Spring straight section
l, kpnnum+15, kpnnum+1, sldiv
l, kpnnum+4, kpnnum+16, sldiv

al, lnum+40, lnum+5, lnum+41,
lnum+36

! Linkage
k, kpnnum+18, x0+ll, y0+lt+st+sg+st+lt,
z0
k, kpnnum+17, x0-ll, y0+lt+st+sg+st+lt,
z0

l, kpnnum+10, kpnnum+18, ldiv
l, kpnnum+18, kpnnum+17, ldiv
l, kpnnum+17, kpnnum+12, ldiv

!lesize, lnum+26, , lchang
!lesize, lnum+28, , lchang
al, lnum+24, lnum+42, lnum+43,
lnum+44

! Check if the spring close to proof
mass is drawn then exit
*if, num, EQ, nFrame, EXIT

! Frame linkage
k, kpnnum+19, x0+ll,
y0+lt+st+sg+st+lt+fth, z0
k, kpnnum+20, x0-ll,
y0+lt+st+sg+st+lt+fth, z0

l, kpnnum+18, kpnnum+19, fdiv

l, kpnnum+19, kpnnum+20, ldiv
l, kpnnum+20, kpnnum+17, fdiv

al, lnum+43, lnum+45, lnum+46,
lnum+47

! Frame straight segment
k, kpnnum+21, x0+ll+(fl-(num-
1)*(fg+ft)-ft), y0+lt+st+sg+st+lt, z0
k, kpnnum+22, x0+ll+(fl-(num-
1)*(fg+ft)-ft), y0+lt+st+sg+st+lt+fth, z0
!inside end point of +ve frame

l, kpnnum+18, kpnnum+21, fdiv
l, kpnnum+21, kpnnum+22, fdiv
l, kpnnum+22, kpnnum+19, fdiv

al, lnum+48, lnum+49, lnum+50,
lnum+45

k, kpnnum+23, x0+ll+(fl-(num-
1)*(fg+ft)), y0+lt+st+sg+st+lt, z0
k, kpnnum+24, x0+ll+(fl-(num-
1)*(fg+ft)), y0+lt+st+sg+st+lt+fth, z0
!outside end point of frame

l, kpnnum+21, kpnnum+23, fdiv
l, kpnnum+23, kpnnum+24, fdiv
l, kpnnum+24, kpnnum+22, fdiv

al, lnum+51, lnum+52, lnum+53,
lnum+49

! Frame segment
k, kpnnum+26, x0-ll-(fl-(num-
1)*(fg+ft))+ft, y0+lt+st+sg+st+lt+fth,
z0
k, kpnnum+25, x0-ll-(fl-(num-
1)*(fg+ft))+ft, y0+lt+st+sg+st+lt, z0

l, kpnnum+25, kpnnum+17, fdiv
l, kpnnum+20, kpnnum+26, fdiv
l, kpnnum+26, kpnnum+25, fdiv

!al, lnum+38, lnum+32, lnum+39,
lnum+40
a, kpnnum+17, kpnnum+20, kpnnum+26,
kpnnum+25

Appendix B

```

k, kpnnum+28, x0-ll-(fl-(num-
1)*(fg+ft)), y0+lt+st+sg+st+lt+fth, z0
k, kpnnum+27, x0-ll-(fl-(num-
1)*(fg+ft)), y0+lt+st+sg+st+lt, z0

l, kpnnum+27, kpnnum+25, ftdiv
l, kpnnum+26, kpnnum+28, ftdiv
l, kpnnum+28, kpnnum+27, ftdiv

al, lnum+57, lnum+56, lnum+58,
lnum+59

kpnnum = kpnnum+28
vpnum = vpnum+8
x0 = x0
y0 = y0+lt+st+sg+st+lt+fth
z0 = 0
lnum = lnum+60

*enddo

! Exit point once all the springs and
frames are drawn
! Draw proof mass half
kpnnum = kpnnum+18
x0 = x0
y0 = y0+lt+st+sg+st+lt
z0 = 0

k, kpnnum+1, x0+ml, y0
k, kpnnum+2, x0-ml, y0

l, kpnnum-1, kpnnum+1, mldiv
l, kpnnum, kpnnum+2, mldiv

! Draw the mirror portion of the spring-
frame just rotate the csys so the y is
pointing up and offset
wplane, -1, x0, y0+mw/2, z0 !define a
new working plane offset to the center
of proof mass
csys,4 !changing
active CS to the defined working plane

arsym, y, all, , , , 0, 0

! Generate lines on the mirrored copy as
area mirror doesn't generate line
kpnnum_last = kpnnum+2+36*(nFrame-
1)+26+2

k, kpnnum_last+2, x0-ml, mw/2, z0
k, kpnnum_last+1, x0+ml, mw/2, z0

l, kpnnum_last-1, kpnnum_last+2, mldiv
l, kpnnum_last, kpnnum_last+1, mldiv

!connect the two mirrored images
kpnnum1 = kpnnum+2
kpnnum2 = kpnnum_last

l, kpnnum1-1, kpnnum2+1, mwdiv
l, kpnnum1, kpnnum2+2, mwdiv
l, kpnnum1-2, kpnnum2, mwdiv
l, kpnnum1-3, kpnnum2-1, mwdiv

lnum = lnum+36+2
lnum2 = 2*lnum

!proof mass areas
a, kpnnum1, kpnnum1-3, kpnnum2-1,
kpnnum2+2
a, kpnnum1-3, kpnnum1-2, kpnnum2,
kpnnum2-1
a, kpnnum1-2, kpnnum1-1, kpnnum2+1,
kpnnum2

! Connect frames on both sides
*do, i, ini, fin-1, 1

kpf1 = 28*(i-1)+4
kpf2 = kpnnum1+36*(i-1)

l, kpf1+22, kpf2+32, fwdiv
l, kpf1+24, kpf2+34, fwdiv
l, kpf1+26, kpf2+35, fwdiv
l, kpf1+28, kpf2+38, fwdiv

a, kpf1+26, kpf1+28, kpf2+38, kpf2+35
a, kpf1+22, kpf1+24, kpf2+34, kpf2+32

*enddo

l, 1, 2, vdiv ! line defining the
vertical extrude
*GET, exline, LINE, ,NUM, MAX

! Define Material
MP,DENS,1,2.329e-15 ! Density of
Silicon

```

```
! Set Silicon anisotropic property
C11=1.657e5 ! Stiffness Matrix
Components for Silicon
C12=0.639e5 ! After W.A. Brantley, J.
Appl. Phys. 44 (1), 1973, 534.
C44=0.7956e5 !
```

```
TB,ANEL,1,1 ! Stiffness Matrix for
Silicon
TBDATA,1, C11,C12,C12,0,0,0
TBDATA,7, C11,C12,0,0,0,C11
TBDATA,13, 0,0,0,C44,0,0
TBDATA,19, C44,0,C44
```

```
! Choose Elements
ET,1,PLANE42 ! 2D Element
ET,2,SOLID64 ! 3D Anisotropic
Solid
```

```
! Map mesh
ESIZE, 100
TYPE, 1 !assigns element
number to elements defined
MSHAPE, 0, 2D !use quads for
area
MSHKEY, 1 !mapped meshing
```

```
AMESH, ALL
```

```
TYPE, 2
EXTOPT, ACLEAR, 1 !remove
area meshes
VDRAG, ALL, , , , , , exline
```

```
! Specify Boundary conditions
csys, 0
alls
```

```
! Select the starting and ending springs
ends
asel, s, loc, x, 0
asel, r, loc, y, 0
asel, a, loc, y,
(nframe*(lt+st+sg+st+lt+ft)-ft)*2+mw
```

```
! Anchor the springs
da, all, ux, 0
da, all, uy, 0
da, all, uz, 0
```

```
alls
nummrg, all
```

```
! Solve using Blank Lanczos solver
antype, modal, new
modopt, lanb, 10, 0, 1000,,off,,2
!select Block Lanczos solver
mxpand,10,,,0
!expand 10 modes
solve
!solve
```

! Use postprocessor (/POST1) to get the frequencies and mode shapes
! The layout is as seen in figure b3.

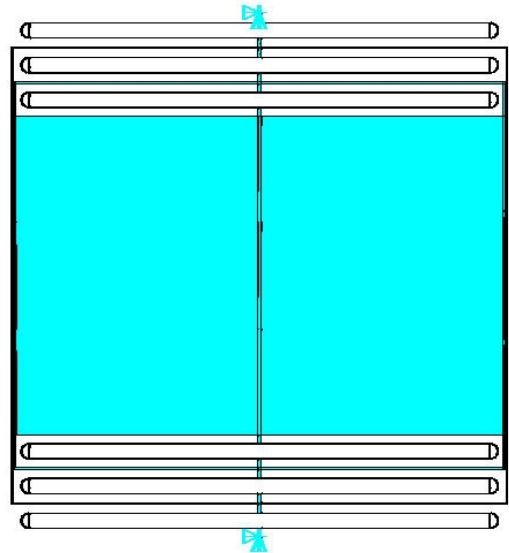


Figure b3: Suspension with three spring sets and two intermediate frames.

III. Suspension with intermediate frames and rectangular rigid end connector (Used for verifying the accuracy of analytical models)

```
! Sunil Kumar, 3 June 2005
! Multiple spring with intermediate
frames suspension model to verify
analytical formulae from Chapter 3.
! Rectangular end connector – made
rigid to correspond better to analytical
model
```

```
/PREP7
/TITLE, MODAL ANALYSIS OF
LATERAL SUSPENSION
```


Appendix B

```

/unit, SI
wt = 528 !wafer
thickness

! Units set to umKsV
! All length units in um (micrometer)

! Parameter nomenclature
! linkage - connector between spring &
frame - [l]
! spring [s]
! frame [f]
! proof-mass [m]

*afun, deg !set unit of measurement
of angles to degrees

springL = 8320 ! 1/2 the
spring length - straight section
nFrame = 1+4 ! number
of internal frames + 1

ll = 70 ! 1/2
linkage length
lt = 492/2 ! linkage
thickness

vst = 24 ! vertical
spring thickness
sl = springL-vst ! spring
length of straight section - one side
st = 24 !18.2 !24 ! spring
thickness
sg = 2*lt ! spring
gap between two beams of spring
element

sfg = 176+sr1+st ! extra
spring frame gap besides fg for the
spring closest to the proof mass
fg = 40 ! etch
channel width between frames
ft = 200 !60 ! frame
thickness

ml = 8960 !8840 !half the
proof mass length
fl = ml + (nFrame-1)*(fg + ft) -ll
!frame length
mw = 2*6030 ! proof
mass width

! Parameter check
! Check last spring is still smaller than
the last frame
! Check proof mass is smaller than last
frame

! Mesh settings
sldiv = 100 !spring segment
division
stdiv = 3 !spring thickness
divisions
scang = 10 !spring curved
section division
ldiv = 5 !linkage
horizontal divisions
lvddiv = 10 !linkage vertical
divisions
fldiv = 100 !to keep the element
sized to 100 - will vary depending on
frame
ftdiv = 2 !frame thickness
divisions
fwdiv = 100 !frame width divisions
(frame segment linking two sides of the
PM frame)
mwddiv = 10 !proof mass
width divisions
mldiv = 5 !proof mass
length divisions
vdiv = 5 !vertical divisions
vsdiv = 10 !vertical spring
segment divisions

! Draw Model
! Going ccw from right-bottom for KP,
for lines from bottom side

x0 = 0 ! define starting point in
Global CSYS
y0 = 0
z0 = 0

! Move WP using wpooffs, 0, yoff, 0 so
its always top centered wrt the area
! Using *do - *enddo to develop all the
spring and frames

```

Appendix B

```

ini = 1
fin = nFrame

! Draw spring and frames
! Repeat loop for all spring and frames

k,3, x0-ll, y0, z0
k, 4, x0+ll, y0, z0
l, 3, 4, ldiv

kpnnum = 4    !endingkeypoint number
lnum = 2      !line number

*do, num, ini, fin, 1

! Draw linkage
k, kpnnum+1, x0-ll, y0+lt, z0
k, kpnnum+2, x0+ll, y0+lt, z0

*if, num, EQ, 1, then
l, 4, kpnnum+2, lvdiv
l, kpnnum+1, kpnnum+2, ldiv
l, kpnnum+1, 3, lvdiv
*endif

*if, num, GT, 1, then
l, kpnnum-9, kpnnum+2, lvdiv
l, kpnnum+1, kpnnum+2, ldiv
l, kpnnum-8, kpnnum+1, lvdiv
*endif

*if, num, EQ, 1, then
al, lnum-1, lnum, lnum+1, lnum+2
*endif

*if, num, GT, 1, then
al, lnum-14, lnum, lnum+1, lnum+2
*endif

! Draw spring-link contact
k, kpnnum+3, x0+ll, y0+lt+st, z0
k, kpnnum+4, x0-ll, y0+lt+st, z0

l, kpnnum+2, kpnnum+3, sldiv
l, kpnnum+3, kpnnum+4, ldiv
l, kpnnum+4, kpnnum+1, sldiv

al, lnum+1, lnum+3, lnum+4, lnum+5

!draw spring straight sections
k, kpnnum+5, x0+ll+sl, y0+lt, z0
k, kpnnum+6, x0+ll+sl, y0+lt+st, z0

l, kpnnum+2, kpnnum+5, sldiv
l, kpnnum+5, kpnnum+6, sldiv
l, kpnnum+6, kpnnum+3, sldiv

al, lnum+6, lnum+7, lnum+8, lnum+3

!spring vertical section
k, vnum+1, x0+ll+sl+vst, y0+lt, z0
k, vnum+2, x0+ll+sl+vst, y0+lt+st, z0

l, kpnnum+5, vnum+1, sldiv
l, vnum+1, vnum+2, sldiv
l, vnum+2, kpnnum+6, sldiv

al, lnum+9, lnum+10, lnum+11, lnum+7

! Spring Vertical segment
k, kpnnum+8, x0+ll+sl, y0+lt+st+sg, z0
k, kpnnum+7, x0+ll+sl, y0+lt+st+sg+st,
z0

l, vnum+3, kpnnum+7, sldiv
l, kpnnum+7, kpnnum+8, sldiv
l, kpnnum+8, vnum+4, sldiv

al, lnum+13, lnum+15, lnum+16,
lnum+17

l, kpnnum+8, kpnnum+6, vsdiv
l, vnum+2, vnum+4, vsdiv

al, lnum+11, lnum+19, lnum+17,
lnum+18

! Spring straight section
k, kpnnum+10, x0+ll, y0+lt+st+sg+st, z0
k, kpnnum+9, x0+ll, y0+lt+st+sg, z0

l, kpnnum+9, kpnnum+8, sldiv
l, kpnnum+7, kpnnum+10, sldiv
l, kpnnum+10, kpnnum+9, sldiv

al, lnum+20, lnum+16, lnum+21,
lnum+22

! Linkage-spring contact
k, kpnnum+12, x0-ll, y0+lt+st+sg+st, z0

```

Appendix B

```

k, kpnum+11, x0-ll, y0+lt+st+sg, z0

l, kpnum+11, kpnum+9, ldiv
l, kpnum+10, kpnum+12, ldiv
l, kpnum+12, kpnum+11, stdiv

al, lnum+23, lnum+22, lnum+24,
lnum+25

! Spring straight section
k, kpnum+14, x0-ll-sl, y0+lt+st+sg+st,
z0
k, kpnum+13, x0-ll-sl, y0+lt+st+sg, z0

l, kpnum+13, kpnum+11, sldiv
l, kpnum+12, kpnum+14, sldiv
l, kpnum+14, kpnum+13, stdiv

al, lnum+26, lnum+25, lnum+27,
lnum+28

! Spring vertical segment
k, vpnum+6, x0-ll-sl-vst,
y0+lt+st+sg+st, z0
k, vpnum+5, x0-ll-sl-vst, y0+lt+st+sg,
z0

l, vpnum+5, kpnum+13, stdiv
l, kpnum+14, vpnum+6, stdiv
l, vpnum+6, vpnum+5, stdiv

al, lnum+29, lnum+28, lnum+30,
lnum+31

! Vertical spring segment
k, kpnum+15, x0-ll-sl, y0+lt, z0
k, kpnum+16, x0-ll-sl, y0+lt+st, z0

l, vpnum+7, kpnum+15, stdiv
l, kpnum+15, kpnum+16, stdiv
l, kpnum+16, vpnum+8, stdiv

al, lnum+35, lnum+36, lnum+37,
lnum+33

l, kpnum+16, kpnum+13, vsdiv
l, vpnum+5, vpnum+8, vsdiv

al, lnum+37, lnum+38, lnum+29,
lnum+39

!spring straight section
l, kpnum+15, kpnum+1, sldiv
l, kpnum+4, kpnum+16, sldiv

al, lnum+40, lnum+5, lnum+41,
lnum+36

! Linkage
k, kpnum+18, x0+ll, y0+lt+st+sg+st+lt,
z0
k, kpnum+17, x0-ll, y0+lt+st+sg+st+lt,
z0

l, kpnum+10, kpnum+18, ldiv
l, kpnum+18, kpnum+17, ldiv
l, kpnum+17, kpnum+12, ldiv

al, lnum+24, lnum+42, lnum+43,
lnum+44

! Check if the spring close to proof
mass is drawn then exit
*if, num, EQ, nFrame, EXIT

! Frame linkage
k, kpnum+19, x0+ll,
y0+lt+st+sg+st+lt+ft, z0
k, kpnum+20, x0-ll,
y0+lt+st+sg+st+lt+ft, z0

l, kpnum+18, kpnum+19, ftdiv
l, kpnum+19, kpnum+20, ldiv
l, kpnum+20, kpnum+17, ftdiv

al, lnum+43, lnum+45, lnum+46,
lnum+47

! Frame straight segment
k, kpnum+21, x0+ll+(fl-(num-
1)*(fg+ft)-ft), y0+lt+st+sg+st+lt, z0
k, kpnum+22, x0+ll+(fl-(num-
1)*(fg+ft)-ft), y0+lt+st+sg+st+lt+ft, z0
!inside end point of +ve frame

l, kpnum+18, kpnum+21, fldiv
l, kpnum+21, kpnum+22, ftdiv
l, kpnum+22, kpnum+19, fldiv

```

Appendix B

```

al, lnum+48, lnum+49, lnum+50,
lnum+45

k, kpnum+23, x0+ll+(fl-(num-
1)*(fg+ft)), y0+lt+st+sg+st+lt, z0
k, kpnum+24, x0+ll+(fl-(num-
1)*(fg+ft)), y0+lt+st+sg+st+lt+ft, z0
!outside end point of frame

l, kpnum+21, kpnum+23, ftdiv
l, kpnum+23, kpnum+24, ftdiv
l, kpnum+24, kpnum+22, ftdiv

al, lnum+51, lnum+52, lnum+53,
lnum+49

! Frame segment
k, kpnum+26, x0-ll-(fl-(num-
1)*(fg+ft))+ft, y0+lt+st+sg+st+lt+ft, z0
k, kpnum+25, x0-ll-(fl-(num-
1)*(fg+ft))+ft, y0+lt+st+sg+st+lt, z0

l, kpnum+25, kpnum+17, fldiv
l, kpnum+20, kpnum+26, fldiv
l, kpnum+26, kpnum+25, ftdiv

!al, lnum+38, lnum+32, lnum+39,
lnum+40
a, kpnum+17, kpnum+20, kpnum+26,
kpnum+25

k, kpnum+28, x0-ll-(fl-(num-
1)*(fg+ft)), y0+lt+st+sg+st+lt+ft, z0
k, kpnum+27, x0-ll-(fl-(num-
1)*(fg+ft)), y0+lt+st+sg+st+lt, z0

l, kpnum+27, kpnum+25, ftdiv
l, kpnum+26, kpnum+28, ftdiv
l, kpnum+28, kpnum+27, ftdiv

al, lnum+57, lnum+56, lnum+58,
lnum+59

kpnum = kpnum+28
vpnum = vpnum+8
x0 = x0
y0 = y0+lt+st+sg+st+lt+ft
z0 = 0
lnum = lnum+60

*enddo !exit point

! Draw proof-mass half
kpnum = kpnum+18
x0 = x0
y0 = y0+lt+st+sg+st+lt
z0 = 0

k, kpnum+1, x0+m1, y0
k, kpnum+2, x0-m1, y0

l, kpnum-1, kpnum+1, mldiv
l, kpnum, kpnum+2, mldiv

! to draw the mirror portion of the
spring-frame just rotate the csys so the y
is pointing up and offset
wplane, -1, x0, y0+mw/2, z0 !define a
new working plane offset to the center
of proof mass
csys,4 !changing
active CS to the defined working plane

arsym, y, all, , , , 0, 0 !mirror
across Y-axis

! Generate lines on the mirrored copy as
area mirror doesn't generate line
kpnum_last = kpnum+2+36*(nFrame-
1)+26+2
k, kpnum_last+2, x0-m1, mw/2, z0
k, kpnum_last+1, x0+m1, mw/2, z0

l, kpnum_last-1, kpnum_last+2, mldiv
l, kpnum_last, kpnum_last+1, mldiv

!connect the two mirrored images
kpnum1 = kpnum+2
kpnum2 = kpnum_last

l, kpnum1-1, kpnum2+1, mwdiv
l, kpnum1, kpnum2+2, mwdiv
l, kpnum1-2, kpnum2, mwdiv
l, kpnum1-3, kpnum2-1, mwdiv

lnum = lnum+36+2
lnum2 = 2*lnum

! Proof-mass areas

```

Appendix B

```

a, kpname1, kpname1-3, kpname2-1,
kpname2+2
a, kpname1-3, kpname1-2, kpname2,
kpname2-1
a, kpname1-2, kpname1-1, kpname2+1,
kpname2

! Connect frames on both sides
*do, i, ini, fin-1, 1

kpf1 = 28*(i-1)+4
kpf2 = kpname1+36*(i-1)

l, kpf1+22, kpf2+32, fwdiv
l, kpf1+24, kpf2+34, fwdiv
l, kpf1+26, kpf2+35, fwdiv
l, kpf1+28, kpf2+38, fwdiv

a, kpf1+26, kpf1+28, kpf2+38, kpf2+35
a, kpf1+22, kpf1+24, kpf2+34, kpf2+32

*enddo

l, 1, 2, vdiv ! line defining the
vertical extrude
*GET, exline, LINE, ,NUM, MAX

! Define Material
MP, EX, 1, 129e3
MP, PRXY, 1, 0.23
MP, DENS, 1, 2.33e-15

MP, EX, 2, 129e3
MP, PRXY, 2, 0.23
MP, DENS, 2, 2.33e-25

! Choose Elements
ET, 1, 42
ET, 2, 45

! select spring link and set to a different
material for massless springs
!asel, u, loc, x, -springL, springL,
springL*2
!aatt, 2

!set frame to rigid material
asel, s, area,, 16, 19
asel, a, area,, 35, 38
asel, a, area,, 54, 57

asel, a, area,, 73, 76

asel, a, area,, 106, 109
asel, a, area,, 125, 128
asel, a, area,, 144, 147
asel, a, area,, 163, 166

asel, a, area,, 184, 191
aatt, 2

alls

! Map mesh
ESIZE, 100
TYPE, 1 !assigns element
number to elements defined
MSHAPE, 0, 2D !use quads for
area
MSHKEY, 1 !mapped meshing

AMESH, ALL

TYPE, 2
EXTOPT, ACLEAR, 1 !remove
area meshes
EXTOPT, ATTR, 1, 0, 0
VDRAG, ALL, , , , , exline

nummrg, all

! Specify non-displacement boundary
conditions on the spring end faces
csys, 0
alls
asel, s, loc, x, 0
asel, r, loc, y, 0
asel, a, loc, y,
(nframe*(lt+st+sg+st+lt+ft)-ft)*2+mw
asel, r, loc, x, 0

da, all, ux, 0
da, all, uy, 0
da, all, uz, 0

alls

! apply BC on PM end for x1 mode – to
cross-check x1 mode
!asel, s, area,,545
!asel, a, area,,901

```

```
!alls
!nummrg, all
```

```
! Solve for the mode frequencies and
mode shapes
/SOLU
antype, modal, new
modopt, lanb, 10, 0, 1000,,off,,2
!use Blank Lanczos solver
mexpand,10,,0
!expand 10 modes
solve
!solve
```

! Use postprocessor (/POST1) to get the frequencies and mode shapes
! The layout is as seen in figure b4.

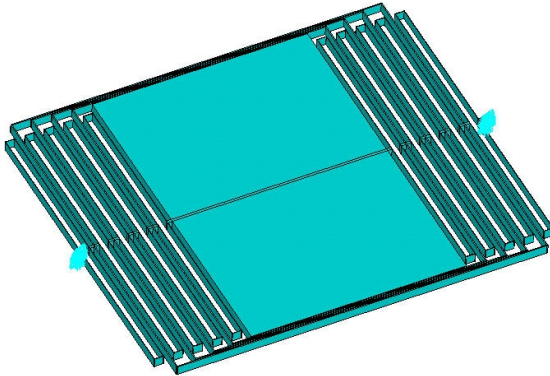


Figure b4: Suspension model with ability to set rigidity and mass on spring and frames to better correlate to the analytical model.

IV. Linkage stress analysis

The linkage geometry was exported from Vectorworks as an iges 3D model and then imported in Ansys Workbench. The anisotropic silicon material property were applied to the model and the deflection and stress at the linkages and spring end connectors was calculated as shown in figure b5.

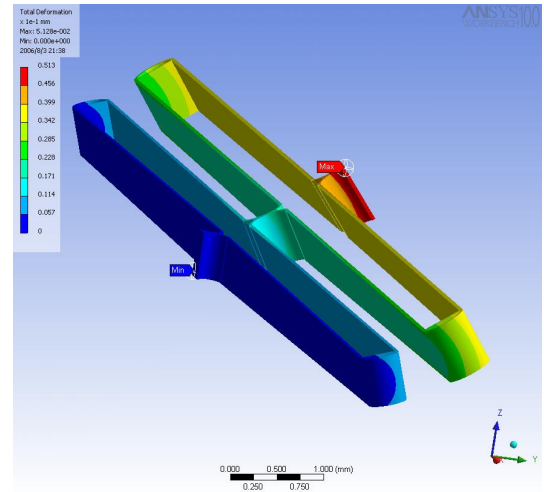


Figure b5: IGES CAD file imported from vectorworks used for doing the stress analysis in Ansys Workbench.

V. Magnetic simulation to calculate the bevelling angle for the pole pieces

! Microsiesmometer – magnetic circuit simulation
! Initial version: Kin Wei Lee, 17-04-03
! Modified Sunil Kumar, 20 April 2005
! Corners ~45degrees and large yoke

```
/prep7
```

```
! Define elements
et,1,53      !8-node mag solid
plane53
et,2,53,2   !AZ. CURR degrees of freedom
et,3,110    !2D infinite solid
```

```
! Define material properties
!1-air, 2-iron, 3-1st magnet(+), 4-2nd magnet(-)
```

```
mp,murx,1,1      !air
mp,murx,3,1.05   !magnet1
mp,mgyy,3,8.8e5  !magnet1
mp,murx,4,1.05   !magnet2
mp,mgyy,4,-8.8e5 !magnet2
mp,murx,5,1.02   !coil
```

```
!steel with made up b-h curve from
vm165
mat,2
/input,emagSa1010.SI_MPL
```

Appendix B

```

/prep7
!define parameters
solder_h = 48e-6      !gap between PM
die and DT die
frit_h = 1.5e-4      !gap between PM
die and Cavity die
glass_h = 1.1e-3     !thickness of
glass wafer used for making DT and
Cavity die

mass_w=10e-3        !proof mass
mass_h=525e-6      !wafer thickness

! Coil parameters
coil_I=1e-3         !coil current
coil_w=1e-3         !Width
coil_h=10e-6        !Height
coil_disp_x=0

gap_h=mass_h+2*glass_h+frit_h+solder_h
r_h      !vertical gap between magnet
pole pieces incl. yoke2
gap_w=2e-3
      !gap between pole pieces

yoke_h=4e-3         !yoke 1
yoke_w=16e-3

mag_h=1.5e-3        !magnet
mag_w=(yoke_w-gap_w)/2

y2_h=0.50e-3        !yoke2 - soft iron
yoke over magnet - thin one
y2_w1=mag_w

air_w=yoke_w*5
air_h=(gap_h+mag_h*2+yoke_h*2)*5

! Vary bevel1 and bevel2 to vary
parameters
bevel_y=yoke_h*.5
bevel1 = y2_h*7/5
      !700microns
bevel2 = y2_h*(1-.002)      !1
micron
inf_w=air_w
inf_h=air_h

! Draw Yokes
k,1,-yoke_w/2,gap_h/2+mag_h+y2_h
k,2,-
yoke_w/2,gap_h/2+mag_h+yoke_h-
bevel_y+y2_h
k,3,-
yoke_w/2+bevel_y,gap_h/2+mag_h+yoke_h+y2_h
k,4, yoke_w/2-
bevel_y,gap_h/2+mag_h+yoke_h+y2_h
k,5,
yoke_w/2,gap_h/2+mag_h+yoke_h-
bevel_y+y2_h
k,6, yoke_w/2,gap_h/2+mag_h+y2_h
a,1,2,3,4,5,6
xx=500e-6
yy=500e-6
cut_y=1.0e-3

cyl4,0,gap_h/2+y2_h+mag_h,gap_w/2

asba,1,2
arsym,y,all

! Draw Magnets
blc4,-
yoke_w/2,gap_h/2+y2_h,mag_w,mag_h

! Draw Pole pieces
k,123,-yoke_w/2,gap_h/2+bevel2
k,124,-yoke_w/2+bevel1,gap_h/2
k,125,-gap_w/2-bevel1,gap_h/2
k,126,-gap_w/2,gap_h/2+bevel2
k,127,-gap_w/2,gap_h/2+y2_h
k,128,-yoke_w/2,gap_h/2+y2_h

a,123,124,125,126,127,128

asel,s,loc,x,-yoke_w/2,-gap_w/2
arsym,y,all
asel,s,loc,x,-yoke_w/2,-gap_w/2
arsym,x,all
allsel

! Air area
blc4,-air_w/2,-air_h/2,air_w,air_h

! Draw coil
blc4,3.5e-
3+coil_disp_x,mass_h/2,coil_w,coil_h

```

Appendix B

```

blc4,-3.5e-3+coil_disp_x,mass_h/2,-
coil_w,coil_h
blc4,3.5e-3+coil_disp_x,-
mass_h/2,coil_w,-coil_h
blc4,-3.5e-3+coil_disp_x,-mass_h/2,-
coil_w,-coil_h

allsel
aovlap,all

!infinite element
k,,-inf_w,inf_h,0
k,,inf_w,inf_h,0
k,,inf_w,-inf_h,0
k,,-inf_w,-inf_h,0

! Infinite areas
a,kp(-
air_w/2,air_h/2,0),kp(air_w/2,air_h/2,0)
,kp(inf_w,inf_h,0),kp(-inf_w,inf_h,0)
a,kp(-air_w/2,air_h/2,0),kp(-
inf_w,inf_h,0),kp(-inf_w,-inf_h,0),kp(-
air_w/2,-air_h/2,0)
a,kp(-air_w/2,-air_h/2,0),kp(air_w/2,-
air_h/2,0),kp(inf_w,-inf_h,0),kp(-
inf_w,-inf_h,0)
a,kp(air_w/2,air_h/2,0),kp(inf_w,inf_h,
0),kp(inf_w,-inf_h,0),kp(air_w/2,-
air_h/2,0)

! Mesh lines
lsel,s,loc,x,-inf_w,-air_w/2
lsel,a,loc,x,inf_w,air_w/2
lsel,u,loc,y,-inf_h
lsel,u,loc,y,-air_h/2,air_h/2
lsel,u,loc,y,inf_h
lesize,all,,1
allsel

! Infinite surfaces
lsel,s,loc,y,inf_h
lsel,a,loc,y,-inf_h
lsel,a,loc,x,inf_w
lsel,a,loc,x,-inf_w
sfl,all,inf
allsel

! Select infinite areas only
asel,s,loc,x,-air_w/2,air_w/2
asel,r,loc,y,-air_h/2,air_h/2
asel,inve
!asel,s,area,,1,4
aatt,1,,3
allsel

! Select air only
asel,s,loc,x,0,0,0
asel,r,loc,y,0,0,0
cm,air,area
aatt,1,,1
allsel

! Select yokes
asel,s,loc,y,gap_h/2+mag_h+y2_h,gap_
h/2+mag_h+yoke_h+y2_h
asel,a,loc,y,-gap_h/2-mag_h-y2_h,-
gap_h/2-mag_h-yoke_h-y2_h
cm,yokes,area
aatt,2,,1
allsel

! Select bevel
asel,s,loc,y,gap_h/2,gap_h/2+y2_h
asel,a,loc,y,-gap_h/2,-gap_h/2-y2_h
cm,y2,area
aatt,2,,1!change 2 to 1 to make it look
like air
allsel

! Select left hand side magnets
asel,s,loc,x,-yoke_w/2,-gap_w/2
asel,u,loc,y,-gap_h/2-
y2_h,gap_h/2+y2_h
cm,l_mag,area
aatt,4,,1
allsel

! Select right hand side magnets
asel,s,loc,x,yoke_w/2,gap_w/2
asel,u,loc,y,-gap_h/2-
y2_h,gap_h/2+y2_h
cm,r_mag,area
aatt,3,,1
allsel

! Select coils attributes
asel,s,loc,y,mass_h/2,+gap_h/2
asel,a,loc,y,-mass_h/2,-gap_h/2
!asel,s,area,,20,22,2

```


Appendix B

```

!asel,a,area,,19,21,2
!aatt,5,1,2
!asel,s,area,,21,22
cm,coil_a,area
aatt,5,,1
allsel

! Set mesh attributes
esize,,10
mshape,0,2d
asel,s,loc,x,-air_w/2,air_w/2
asel,r,loc,y,-air_h/2,air_h/2
asel,inve
amesh,all
allsel

MSHAPE,1,2D

esize,500e-6
asel,s,loc,x,-air_w/2,air_w/2
asel,r,loc,y,-air_h/2,air_h/2
amesh,all
allsel

!coil parameters
esel,s,mat,,5
cm,coil,elem

coilcurrent=coil_I/10e-6**2
allsel
asel,s,mat,,5
fmagbc,'coil'

asel,s,area,,20,22,2
bfa,all,js,,-coilcurrent
asel,s,area,,19,21,2
bfa,all,js,,coilcurrent
allsel

allsel
lsel,s,loc,x,-air_w/2
lsel,a,loc,x,air_w/2
lsel,a,loc,y,-air_h/2
lsel,a,loc,y,air_h/2
dl,all,,all,0
allsel
finish

/solu
neqit,5

MAGSOLV,0,3,0.0001, ,25,

finish

! Postprocessing of results to save the
force value to file
/post1
fmagsum,'coil'

*get,fvwx,ssum,fvw_x
*get,fmx,ssum,fm_x
*cfdopen,forceresults10,txt,,append
*vwrite,coil_disp_x,fvwx,fm_x
('disp ',E8.2,' vw ',E20.14,' fmx
',E20.14)
*cfdclose
finish
*enddo

/post1
path,fluxline,2,5,200
ppath,1,,-yoke_w/2*(1+.2),mass_h/2,0
ppath,2,,yoke_w/2*(1+.2),mass_h/2,0
pdef,ffli,b,y
paget,palist,table
*cfdopen,pathlist-%gap_h%,txt
*vwrite,palist(1,5)
(f16.9)
*cfdclose

File: emagSa1010.SI_MPL – contains
B-H curve for SmCo magnet

! ANSYS $RCSfile:
emagSa1010.SI_MPL $
! Modified on $Date: 2001/05/29
17:39:40 $
! Source ID = $Revision: 10.1 $
/NOP
/COM,Internal UNITS set at file
creation time = SI (MKS)
/COM,SA1010 Steel
/COM,***** Typical B-H
properties for demo purposes
*****
TBDEL,ALL,_MATL
MPDEL,ALL,_MATL
TB,BH,_MATL,1,40
TBTEM,0.000000000E+00,1
TBPT,,90.0000000,0.500000000

```

Appendix B

TBPT,, 270.000000	, 1.00000000	TBPT,, 6081.34000	, 1.75825000
TBPT,, 318.250000	, 1.10000000	TBPT,, 8581.09000	, 1.80875000
TBPT,, 384.500000	, 1.20000000	TBPT,, 11066.4000	, 1.85000000
TBPT,, 479.500000	, 1.30000000	TBPT,, 14985.7000	, 1.90250000
TBPT,, 608.562000	, 1.38750000	TBPT,, 33003.3000	, 2.05000000
TBPT,, 755.437000	, 1.45000000	TBPT,, 59203.3000	, 2.15000000
TBPT,, 939.185000	, 1.50000000	TBPT,, 93214.9000	, 2.22625000
TBPT,, 1188.93000	, 1.54500000	TBPT,, 118884.000	, 2.27000000
TBPT,, 1407.93000	, 1.57500000	TBPT,, 163558.000	, 2.33375000
TBPT,, 2077.31000	, 1.62750000	TBPT,, 220788.000	, 2.40750000
TBPT,, 3117.93000	, 1.67375000	TBPT,, 373973.000	, 2.60000000
TBPT,, 3969.37000	, 1.70225000	TBPT,, 692281.000	, 3.00000000
TBPT,, 4843.66000	, 1.72750000	/GO	

Simulation layout is shown in figure b6 along with the magnetic vector lines.

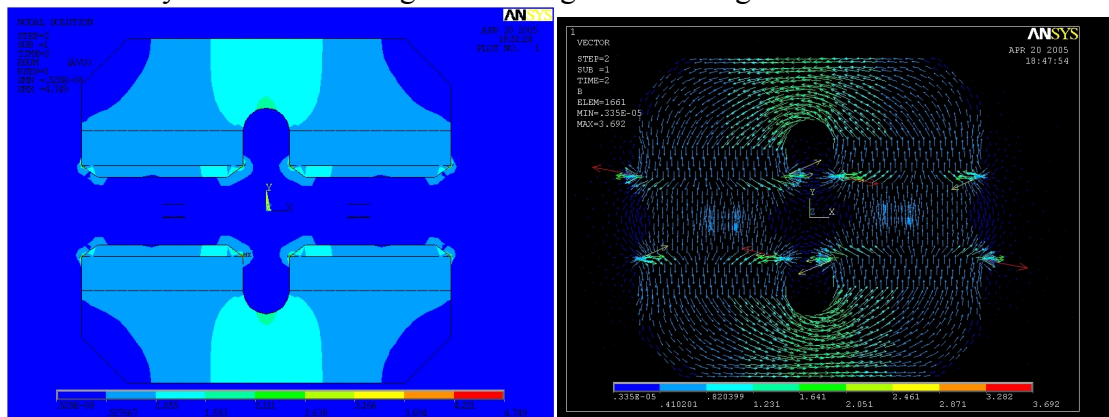


Figure b6: Layout of the magnetic assembly and the magnetic flux density vector lines.

B5. Bibliography

- [B.1] J. N. Reddy, *An introduction to finite element method*, 2 ed: McGraw-Hill, 1993.
- [B.2] Ansys Multiphysics, Ansys inc., Southpointe, 275 Technology dirve, Canonsburg, PA 15317 USA <http://www.ansys.com>.
- [B.3] W. A. Brantley, "Calculated elastic constants for stress problems associated with semiconductor devices," *Journal of Applied Physics*, vol. 44, pp. 534-535, 1973.
- [B.4] R. G. Grimes, J. G. Lewis, and H. D. Simon, "A shifted block lanczos algorithm for solving sparse symmetric generalized eigenproblems," *SIAM Journal Matrix Analysis Applications*, vol. 15, pp. 228-272, 1994.

Appendix C: Fabrication process flow

C1. Process Flow for Microseismometer Sensor Unit

Proof-mass (PM) wafer (n-type {100} Silicon - 525 micron thick)

	Description	Process name	Material	Thickness/depth
1	Oxide insulator layer on wafer	Oxidation	SiO ₂	200 nm
2	Photoresist for ohmic contact lift-off	Spin coat	SPR1813	1 micron
3	Oxide etch holes for ohmic contact	SiO ₂ etch	HF	
4	Lift-off - ohmic contact	Evaporation	AuSb/NiCr/Au	75nm/25nm/200nm
5	Photoresist strip	Strip	Acetone	
6	Anneal for ohmic contact	Anneal	Oven, 400C	
7	Deposit metal-1 layer	Sputter	Cr/Cu	15nm/200nm
8	Pattern metal-1 layer	Etch	Cr-etch/Cu-etch	
9	Photoresist strip	Strip	Acetone	
10	Insulator layer	Spin coat	Photoneece	3 micron
11	Pattern insulator layer	Expose UV	Aligner/Photoneece developer	
12	Anneal insulator layer	Anneal	Oven, 300C	
13	Electroplate seed layer	Sputter	Cr/Cu	15nm/200nm
14	Photoresist mold	Spin coat	AZ9260	9 micron
15	Electroplate metal-2	Electroplate	Cu	5 micron
16	Photoresist strip	Strip	Acetone	
17	Etch seed layer	Sputter etch	Sputter coater	
18	Backside Al layer	Evaporate	Al	500 nm
19	Photoresist for DRIE	Spin coat	AZ9260	14 micron
20	DRIE - Etch 1	DRIE	Si	400 micron
21	Backbond to handle wafer			
22	DRIE - Etch 2	DRIE	Si	125 micron
23	Release from handle wafer	Release	Acetone	

DT Capping wafer (Glass - Borosilicate - 1mm thick)

	Description	Process name	Material	Thickness/depth
1	Metal seed layer	Sputter coat	Cr/Cu	15 nm/200 nm
2	Electroplate Cu	Electroplate	Cu	5 micron
3	Electroplate Solder/Solder balls	Electroplate	Sn/Pb (~85%/15%)	40 micron
4	Remove seed layer	Sputter etch	Sputter coater	
5	Glue decal mask to the front and backside			
6	Etch Backside dicing lines	Sand blasting	High velocity SiO ₂	200 micron
7	Etch Frontside cavity	Sand blasting	High velocity SiO ₂	800 micron
8	Release decals	Release	Acetone	

Cavity Capping wafer (Glass - Borosilicate - 1mm thick)

	Description	Process name	Material	Thickness/depth
1	Glue deal mask to front and back of wafer			

2	Etch Backside dicing lines	Sand blasting	High velocity SiO ₂	200 micron
3	Etch Frontside cavity	Sand blasting	High velocity SiO ₂	800 micron
4	Release decals	Release	Acetone	
5	Screen print glass frit	Screen print	Glass frit	60 micron finally

Assembly

	Description	Process name	Material	Thickness/depth
1	Align Cavity capping and PM wafer	Reflow rig		
2	Reflow Glass frit	Reflow	Glass frit	365C
3	Align DT capping and PM wafer	Reflow rig		
4	Reflow solder	Reflow	Solder	185C

C2. DRIE Processing of Lateral Suspensions

(steps for suspension without metal traces)

- 1) Evaporate 500nm Aluminium in thermal evaporator
- 2) Dehydrate wafer in 110 °C oven for 30 min.
- 3) Remove from the oven and spin HMDS: spread@1000/1000/60” with lid open..
- 4) Dispense 5ml AZ9260 on wafer
- 5) Program spinner for photoresist coat: spread @ 500/500/10 with closed lid, then spin @ 1000/1000/60 with closed lid, then EBR with 4000/5000/2, closed lid.
- 6) After spin cycle allow to stand in spinner for 5 minutes after end of spin.
- 7) Place wafer on hotplate, switch ON hotplate (in case the plate is hot already cool it down by placing the chuck on a cold large metal sheet or under water).
- 8) Let the hotplate reach 60-70 °C, switch off hotplate and start timer for 3 min countdown.
- 9) Switch on hotplate again, let it reach 90 °C and then switch off and countdown on timer for 3 min.
- 10) Switch on hotplate and let it reach 116 °C, switch off and let the timer count down for 3 min.
- 11) Allow to cool and rehydrate for atleast 30 min or more before attempting exposure.
- 12) Clean proof mass wafer mask with acetone, IPA and DI, then blow dry.
- 13) Expose wafer with mask for 50 s at 5 mW/cm² wait 5 minutes and expose for another 40s at same settings.
- 14) Prepare 1:4 AZ400K:DI @ 25-27 °C, suggested quantity 200ml DI:50ml AZ400K
- 15) Develop for 6-7 minutes, stirring every minute – check that the pattern has developed cleanly in bigger areas and then develop for an additional 30 seconds.
- 16) Once pattern looks cleanly developed and all fine features are intact, dektak wafer to check resist thickness (8.5 µm).

- 17) Place wafer in System 80 for de-scum for 1 min with 60 sccm O₂ flow and 100W power to remove any leftover AZ9260 in developed regions.

ETCH 1

- 18) Etch wafer in STS ICP DRIE system using recipe DARK3S (Parameters same as) for 4 hours.
- 19) Unload wafer – check channel depth and calculate time required for etching through the wafer (nominal thickness = 525µm).

ETCH 2 – WITH HANDLE WAFER

- 20) Prepare handle wafer – Dehydrate bake SSP (single side polished) wafer at 150C for 15’.
- 21) Spin SPR 1813: spread @ 500/500/10 with open lid, then spin @ 1000/1000/20 with open lid.
- 22) Align the flats of device and handle wafer and press on the featureless portions to bond the wafers together.
- 23) Place the sandwich on a cold hotplate with max temp set to 116C.
- 24) Bake on the hotplate at 110°C for 1’.
- 25) After cooldown, place wafer sandwich in STS ICP DRIE for etching.
- 26) Set etch time to 30’ and watch the wafer to see the dies turning bright when the Al on backside starts getting exposed to plasma – etch for a further 15’ after the center die appears bright.

RELEASE

- 27) Place wafer sandwich in a beaker with 300ml acetone, cover with a Al foil and heat to 80C, leave for 30-60’ for the handle wafer to detach on its own.
- 28) Remove device wafer and place it in a clean acetone bath possibly at 80C to minimize temperature gradient.
- 29) Clean the device wafer using acetone, IPA and DI.
- 30) Break the wafer into dies.
- 31) Individually clean each die into acetone, IPA and DI.
- 32) Fill a small 200ml beaker with 50-100 ml of MF319
- 33) Place each die into MF319 – it takes about 7-10’ for the Al on wafer backside to etch off
- 34) Rinse the die in DI
- 35) Place each die on a wipe and blow dry the top portion
- 36) Lift gently (the die could be stuck to the wipe strongly due to the soaked DI so be careful) and turn it on its back – blow dry the other side.
- 37) Inspect in the microscope to check for any resist residue or dirt particles.

Page left blank intentionally

